Laser-driven discharges and electromagnetic fields

Philip Wykeham Bradford

Doctor of Philosophy

University of York

Physics

December 2020

0.1 Abstract

When high intensity lasers interact with solid targets, hot electrons are produced that can exit the material and leave behind a positive electric charge. As this accumulated charge is neutralised by a cold return current, radiation is emitted with characteristics dependent on laser and target properties. This thesis examines how electromagnetic radiation is emitted in experiments with long-pulse and short-pulse lasers.

Radiofrequency electromagnetic pulses emitted during ps-duration laser interactions can disrupt scientific measurements and damage electronic equipment close to the target. A study of electromagnetic pulses produced by the Vulcan laser is presented. Strong fields exceeding 100 kV/m and 0.1 mT were measured 1.5 m from the target using conducting probes. Scaling of the EMP field with laser and target parameters shows qualitative agreement with target charging models. A novel EMP mitigation scheme is presented using a dielectric spiral target holder. Experimental results are used to benchmark a frequency-domain dipole antenna model of EMP emission that connects charging physics to EMP fields measured at an arbitrary distance from the target.

In a separate experiment, coil targets were driven with three ns laser beams from the Vulcan laser, generating multi-tesla quasi-static magnetic fields. Dual-axis proton deflectometry was used to measure electric and magnetic fields around the coils. Results suggest that wire electric fields of order 0.1 GV/m develop on a 100 ps timescale. Maximum currents of 10 kA were observed towards the end of the laser drive for 1 mm- and 2 mm-diameter loop targets, corresponding to an axial magnetic field of $B_0 \approx 12$ T in the 1 mm loops. Deflectometry results agree well with a plasma diode model, whereas B-dot probe measurements of the magnetic field were approximately $10\times$ larger. Analytic and computational modelling of charged particle motion in electric and magnetic fields is presented. Prospects for an all-optical platform for magnetized high energy density physics experiments are discussed.

Contents

List of Tables

List of Figures

0.2 Acknowledgements

I have spent a considerable amount of time 'on experiment' during my PhD and I owe a tremendous debt of gratitude to all those who helped me at the CLF, CELIA, Livermore and LULI laboratories. I would also like to thank the following people in particular:

M. P. Read, A. Dearling, L. Antonelli, L. Döhl, M. Khan, C. Arran and the entire

2016-entry York Plasma Institute CDT cohort for your support and friendship.

P. Hill and C. P. Ridgers for making me laugh and for teaching me that computers are not to be feared.

M. Ehret, J.J. Santos, J.-L. Dubois, D. Blackman, J. Trela and V. Tikhonchuk for making my collaboratory project so enjoyable, for sharing your work and expertise with me and for introducing me to Bordeaux culture.

V. Ospina, X. Vaisseau, S. Malko for keeping me company in Paris and for being such fun inside and outside the LULI laboratory.

C. Danson for advice on everything from high power lasers to birdwatching. Also for your friendship and good times in York and Saint Malo.

A. Poyé, D. Minenna, G. Hicks, G. G. Scott, Y. Zhang, G.-Q. Liao, H. Liu and Y.-T. Li variously for your warmth and assiduity, for the great opportunities you have given me and ultimately for pulling me up behind you.

F. Consoli for making me feel at home all over the world. If my PhD had been longer (or I had been a better student) it would have been wonderful to have worked more closely with you and your colleagues.

D. Carroll, M. Notley and P. Oliveira for your sage advice and selfless efforts over the course of several experiments.

B. Pollock and J. Moody for numerous insights and interesting discussions. I never finished a conversation with you without fresh ideas and an afterglow of excitement.

D. Cook and Lawrence Livermore National Laboratory for their financial support, for enabling me to see fireflies and hummingbirds and for teaching me how to escape from minefields.

Sincere thanks to my supervisor Prof. Nigel Woolsey, who has consistently believed in me and pushed me to the limits of my potential. You have completely changed the way I look at the world and I am grateful for the opportunities you deliberately sent my way. Though I have little else in common with the 1^{st} Earl of Essex, like him I am immensely proud of having been taught by a Wo(o)lsey.

Some debts are too great to be reckoned, but I would like to thank my brother and parents nonetheless.

Finally, I dedicate this thesis to the memory of Prof. David Neely, who was instrumental in its completion and who taught me how to think as a scientist.

0.3 Declaration

The experimental results described in this thesis were taken from the Vulcan laser with the help of many people. Except where cited or otherwise explicitly stated, the analysis of results was conducted by the author. The author also contributed towards planning, set-up and measurement procedures on each experiment. I would like to add that the cable correction calculations in Sec. 3.2 were completed with the help of M. Ehret and the frequency-domain dipole model in Sec. 4.4 was created by V. Tikhonchuk, A. Poyé and D. Minenna.

I, Philip Wykeham Bradford, declare that this thesis is a presentation of original work and that I am the sole author. This work has not previously been presented for an award at this, or any other, university. All sources are acknowledged as references.

The following publications contain work that is discussed in this thesis:

1. P. Bradford, N. C. Woolsey, G. G. Scott, G. Liao, H. Liu, Y. Zhang, B. Zhu, C. Armstrong, S. Astbury, C. Brenner, P. Brummitt, F. Consoli, I. East, R. Gray, D. Haddock, P. Huggard, P. J. R. Jones, E. Montgomery, I. Musgrave, P. Oliveira, D. R. Rusby, C. Spindloe, B. Summers, E. Zemaityte, Z. Zhang, Y. Li, P. McKenna and D. Neely, "EMP control and characterization on high-power laser systems". In: *High Power Laser Science and Engineering*, 6 (2018), E21. DOI: 10.1017/hpl.2018.21

2. P. Bradford, M. P. Read, M. Ehret, L. Antonelli, M. Khan, N. Booth, K. Glize, D. Carroll, R. J. Clarke, R. Heathcote, S. Ryazantsev, S. Pikuz, C. Spindloe, J. D. Moody, B. B. Pollock, V. T. Tikhonchuk, C. P. Ridgers, J. J. Santos and N. C. Woolsey, "Proton deflectometry of a capacitor coil target along two axes". In: *High Power Laser Science and Engineering*, 8 (2020), E11. DOI: 10.1017/hpl.2020.9

3. D. F. G. Minenna, A. Poyé, P. Bradford, N. Woolsey, and V. T. Tikhonchuk, "Electromagnetic pulse emission from target holders during short-pulse laser interactions". In: *Physics of Plasmas*, 27.6 (2020), p. 063102. DOI: 10.1063/5.0006666

4. F. Consoli, V. T. Tikhonchuk, M. Bardon, P. Bradford, D. C. Carroll, J. Cikhardt, M. Cipriani, R. J. Clarke, T. E. Cowan, C. N. Danson, R. De Angelis, M. De Marco, J.-L. Dubois, B. Etchessahar, A. L. Garcia, D. I. Hillier, A. Honsa, W. Jiang, V. Kmetik, J. Krása, Y. Li, F. Lubrano, P. McKenna, J. Metzkes-Ng, A. Poyé, I. Prencipe, P. Rączka, R. A. Smith, R. Vrana, N. C. Woolsey, E. Zemaityte, Y. Zhang, Z. Zhang, B. Zielbauer and D. Neely, "Laser produced electromagnetic pulses: Generation, detection and mitiga-

tion". In: *High Power Laser Science and Engineering*, 8 (2020), E22. DOI: 10.1017/hpl.2020.13

Part I

Introduction

Chapter 1

Plasmas, ICF and EM fields

The emission of hot electrons from a high power laser target generates a positive potential that draws a neutralisation current from the nearest ground. As this neutralisation current travels along the target holder towards the laser focal spot, radiation is emitted according to the amplitude and duration of the target potential, as well as the material and geometry of the target itself. Laser targets can be designed to direct currents along metal wires or miniature coils, producing electromagnetic fields greater than $E = 100$ kVm^{-1} and $B = 10$ T in magnitude. These electromagnetic fields can then be used for a range of applications across high energy density physics.

The applications of electromagnetic fields generated by charge accumulation in solid targets depend on the intensity of the laser interaction. Laser technology has divided high power laser physics into two principal regimes: a lower intensity regime ($I_L \lesssim 10^{17}$ Wcm^{-2}) produced by 'long-pulse' lasers with relatively high energies and pulse durations of 1 ns or longer, and a higher intensity regime ($I_L \gtrsim 10^{17}$ Wcm^{-2}) corresponding to 'short-pulse' lasers that are generally less energetic and have pulse durations of under ~ 10 ps. This thesis deals with the generation and characterisation of electromagnetic fields by high power lasers in both long- and short-pulse regimes, covering intensities from $10^{14} - 10^{19}$ Wcm^{-2}. In the long-pulse regime, energetic lasers have been used to drive currents exceeding 10 kA in wires connected to metallic disk targets [19, 158, 46]. If the wires are bent into loops or coils, magnetic fields tens to hundreds of tesla in strength can be generated in millimetric volumes. These fields are quasi-static on a ns-timescale and reasonably uniform along the coil axis, which means they are well-suited to experiments at high energy density. Studies suggest that kT-level magnetic fields can be used to trap fusion alpha particles and hot electrons, relaxing implosion requirements for ignition in inertial confinement fusion [90, 138]. Strong magnetic fields can also be used to enhance relativistic electron beam transport [10, 33] or to create conditions relevant to astrophysics in the laboratory [182, 79, 39]. At higher laser intensity, potent

electromagnetic pulses are generated at GHz frequencies that last up to several hundred ns. While these fields can pose a problem for electronic devices close to the laser target, experiments have shown they can be used to manipulate the energy and divergence of charged particles [97, 173]. More broadly, understanding hot electron dynamics at the target-vacuum interface is important for increasing the energy of laser-driven ion beams [121, 133], for optimizing x-ray and THz radiation sources [110, 109, 6] and minimizing fuel pre-heat in inertial confinement fusion [160].

A major outstanding problem is developing accurate models of electron emission and target discharge so that laser-driven electromagnetic fields can be enhanced in some situations and minimised in others. For example, a new generation of lasers with powers $\gtrsim 10$ PW are expected to produce MVm^{-1} EMP fields that could destroy electronics and hamper experimental progress [29]. Building on contemporary models of laser-induced charging, it may be possible to reduce these EMP fields [27] or develop targets that produce bespoke magnetic field profiles for applications [28].

Before electromagnetic emission from laser-irradiated solid targets can be discussed in detail, it is first necessary to understand the plasma state, the mechanisms that give rise to hot electrons and how they escape the laser target. This thesis is therefore divided into three parts. The first part introduces key plasma physics concepts and looks at the state of the art in laser-induced electromagnetic field generation prior to the experiments reported in Part III. The second part describes the theory of laser-target charging and introduces several diagnostics used to measure electromagnetic fields in experiments at high energy density. Finally the third part contains experimental results and conclusions.

1.1 The Plasma State

1.1.1 Definition of a Plasma

Plasma is the most abundant of the four states of ordinary matter, occurring naturally in stars, interstellar space and planetary atmospheres throughout the visible universe. On Earth, plasma can be created artificially by heating a neutral gas to the point of ionisation or through application of a strong electric field. A formal worded definition of a plasma is provided by F. Chen [36]:

"[A plasma is] a quasi-neutral gas of charged and neutral particles that exhibits collective behaviour."

A quasi-neutral medium contains an equal number of positive and negative charges overall, but allows concentrations of charge to develop locally. In a plasma, currents and charges can build up and produce electric and magnetic fields that affect particles far away. This 'collective' behaviour is important because it distin-

guishes plasma motion from ideal fluid and molecular motion, which is determined entirely by collisions.

Plasmas can be successfully described on a number of different levels according to context. A major challenge of plasma modelling is that one must account for different particle species with very different masses (protons are almost 2000× heavier than electrons) and therefore different response times. A single plasma can support particle populations with different temperatures that respond over a range of spatial and temporal scales. In order of decreasing accuracy, plasmas can be viewed: on a particulate level, where we examine the individual motion of constituent particles using Maxwell's equations and the standard equations of motion in vacuum; using kinetic theory, where distribution functions are used to make statistical approximations of large numbers of particles; or using a fluid model, like magnetohydrodynamics, that considers averaged quantities (moments of the particle distribution function e.g. density) in local thermodynamic equilibrium under certain assumptions of closure; then there are situations, usually at high temperature, when radiation effects must be considered. Each treatment has its advantages and disadvantages and different regimes of applicability. It is frequently impractical to calculate the motion of lots of plasma particles individually, though particle-in-cell (PIC) computer codes can produce very accurate results if spatial and temporal scales are kept relatively small. A PIC code uses aggregate super-particles to approximate the motion of large numbers of smaller particles. These super-particles move continuously through space, while moments of the distribution, as well as electric and magnetic fields, are calculated on a fixed grid of points [4]. Solving for plasma properties on larger spatial and temporal scales requires fluid or kinetic codes. Generally speaking, kinetic theory is used to describe plasmas outside of thermodynamic equilibrium, where particle kinetic energy dominates over the electrostatic potential, while fluid theories apply to plasmas where local thermodynamic equilibrium can be assumed.

Before a quantitative understanding of plasma can be developed, it is important to make a short comment on the definition of temperature. Plasma particles with mass m and temperature T have an associated thermal velocity v_{th} that is defined by $k_B T = \frac{1}{2} m v_{th}^2$ [36]. The quantity $k_B T$ represents the average kinetic energy of the particles and $k_B = 1.38 \times 10^{-23}$ JK^{-1} is the Boltzmann constant. In this thesis, whenever the plasma temperature appears in a formula it will be quoted in units of energy that can be converted to kelvin using:

$$T_J = k_B T_K$$

where T_J is the kinetic temperature measured in joules and T_K is the temperature measured in kelvin. It is also common to quote the temperature in units of electron-

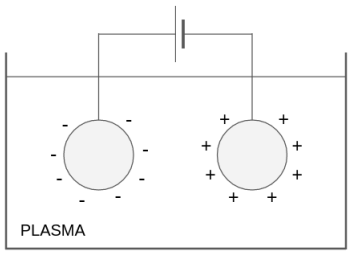

Figure 1.1: Two electrodes suspended in a plasma will attract a thin layer of charge that screens the electrode voltage from the surrounding material.

volts (eV) or kilo-electron-volts (keV). Where this occurs in the text it is explicitly stated.

1.1.2 Debye Shielding

A signal property of plasma is its ability to quickly screen internal electric fields in a process called *Debye shielding* [36]. Consider two electrodes that are maintained at fixed potential V and immersed in a bath of plasma as shown in Fig. 1.1. Almost immediately, free charges will move to screen the voltage on the electrodes. If the particles in the plasma have no thermal motion themselves, each electrode will accrete an infinitely thin layer of charge that screens the electrode potential from the main body of the plasma. If, however, the plasma particles have an associated temperature, the shielding will take place over a finite width that increases with temperature. In the limit that the particle kinetic energy is comparable to the electrode potential, the particles will no longer be confined by the electrode potential well, shielding will no longer be perfect and a potential can extend into the plasma bulk. We will use this concept of distributed screening in our definition of a quasi-neutral plasma.

A numerical value for the width of the plasma sheath around each electrode can be derived using a kinetic model in one dimension. The sheath width is estimated based on the spatial variation of the plasma potential $V(x)$ around each electrode. Suppose a positive point electrode with potential V_0 is located at position $x = 0$. Consider also a singly-ionised plasma ($Z = 1$) with ion charge $q_i = -q_e = e$. Since ion inertia dominates over electron inertia, the ions are assumed to be stationary and uniformly distributed with $n_i = n_\infty$. Far away from the potential, the electrons will have the same density as the ions ($n_e \to n_\infty$ as $x \to \infty$). Poisson's equation linking charge density and potential in one dimension is:

$$\frac{d^2V}{dx^2} = -\frac{e}{\epsilon_0}(n_i - n_e) \tag{1.1}$$

where ϵ_0 is the permittivity of free space. We will assume the electrons are in collisional equilibrium and have a 1D Maxwell-Boltzmann distribution:

$$f_e(E) = n_e \left(\frac{m_e}{2\pi T_e}\right)^{\frac{1}{2}} e^{-\frac{E}{T_e}}$$

where $E = m_e v^2/2 - eV$ is the non-relativistic electron energy, v is the corresponding electron velocity and m_e the electron mass. Expanding in terms of the electron energy, we find:

$$f_e(v, V) = n_e \left(\frac{m_e}{2\pi T_e}\right)^{\frac{1}{2}} e^{-\frac{m_e v^2}{T_e}} e^{\frac{eV}{T_e}}$$

Notice that this equation reduces to the standard expression for a 1D Maxwellian velocity distribution when $V = 0$. By definition of the distribution function[1],

$$n_e(V) = \int_{-\infty}^{\infty} f_e(v, V) dv = n_\infty e^{\frac{eV}{T_e}}$$

which is the Boltzmann relation for electrons, where we have observed that $n_e(V \to 0) = n_\infty$. Substituting the Boltzmann relation into the Poisson equation, we have

$$\frac{d^2V}{dx^2} = -\frac{en_\infty}{\epsilon_0}\left(1 - e^{\frac{eV}{T_e}}\right)$$

Though there is no analytic solution for $V(x)$, we can restrict ourselves to a limiting regime where $eV/T_e \ll 1$; that is, we assume the thermal energy of the electrons is much greater than their potential energy (we might also look for a solution far away from the electrode). Taylor expanding the exponential up to the second term yields:

$$\frac{d^2V}{dx^2} \approx \frac{e^2 n_\infty}{\epsilon_0 T_e} V$$

If we then define

$$\lambda_D = \sqrt{\frac{\epsilon_0 T_e}{e^2 n_\infty}}$$

we can integrate and apply boundary conditions on V ($V \to -\infty$ as $x \to -\infty$ and $V(0) = V_0$) to yield the solution

$$V(x) = V_0 e^{-x/\lambda_D}$$

[1] In plasma physics, the Maxwell-Boltzmann probability density function is multiplied by the particle density so that $\int_{-\infty}^{\infty} f_e(v) dv = n_\infty$

The Debye length, λ_D, is a proxy for the width of the sheath around each electrode. If L is the characteristic size of the plasma, we require that $\lambda_D \ll L$ for a plasma to be considered "quasi-neutral".

1.1.3 Plasma Parameter and Plasma Frequency

Two further conditions are required to complete our definition of a plasma. First of all, it is important to notice that the Debye shielding mechanism can only proceed if there is a sufficient number of free charges within the plasma to counteract an applied voltage. For the case of a point electrode, this can be quantified using the dimensionless plasma parameter:

$$\Lambda = \frac{4}{3}\pi\lambda_D^3 n$$

where n is the particle number density and Λ represents the number of free charges in a sphere surrounding the electrode with radius λ_D. If $\Lambda \gg 1$, the sheath will contain enough ions to neutralise a given potential. In many solid-density plasmas produced by laser ablation, however, Λ is small and so the ideal-plasma approximation is invalid.

The final condition in our definition of a plasma requires that the plasma responds faster than the collisions between ions and neutral particles. When this is true, electromagnetic interactions will dominate over the hydrodynamics of an ordinary gas and the plasma exhibits 'collective behaviour'. In quantitative terms, if ω_p is the frequency of plasma oscillations (usually the electron frequency) and τ is the time between particle collisions, then a plasma must satisfy $\omega_p\tau > 1$.

The plasma frequency defines the plasma temporal response to external electric fields. Consider a uniform plasma where the entire electron population is suddenly displaced by some small distance relative to a background of fixed ions. The electrons will experience an electrical restoring force that leads to simple harmonic motion with a characteristic oscillation frequency ω_p. More generally, the non-relativistic plasma frequency for an arbitrary particle species is:

$$\omega_p = \sqrt{\frac{ne^2}{\epsilon_0 m}} \tag{1.2}$$

where m is the particle mass, n the number density and e the unit charge. Different particle species oscillate at different speeds according to the $\sqrt{1/m}$ dependence of ω_p. Since electrons are much less massive than ions, the electron frequency ω_{pe} is much higher and usually more important. Plasma behaviour can only be observed on timescales longer than a plasma period $t_{pe} = 1/\omega_{pe}$.

Definition of a Plasma

Plasma behaviour is only observed on length scales longer than a Debye length and timescales longer than a plasma period. A plasma must be quasi-neutral and behave collectively. In other words, it must satisfy three quantitative conditions:

1. $\lambda_D \ll L$
2. $\Lambda \gg 1$
3. $\omega_p \tau > 1$

1.2 Inertial Confinement Fusion

Inertial confinement fusion (ICF) is a major branch of fusion research and laser-plasma physics that attempts to induce fusion by rapidly compressing small capsules of fuel. As the name suggests, ICF relies on material inertia to keep the fuel together long enough for a significant fraction of it to fuse. Energy is liberated as lighter elements fuse into heavier elements and release energy. Some of this energy can be used to heat the fuel and sustain the fusion reaction. The fusion fuel is therefore able to ignite and burn under certain conditions of high temperature and density [56]. Applications of ICF are strongly dependent on the energy gain of an ICF reaction. Defining 'energy gain' as the energy of the useful fusion products divided by the energy delivered to the fusion fuel, a gain of order ~ 100 could enable laser-driven ICF to become a viable source of electrical energy[2].

The favourite ICF fuel is currently a 50:50 mixture of deuterium (D) and tritium (T) with fusion reaction:

$$\mathrm{D} + \mathrm{T} \rightarrow \mathrm{n}\ (14.1\ \mathrm{MeV}) + {}^{4}\mathrm{He}\ (3.5\ \mathrm{MeV})$$

The DT reaction has the highest fusion cross-section at temperatures below 100 keV and produces two energetic fusion products: an α-particle and a neutron [20]. Some of the energy from the α-particles will be deposited in the fuel, allowing for the possibility of self-heating and runaway burn if the fuel areal density is high enough to confine the heating to a small volume. Fusion neutrons can then be used for a variety of applications, including the production of electrical energy. Existing

[2]This high gain is needed primarily because the conversion efficiency of the laser amplification process is extremely low ($\lesssim 1\%$) on existing flashlamp-pumped laser systems like the National Ignition Facility [166]. Improvements in laser technology, such as the use of diode-pumped lasers, could reduce the required gain considerably [15].

designs for inertial fusion plants require fusion neutrons to deposit their energy in a lithium-based heat exchanger that boils water to power a steam turbine and breeds T for use in future fusion reactions [60, 126].

A typical fuel capsule is spherical in shape and a few mm in radius; it consists of a solid (low-Z) outer shell called an *ablator*, followed by a layer of DT ice and a gaseous DT core [20]. Some advanced capsule designs feature multi-layered ablators with high-Z material dopants [65]. Rapid heating of the ablator causes it explode outwards and compress the DT fuel, which implodes by conservation of momentum. When the capsule stagnates at the point of maximum compression, the kinetic energy of the imploding material is converted to internal energy. Implosion velocities exceeding 0.3 mm/ns are needed to form a hot spot at the requisite temperature and areal density to overcome radiative and thermal losses [162].

Two primary methods have been proposed to heat the ablator and drive an implosion. In *direct drive*, laser beams illuminate the capsule surface directly [111]. In *indirect drive*, the capsule is enclosed in a high-Z cylindrical canister called a hohlraum. Laser beams enter through holes along the hohlraum axis, irradiating its inner surface and generating a bath of thermal X-rays that drive ablative compression of the capsule. The chief advantage of indirect drive over direct drive is that it relaxes conditions on laser beam uniformity. In both techniques, laser spatial and temporal profiles are chosen so that a dense sphere of cold fuel surrounds a lower density hot spot at stagnation. High gain is achieved by designing the implosion so that only a small, central portion of the fuel is heated to ignition. The surrounding fuel is kept cold, which minimises the energy required to compress it to high density. When the hot spot ignites, a burn wave propagates outwards into the cool, dense outer layers.

The most energetic laser ICF experiment is located at the National Ignition Facility (NIF), which implodes DT capsules via indirect drive. So far, the fusion yield is too low to initiate α-particle bootstrap heating and the fuel is compressed to approximately half the value required for ignition [138]. Major processes that limit the implosion performance are implosion symmetry and the growth of hydrodynamic instabilities as the fuel is compressed. In order to achieve maximal heating and compression of the fuel, it is vital the capsule implosion proceeds as uniformly as possible. For example, if the capsule is heated more strongly at the poles than on the equator, the implosion will form a pancake and compression will be reduced versus a spherical implosion. An imploding fuel capsule is susceptible to the growth of hydrodynamic instabilities throughout the implosion. Rayleigh-Taylor and Richtmeyer-Meshkov instabilities break up the capsule, mix ablator material into the DT fuel and radiatively cool the hot spot. This reduces the hot spot temperature, quenching the fusion reactions and lowering the neutron yield [135].

1.2.1 Magnetized laser-driven ICF

Reducing energy transport out of the fusion hot spot is essential to initiating thermonuclear burn in ICF [35]. In the magnetized ICF scheme, a magnetic field is used to improve thermal insulation of the hot spot. This keeps the hot spot hot and reduces pre-heating of the surrounding cold fuel, thereby relaxing stringent requirements on implosion symmetry and velocity [162]. A diagram of the magnetized ICF scheme can be seen in Fig. 1.2, where a uniform 'seed' magnetic field is applied along one axis of a standard fusion capsule prior to compression. If the magnetic field is sufficiently strong, it will inhibit the motion of hot electrons and α-particles perpendicular to magnetic field lines, increasing the hot spot temperature and enhancing the fusion yield.

To significantly modify particle trajectories in the fusion hot spot the magnetic fields must be very large - much larger than can be produced by a strong permanent magnet ($\sim$ 1 T) [54]. A charged particle of mass m and charge q moving perpendicular to a magnetic field B with speed $v_\perp$ will execute Larmor orbits at frequency $\omega_L = qB/\gamma m$ and radius $r_L = \gamma m v_\perp / qB$. Here, $\gamma = 1/\sqrt{1-(v/c)^2}$ is the relativistic Lorentz factor and v the overall particle speed. The dependence of these quantities on the particle charge-to-mass ratio shows it is much easier to magnetize electrons than ions at a given energy. Taking the product of the particle Larmor frequency and collision period yields the Hall parameter, $\omega_L \tau$, which can be used to quantify the degree of magnetization. If $\omega_L \tau > 1$, the magnetic field will have a bigger impact on particle motion than collisions and the species can be said to be magnetized. For a typical hotspot density of $\rho = 30$ gcm^{-3} and temperature $T_e = 5$ keV, a magnetic field exceeding $\sim$ 1 kT is needed to ensure the electrons satisfy $\omega_L \tau > 1$ [90]. Confining α-particle heating to the hot spot region requires that their Larmor radius be of order the hot spot radius. For 3.5 MeV α-particles and a hot spot radius of $r_{spot} \sim 40$ μm this requires a magnetic field of $\sim$ 7 kT [90].

We will see in Sec. 1.3 that kT-level magnetic fields are difficult to generate directly, however magnetic flux compression can amplify seed fields of a few tesla by factors of a hundred or more [138]. In ideal magnetohydrodynamics (MHD), where the resistivity of a fluid is ignored and conductivity is infinite, Alfvén's theorem states that magnetic field lines are fixed such that they will have to follow precisely the motion of the fluid. This means that if the fluid is compressed the magnetic flux density will increase commensurately (see Fig. 1.2). By conservation of magnetic flux, we have:

$$B_1 = B_0 \left(\frac{r_1}{r_0} \right)^2 \tag{1.3}$$

where B_0/B_1 and r_0/r_1 are the magnetic field and capsule radius at the point of minimum/maximum compression. Taking plasma resistivity into account, the magnetic

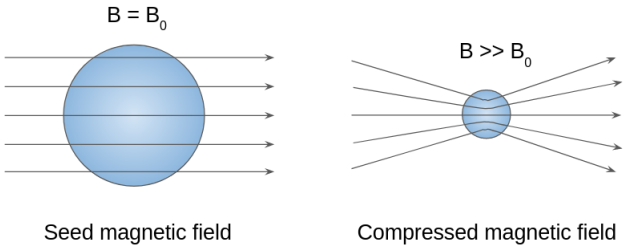

Figure 1.2: In magnetized ICF, a seed magnetic field is applied along one axis of a standard fusion capsule. Assuming ideal MHD, the magnetic field is trapped when the capsule is ionized and the magnetic flux density increases as the capsule is compressed.

field will diffuse through the fluid at a finite speed. The importance of magnetic diffusion can be estimated by comparing two characteristic times: the magnetic diffusion time $\tau_B = r_0^2/D_B$, where D_B is the magnetic diffusivity, and the implosion time $\tau_i = r_0/v_i$, where v_i is the implosion velocity. The standard formulation of the magnetic Reynolds number is $\mathrm{Re}_m = Lv/D_B = r_0 v_i/D_B$ for a fusion capsule, where I have taken the spatial scale L and characteristic velocity v of the flow to be r_0 and v_i respectively. Rewriting in terms of our characteristic times, $\mathrm{Re}_m = \tau_B/\tau_i$ and Eq. (1.3) can be generalised to:

$$B_1 = B_0 \left(\frac{r_1}{r_0}\right)^{2(1-1/\mathrm{Re}_m)}$$

For a typical ICF implosion velocity of ~ 0.3 mm/ns, the fuel is ionised and compressed sufficiently quickly to satisfy $\mathrm{Re}_m \gg 1$ and trap the magnetic field [90]. Neglecting extended MHD effects such Nernst advection and Righi-Leduc heat flow [172], an ICF implosion with radial convergence factor ~ 30 will amplify a seed magnetic flux density by ~ 900 times.

As the capsule implodes and magnetic field lines are compressed, they will exert a pressure $B^2/2\mu_0$ that counteracts the implosion perpendicular to the magnetic field axis. MHD simulations suggest that plasma ablation pressure dominates the implosion dynamics, with an insignificant impact on capsule compression and initial hot spot geometry from an imposed magnetic field of $B_0 < 10$ T [100]. Seed fields of $B_0 \geq 100$ T may deform the hotspot and reduce the fusion yield, though there is evidence to suggest that magnetic stabilization of the RT instability may prove beneficial [138].

The potential of the magnetized ICF scheme has been demonstrated in experiments on the OMEGA laser [100, 35, 90]. In Ref. [90], a pulsed power delivery system called MIFEDS was used to generate seed fields of ~ 8 T in a deuterium

gas-filled fusion capsule. Using proton radiography, these fields were measured to have amplified to 4 kT at stagnation. Implosions with an applied magnetic field enhanced the ion temperature by $\sim 15\%$ and increased the neutron yield by $\sim 30\%$ versus unmagnetized shots. Recent work by J. Moody *et al.* [128] has identified hohlraum materials that will allow strong magnetic fields to be used in an indirect drive scheme, with a reduced impact on target preheat and laser alignment.

Building on these results will require more experiments with strong magnetic field sources and an improved understanding of how magnetic fields are transported in high energy density plasmas. Two-dimensional MHD simulations suggest that though there is a clear temperature and fusion yield enhancement for magnetized implosions, there may be a maximum desirable seed magnetic field [138]. If the seed magnetic field is too strong, an α-particle burn wave will propagate along the magnetic field axis rather than isotropically and so fusion yields will be lower. There are also extended MHD processes to consider, of which the most important is likely the Nernst advection of magnetic fields down temperature gradients [87]. Nernst advection inside a fusion hot spot can pull an applied magnetic field out of the hot spot and degrade its insulating properties.

1.3 Pulsed Power Devices

If one would like to generate a magnetic field that exceeds the maximum field achievable by a permanent magnet ($B \sim 1$ T), the standard approach uses a circulating current to induce a magnetic field via Faraday's Law. The strongest fields achieved in the laboratory without magnetic flux compression use pulsed power devices to discharge a network of capacitor banks through a current delivery system such as a single wire loop, solenoid or Bitter plate assembly.

The magnetic fields that can be produced by pulsed power devices are several hundred tesla higher than can be generated by superconducting magnets. Some recent records include 23.5 T for a superconducting magnet, 45.5 T for the highest steady field from a composite superconducting and resistive magnet [85] and 300 T for the highest uncompressed single shot field from a pulsed power device [54]. The maximum magnetic field attainable by pulsed power is limited by the available electrical energy, material strength and cooling rate [54]. Higher fields can be reached in a destructive manner using explosive flux compression [32, 75] or theta-pinch machines [131], though these experiments take place at dedicated facilities with specialist infrastructure and require the current delivery system to be replaced after each discharge.

The magnetic fields produced by pulsed power devices have many useful properties that make them ideal for studies of high energy density physics. They are

reproducible, relatively easy to characterize, high efficiency and can be generated over large (cm-scale) volumes. Pulsed power magnetic fields are also ideally suited to Z-pinch experiments and the MagLIF [162] fusion scheme, where they can be used to drive the compression of fusion fuel, stabilize Rayleigh-Taylor perturbations and trap charged particles [86]. On the other hand, there remain practical obstacles to using pulsed power devices in many high power laser experiments and to laser-driven ICF in particular. The equipment required for pulsed power delivery takes up space that may degrade irradiation uniformity and limit diagnostic access to the target. There are also questions of cost and operating personnel that must be considered. One of the major goals of this thesis is to develop an optical, open-geometry magnetic field source that can be easily fielded in experiments with high power lasers.

1.4 Capacitor Coils

I prefix this section on optical sources of magnetic fields by quoting J. F. Seely from his 1983 paper on the same subject [158]:

When a plasma is created by focusing an intense laser beam onto a solid target, density and temperature gradients occur which generate large electron currents and magnetic fields. The field strength in the plasma near the surface of the target is believed to be as high as [1 kT]. This is greater than the magnetic fields that are available from the more conventional field generation devices such as capacitor-driven coils, and it is interesting to consider the conditions under which a laser-driven field would be useful for high-field material studies. One requirement is that the laser-driven electron current must be diverted into an external coil so that a material sample in the bore of the coil can be isolated from the interaction region.

The interaction of an intense laser with a solid target can produce electron currents and circulating magnetic fields of order 1 kT [17]. Strong magnetic fields ($\sim$ 100 T) may also arise spontaneously out of plasma flows with crossed density and temperature gradients[3] or from laser-plasma instabilities [156, 21]. While these spontaneous magnetic fields are strong enough to be used for a range of applications, they are embedded in a plasma and cannot easily be applied to material samples [184].

The first study of optical sources of magnetic fields was recorded by Korobkin and Motylev in 1979, where a 2 kA current was generated in a small loop of wire by

[3]More information about the Biermann Battery mechanism can be found in Ref. [88, 164, 165, 84].

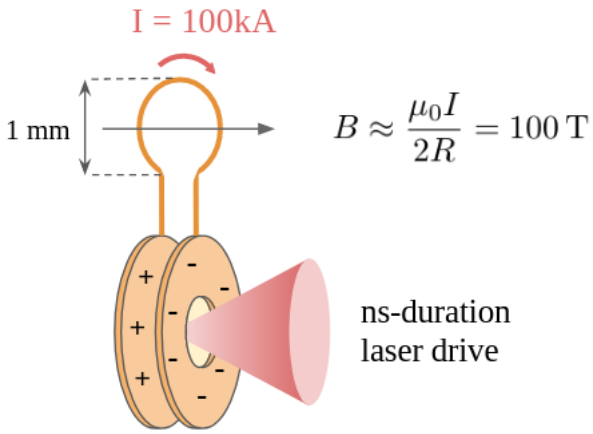

Figure 1.3: Capacitor coil target driven by an energetic ns-duration laser pulse. Typical values of the coil radius R, current I and magnetic field B are included.

focusing an intense laser onto a wire tip [102]. Experimental techniques have evolved considerably since the publication of that germinal paper and the laser targets have become known as *capacitor coils*.

Capacitor coils are a type of laser-driven solenoid that consist of two metal plates held in parallel, connected by a loop of wire or metallic ribbon. A high power laser beam is used to accelerate hot electrons from the rear plate onto the front plate, establishing a voltage and return current along the connecting loop. It is this strong current that generates a quasi-static magnetic field. A schematic diagram of the procedure can be seen in Fig. 1.3.

There are various benefits and drawbacks associated with all-optical sources of strong magnetic fields. Being small, capacitor coils produce less debris than pulsed power devices. This means optical field sources can be used in parallel with diagnostics that contain delicate components, like proton deflectometry or x-ray backlighters. They can also be fielded on laser facilities where access to the target is limited and it may be difficult to accommodate bulky pulsed power feedthroughs. Experiments suggest capacitor coils can produce currents of order 100 kA, with 100 T-level magnetic fields generated in mm^3 volumes for $\sim$ 10 ns or more [130]. These magnetic fields are ideal for a range of applications, for instance in focusing charged particle beams [10, 154] or experiments relevant to astrophysics [182] and magnetic reconnection [39, 137]. Seed magnetic fields exceeding 10 T can thermally insulate the fusion hot spot and enhance neutron yield in a magnetized ICF scheme, as discussed in Sec. 1.2.1. In indirect drive experiments, the $\sim$ 1 ns rise-time of these magnetic fields will cause eddy currents in the hohlraum that impede fuel magnetization, degrade drive symmetry and provoke x-ray emission that preheats the capsule [127]. If the capacitor coil could be integrated into the hohlraum itself

[82] and the pulse duration of the drive lasers extended, then these issues may be overcome. For other applications, an all-optical field may be too transient or vary too steeply over the course of the laser drive. Capacitor coil currents are also much smaller than the MA currents that can be produced on large pulsed-power facilities, which can generate strong magnetic fields in cm^3 volumes [132]. If the laser system is relatively low-energy ($\ll$kJ), or the application requires a $\gtrsim 0.1\mu$s-duration static magnetic field, then a pulsed power device or superconducting magnet may be a more suitable magnetic field source. Ongoing research is aimed at diagnosing the fields from all-optical magnetic field sources to ensure they are reproducible and well-characterised in space and time. Some important experiments involving capacitor coil targets are reviewed over the next three sections.

1.4.1 CO_2 Laser Experiment by Daido *et al.*

In Ref. [46], Daido *et al.* describe a capacitor coil experiment conducted on the LEKKO-VIII CO_2 laser. The experiment was conducted at fixed intensity and investigated the effect of target geometry on the measured magnetic field. As shown in Fig. 1.4a, targets were composed of two copper disks/plates, 50 μm-thick by 2 mm in diameter. The front plate had a 1 mm-diameter hole to allow the lasers to focus onto the inside surface of the rear plate. These two plates were connected by a 2 mm-diameter wire loop made from 80 μm-diameter copper wire. Using a B-dot probe[4], Daido *et al.* recorded magnetic fields at the coil centre between 10 and 60 T, with maximum currents of 100 kA and maximum voltages of 220 kV. Laser energy was supplied by one arm of the LEKKO-VIII system, delivering 100 J in 1 ns, focused to an intensity of $1.3 \pm 0.2 \times 10^{14}$ Wcm^{-2} using $f/1.5$ optics. The current and magnetic field were calculated from B-dot probe signals (see Ref. [46] or Sec. 3.1), while the voltage between the metal plates was estimated based on a simple lumped-element circuit equation relating the plate voltage V and the coil current I:

$$V = LdI/dt + RI$$

Here, L is the coil inductance and R the room-temperature coil resistance.

Typical soft x-ray signals (0.1 keV $< h\nu <$ 1 keV) are shown as white regions in Fig. 1.4b. X-rays seen on the inner surface of both plates suggest that hot electrons are traversing the gap. Fig. 1.5a shows the maximum magnetic field and wire current as a function of the plate separation d. The solid circles and the triangle represent data for a one-turn coil made of wire and a cylindrical target,

[4]A B-dot probe is a small induction coil that measures the rate of change of a magnetic field passing through the coil. More details can be found in Sec. 3.1.

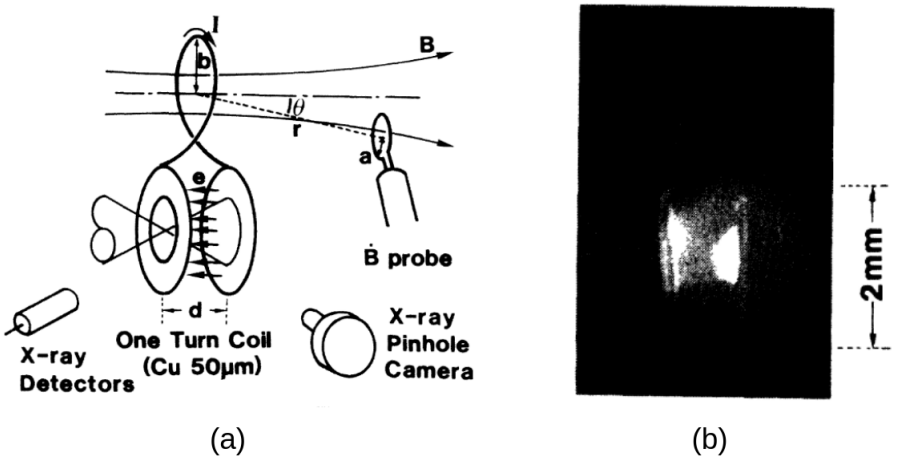

Figure 1.4: (a) Schematic diagram of a wire coil target and the observation system. (b) X-ray signal (white regions) in the gap between the capacitor coil plates. The laser enters from the left, passes through a hole in the front disk and irradiates the rear disk. Both figures are taken from Daido *et al.* [46] with permission.

respectively. A schematic of the cylindrical target is shown at the top of Fig. 1.5a. The magnetic field is proportional to d when it is smaller than 700 μm; then, when the plate separation reaches 1 mm, the field strength approximately halves. It is important to note that the magnitude of the magnetic field in the cylinder-type coil is two times larger than that for the wire-type coil. This is thought to be due to the smaller inductance and resistance in the cylindrical coil. This is supported by Fig. 1.5b, which shows the peak voltage plotted against plate separation. The peak voltage between the plates is similar for the cylinder and single loop targets. The ratio of laser energy to magnetic field energy was estimated to be ~ 0.1.

Results were explained using an analytic model that combined expansion of the critical plasma with lateral spreading of hot electrons due to an $E \times B$ drift. When the plate gap is too large, $E \times B$ drift prevents hot electrons from reaching the front plate and the inter-plate voltage is reduced. Daido *et al.* proposed that the voltage is developed by hot electrons that quickly traverse the gap and that the voltage grows until the slower moving, quasi-neutral plasma arrives and the plates are shorted. Good agreement was found between semi-analytic calculations of the peak voltage ($V = 222$ kV) and experimental results.

Several important conclusions can be drawn from this experiment:

- Plate separation is demonstrated to be an important parameter in optimising the coil magnetic field. The magnetic field rises linearly up to a separation of ~ 0.7 mm, beyond which it drops sharply.

- The maximum coil current and magnetic field are partially determined and limited by the time required for the gap to fill with critical-density plasma.

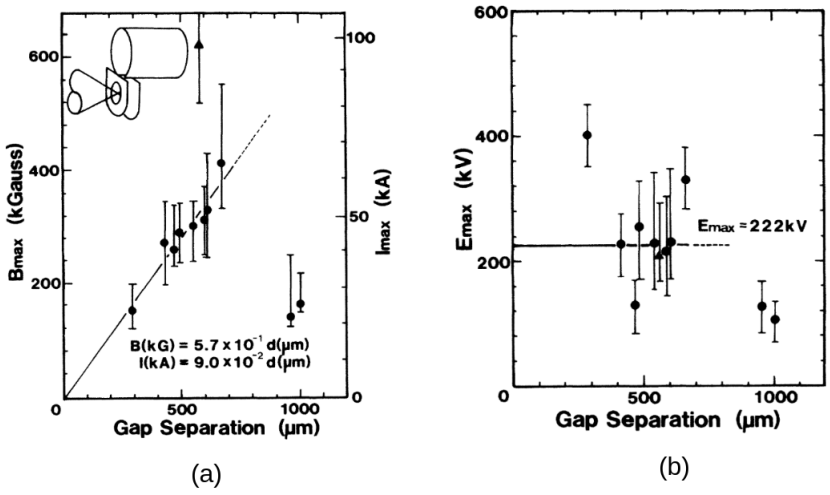

Figure 1.5: (a) Maximum coil magnetic field and coil current as a function of plate separation. The solid circles and the triangle represent data for a one-turn coil made of wire and a cylindrical target respectively. A schematic of the cylindrical target is shown in the top left hand corner. (b) Maximum plate voltage as a function of plate separation (inferred from current measurements using a lumped-element circuit model). Notice that the voltage is similar for wire and cylinder targets. Figures are taken from Daido *et al.* [46] with permission.

- Significantly stronger magnetic fields can be reached with a cylindrical target as opposed to a thin wire loop.

1.4.2 Multi-probe experiment by Santos *et al.*

In Ref. [153], Santos *et al.* compared measurements from B-dot probes, Faraday rotation and proton radiography in a bid to robustly characterise the magnetic field of a capacitor coil target. Previous experiments had focused on a single diagnostic technique [46, 44, 77] and reports of unphysical magnetic fields exceeding 1 kT highlighted the importance of combining multiple independent measurements[5].

Santos *et al.* conducted their experiment at the LULI pico 2000 laser facility. Capacitor coil targets were driven by a 1.053 μm wavelength, 1 ns duration flat-top laser pulse ($\approx$ 100 ps rise time) containing 500 J and focused to intensities of $\sim 1 \times 10^{17}$ Wcm^{-2}. Targets were laser-cut from a variety of different metals (see Fig. 1.6a) and bent into shape. They consisted of two metal disks (3.5 mm in diameter, 50 μm thick, separated by 900 ± 200 μm) connected by a wire loop with radius 250 μm. The target and diagnostic arrangement is illustrated in Fig. 1.6b.

[5]In 2012, Fujioka *et al.* used Faraday rotation to infer a capacitor coil B-field of 1.5 kT, generated by two beams from the GEKKO-XII laser [77]. Integrating the magnetic pressure ($B^2/2\mu_0$) over the coil region, however, yields a magnetic field energy larger than the input laser energy of 1 kJ [153]. Potential sources of error include: uncertainties in the Verdet constant of the birefringent crystals when they are exposed to strong and rapidly changing B-fields, or damage to crystal transmission properties by x-rays and fast particles from the laser interaction.

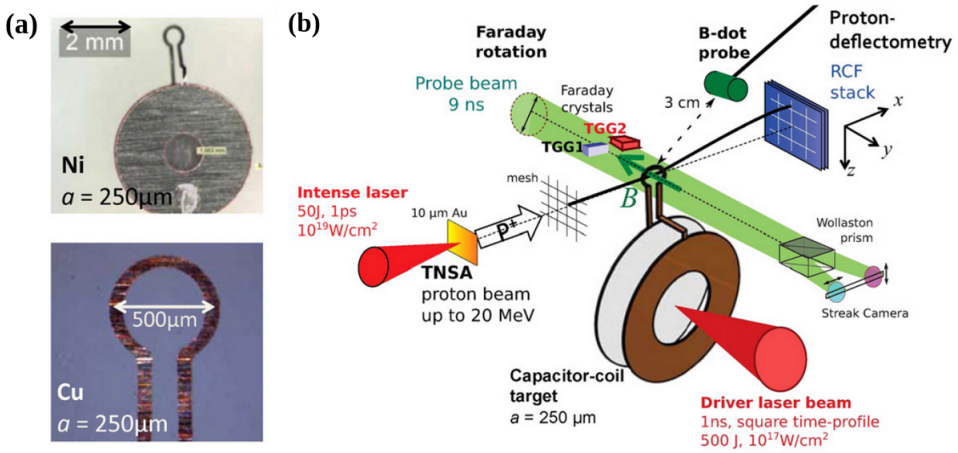

Figure 1.6: (a) Photographs of Ni and Cu capacitor coil targets used in the experiment (b) Full experimental set-up showing the B-dot probe, Faraday rotation probe beam and proton radiography diagnostics. Figures are taken from Santos *et al.* [153] with permission.

B-dot data was bandpass filtered with minimum cut-off frequency $\nu_{min} = 1$ MHz to remove DC and $1/\nu$ noise [171] and maximum cut-off frequency $\nu_{max} = 1.5$ GHz to minimise EMP signals from target-chamber discharge currents. The filtered data was integrated and then extrapolated from the probe head to the coil target using static simulations of the coil magnetic field geometry. Extrapolated B-field values of $B_0 = 600$ T and $B_0 = 800$ T at the coil centre were measured on several shots with Ni and Cu targets respectively. On the other hand, magnetostatic simulations of a perfectly circular coil with radius 250 μm produced an inferred B-field of $B_0 = 20$ kT. This significant overestimation demonstrates the importance of accurately simulating the current geometry in the coil, particularly the break at the bottom of the loop. To test the quality of the B-dot probe signal, two control shots were made using parallel plates with no connecting coil and parallel plates connected by a straight wire (no loop). Both shots produced small signals that suggest the B-dot was more sensitive to currents in the coil loop than the ns laser-plasma interaction or induced currents in surrounding objects. It should be noted, however, that the ps-duration radiography beam was not fired during these control shots. Since the radiography beam was fired on shots involving B-dot probes and short-pulse interactions are potent sources of electromagnetic noise, it is possible that the strong B-dot signal and irregular waveforms were caused by laser-driven EMP.

Faraday rotation measurements were taken using Terbium Gallium Garnet (TGG) crystals located 3.5 mm from the coil centre, in line with the coil axis. TGG crystals were deliberately chosen for their high Verdet constant so they could be placed as far as possible from the laser spot. The inferred magnetic field at the coil centre was over 400 T in magnitude and is shown in Fig. 1.7b. Measurements taken with the

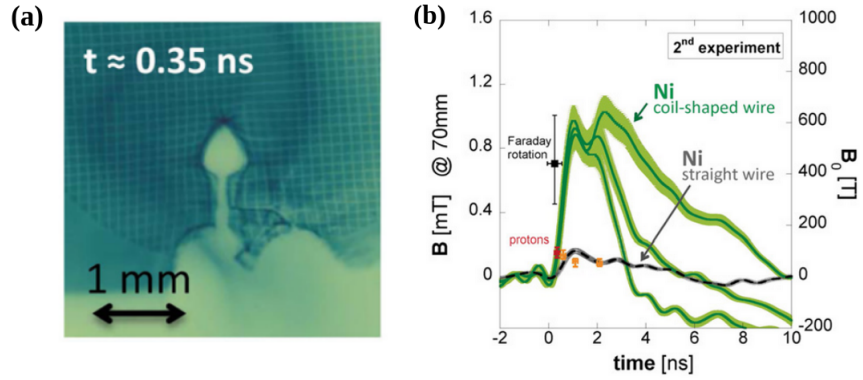

Figure 1.7: (a) Sample RCF image taken using 13 ± 1 MeV protons that crossed the target $t \approx 0.35$ ns after the beginning of the laser drive. The spatial scale represents distance in the plane of the coil (b) The solid grey and dashed grey curves correspond to B-dot probe measurements taken during two control shots on the rear disk: a shot with two Cu disks held in parallel without a connecting wire and a Ni target with a straight wire between the disks (no coil) respectively. All the individual symbols represent the B-field at the coil centre, B_0, for Ni capacitor coil targets. Measurements were obtained using Faraday rotation (square at $t \approx 0.2$ ns) and proton deflectometry (red circle at $t \approx 0.35$ ns and orange circles obtained at later times). The discrepancy between the B-dot probe signals and proton measurements is explained in the article by plasma electrons trapped close to the coil that attract protons via the electric force. Both figures are taken from Santos *et al.* [153].

crystal closer than 3.5 mm were marred by signal blackout from hard x-rays and fast particles emanating from the interaction region; measurements taken further away were too weak to estimate the magnetic field.

An ultraintense ps-duration laser was focused onto thin Au foils to generate proton beams for radiographic imaging of the coil magnetic field. Fig. 1.7a shows a typical RCF layer from the experiment, with a teardrop-shaped proton void at the centre of the image caused by magnetic field deflections. Monte-Carlo simulations of protons passing through magnetic fields agreed well with the RCF image in (a), corresponding to a coil current of 40 kA and central field of $B_0 = 95$ T. Results from all B-field diagnostics are shown in Fig. 1.7b. It is striking that the radiography measurements do not agree with the other diagnostics for $t > 0.35$ ns after the arrival of the laser. Furthermore, the proton-measured B-fields actually *decrease* in time after $t \approx 0.35$ ns - before the laser pulse has ended. In addition to the central teardrop shape, RCF data featured a circular imprint (evident in Fig. 1.7a) that was ascribed to relativistic electrons. The radius of the circular imprint increases with time, which could be explained by an increase of plasma electrons collecting around the coil during the laser drive. The effect of these trapped electrons is to cause extra expansion of the electron beam and a contraction of the quasi-neutral proton beam.

The experiment described in Ref. [153] produced several major results:

- A reproducible, quasi-static magnetic field was generated by capacitor coil targets made from Cu, Ni and Al. Peak field strengths of several hundred Tesla were measured over a mm^3 volume, with the largest fields observed for Cu coils.

- Faraday Rotation and proton radiography results were broadly consistent with B-dot data early in the laser drive ($t \leq 0.35$ ns); deviation at later times was caused by blackout of the TGG birefringent crystal and a possible negative electric field caused by plasma electrons trapped in the magnetic field of the coil.

- All three high-field diagnostics demonstrated an extreme complexity of interpretation that requires further study.

1.4.3 Summary of Capacitor Coil experiments

A developing application of laser-driven currents is the generation of strong, quasi-static magnetic fields for use in experiments at high power laser facilities. Table 1 contains magnetic field measurements for capacitor coil targets driven by nanosecond lasers produced before the work in this thesis was undertaken. Data is presented in order of increasing $I\lambda^2$ and results for picosecond and femtosecond laser-driven coils are omitted (see Ref. [185, 184, 173] for more details). The table shows that many different capacitor coil-type targets have been used at different facilities, ranging from the standard capacitor coil geometry (CC) seen in Ref. [46], to Helmholtz coils [79, 182, 44] and a U-shaped metallic ribbon [82]. This great variety makes it difficult to make general comments about underlying physics because the coil current is a strong function of target geometry (as seen in Sec. 1.4.1). Broadly speaking, the coil current and magnetic field are expected to increase with laser energy and $I\lambda^2$, since the number of hot electrons and the hot electron temperature will increase [71, 169]. A strong sensitivity to the laser wavelength is evident from calculations of the laser energy to magnetic field energy conversion efficiency [169]. In Ref. [78], Gao *et al.* report a conversion efficiency of approximately 0.01% for a 0.35 μm laser - 10$\times$ lower than Courtois *et al.* [44] at a wavelength of 1.053 μm and 100$\times$ lower than Daido *et al.* at a wavelength of 10.6 μm [46].

Laser Facility	E_{las} / kJ	$I\lambda^2$ / $\mathrm{Wcm^{-2}\mu m^2}$	Coil Design	J / kA	B_0 / T
Omega [82]	0.75	5×10^{14}	U-shaped ribbon	180	210
Omega [79]	1.25	2×10^{15}	CC and Helmholtz	22	50
Gekko VII [137]	1	3×10^{15}	Helmholtz	82	60
Lekko VIII [46]	0.1	1×10^{16}	U-shaped ribbon and CC	100	60
Gekko VII [105]	1	2×10^{16}	2×CC	250	610
Vulcan [44]	0.3	4×10^{16}	Helmholtz	n/a	7.5
Gekko VII [77]	1.5	5×10^{16}	CC	8600	1500
LULI [153]	0.5	1×10^{17}	CC	340	800

Table 1.1: Coil current (J) and central magnetic field (B_0) measured in experiments with capacitor coil targets. Standard capacitor coil targets with a single wire loop connecting two metal plates are denoted by 'CC'. All experiments used nanosecond-duration laser pulses to drive the capacitor coil and results are placed in order of increasing $I\lambda^2$ [184].

1.5 Laser-driven Electromagnetic Pulses

1.5.1 Introduction to EMP

An electromagnetic pulse (EMP) can be defined as a transient burst of electromagnetic energy. Being of short duration, the EMP spectrum is spread over a broad frequency range that arbitrarily excludes optical and ionising radiation. Radio-frequency EMPs have been systematically studied since the first nuclear tests in the 1940s and increasingly throughout the Cold War, when it was realised that EMP from a high altitude nuclear explosion could be used as a weapon to disrupt or damage electrical infrastructure [14]. Nuclear EMP can be divided into several components, each with distinct amplitudes, spectra and pulse durations [74]. In 1959, A. S. Kompaneets observed that a major source of nuclear EMP derived from a Compton current produced by γ-radiation emanating from the explosion [101]. Then, in 1963, C. L. Longmire described how these Compton-scattered electrons interact with the Earth's magnetic field to produce an intense pulse of synchrotron radiation [113, 114]. From the 1970s onwards, efforts to protect electronic devices from EMP grew into an important branch of 'electromagnetic compatibility' engineering and scientific interest extended into other contexts. EMP technologies found application in laboratories dedicated to pulsed power devices [174] and high power laser systems [43]; research was also conducted into EMP arising from natural sources such as lightning [91] and solar flares [186].[6] Since the damage caused by EMPs is determined by the amplitude and spectrum of their constituent fields, technologies developed to protect against nuclear EMP or lightning strikes (e.g. shielded cables, filtered power supplies, Faraday cages) can be applied to EMP generated from different sources as well, provided there is some overlap in their spectral properties. Indeed, many of the techniques used to combat EMP emitted during laser-solid interactions have been borrowed from the existing literature.

Intense electromagnetic pulses (EMPs) can be produced in the target chambers of high power lasers as a by-product of the laser interaction. Early measurements with conducting antennae revealed EMP to be a broadband electrical noise signal with multi-100 ns duration and an exponentially decaying amplitude [122, 30]. Shortly after the arrival of the laser, a radiofrequency pulse is emitted that can damage laboratory equipment and impair electronic measurements. EMP is also emitted at THz [110, 109] and MHz [122, 61] frequencies. Though the EMP amplitude is strongest inside the target chamber, it can escape through openings in the chamber walls to pervade the entire experimental area [58]. Disruption to facility operation by laser-driven EMPs became more significant with the advent of chirped pulse am-

[6] A comprehensive history of EMP can be found in Ref. [14] and the references therein.

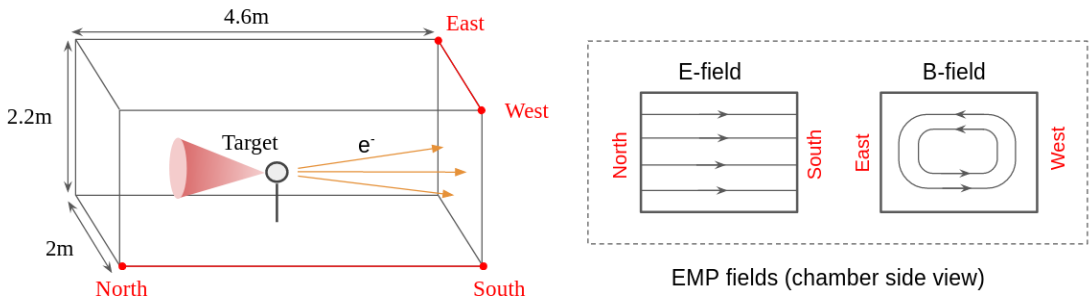

Figure 1.8: Vulcan Petawatt target chamber in 2004. The east-west and north-south axes are marked in red. The laser is visible as a cone entering from the north, exciting a beam of energetic electrons that are propelled towards the south wall. The dashed box contains two chamber cross-sections with the electric and magnetic fields illustrated with arrows.

plification (CPA) and ultraintense lasers because sub-ps laser interactions produce much stronger EMPs than nanosecond interactions at the same energy [124]. If steps are not taken to reduce EMP emission and shield electronic equipment, scientists may be prevented from capitalizing on recent advances in laser technology such as high-repetition, high-intensity lasers [49, 124].

Investigating sources of EMP is a challenge because the phenomenon is not limited to a single physical process. EMP in the THz domain is generated from electron oscillations in the target and is characterized by the duration of electron ejection [110, 43]. At the same time, electron beams and electromagnetic fields propagating through an interaction chamber will activate all the metallic parts, emitting EMP at lower frequencies ($\sim$ 100 MHz) as chamber proper modes [122]. In this thesis, we will focus on EMPs in the GHz frequency domain ($10^8 < f[\text{Hz}] < 10^{10}$) which are most disruptive to electronic equipment[7].

Once EMP had been identified as a serious issue for short pulse laser systems, dedicated campaigns were set up to investigate the origin of the emission and reduce its intensity [122, 61, 58]. Interest in EMP research has therefore followed, in part, developments in high power laser technology [49]. Some important EMP experiments conducted prior to the work presented in Part III will be discussed in the next few sections.

1.5.2 Vulcan Petawatt experiment by Mead *et al.*

In Ref. [122], Mead *et al.* describe preliminary EMP measurements on the Vulcan Petawatt laser that were used to predict the severity of EMP that would be encoun-

[7]GHz frequencies are particularly damaging because electronic hardware, such as cables and oscilloscopes, are designed to respond at these frequencies. Electronic equipment usually contains conducting parts ranging from metres to millimetres in size, corresponding to wavelengths in the GHz regime.

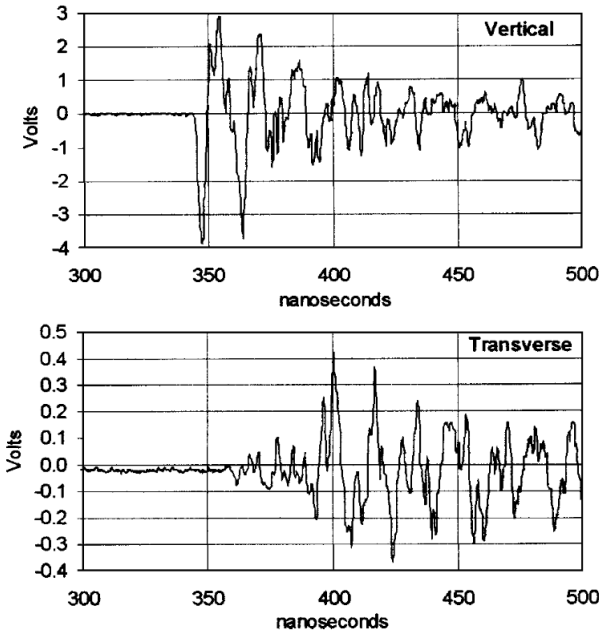

Figure 1.9: Sample voltage waveforms measured using Moebius loop antennae inside the Vulcan Petawatt target chamber. Images taken from Mead *et al.* [122]. The 'Transverse' waveform was measured along the east-west chamber axis (see Fig. 1.8).

tered on the Orion laser. Unlike the Vulcan system, Orion was planned to have a spherical (rather than cuboidal) target chamber and it would feature two CPA laser beams with similar characteristics to Vulcan. Measurements of the rate of change of the magnetic field were made with Moebius loop antennae [59] placed inside the Vulcan experimental chamber. A diagram of the Vulcan target chamber is contained in Fig. 1.8, with the east-west and north-south chamber axes marked in red. The antennae were oriented to measure east-west and vertical field components. Voltage signals from the antennae were integrated to produce the magnetic field and Fourier transformed to gain spectral information. Mead *et al.* also developed a theoretical model to account for the measured amplitude and frequency of EMP: when the laser interacts with the target, a beam of energetic electrons is emitted along the line of the laser that charges the chamber south wall, causing the chamber to resonate at its natural frequency.

Fig. 1.9 shows voltage waveforms recorded on 300 MHz analogue bandwidth oscilloscopes sampling at 2.5 GS/s. These results were typical of EMP signals produced by Al and Cu foil targets with on-target laser energy between 330 J and 450 J for a fixed pulse duration of ~ 0.5 ps. The waveforms feature harmonics and GHz-frequency noise, with two weakly coupled modes of slightly different frequency. The relative amplitude and temporal evolution of the signals from each probe indicate a vertical B-field mode which gradually transfers energy to a tranverse B-field mode at reduced amplitude.

According to Mead's theoretical model, laser interactions will produce a beam of $\sim 10^{12}$ electrons along the line of the laser which strike the target chamber south wall. The ensuing charge imbalance excites a dominant north-south E-field mode, generating a circulating B-field in a vertical east-west plane (see Fig. 1.8). Though the chamber resonance was calculated at 101 MHz, probe signals revealed a lower resonance at 63 MHz. The model also estimated a peak B-field of 15 μT - larger than the value of 5.4 μT measured by the east-west probe. Mead explains that a downshift in the chamber resonant frequency may be caused by conducting objects inside the target chamber that alter its cuboid geometry, while the smaller B-field amplitude may be caused by the production of fewer high energy electrons than predicted.

A clear advantage of the electron beam model is that it can be easily adapted to different facilities provided the chamber geometry is simple. Switching from a cuboid to a 2 m-radius sphere, Mead *et al.* estimate that the maximum EMP electric and magnetic fields inside the Orion chamber will be 7 kVm^{-1} and 15 μT respectively. Though the Vulcan measurements were not part of a dedicated EMP experiment, some significant conclusions can be drawn:

- EMP amplitude is linked to the number of electrons that escape the laser target. Peak electric and magnetic fields can be estimated from the number of escaping electrons and the proportions of the target chamber. Future studies will need to record the number of emitted electrons to establish a connection with EMP.

- A chamber resonance mechanism is identified as a potential source of EMP but measurements are limited by sub-GHz magnetic probes that were only sensitive to one component of the dominant TE mode. Accurate computer simulations of the chamber, including all internal conducting objects, would give a better idea of the EM field structure and resonant frequency. Simulations can later be compared with multi-axis data from several high-frequency antennae.

1.5.3 Lawrence Livermore EMP Campaign

An important experimental campaign was conducted on the Titan [167] laser (E_{las} = 200 J nominal energy) by researchers from Lawrence Livermore National Laboratory [61, 29]. The primary aim of the experiments was to estimate the strength of the EMP that would be generated by the Advanced Radiographic Capability (ARC [119]) at the National Ignition Facility (NIF). The ARC diagnostic uses four NIF beams ($E = 4$ kJ) compressed to picosecond durations for backlighting fusion capsules and other applications. A variety of different antennae were used, covering

several hundred MHz to GHz frequencies. An image plate was used to characterise the spatial distribution of emitted electrons with energies exceeding 1 MeV, while the electron energy spectrum was measured using a Faraday Cup and compact electron spectrometers. The electron spatial and energy distributions were then used as inputs to the *EMSolve* code [175, 69] that modelled time-varying EM fields in a simulated chamber. Based on measurements of $\sim 5 \times 10^{12}$ electrons being ejected from the target, reasonable agreement was found between the simulated amplitude and frequency of the EMP compared with B-dot probe data.

To test how much of the EMP energy was contained at high frequencies, a high-pass filter was installed on a high-frequency B-dot probe. The filter blocked signals below 2 GHz and a factor 2 reduction in EMP was observed.

Another key observation was that larger laser targets emitted stronger EMP, possibly because of a reduced target potential barrier that allowed more lower energy electrons to escape. Since the amount of ionizing radiation (gamma rays, UV emission) was found to be constant with increasing target size, this also demonstrated that photoionization of nearby surfaces in the experimental chamber contributed less to the EMP than the electron ejection current.

Having established a correlation between EMP amplitude and the number of emitted electrons, a mitigation scheme was developed using electron beam dumps. Planar beam dumps positioned behind the laser target had no significant effect on the EMP, while spherical beam dumps (that partially enclosed the target) reduced the EMP amplitude by a factor of ~ 3. Extrapolating from a laser energy scan on the Titan laser with fixed pulse duration $t_{las} = 2$ ps, Eder *et al.* predicted that MVm^{-1} EMP fields would be generated on PW-class laser systems like ARC and OMEGA-EP.

We can summarize some of the most important results from the Livermore campaign as follows:

- Measurements of the quantity, energy spectrum and divergence of charged particles ejected from the laser target were compared with electromagnetic field measurements, establishing a clear link between the number and energy of emitted electrons and EMP. The frequency dependence of the EMP was found to be very broad, with approximately half the energy above 2 GHz.

- Results from the image plate, Faraday Cup and electron spectrometers were used as inputs for computer simulations of electron beam propagation inside a conducting chamber. The simulations produced values of the EMP amplitude and frequency that showed reasonable agreement with B-dot probe measurements.

- A laser energy and pulse duration scan showed that EMP increases strongly with laser energy at fixed pulse duration and also intensity at fixed energy. More data needed to establish scaling laws, particularly with intensity.

- A mitigation strategy was developed that reduced the emitted EMP amplitude by a factor ~ 3. It is not practical for most applications, however, since the target must be partially enclosed by an electron beam dump.

1.5.4 EMP Campaign at CELIA

Researchers from the University of Bordeaux developed the work at Livermore and Vulcan by focusing on the EMP produced by short pulse lasers at intensity $I_{las} = 10^{18}$-10^{20} Wcm^{-2} and pulse durations $t_{las} \lesssim 1$ ps. Previous work had shown that EMP strength is related to the ejection of hot electrons from the laser target, but it was unclear whether the vacuum ejection current or target discharge was responsible for the emission of radiation. Combining theory and experiment, the Bordeaux team identified the primary source of GHz EMP as antenna emission from the laser target support. The emission process begins when an intense laser pulse ($t_{las} \lesssim 1$ ps) excites a population of hot electrons in a solid. A fraction of these hot electrons can escape the target if they are able to overcome the target potential barrier, leaving behind an accumulated positive charge. Hot electrons cool via collisions on a timescale of a few ps or less, so the target is charged on the hot electron cooling timescale and emits EMP at terahertz frequencies. The positive charge in the target then draws a neutralization current on a ns-timescale from the nearest ground. If the shape and conductivity of the target support permits, this current will oscillate and a strong GHz EMP is emitted.

PIC [58] and dynamic electromagnetic simulations [29, 27] of target charging and EMP emission are complicated and computationally expensive, so a numerical model of laser-induced charging of thick[8] targets was developed over the course of three papers [58, 142, 140]. The model is called ChoCoLaT and it solves a system of coupled differential equations that describe the expansion of a laser-accelerated cloud of hot electrons into a solid target, accounting for collisional cooling and backscattering of electrons that may exit the target surface and leave behind an electrostatic charge. Electrons can escape the target if their energy exceeds the target electrostatic potential, so the evolution of the target potential was modelled as well. The target neutralisation current was ignored in the short pulse regime because the electrons are expected to cool on a multi-ps timescale that is much faster

[8] A 'thick' target refers to a target whose width is greater than the hot electron range in the material, so electrons can only escape from the same surface as the laser is irradiating.

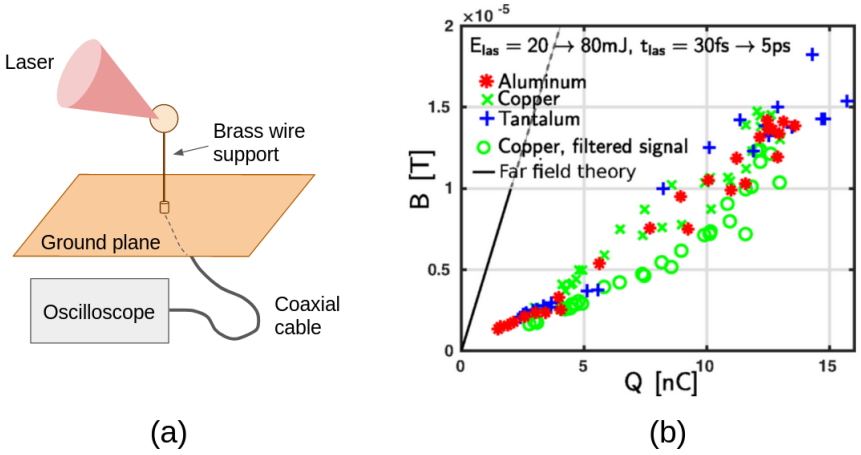

Figure 1.10: (a) Schematic of the coaxial current diagnostic reported in Dubois *et al.* [58]. The target diameter varied between 5 mm and 1.5 mm, the brass wire support is 5 cm in height and 1 mm in diameter and the ground plane measured 20 cm×20 cm. (b) Magnitude of the magnetic field measured by a B-dot probe plotted against the target charge for a range of laser and target parameters. The solid black line represents the expected EMP magnitude based on ChoCoLaT calculations of the target charge and a far-field dipole antenna model. This antenna model is corrected in Minenna *et al.* [124] and discussed in Part III. Figure reproduced from Poyé *et al.* [141] with kind permission of the author.

than the ns-long duration of the neutralization pulse[9]. ChoCoLaT outputs a time-varying current and total target charge that can be compared with experimental measurements. If this target charge is inserted into an antenna radiation model or electromagnetic simulation, the EMP amplitude and directionality can be estimated.

To test the ChoCoLaT model of thick-target charging, Dubois *et al.* pioneered voltage stripline measurements of the target return current from which an estimate of the accumulated charge could be extracted [58]. Measurements were conducted on the Eclipse laser system, which can achieve a maximum energy of 100 mJ compressed into a 50 fs pulse at 800 nm wavelength. The laser was focused to a Gaussian spot (7.5 μm FWHM) on 3 mm-thick Cu targets - thicker than the 1 mm range of 1 MeV electrons. Each target was supported by a brass wire that was fixed to a connector at the centre of a 20 cm×20 cm ground plane. Current measurements were made by connecting the base of the brass wire to the inner conductor of a coaxial cable that carried the signal to an oscilloscope, as shown in Fig. 1.10a. Integration of the current waveform over time then produced an estimate of the target charge. The duration of the discharge current pulse was measured to be on the order of a few ns - much longer than the multi-ps charging time calculated from laser-target parameters. This supports the central assumption of the ChoCoLaT model, which

[9]The duration of the neutralization pulse is determined by the impedance and capacitance of the target and target holder (characteristic time $\tau = RC$).

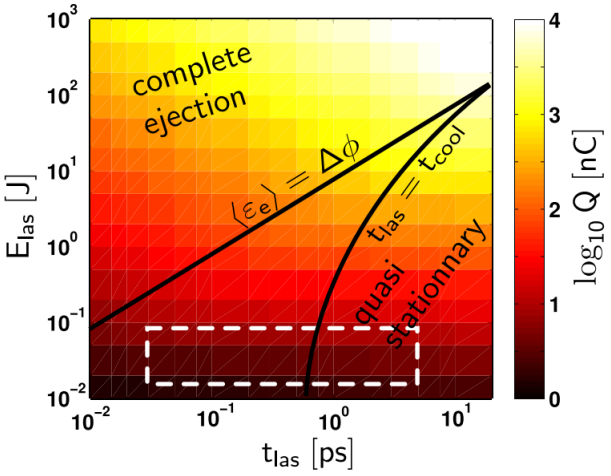

Figure 1.11: Target charge calculated using the ChoCoLaT model for a laser with focal spot radius $r_{las} = 6$ μm, wavelength 800 nm and laser-to-hot-electron conversion efficiency of $\eta_h = 0.4$. The dashed white box represents the parameter space accessed by the ECLIPSE laser. Figure reproduced from Poyé *et al.* [142] with permission.

ignores neutralisation of the target by a return current.

Target charge was studied as a function of the target diameter, laser energy and laser pulse duration. The charge and maximum current were both found to increase linearly with laser energy and decrease with target diameter. A weak dependence on laser pulse duration was discovered between 50 and 550 fs.

A B-dot probe was fielded in order to record the magnitude of the EMP emission, which was examined in Ref. [142]. A common resonance at ~ 1 GHz was identified in Fourier spectra of the target return current and the magnetic field. This resonance was comparable to the emission frequency of a dipole antenna with quarter-length equal to the height of the laser focal spot above the ground plane. Comparing the magnitude of the EMP with target charge, Poyé *et al.* [142] found a close correlation (see Fig. 1.10b) and concluded that EMP emission was caused primarily by dipole emission as a discharge current oscillates up and down the target holder.

Although the Eclipse laser could only verify the ChoCoLaT model at low energy, simulations revealed three major charge ejection regimes that occur for different combinations of laser energy and pulse duration [142]. Fig. 1.11 shows these three regimes overlaid on a colour map of the laser-ejected charge. Target charge is plotted on a logarithmic scale ranging from nC to μC and a dashed white box marks the range of parameters studied during the Eclipse experiment. 'Quasi-stationary' ejection occurs when the laser pulse duration is much longer than the electron cooling time and the hot electron population is relatively cold (i.e. cooler on average than the target potential barrier). Under these conditions, hot electron emission is sustained by the laser and stops quickly after the pulse has ended; the ejection

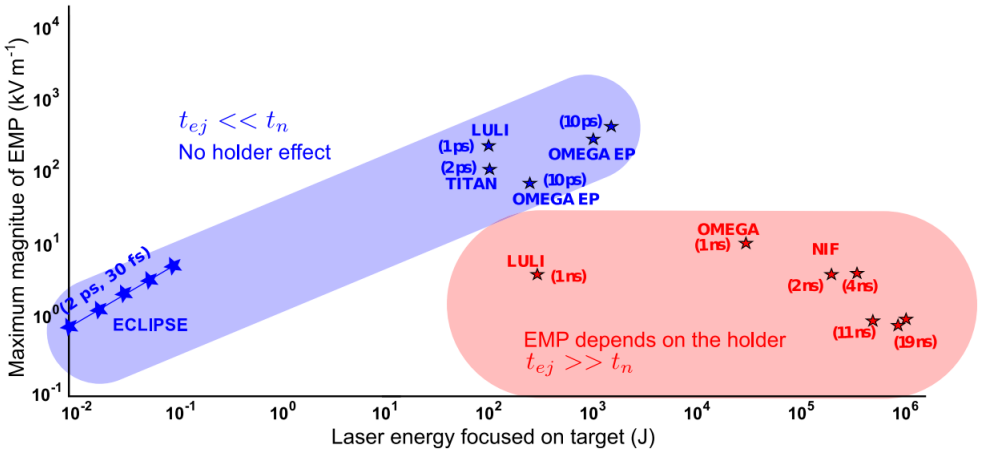

Figure 1.12: Electric field measured 0.5 m from the laser target at different facilities. Blue points correspond to shots where the neutralisation current does not significantly affect target charging and red points shots where the neutralization current curbs the target charging. Figure reproduced from Poyé *et al.* [140] with permission. An updated graph including measurements from this thesis can be found in Fig. 75 of Consoli *et al.* [43].

current can be expressed as $J \approx Q/t_{las}$, where Q is the total charge ejected over the course of the interaction and t_{las} is the laser pulse duration. In the 'complete ejection' regime, the average hot electron energy is higher than the potential barrier and nearly all of the hot electrons generated by the laser will escape the target. Note that this does not necessarily imply that the escaped charge will be high if the laser energy is low and few hot electrons are produced. The 'thermal ejection' regime lies in between the first two, occurring when the laser pulse duration is shorter than the electron cooling time but the target potential barrier is still significant.

Experiments with different target sizes and materials on Eclipse revealed that EMP emission could be reduced by manipulating target conductivity and geometry [140]. As observed on the Titan laser, targets with smaller surface areas emitted fewer electrons and weaker EMP [61]. This is accounted for in the ChoCoLaT model by setting a minimum value of the target potential. Small targets confine the target positive charge to a fixed area during the electron ejection process, enhancing the potential and preventing hot electrons from leaving the target. Calculations of the target radius at which this potential enhancement takes place agree reasonably well with target charge measurements. Dielectric targets were also shown to reduce the measured target charge and EMP. When dielectric targets were irradiated with shorter laser pulses ($t_{las} \lesssim 0.5$ ps) they accumulated a similar charge to metallic targets, but longer pulse durations (up to ~ 1 ps) accumulated less charge. A model is presented where the charging is reduced in dielectric targets because electrons in the material cannot reorganize to minimize the target electrostatic potential. Electrical

isolation between the laser spot and the target support means the neutralisation current is significantly reduced for shots on dielectric targets even if the target charge is relatively high.

In Ref. [140], a distinction is made between the high intensity short pulse regime in which ChoCoLaT is valid and the long pulse laser interactions relevant to fusion experiments and capacitor coil targets. ChoCoLaT assumes that the neutralization current travelling up from the ground arrives after the target charging process is complete. The situation is analogous to a target holder with a large inductance that delays the onset of the neutralization current and maximizes target charging. Poyé *et al.* estimate the characteristic neutralization time as equivalent to the time needed for a charge pulse to propagate up a conducting holder of height h from the ground. The neutralization time is $h/c \approx 200$ ps for a 5 cm holder, which is much longer than the hot electron cooling time for a 30 fs laser interaction on ECLIPSE. It is, however, considerably shorter than the ns-duration interactions performed on OMEGA or NIF. Fig. 1.12 shows the EMP electric field measured 0.5 m from a laser target at several different laser facilities. Blue points represent shots where the charging process finishes before the neutralization current is established, so charging is efficient and EMP is relatively strong. Red points correspond to shots where the laser pulse duration is much longer than the neutralisation time, which means charging is limited. The neutralisation current concept helps to explain why fs-duration shots on ECLIPSE with 100 mJ laser energy produce EMP of similar magnitude to OMEGA and NIF with > 1 kJ compressed into ns beams. ChoCoLaT can be modified [140] to account for a neutralization current by adding an extra voltage term $V_n = -LdI_n/dt + RI_n$ in its expression for the target potential, where I_n is the neutralization current and L and R the inductance and resistance of the target holder. This modified ChoCoLaT is capable of simulating ns-duration interactions including those involving capacitor coil targets. If a capacitor coil target is insulated from the ground, a neutralization current will pass through the coil connecting the capacitor plates. Running a simulation with parameters for the experiment by Santos *et al.* (already discussed in Sec. 1.4.2), ChoCoLaT predicts that a 60 μC charge is generated over 1 ns, forming a 60 kA average current [153, 140]. This current corresponds to a magnetic field of ~ 150 T in a coil with diameter 0.5 mm.

The work contained in references [58], [142] and [140] comprised a significant leap forward in the understanding of laser-driven EMP. The major results can be summarised as:

- Development of a target charging model that is accurate to the nearest order of magnitude for sub-ps interactions and laser energies up to ~ 100 mJ.

- Target charge is correlated with the strength of EMP emission from the target,

though magnetic field estimates based on target charge are not presented.

- Regimes of strong EMP emission identified and an explanation presented for results at different facilities.

- Identified ways to reduce EMP emission by changing the target material and size.

1.6 Research Goals and Thesis Structure

In this thesis, I will present the results of two experiments conducted at the Central Laser Facility using the Vulcan laser. One experiment aims to develop capacitor coil targets as a platform for generating magnetic fields suitable for magnetised HED experiments, while the other attempts to characterise and control the emission of EMPs from ps interactions. In Sec. 1.4 and 1.5 I have tried to summarise progress made in understanding these phenomena and highlight some outstanding problems addressed by the experiments in this thesis.

Numerous experiments have shown that capacitor coil targets are a versatile magnetic field source that may be useful for research in ICF, laboratory astrophysics and magnetized transport [39, 82, 154, 182, 172]. Despite promising results with multiple diagnostics, questions remain about how these strong magnetic fields can be optimised for applications. Furthermore, robust testing of theoretical models is complicated by experiments that are conducted on different facilities with different target geometries. In Part III Chap. 5, I will present results from a capacitor coil experiment with a dual-axis proton radiography diagnostic. Proton probing is conducted at a range of times and along two axes to help separate electric and magnetic field measurements and build a picture of the electromagnetic field evolution with time. The implications for leading theoretical models of capacitor coil magnetic fields is discussed.

In the short pulse regime of EMP, the most important problems are how EMP emission can be reduced and how can the EMP field be predicted given laser and target parameters. The work summarised in Sec. 1.5 reveals an intimate connection between EMP and laser-target charging. Combining estimates of hot electron emission with full-scale electromagnetic simulations of the target chamber shows reasonable agreement with antenna measurements, however a simple model that links target charging physics to the emission of a dipole radiation field is desirable. This is particularly important at high energy and intensity ($I_L\lambda^2 > 10^{18}$) when EMP is strongest. In Part III Chap. 4, I will describe an EMP study which characterises EMP in the $10^{17} < I_L\lambda^2 < 10^{19}$ intensity regime and presents an effective mitigation

scheme. Building on the work in Poyé *et al.* [141, 142], a theoretical model that links target charging to magnetic field emission is also presented.

Over the course of this thesis I aim to demonstrate that these two projects are really two facets of the same problem: understanding target charging by laser acceleration of hot electrons. The charging and discharging processes that generate capacitor coil and EMP fields are different due to different laser absorption physics, target geometries and interaction timescales. Ultimately, however, the strength of the electromagnetic field depends on how many hot electrons can be produced at what energy and whether the interaction is fast enough to ignore a neutralisation current. Many of the ideas broached in this thesis can be extended beyond capacitor coil targets and radiofrequency EMPs. Studies have shown that electromagnetic pulses propagating along helical coils can enhance the energy and directivity of laser-accelerated ion beams [97, 1], while 'escargot' targets can emulate magnetic reconnection processes around black holes by channelling hot electrons along the target's inside surface [106, 139]. In Part II, the broad theoretical concepts underpinning laser absorption and field generation will be discussed. There will also be an introduction to the experimental techniques used to produce the results in Part III.

Part II

Laser-plasma Interactions and Target Charging

Chapter 2

High power laser interactions with solid matter

This chapter examines micron-wavelength high power laser interactions with solid matter in short pulse (ps-duration) and long pulse (ns-duration) intensity regimes. A portion of the laser energy absorbed by solid targets is converted into 'hot' electrons that have much higher energies than those produced by collisional absorption processes. Emphasis is placed on how these hot electrons are ejected from the target surface, since hot electron depletion is thought to be an important mechanism that drives GHz EMP and magnetic field generation in capacitor coils. Simple models of plasma expansion and sheath formation will also be considered, motivating more complex theories of laser-driven electromagnetic field generation.

2.0.1 Optical Field Ionisation Processes

When an infrared (micron-wavelength) high power laser is focused onto a solid target it will ionise atoms and form a plasma. There are three major processes by which this can occur, depending on the intensity of the incident light. *Multi-photon ionisation* begins at intensities above 10^{10} Wcm^{-2}, when several photons are absorbed simultaneously by an electron which gains enough energy to overcome the Coulomb potential barrier holding it in the target. Infrared photons do not have sufficient energy[1] to photoionise a material with a work function of a few eV, so several photons must be absorbed at the same time for ionisation to be successful. A high power laser can produce a plasma by multi-photon ionisation after a few femtoseconds of illumination, which is near-instantaneous on the timescale of a picosecond-duration laser pulse. At higher intensities, the laser field can distort the potential barrier of atoms and molecules [26]. *Tunnel ionisation* occurs when the height and width of

[1]Photon energy E_γ is proportional to photon frequency ν via $E_\gamma = h\nu$, where $h = 6.63 \times 10^{-34}$ m^{2}kgs^{-1} is Planck's constant.

the Coulomb potential barrier is reduced until electrons can quantum tunnel through to the continuum [80]. Further suppression of the Coulomb potential can push it below the electron ionisation energy and cause electrons to escape spontaneously via *barrier suppression ionisation*. The Keldysh parameter K can be used to distinguish between dominant regimes of multi-photon absorption and tunnel ionisation [120]. If $\langle U \rangle$ is the average quiver energy of an electron in the laser field (see Sec. 2.0.2) and E_a is the binding energy of the atom, the Keldysh parameter can be expressed as [80]:

$$K = \sqrt{\frac{E_a}{\langle U \rangle}}$$

For $K \ll 1$ and $K \gg 1$, ionisation will be dominated by tunnel ionisation and multi-photon absorption respectively. Multi-photon ionisation is generally more common at shorter laser wavelengths (e.g. UV) when $K > 1$ and tunnel ionisation dominates for infrared wavelengths when $K < 1$. This can change as the laser intensity increases and multi-photon ionisation dominates at infrared wavelengths too.

2.0.2 Single particle motion in a laser field

A charged particle will oscillate in an electromagnetic field according to the Lorentz force:

$$\frac{d\underline{p}}{dt} = -q(\underline{E} + \underline{v} \times \underline{B}) \tag{2.1}$$

where q is particle charge, $\underline{v}$ is the particle quiver velocity and $\underline{p} = \gamma m \underline{v}$ is the relativistic particle momentum. Since electrons are much less massive than ions, direct ion acceleration in the laser field is generally insignificant[2].

High power lasers are focused and compressed in time which leads to significant intensity variations along the length of the pulse. However, in the following derivations we will make the simplifying assumption that such a laser can be approximated as a linearly-polarised plane electromagnetic wave. Equations for the electric and magnetic field are propagating in the z-direction are:

$$\underline{E} = -\frac{\partial \underline{A}}{\partial t} = E_0 e^{kz-\omega t} \underline{\hat{x}} \tag{2.2}$$

$$\underline{B} = \nabla \times \underline{A} = B_0 e^{kz-\omega t} \underline{\hat{y}} \tag{2.3}$$

where $\underline{A}$ is the vector potential of the field, k is the magnitude of the wave vector

[2]At laser intensities above $\sim 10^{20}$ Wcm^{-2}, this picture can change due to relativistic increase of the electron mass and radiation pressure acceleration of ions [149].

(oriented along z) and E_0/B_0 is the amplitude of the electric/magnetic field. The intensity of an electromagnetic wave is given by the Poynting vector averaged over one laser cycle:

$$I_L = \frac{1}{\mu_0}\langle|\underline{E} \times \underline{B}|\rangle = \frac{\epsilon_0 c}{2}E_0^2 \tag{2.4}$$

where μ_0 is the permeability of free space. The intensity of the laser can also be expressed in terms of a reduced vector potential:

$$a_0 = \frac{eA_0}{m_e c} = \frac{eE_0}{m_e c\omega_0} \tag{2.5}$$

Here A_0 is the peak value of the vector potential and ω_0 is the laser frequency. The a_0 parameter is useful because it provides a clear definition of when relativistic effects become important - see Eq. (2.7). Capacitor coil targets are usually driven by long-pulse lasers at $a_0 < 1$, while strong EMP emission is seen for $a_0 > 1$.

Substituting the definition of the reduced vector potential into Eq. (2.4) allows us to relate the reduced vector potential to the normalised laser intensity:

$$I_L\lambda_\mu^2 = 1.37 \times 10^{18} a_0^2 \tag{2.6}$$

where λ_μ is the laser wavelength in units of microns and I_L is the laser intensity in units of Wcm^{-2}. This equation shows the relationship between the laser intensity and wavelength are important and that relativistic effects will be significant for $I_L\lambda_\mu^2 \geq 10^{18}$ $\mathrm{Wcm}^{-2}\mu\mathrm{m}^2$.

Since $|\underline{E}| = c|\underline{B}|$ for a plane wave, Eq. (2.1) suggests that the electric field dominates the electron motion until the electron velocity becomes relativistic. In the non-relativistic regime, the electron will therefore oscillate back and forth in the electric field direction with:

$$\frac{d^2x}{dt^2} = -\frac{e}{m_e}E_0\cos(\omega_0 t)$$

$$\frac{dx}{dt} = -\frac{e}{m_e\omega}E_0\sin(\omega_0 t) \tag{2.7}$$

This classical approximation will break down as the electron quiver velocity dx/dt approaches c, or equivalently $a_0 \to 1$. The reduced vector potential is therefore very useful for assessing both the strength of a laser field and when relativistic effects are likely to be important. The electron kinetic energy is

$$U = \frac{1}{2}m_e\left(\frac{dx}{dt}\right)^2 = \frac{e^2E_0^2}{2m_e\omega^2}\sin^2\omega t$$

Averaging over one laser cycle ($0 < \theta < 2\pi$) gives

$$\langle U \rangle = \frac{e^2 E_0^2}{4 m_e \omega^2}$$

The average quiver energy of electrons in an electromagnetic field is called the *ponderomotive potential*.

2.0.3 Laser propagation in uniform plasma

Consider an electromagnetic wave propagating through a uniform plasma of electrons and cold ions such that $a_0 \ll 1$ and the $\underline{v} \times \underline{B}$ component of the electron motion can be neglected. The dispersion relation of the electromagnetic wave is given by:

$$k^2 = \frac{\omega^2}{c^2} - \frac{n_e e^2}{\epsilon_0 m_e c^2} = \frac{\omega^2 - \omega_p^2}{c^2} \tag{2.8}$$

For the wave to propagate in a forward direction we require $k > 0$. The laser will propagate into the plasma up to the point where $\omega = \omega_p$, i.e. through plasma of increasing density until the plasma frequency equals the frequency of the incident light. The critical density is defined as the material density at which the plasma frequency equals the laser frequency. Rearranging Eq. (1.2), the critical density of an electromagnetic wave with frequency ω_0 is

$$n_{cr} = \frac{\epsilon_0 m_e \omega_0^2}{e^2}$$

which can be rewritten in the following convenient form:

$$n_{cr}[\mathrm{cm}^{-3}] = 1.1 \times 10^{21} \lambda_\mu^{-2} \tag{2.9}$$

where λ_μ is the laser wavelength in microns. When $n_e < n_{cr}$ the plasma is underdense and the laser can propagate through. When $n_e > n_{cr}$, the plasma is overdense and electromagnetic waves are screened out.

2.0.4 Laser propagation into expanding plasma

Consider the case of a high power laser interacting with a solid target. The rising edge of the laser intensity profile will ionise the material and produce a thin layer of overdense plasma in the focal spot. Electron pressure will cause the plasma to expand outwards, chiefly normal to the surface and electric fields from the charge separation will pull ions into vacuum as well (see Sec. 2.3). This can be approximated by a planar expansion from the surface where the plasma density decreases approximately exponentially into vacuum. The 1D expansion model will break down on scales comparable to or larger than the laser focal spot. As the plasma column expands, a rarefaction wave will propagate inwards from the plasma edge. When

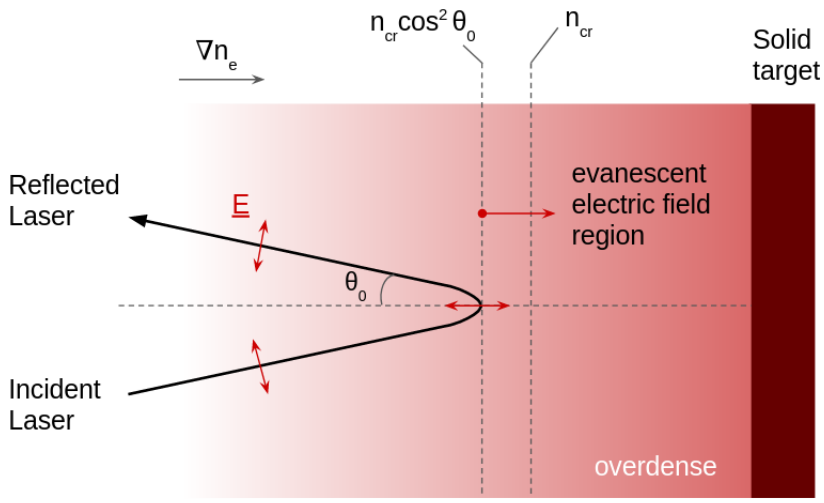

Figure 2.1: Laser propagation into an expanding plasma. The plasma expands in 1D - normal to the surface of the solid target - with an exponentially decreasing density profile.

the rarefaction wave reaches the centre of the plasma column the expansion will be multi-dimensional.

The bulk of the laser pulse will interact with this expanding plasma. The length of the plasma can be characterised by the density scale length, $L_p = n_e/\nabla n_e$. This is true of both long-pulse and short-pulse interactions, although in the short-pulse interaction the plasma scale length is generally much shorter because the plasma does not have time to expand.

The refractive index of the plasma can be expressed as $\eta = kc/\omega$. Using Eq. (2.8), we can re-write this as

$$\eta = \sqrt{1 - \frac{\omega_p^2}{\omega_0^2}} = \sqrt{1 - \frac{n_e}{n_{cr}}} \tag{2.10}$$

As the laser propagates into plasma of increasing density, the refractive index of the plasma will decrease and the beam will refract until it reverses direction. The density at the turning point is given by $n_e = n_{cr}\cos^2\theta_0$ where θ_0 is the incidence angle of the laser. The path of the laser is illustrated in Fig. 2.1. Although the laser cannot propagate past the turning point, the electric field continues as an evanescent wave until the density reaches n_{cr}. Beyond the critical density surface the electric field will decay to $1/e$ its original value over a collisionless skin depth $l_s = c/\omega_0$ [80].

2.1 Laser Absorption Mechanisms

In this section I will outline the major absorption mechanisms relevant to long pulse (nanosecond duration) and short pulse (picosecond duration) laser interactions with overdense plasmas. The relative importance of each mechanism depends sensitively on laser intensity and wavelength as well as plasma conditions (e.g. density, temperature and density scale length).

Laser absorption in the non-relativistic regime ($I_L\lambda_\mu^2 \lesssim 10^{17}$ Wcm$^{-2}\mu$m^2 and $a_0 < 1$) occurs through a variety of collisional and collisionless processes. Inverse bremsstrahlung dominates for $I_L\lambda_\mu^2 < 10^{15}$ Wcm$^{-2}\mu$m^2, when the plasma is relatively cool and collisions are important, generating electrons with energies up to ~ 1 keV. At higher intensity, resonance absorption and parametric instabilities will produce hot electrons up to a few 10-100 keV in energy [179]. These absorption mechanisms are important to the high energy, ns-duration laser pulses used to drive capacitor coil targets. At relativistic laser intensities ($I_L\lambda_\mu^2 > 10^{18}$ Wcm$^{-2}\mu$m^2 and $a_0 \geq 1$) the ponderomotive force becomes an important source of hot electrons. Ponderomotively-accelerated electrons can reach energies exceeding 1 MeV and are relevant to the ps-duration laser pulses that produce large EMPs.

2.1.1 Inverse Bremsstrahlung

Early in the laser-target interaction, before the overdense plasma has had an opportunity to expand, the laser electric field will interact directly with electrons on the surface of the material. Later, as the plasma expands, the laser will start to heat the plasma by a collisional absorption process called *inverse bremsstrahlung*[3]. Electrons absorb energy from the laser by scattering off plasma ions and decoupling from the laser electric field. Subsequent collisions with ions can transfer this energy to the bulk plasma, although the transfer can be slow if $T_e \gg T_i$. Overall, inverse bremsstrahlung leads to damping of the laser energy and heating of the plasma. The fractional absorption due to inverse bremsstrahlung in a linearly increasing density profile with scale length L_p can be expressed as [179]:

$$f_{ib} = 1 - \exp\left(-\frac{32}{15}\frac{\nu_{ei}(n_{cr})}{c}L_p\right) \tag{2.11}$$

where $\nu_{ei}(n_{cr})$ is the electron-ion collision frequency evaluated at the critical density. The electron-ion collision frequency is related to the plasma temperature T_e, electron density n_e and atomic number Z via:

[3]This is the reverse process to *bremsstrahlung* ('braking radiation'), where an electron decelerates in the electric field of an ion and emits a photon. Bremsstrahlung is the major source of x-ray emission in high power laser experiments.

$$\nu_{ei} \propto \frac{n_e Z}{T_e^{3/2}} \tag{2.12}$$

Taken together, equations (2.11) and (2.12) show that high Z, low temperature plasmas with long density gradients will experience more inverse bremsstrahlung absorption. The result is that inverse bremsstrahlung is the dominant laser absorption mechanism for intensities below 10^{15} $\mathrm{Wcm^{-2}\mu m^2}$, producing a thermal (i.e. Maxwellian) population of electrons with energies up to 1 keV. These can be contrasted with the hot, or suprathermal, electrons that are generated at higher intensity, when the plasma becomes too hot to support collisions and collisionless heating processes take over.

2.1.2 Resonance Absorption

Resonance absorption occurs when a p-polarised laser is resonantly coupled to a Langmuir wave at the critical density surface, propelling high energy electrons into the target. Consider again the situation in Fig. 2.1: a plasma is undergoing planar expansion from a solid surface with density gradient ∇n_e; a laser enters the plasma with angle of incidence θ_0, propagating until the electron density reaches $n_e = n_{cr}\cos\theta_0$ and the beam is reflected. If the laser is p-polarised (i.e. $\underline{E} \cdot \nabla n_e \neq 0$) then an evanescent electric field will extend beyond the laser turning point up to the critical density surface, where it undergoes a localised increase in amplitude. Electrons near the critical surface are resonantly driven across the boundary with frequency ω_0,[4] forming a Langmuir wave. The large electric field at n_{cr} is capable of accelerating electrons to supra-thermal energies above 10 keV.

The hot electrons accelerated by resonance absorption form a population of high energy electrons that is superimposed on the cooler thermal electron distribution produced by collisional absorption. A typical laser-heated electron distribution can therefore be approximated by a two-temperature Maxwellian, where the lower energy particles represent the thermal background and the higher energy energy electrons are accelerated by resonance absorption with temperature T_h [67].

The amount of laser energy transferred to hot electrons via resonance absorption depends on the laser angle of incidence and plasma density scale length L_p. In steep density gradients where $L_p < \lambda_L$, a plasma wave cannot be supported and resonance absorption ceases to function in the same way. Instead, the laser electric field will interact directly with electrons at the plasma-vacuum interface. Under the action of the oscillating electric field, free electrons are pulled into vacuum and driven back into the target. Since the electric field can only penetrate to a skin depth $\sim c/\omega_p$ in the overdense plasma, these electrons will decouple from the field and thermalize

[4] since the plasma frequency is equal to the laser frequency at the critical surface

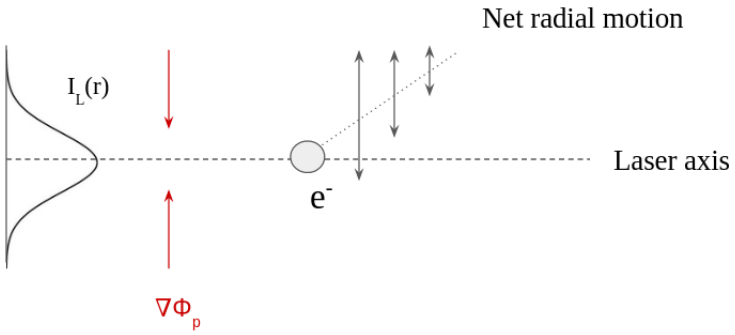

Figure 2.2: Electron motion from the radial ponderomotive force ($a_0 < 1$). As the electron oscillates in the laser focus, it will sample regions of differing intensity. During the first half of its oscillation, the electron will move to a region of lower intensity where the electric field is weaker. The restoring force will be reduced now it is further from the focus, so the electron will gain a net radial motion over the course of several oscillations [80].

on a sub-ps timescale, removing energy from the laser and heating the surrounding material. This "not-so resonant" resonance absorption is called Brunel - or vacuum - heating [31].

2.1.3 Ponderomotive Acceleration

Tight focusing of a high power laser pulse will lead to a strong radial intensity gradient and hence a radial variation in the ponderomotive potential (time-averaged electron quiver energy) [80]. Fig. 2.2 shows how this gives rise to a ponderomotive force $\underline{F} = -\nabla\Phi_p$ that acts to push charged particles down the intensity gradient and radially out of the path of the beam. The effect is much stronger for electrons because the ponderomotive force is inversely proportional to the particle mass. At high intensity ($a_0 > 1$), the magnetic component of the Lorentz force becomes important and electrons experience a relativistic drift in the laser forward direction [103]. The forward-directed, relativistic acceleration of electrons and subsequent collisional heating of the material is referred to as $\underline{J} \times \underline{B}$ heating, where $\underline{J}$ is the current density associated with the $\underline{v} \times \underline{B}$ component of the Lorentz force. For linearly polarised lasers, $\underline{J} \times \underline{B}$ is an oscillating component of the ponderomotive force [103] that drives electrons along the laser axis at twice the laser frequency [176]. At $I_L\lambda_\mu^2 > 10^{18}$ Wcm$^{-2}\mu$m^2, the ponderomotive acceleration of hot electrons to MeV-energies becomes an important absorption mechanism.

Instability	Wave 1	Wave 2	Region
SRS	EM wave ($\omega_0/2$)	Plasmon ($\omega_0/2$)	$n_e \leq n_{cr}/4$
SBS	EM wave ($\sim \omega_0$)	Ion acoustic wave ($\ll \omega_0$)	$n_e \leq n_{cr}$
TPD	Plasmon ($\omega_0/2$)	Plasmon ($\omega_0/2$)	$n_e = n_{cr}/4$

Table 2.1: List of parametric instabilities and their wave products. Note that the wave frequencies are consistent with Eq. (2.13).

2.1.4 Parametric Instabilities

The expanding underdense plasma formed during high power laser-solid interactions can support a variety of waves that couple non-linearly to the laser field. As these waves grow, they may scatter significant portions of the incident laser light and modify laser absorption dynamics [56]. Wave-breaking then produces hot electrons with energies up to several tens of keV. The three most important instabilities relevant to the high-field generation schemes in this thesis are stimulated Raman scattering (SRS), stimulated Brillouin scattering (SBS) and two-plasmon decay (TPD). All three processes involve the decomposition of a laser wave into two new waves with frequencies ω_1 and ω_2 [55]. These new waves may be electromagnetic waves, plasmons (i.e. electron plasma waves) or ion acoustic waves, provided they satisfy the following phase-matching conditions:

$$\omega_0 = \omega_1 + \omega_2 \qquad \underline{k_0} = \underline{k_1} + \underline{k_2} \tag{2.13}$$

When electron or ion density fluctuations beat with the laser they can produce scattered light waves. SRS occurs when a laser photon decays into a plasmon and a scattered photon. It occurs throughout the plasma up to the quarter critical surface ($n_e < n_{cr}/4$). SBS is analogous to SRS, where the second driven wave is an ion acoustic wave instead of a plasmon. SBS occurs up to the critical density surface ($n_e < n_{cr}$). SRS and SBS generally degrade plasma heating by transferring energy to highly penetrating electrons. They can also destroy optical components by scattering laser light back up the optical chain.

Another important instability is TPD, where a laser photon decays into two plasmons at the quarter critical surface ($n_e = n_{cr}/4$). Following Drake in Ref. [56], a summary of these three parametric instabilities can be found in Table 2.1.4.

2.1.5 Hot electron temperature

For 10^{14} Wcm$^{-2}\mu$m$^2 \lesssim I_L\lambda_\mu^2 \lesssim 10^{16}$ Wcm$^{-2}\mu$m^2, the primary source of hot electrons is laser resonance absorption. Combining theory, simulation and experiment [73], the hot electron density and temperature scale with the laser intensity via [169]:

$$n_{h0}/n_{cr} = 0.2(I_{15}\lambda_\mu^2/T_c)^{0.5}, \quad T_h[\text{keV}] = 0.9(I_L\lambda_\mu^2)^{0.25} \tag{2.14}$$

where n_{cr} can be calculated from Eq. (2.9), T_c is the temperature of electrons in the thermal background plasma in units of keV, I_{15} is the laser intensity in units of PWcm^{-2} and the laser wavelength λ_μ is in microns.

For laser intensities $I_L\lambda_\mu^2 \gtrsim 10^{16}$Wcm^{-2}, simulation [67] and experiment [145] suggest that the temperature scaling must be modified [169]:

$$T_h[\text{keV}] = 12(I_L\lambda_\mu^2)^{0.42} \tag{2.15}$$

where the units are unchanged from Eq. (2.14). The hot electron density can then be estimated using a power balance $\eta I_L \approx n_{h0}v_hT_h$, where n_{h0} is the average hot electron density, $v_h = \sqrt{T_h/m_e}$ is the hot electron average velocity and η is the conversion efficiency of laser energy to hot electrons [80]. The conversion efficiency η varies between 0.01 and 0.1 for Nd-glass lasers with ns pulse durations at the third harmonic [82], however shorter pulse durations and longer wavelengths can enhance absorption beyond $\eta \gtrsim 0.5$ [67, 80].

For laser intensities of $\sim 1\times10^{17}$ Wcm^{-2} up to $\sim 5\times10^{18}$ Wcm^{-2} Beg's empirical scaling applies [16]:

$$T_h[\text{keV}] = 215(I_{18}\lambda_\mu^2)^{\frac{1}{3}} \tag{2.16}$$

where I_{18} is the laser intensity normalised to 10^{18} Wcm^{-2} and λ_μ is the laser wavelength in microns. For $I\lambda_\mu^2 \gtrsim 10^{19}$ Wcm^{-2}, the ponderomotive force dominates and the hot electron temperature follows [177]:

$$T_h = m_ec^2(\gamma - 1) \tag{2.17}$$

where γ is the relativistic Lorentz factor of the oscillating electrons. Eq. (2.17) can also be reformulated as a laser intensity scaling [117]:

$$T_h[\text{keV}] = 511\left[(1 + 0.73I_{18}\lambda_\mu^2)^{\frac{1}{2}} - 1\right] \tag{2.18}$$

Using an electron spectrometer positioned in line with the laser propagation axis in the forward direction, Malka and Miquel have experimentally verified the ponderomotive scaling up to 2×10^{19} Wcm^{-2} [117].

Following Ref. [179], Eq. (2.17) can be derived using a simplified fluid model of electron motion in laser electromagnetic fields. Consider an intense laser with electric field $\underline{E}$ and magnetic field $\underline{B}$ that has penetrated a skin depth into overdense plasma. The equation of motion of an electron fluid element close to the plasma-vacuum boundary can be expressed as:

$$\frac{d\underline{p}}{dt} = \frac{\partial \underline{p}}{\partial t} + (\underline{v} \cdot \nabla)\underline{p} = -e\big[\underline{E} + \underline{v} \times \underline{B}\big] \tag{2.19}$$

where $d/dt = \partial/\partial t + (\underline{v} \cdot \nabla)$ is the convective derivative, $\underline{v}$ is the fluid velocity and $\underline{p}$ the fluid momentum. Eq. (2.19) can be rewritten in terms of the electrostatic scalar potential ϕ and the magnetic vector potential $\underline{A}$ using $\underline{E} = \nabla\phi + \partial\underline{A}/\partial t$ and $\underline{B} = \nabla \times \underline{A}$. The vector calculus identity $\underline{v} \times (\nabla \times \underline{A}) = \nabla_A(\underline{v} \cdot \underline{A}) - (\underline{v} \cdot \nabla)\underline{A}$ can then be applied:

$$\frac{d\underline{p}}{dt} = e\nabla\phi + e\frac{\partial \underline{A}}{\partial t} - e\big[\nabla_A(\underline{v} \cdot \underline{A}) - (\underline{v} \cdot \nabla)\underline{A}\big] \tag{2.20}$$

Here, ∇_A represents the gradient operator applied to $\underline{A}$, with $\underline{v}$ assumed constant in space. By definition of the convective derivative, $d\underline{A}/dt$, this equation can be rearranged to yield:

$$\frac{d}{dt}(\underline{p} - e\underline{A}) = e\nabla\phi - e\big[\nabla_A(\underline{v} \cdot \underline{A})\big] \tag{2.21}$$

Eq. (2.21) represents a force balance with two separate terms on the right hand side. The first term is the standard expression for an electrostatic force and the second term represents the laser ponderomotive force. Taking the longitudinal component of each side (parallel to the axis of laser propagation) and rewriting the fluid momentum $\underline{p}$ in terms of the relativistic Lorentz factor γ, the longitudinal component of the ponderomotive force can be expressed as [179]:

$$F_p = m_e c^2 \nabla(\gamma - 1) \tag{2.22}$$

with corresponding potential given by $U_p = m_e c^2(\gamma - 1)$. If the energy transferred to the electrons is equivalent to the ponderomotive potential they experience in the laser field, then U_p can be associated with an effective temperature, as indicated in Eq. (2.17).

2.2 Hot electron transport and return currents

Laser absorption and collisional heating tends to be concentrated around the critical density surface because a laser can typically only penetrate a skin depth past the critical density. Hot electrons produced by collisionless absorption processes can penetrate much further into the target than thermal electrons, which means that they determine the depth and temperature to which the target is heated as well as plasma conditions at the surface where the laser is absorbed [17]. The response of a target to laser irradiation is therefore strongly dependent on hot electron transport. Experiments with intense lasers have shown beams of hot electrons with MeV

energies and MA associated currents. These very high energy electrons have mean free paths larger than the typical target thickness ($\lesssim 3$ mm) so they can leave the target rear surface and contribute towards charging and EMP emission.

When an electron beam enters a plasma, an electric field is established by the separation of charge. This electric field pushes thermal electrons out of the path of the beam and back towards the laser focal spot. These thermal electrons form a return current density J_{cold} that opposes the hot electron current density J_{hot}. The huge magnetic field energy associated with a MA electron beam means that it cannot propagate far without [18]:

$$J_{hot} \approx -J_{cold} \tag{2.23}$$

Where this is not the case, magnetic fields will grow and modify the electron transport. Taking $J_{hot} \approx eN_h v_h/V$ and $J_{cold} \approx eN_c v_c/V$, where N_h/N_c is the number of hot/cold electrons, v_h/v_c is their average velocity and V the beam volume, then Eq. (2.23) shows that an electron beam $100\times$ hotter than the thermal background must be compensated by the slow movement of thermal electrons that are $100\times$ more numerous. A return current will develop on a timescale of order $\sim 1/\omega_p$, or $1/\nu_{ei}$ if the plasma is highly collisional, though the effectiveness of the neutralisation will depend on the conductivity of the plasma medium [9]. One can take $J_{cold} = E_{sc}/\rho_{bg}$, where ρ_{bg} is the resistivity of the background plasma and E_{sc} is the space charge electric field [18]. A high-temperature plasma with few collisions will have a high conductivity, so for a given E_{sc} it will be able to draw a large return current. In reality, the thermal electron distribution will be relatively cold and collisional, more resistive and less able to supply a return current. Without the action of a return current, the hot electron beam current would be limited to a maximum value known as the Alfvén Limit.

2.2.1 The Alfvén Limit

The *Alfvén Limit* is the maximum current that can propagate for an indefinite distance and time in an electrically-neutral beam of charged particles. Above this value, the self-generated magnetic field will be strong enough to divert particles at the beam edge and induce a net backwards motion, preventing the current from increasing further [2]. In his 1939 paper *On the Motion of Cosmic Rays in Interstellar Space*, Alfvén considered an arbitrarily large, cylindrical beam of charged particles with a uniform current density and zero net charge density [51, 2]. He found that the maximum permissible beam current is of order [51]:

$$I_A \approx \frac{4\pi}{e\mu_0} p \tag{2.24}$$

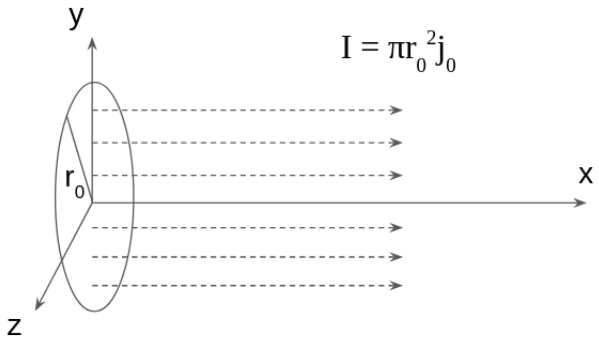

Figure 2.3: Diagram of a charge-neutral particle beam based on Fig. 1 from Ref. [2]. The picture is valid after transient space-charge processes have finished, when the beam current is small and the influence of the beam magnetic field on particle trajectories is negligible. The radial coordinate r is measured from the x-axis and the beam radius is fixed at $r = r_0$. Dashed arrows represent particle trajectories and the total beam current I is given as a function of the fixed current density j_0.

where $p = \gamma m_e v_e$ is the relativistic electron momentum. Fig. 2.3 shows the physical picture used by Alfvén to derive his expression for the Alfvén current I_A. Identical particles with rest mass m_0, positive charge q and kinetic energy E_K are emitted from a circular region of radius r_0 in the positive x-direction. Suppose first that the current is small, such that the beam has uniform charge density j_0 with total beam current $I = \pi r_0^2 j_0$. Any charge separation brought about by the flow of beam particles is neutralised by a slow current of ions in the background medium, allowing the beam to move exclusively under the influence of its own magnetic field. Consider the system after it has reached an equilibrium state and the beam forms a uniform cylinder centred on the positive x-axis. At a radius r from the beam axis, Ampère's law implies that the magnetic field generated by the beam current is:

$$B = \frac{\mu_0 I r}{2\pi r_0^2} \qquad r \leq r_0 \tag{2.25}$$

$$B = \frac{\mu_0 I}{2\pi r} \qquad r > r_0 \tag{2.26}$$

As the beam current increases, eventually the magnetic field will be strong enough to divert positive charges at the beam edge towards the axis. The radius of curvature of each particle trajectory is given by:

$$\rho_C = \left| \frac{(1 + dr/dx)^{\frac{3}{2}}}{d^2 r/dx^2} \right| \tag{2.27}$$

which follows from differential geometry [99]. To a first approximation, one can

assume the magnetic field is fixed throughout the beam volume[5]. The radius of curvature can then be equated to the Larmor radius r_L of each particle:

$$r_L = \frac{p}{qB}$$

where p is the particle momentum, which is everywhere perpendicular to the poloidal magnetic field. The momentum can be expressed in terms of the particle kinetic energy E_K using the canonical energy-momentum relation, $(E_K + m_0c^2)^2 = p^2c^2 + (m_0c^2)^2$:

$$p = \frac{1}{c}\left(E_K^2 + 2m_0c^2E_K\right)^{\frac{1}{2}}$$

Substituting into our expression for the Larmor radius gives:

$$r_L = \frac{(E_K^2 + 2m_0c^2E_K)^{\frac{1}{2}}}{qcB} \tag{2.28}$$

Then setting $q = e$ and $E_K = eV$, where V is the particle energy in electronvolts, Eq. (2.28) becomes:

$$r_L = \frac{((eV)^2 + 2m_0c^2eV)^{\frac{1}{2}}}{ecB}$$

If $eV \gg m_0c^2$, the Larmor radius simplifies to $r_L = V/cB$. Equating to the expression from Eq. (2.27), the equation of motion is:

$$\rho_C = \left|\frac{(1 + dr/dx)^{\frac{3}{2}}}{d^2r/dx^2}\right| = V/cB \tag{2.29}$$

Or equivalently,

$$\rho_C = \frac{2\pi r_0^2}{c\mu_0 r}\frac{V}{I} \qquad (r \leq r_0)$$
$$\rho_C = \frac{2\pi r}{c\mu_0}\frac{V}{I} \qquad (r > r_0)$$

which can be solved using elliptic integrals. Particles originating at different radii from the beam axis will follow different trajectories in the magnetic field according to their equation of motion. For a given beam current, particles are directed forwards and contribute towards the beam current if they originate at some radial point up to a maximum $r' \leq r_0$. Beyond this radius r', the magnetic field is strong enough to divert particle trajectories backwards. Setting $r' = r_0$, particles originating outside of the beam are still pulled backwards by the magnetic field. The $r' = r_0$ condition

[5]This constant magnetic field approximation is sufficient for an order of magnitude estimate of I_A. A more general treatment can be found in Ref. [53].

therefore corresponds to a maximum current that can propagate indefinitely in the forward direction. The value of the current corresponding to $r' = r_0$ - the Alfvén Limit - is given by [53]:

$$I_A = 1.65 \frac{4\pi}{e\mu_0} p \tag{2.30}$$

Notice that the limit does not depend on the current density or beam cross-sectional area - only on the beam energy. Alfvén also supplies a more convenient equation, $I_A \approx V/30$. For 1 MeV relativistic electrons (relevant to short-pulse interactions and strong EMP), the Alfvén Limit is $I_A = 47.4$ kA, while for 30 keV electrons (relevant to resonance absorption processes at medium laser intensity) the Alfvén Limit is just $I_A = 5.9$ kA. Both of these values are considerably smaller than the currents measured in short-pulse laser-foil interactions and long-pulse capacitor coil experiments. It is important to note that the Alfvén limit applies to the *net* current only. When an electron beam enters a plasma, charge separation will quickly draw a return current of electrons that flows towards the source of electrons. The result is a net current in the forward direction that is much lower than the electron current in the beam. In this way, super-Alfvénic forward currents can be supported in a plasma, provided the plasma density and space charge electric field is sufficiently high to supply a return current.

2.3 Plasma Expansion into Vacuum

Solid targets irradiated by high power lasers will rapidly heat up and expand. The laser ablation process is an important means of removing charge from solid targets, providing the 'engine' for capacitor coil magnetic fields. Furthermore, charge separation in an expanding laser-plasma can accelerate ions to high energy. In Part III Chap. 5, I will present results from an experiment where laser-driven proton beams were used to make radiographic measurements of multi-tesla magnetic fields [28]. To provide some background to this work, it is important to discuss how plasma expands from a plane surface. While the laser is on, it supplies a constant source of heat to the plasma which counteracts expansional cooling. The system can therefore be modelled as an isothermal expansion provided the plasma density and rate of collisional conduction are sufficiently low [56]. For simplicity, we will consider plasma expansion in one dimension, with spatial coordinate x. This picture is valid close to the ablation surface (i.e. for $x < r_h$, where r_h is the laser focal radius on the target). Beyond this point the expansion will become multi-dimensional.

2.3.1 Planar Isothermal Rarefaction

It is instructive to consider a single, electrically-neutral particle species before the more complex case of a two-species plasma is examined. When the laser is switched on and the material reaches a fixed temperature, the system will evolve as a planar isothermal rarefaction. Initially, the material is a cold fluid filling the region $x \leq 0$ with particle number density $n_i = n_0$. For $x > 0$, $n_i = 0$.

The system dynamics can be described by the Euler equations of mass, momentum and energy conservation [56]:

$$\partial_t n_i + u_i \partial_x n_i + n_i \partial_x u_i = 0 \tag{2.31}$$

$$\partial_t u_i + u_i \partial_x u_i + \frac{1}{n_i} \partial_x P = 0 \tag{2.32}$$

$$\partial_t P + u_i \partial_x P - c_s^2 (\partial_t n_i + u_i \partial_x n_i) = 0 \tag{2.33}$$

where u_i is the particle velocity, P the material pressure and c_s the one dimensional sound speed of the material. Here, a subscript notation $\partial_A B$ is employed to denote the partial derivative of some variable B by another variable A.

A fixed temperature produces a fixed expansion velocity, so the system will have the same physical form at all times. These equations therefore admit a *self-similar* solution with spatial scale $R(t)$ and $c_s = \partial_t R$. Defining the dimensionless self-similar variable $\xi = x/R$, one can rewrite the physical variables v_i, n_i and P as a function of ξ multiplied by a characteristic amplitude [56]:

$$\begin{aligned} u_i &= \dot{R} U(\xi) \\ n_i &= n_0 N(\xi) \\ P &= n_0 \dot{R}^2 P(\xi) \end{aligned}$$

where the overdot represents a time derivative. Since $c_s^2 = P/n_i = c_s^2 n_0 P(\xi)/n_0 N(\xi)$, it follows that $P(\xi) = N(\xi)$. For an arbitrary function $g(\xi, t')$, the product rule dictates that:

$$\partial_t g(\xi, t') = \partial_\xi g \partial_t \xi + \partial_t g \partial_t t' \tag{2.34}$$

Hence the mass continuity equation (2.31) can be written:

$$[U(\xi) - \xi] N'(\xi) + N(\xi) U'(\xi) = 0 \tag{2.35}$$

And the momentum equation becomes

$$[U(\xi) - \xi]\, N(\xi)U'(\xi) + N'(\xi) = 0 \tag{2.36}$$

These equations have the straightforward solution

$$N(\xi) = n_0 e^{-\xi}$$
$$U(\xi) = 1 + \xi$$

Substituting for $\xi = x/R = x/c_s t$, the solution can be recast in terms of physical variables:

$$n_i(x,t) = n_0 e^{-\frac{x}{c_s t}}$$
$$u_i(x,t) = c_s(1 + \frac{x}{c_s t}) = c_s + \frac{x}{t}$$

Since $u_i \geq 0$ everywhere, this solution is valid for $x \geq -c_s t$. Key points to take away are that the velocity profile is linear in space and the density profile is exponential.

2.3.2 Planar Isothermal Plasma Expansion

A similar technique can be used to describe the expansion of an isothermal plasma with distinct ion and electron species. The positive ions are modelled as a slab of cold fluid filling the half-plane $x \leq 0$ with uniform number density $n_i = n_{i0}$. For $x > 0$, $n_i = 0$ so there is a sharp boundary at $x = 0$. The electrons, meanwhile, will be have a fixed temperature T_e that is sustained by the drive laser. Since the plasma expansion will take place on a timescale much longer than an electron oscillation period, the electrons will remain in equilibrium with the electric potential and a Maxwell-Boltzmann distribution function can be employed [45]:

$$n_e = n_{e0} e^{eV/T_e} \tag{2.37}$$

Here, Z is the ionization level of the plasma, V the plasma potential and n_{e0} the electron density in the unperturbed plasma. We take $n_{e0} = Z n_{i0}$ by quasi-neutrality. Referring to Fig. 2.4, the spatial offset of the ions and electrons will give rise to an electric field that accelerates ions out of the plasma bulk. The corresponding electrostatic potential can be accounted for using Poisson's equation:

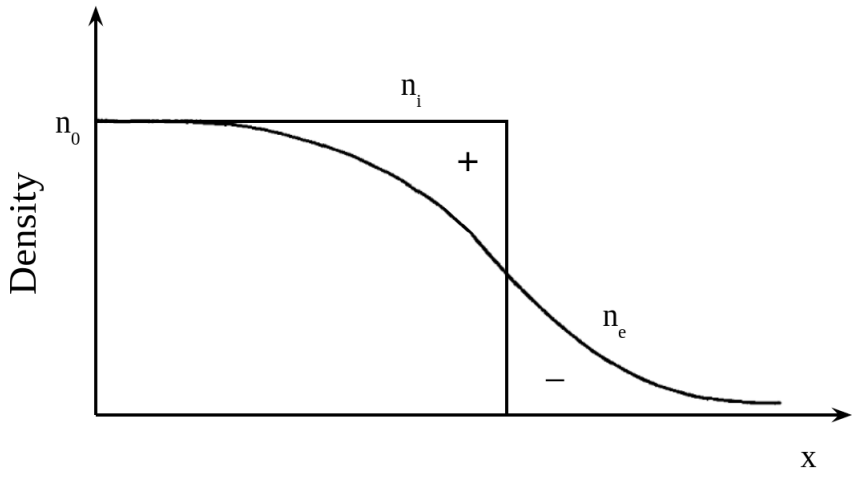

Figure 2.4: Initial conditions on the ion and electron density for a 1D plasma expansion model with $Z = 1$ [45].

$$\epsilon_0 \frac{\partial^2 V}{\partial x^2} = e(n_e - n_i) \tag{2.38}$$

The electrons will screen the plasma potential over a characteristic scale given by the initial Debye length, $\lambda_{D,0} = (\epsilon_0 T_e / e^2 n_{e0})^{\frac{1}{2}}$.

The expansion of the plasma is described by the equations of mass and momentum conservation for a collisionless, non-relativistic fluid:

$$\partial_t n_i + v_i \partial_x n_i + n_i \partial_x v_i = 0 \tag{2.39}$$

$$\partial_t v_i + v_i \partial_x v_i = eE/m_i \tag{2.40}$$

where n_i and v_i are the ion density and ion velocity and E is the electric field. Solving these four equations (2.37)-(2.40) gives solutions for planar isothermal plasma expansion.

Substituting Poisson's equation into Eq. (2.40) yields:

$$\partial_t v_i + v_i \partial_z v_i = -\frac{c_s^2}{n_i} \frac{\partial n_i}{\partial x} \tag{2.41}$$

where $c_s = \sqrt{ZT_e/m_i}$ is the ion sound speed. Following Allen *et al.* [3], a self-similar solution can be found using the variable $\zeta = x/t$.[6] Observing that

$$\frac{\partial}{\partial x} = \frac{1}{t}\frac{d}{d\zeta} \qquad \frac{\partial}{\partial t} = -\frac{\zeta}{t}\frac{d}{d\zeta} \tag{2.42}$$

the mass and momentum conservation equations can be written:

[6] Alternatively, one could use the dimensionless variable $\zeta = x/c_s t$.

$$(u_i - \zeta)\frac{dn_i}{d\zeta} = -n_i\frac{du_i}{d\zeta} \tag{2.43}$$

$$(u_i - \zeta)\frac{du_i}{d\zeta} = -\frac{c_s^2}{n_i}\frac{dn_i}{d\zeta} \tag{2.44}$$

Eliminating $dn_i/d\zeta$, one obtains:

$$(u_i - \zeta)^2 = c_s^2 \tag{2.45}$$

This equation has two roots. The positive root is consistent with a plasma defined for $x < 0$ and ions moving towards $+x$:

$$u_i - \frac{x}{t} = c_s \tag{2.46}$$

As before, the $u_i \geq 0$ condition requires that $x + c_s t \geq 0$. Substituting Eq. (2.46) into Eq. (2.44) yields

$$\frac{du_i}{d\zeta} = -\frac{c_s}{n_i}\frac{dn_i}{d\zeta} \tag{2.47}$$

which can be integrated over ζ to produce:

$$u_i = -c_s \ln(n_i/n_0) \tag{2.48}$$

where we have used the fact that $u_i = 0$ in the bulk plasma, when $n_i = n_0$. Substituting Eq. (2.46) into Eq. (2.48) gives

$$\zeta + c_s = -c_s \ln(n_i/n_0)$$

And rearranging yields a self-similar solution for the ion density:

$$n_i = n_0 e^{-\left(\frac{\zeta}{c_s}+1\right)} = n_0 e^{-\left(\frac{x}{c_s t}+1\right)} \tag{2.49}$$

The electron density follows by quasi-neutrality ($n_e = Zn_i$) and the ion velocity follows directly from Eq. (2.48):

$$u_i = c_s + \frac{x}{t} \tag{2.50}$$

Fig. 2.5a and 2.5b show the spatial variation of the self-similar ion density in a H plasma with $T_e = 10$ keV. Plasma rarefaction begins at the point $x = -c_s t$, propagating into the plasma bulk at speed c_s. Fig. 2.5a shows that this expansion causes the ion density to fall exponentially with distance, forming a corona. In Fig. 2.5b, though most of the ions have only moved a few mm after 1 ns of expansion, some ions are immediately accelerated to infinity for $t > 0$.

A self-similar solution for the electric field follows. By substituting the Maxwell-Boltzmann relation into Eq. (2.48), one can find an expression for u_i in terms of the electric potential:

$$u_i = -c_s \ln(n_i/n_0) = c_s \frac{eV}{T_e} \tag{2.51}$$

The spatial derivative of Eq. (2.46) is:

$$\frac{1}{t} = \frac{du_i}{dx}$$

Then taking the spatial derivative of Eq. (2.51) and observing that $E = -dV/dx$, one can substitute for du_i/dx to reveal the self-similar electric field:

$$E = \frac{T_e}{ec_s t} \tag{2.52}$$

Following Mora [129], the electric field can be rewritten terms of the ion plasma frequency $\omega_{pi} = (Zn_{e0}e^2/m_i\epsilon_0)^{\frac{1}{2}}$ and a characteristic electric field E_0:

$$E = \frac{E_0}{\omega_{pi} t}$$

where $E_0 = (n_{e0}T_e/\epsilon_0)^{\frac{1}{2}}$. The self-similar electric field is uniform inside the expanding plasma, equivalent to the electric field in a capacitor with charge density $\sigma = \epsilon_0 E$. Since the self-similar solution only applies inside the expanding plasma, from the beginning of the rarefaction wave out to the tip of the quasi-neutral plasma, we expect a positively charged surface $+\sigma$ at $x = -c_s t$ and a negative charge surface $-\sigma$ at the plasma edge. An expression for the self-similar voltage follows from Eq. (2.51):

$$V = \frac{T_e}{e}\left(1 + \frac{x}{c_s t}\right) \tag{2.53}$$

The self-similar plasma expansion model is useful because it gives simple estimates of plasma parameters close to an ablating foil. These can be used to estimate the energy of ions accelerated inside the plasma (discussed in the next section) or the voltages induced in laser-targets and their impact on charged particle emission [6, 160]. The picture of an expanding plasma sheath as a capacitor is influential in models of capacitor coils [71, 82] which will be examined in Sec. 2.6.1. Of course the self-similar model also features some important limitations. For example, the self-similar solution is invalid when the plasma density scale length is smaller than or comparable to the plasma Debye length ($c_s t \leq \lambda_D$). This is true at early times, when $\omega_{pi} t \leq 1$. For $\omega_{pi} t \gg 1$, the self-similar model can be applied and we have seen that it predicts an ion velocity that increases without limit as $x \to \infty$. In reality,

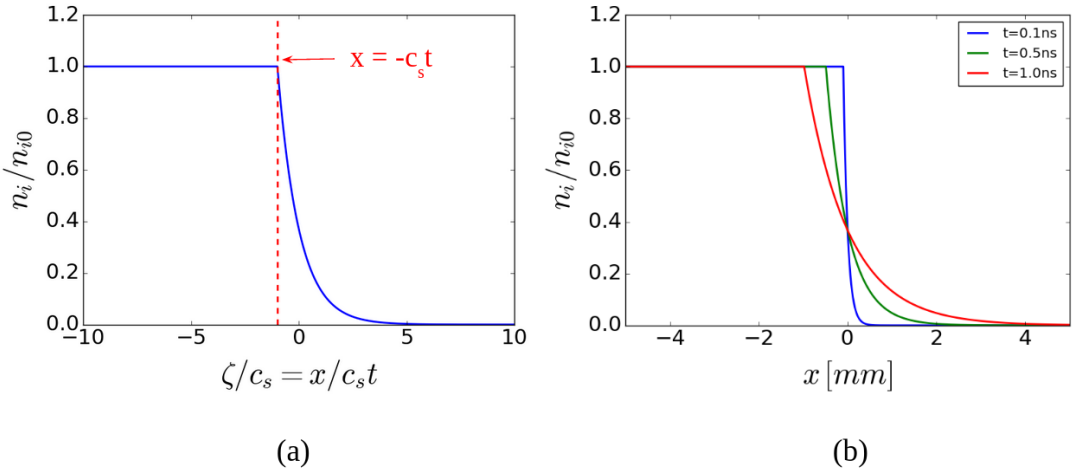

Figure 2.5: Self-similar solution for the ion density in an initially cold H plasma with $T_e = 10$ keV. The normalised density is plotted as a function of (a) x normalised to the plasma scale length (b) x. Note that the density profile in (a) will remain fixed at all times since the solution is self-similar.

of course, the maximum ion velocity will be finite at any given time. Another limitation stems from the condition that $n_e = Zn_i$, which neglects charge separation (space charge) in the expanding plasma [45].

Inaccuracies inherent in the self-similar model can be circumvented by solving Eq. (2.37)-(2.40) numerically [45, 129]. Computation shows that the ions actually form a well defined 'front' as they move towards $+x$, in contrast to the exponential profile of the electrons (see Fig. 2.6). Fig. 2.7 shows results calculated by Mora [129] that were computed at time $\omega_{pi}t = 50$. Fig. 2.7a shows the charge separation $(n_e - Zn_i)/n_{e0}$. Three distinct regions can be distinguished: a concentration of positive charge σ at the point of rarefaction, a second region of positive charge σ inside the plasma behind the ion front and a region of negative charge -2σ beyond the front in the surrounding electron cloud. This agrees well with the self-similar picture of an expanding capacitor described earlier. The electric field in Fig. 2.7b is relatively uniform inside the expanding plasma region and agrees well with the self-similar solution (dotted line) up to the plasma edge. Beyond the ion front, the electric field grows to a peak at approximately twice the self-similar value. As time goes on and the plasma continues to expand, the ion velocity increases without limit. This is a natural consequence of our isothermal condition: the force exerted on the ions is constant and equal to the electron pressure in the plasma bulk [45].

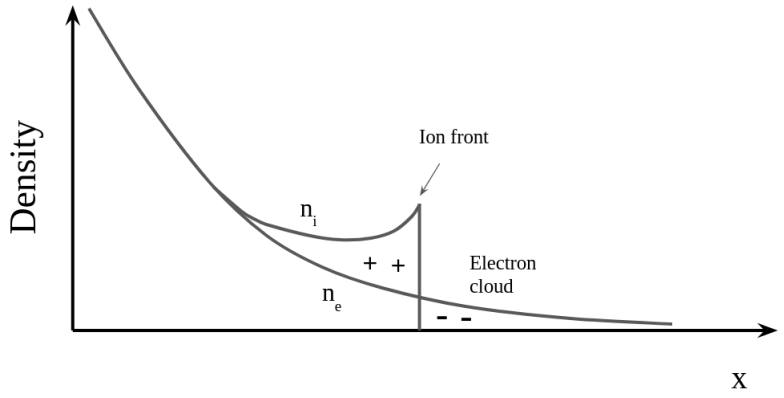

Figure 2.6: Diagram of ion and electron density distributions in a 1D expanding plasma [45].

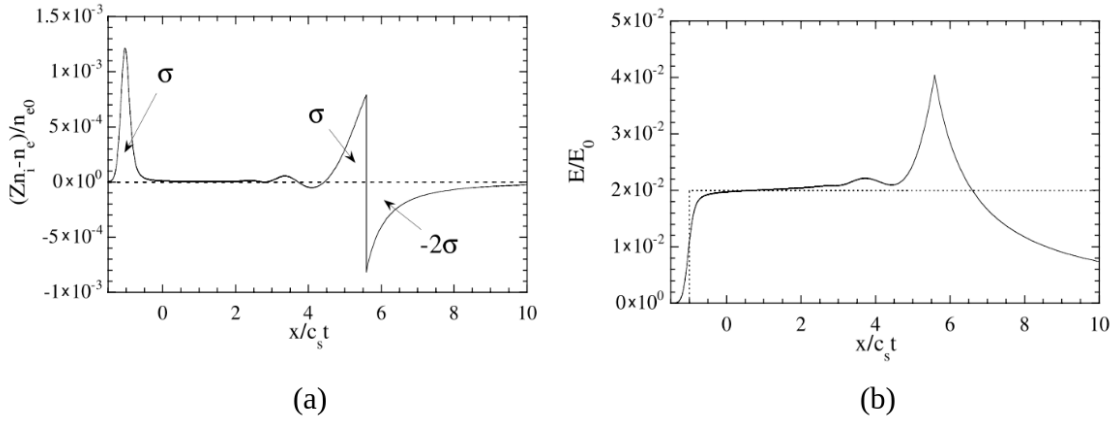

Figure 2.7: Numerical solutions for a semi-infinite plasma expanding in one dimension, plotted at 'time' $\omega_{pi}t = 50$. Both figures are taken from Ref. [129] and are reproduced with permission of the author. (a) Charge separation plotted as a function of normalised space (solid line). The ion front can be clearly distinguished at position $x/c_s t \sim 5.59$ and the dashed line represents a neutral plasma. (b) Electric field plotted as a function of normalised space. There is good agreement between the numerical solution (solid line) and the self-similar solution (dotted line) inside the plasma. Close to the ion front, however, the two solutions diverge and the electric field grows to approximately twice the self-similar value at $x/c_s t \sim 5.59$.

Summary of self-similar plasma expansion in 1D

Initially, the half-plane $x < 0$ is filled with plasma. Cold ions are confined to this neutral plasma with a sharp boundary at $x = 0$, while the electrons are thermally distributed and extend beyond the plasma surface into vacuum ($x > 0$). The voltage satisfies $V(-\infty) = 0$. A self-similar solution is valid after the plasma scale length has grown larger than the Debye length ($\omega_{pi}t >> 1$) and is confined to the region $x > -c_s t$. The self-similar solution is given by:

$$
\begin{aligned}
n_i &= n_{i0} e^{-\left(1+\frac{x}{c_s t}\right)} \\
n_e &= Z n_i \\
v_i &= (x + c_s t)/t \\
E &= \frac{k_B T_e}{e c_s t} \\
V &= \frac{k_B T_e}{e}\left(1 + \frac{x}{c_s t}\right)
\end{aligned}
$$

These equations correspond to a rarefaction wave that burrows into the plasma at the ion acoustic speed, causing the ion density to decay exponentially away from the unperturbed plasma. The electric field is uniform inside the expanding plasma and proportional to the electron temperature. The situation is analogous to a plasma capacitor with anode at the rarefaction front and cathode at the edge of the expanding plasma.

2.4 Target Normal Sheath Acceleration

Through self-similar modelling of an isothermal plasma, we have seen how laser heating can cause the rapid expansion and acceleration of positive ions. This section examines how the acceleration process can be exploited to produce energetic laser-driven ion beams suitable for diagnosing electromagnetic fields. Proton beams are a key diagnostic of magnetic fields produced by electrical discharges in capacitor coils [28, 79] and wire targets [147, 118, 1]. Calculations of the electric field inside a plasma sheath are also used in target charging models [71, 112, 6] (see Sec. 2.6.1).

Beginning in the early 1960s, ions with energy up to tens of keV were routinely observed in laser-matter interactions involving long-pulse (nanosecond) lasers [81]. With the advent of CPA laser technology and short-pulse laser systems, proton beams with energies exceeding 10 MeV were recorded in laser interactions with thin foils [163, 40]. The source of the protons was found to be a layer of hydrogen-

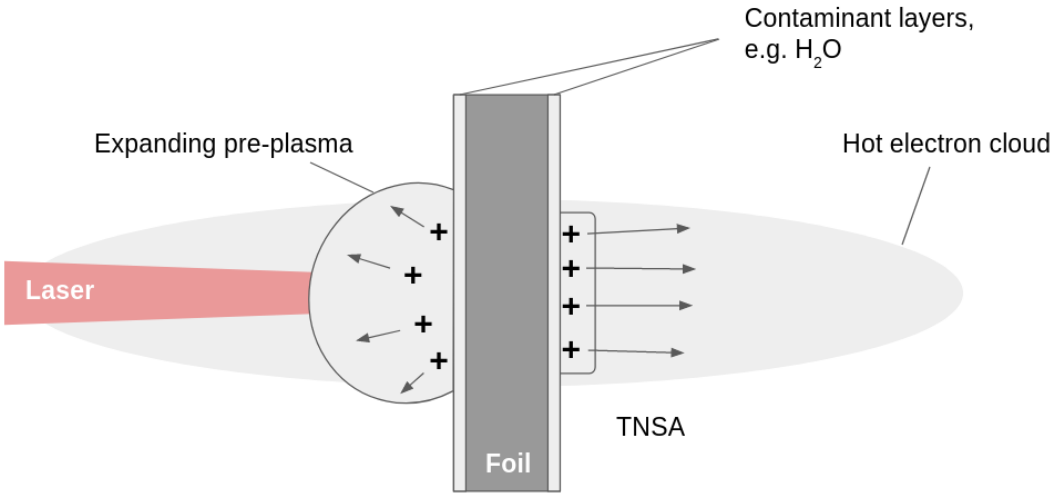

Figure 2.8: Target Normal Sheath Acceleration (TNSA) during the interaction of a high intensity laser with a thin foil. Black crosses represent positive ions from the contaminant layers that are accelerated by sheath fields. First, the laser ASE pedestal generates a pre-plasma that expands over time to ~ 100 μm scale length. When the main laser pulse arrives, it generates suprathermal hot electrons that can propagate forwards into the target or backwards into vacuum. Hot electrons that emerge from the target rear surface will form an electron sheath with micron-scale Debye length. The resulting electric field, of order MV/μm, causes material ionization and accelerates ions to multi-MeV energies [121].

rich contaminant covering the surface of the laser targets [178]. These protons, along with some heavier ions, are accelerated by electric fields generated by charge separation in the expanding laser-plasma. The acceleration mechanism is known as Target Normal Sheath Acceleration, or TNSA, because ions are accelerated normal to the target surface by strong planar sheath fields [178, 24].

A schematic of the TNSA mechanism is presented in Fig. 2.8. The Figure shows a high-intensity CPA laser ($I\lambda_\mu^2 \geq 10^{18}$ Wcm^{-2}) incident on a thin metal foil ($1 - 10$ μm-thick). First, the front surface of the foil is ionized by the laser pre-pulse, forming a pre-plasma. Then, when the main pulse arrives, a population of suprathermal electrons is excited to multi-MeV energies with collisional ranges much larger than the foil thickness. These electrons form a cloud whose boundary quickly overtakes the ions expanding off the front and rear surfaces [121]. A small proportion of these electrons (the most energetic) can leave the target entirely; most, however, will reflux and be confined to an expanding plasma sheath. The electric field caused by the separation of the ion and electron fronts can accelerate ions to high energy over distances of order ~ 1 μm. A simple expression for the electric field follows from the self-similar solution derived in Sec. 2.3.2. Assuming the electric field is constant during the laser pulse when hot electrons are being produced, the

sheath field is given approximately by:

$$E = \frac{T_e}{c_s t} = \frac{T_e}{L_p}$$

for some early time t, where L_p is the plasma scale length during the laser drive. The dependence of E on L_p suggests that the electric field will be much larger on the back of the foil than the front. Since the foil rear surface is flat with a steep density gradient, ions are quickly accelerated to high energy in the forward direction. At the front surface, meanwhile, the pre-plasma has expanded to a scale length of order $L_p \lesssim 100$ μm before the hot electrons arrive; front surface ions are therefore accelerated to lower energies and emitted over $\sim 2\pi$ steradians [178]. Assuming the plasma scale length is of order the initial Debye length, $L_p \sim \lambda_{D0}$, the size of the electric field at the rear surface can be estimated. Typical values for incident laser intensity ($I\lambda_\mu^2 = 10^{19}$ Wcm^{-2}) and hot electron temperature ($T_h = 1$ MeV) correspond to $\lambda_{D0} = 1$ μm and electric fields of $\sim$TVm^{-1} [24]. 2D simulations of the target rear surface agree well with these estimates [178].

Important features of TNSA proton beams are their high energy, small source size, good spatial uniformity and low divergence. If the proton beam enters a material, each particle will deposit the majority of its energy in a peak along the Bragg curve. In light of these peculiar properties, TNSA proton beams may be suitable for a wide range of applications across physics and medicine [116, 47]. In particular, they were used during the Vulcan experiment described in Part III Chap. 5 to map electric and magnetic fields in capacitor coil targets.

2.5 Laser-Induced Target Charging

When a solid target is irradiated by an intense laser it develops a strong electric potential as hot electrons are emitted from the material surface. Early voltage measurements by Pearlman and Dahlbacka showed that 50 ps Nd:glass laser pulses[7] could induce kV voltages lasting for > 10 ns in Al foil targets [136]. These voltages were much higher than predicted from pressure gradients in the plasma; results were explained using a lumped element circuit model of the target chamber and a simple model of electron ejection. All electrons with energy exceeding the maximum target potential $\Phi_E = eV$ can escape the target and strike the chamber wall; electrons with lower energies will return to the target even if they have travelled a considerable distance from the surface. If $f(E)$ is the distribution function of hot electrons produced by a laser, then the number of escaping electrons is given by:

[7]The laser intensity is not provided in Ref. [136], though the temperature of escaping hot electrons was measured to be ~ 0.5 keV.

$$N_{esc} = \frac{\Omega}{4\pi} \int_{E_0}^{\infty} f(E) dE \tag{2.54}$$

where E_0 is the minimum kinetic energy required to overcome the target potential and Ω is a solid angle of emission such that $\Omega/4\pi$ represents the fraction of electrons travelling in the correct direction to escape. The charging model represented by Eq. (2.54) has remained essentially unchanged in papers spanning 40 years [19, 160, 143, 43]. In 1979, Benjamin *et al.* [19] extended these results to shorter wavelengths and longer pulse durations, demonstrating that a potential of 180 kV can be achieved in a 12 mm×15 mm×6 mm Al block upon irradiation by a 133 J CO_2 laser pulse of 1.2 ns duration. Heating of the target support was caused primarily by Ohmic heating as a discharge current propagated to ground. Following the development of proton radiography, measurements of electric and magnetic fields allowed for measurements of multi-kA transient currents and magnetic fields in the target and support wires [147, 97, 118]. In this section we will focus on target charging in the ultra-intense regime ($t_{las} \leq 1$ ps). The interested reader will find a semi-empirical charging model relevant to ns-duration laser pulses and ICF in papers by Sinenian *et al.* [160, 161].

Laser-induced charging of a thick conducting target (i.e. thicker than the electron range) unfolds in several steps [58], as illustrated in Fig. 2.9. First, the laser generates a cloud of hot electrons that expand out from the focal spot. Hot electrons accelerated into the target will diffuse into the solid material. Scattering will be dominated by elastic collisions with nuclei and energy losses are dominated by inelastic collisions with background electrons. These hot electrons will draw a return current on a fs-timescale that maintain charge neutrality. Hot electrons that leave the target surface will generate an electrostatic potential Φ_E. Hot electrons without sufficient energy to overcome Φ_E will reflux in the expanding laser plasma. Differences between the hot electron and ion temperatures in the plasma will establish a thermal potential $\Phi_{th} \sim T_h$ and sheath electric field $E_s \sim T_h/e\lambda_D$ over a Debye length λ_D. The combined electrostatic and thermal potentials prevent all but the most energetic electrons from escaping into vacuum. Hot electrons that escape entirely leave behind a positive charge on the target. Target charging will continue until the laser has stopped and the hot electrons have cooled. The accumulated charge will eventually be neutralised by a cold current of electrons on a ns-timescale. A steady state regime may develop for long laser pulses ($t_{las} \sim$ ns) where a cold neutralisation current flows into the target, partially compensating the hot electrons being ejected by the laser. Charging of a thin target will proceed in much the same way except that hot electrons can also escape from the target rear surface [143].

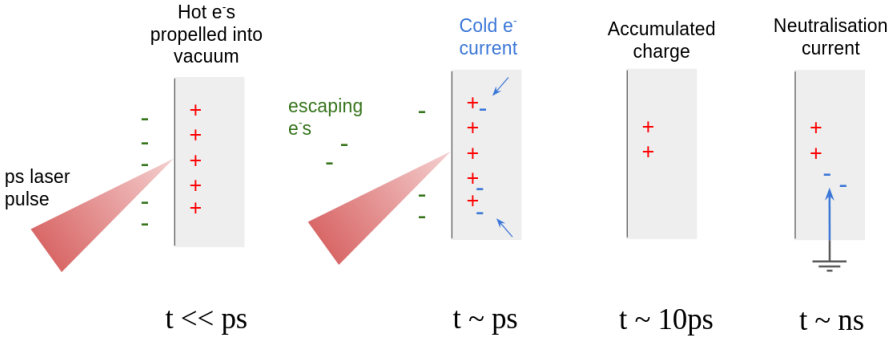

Figure 2.9: The target charging process for a ps-duration laser interaction. Electrons are ejected from the target surface while the laser is on and before the electrons have collisionally cooled - typically on a timescale of $1 - 10$ ps. The target accumulated charge then draws a current from the nearest ground, usually the target chamber, on a ns-timescale determined by the impedance and inductance of the holder.

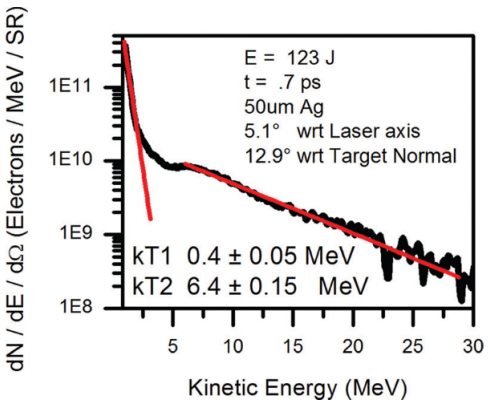

Figure 2.10: Time-integrated electron spectrum (black line) measured during the interaction of an ultra-intense laser with a solid target. The laser had a peak intensity of $\sim 1.5 \times 10^{20}$ Wcm^{-2} and the target was a 50 μm-thick, 1 mm-wide Ag foil. Red curves represent exponential fits to the data. The lower energy red curve has a gradient of 0.4 MeV and the higher energy curve has a gradient of 6.4 MeV. Figure reproduced from Link *et al.* [112] with permission.

When modelling the target charging process, one must explain differences between the escaping electron distribution and the electron distribution generated by the laser. Fig. 2.10 shows a typical time-integrated electron energy distribution measured with an electron spectrometer located behind a metallic foil target between the laser axis and target normal [112]. The laser was s-polarised at near-normal incidence to the target. The red curves are exponential fits to the data at high and low energy, demonstrating that the electron distribution can be divided into two populations with well-defined gradients. Simulations suggest that electrons from the high energy group (kinetic energy > 5 MeV) pass quickly out of the target without refluxing, while electrons in the lower energy group form part of the expanding laser-plasma [112]. A successful model of target charging must account for both of these electron populations.

2.5.1 Capacitor model of target charging

A capacitor model can be used to account for the electrostatic potential that develops as more electrons leave the target. Following Link *et al.* [112], the target voltage can be defined as:

$$V(t) = Q_{esc}(t)/C$$

where Q_{esc} is the number of hot electrons that have left the target surface and C is the target capacitance. At a given time t, if an electron with kinetic energy E_0 satisfies $E_0 > \Phi_E(t) = e\,V(t)$ then it will escape and reach the detector with reduced energy $E_0 - e\,V$. The capacitance of an arbitrary rectangular foil can be approximated by the capacitance of a conducting sphere of the same surface area with effective radius r.

The capacitor model admits two limiting cases that are useful for understanding how target capacitance impacts the charging process. If the target capacitance is very large, the target potential will only increase by a small amount each time an electron escapes the target. The voltage will build slowly and almost all of the hot electrons can escape ($N_{esc} \approx N_h$). Conversely, if the target capacitance is small, the voltage will rise sharply as electrons escape and charge builds in the target. Let E_{max} be the energy of the most energetic electron in the distribution. Once the target potential reaches $\Phi_E = E_{max}$, no more electrons can escape. This will occur at the peak of the laser pulse, when the most energetic electrons are produced. Recall that $V = Q_{esc}/C = eN_{esc}/C$. Since the peak target potential depends only on E_{max} and not the total number of hot electrons generated by the laser, the number of escaping electrons can be estimated via $N_{esc} = CV_{max}/e = CE_{max}/e^2$. Calculations of the escaping electron fraction suggest the target effective radius should be less

than 1 μm to be in the limit of small capacitance and larger than 1 cm to be in the large capacitance limit [112]. Using these limiting values, it is possible to calculate bounding estimates for the charge that can build up on a target. In the large capacitor limit, with $C = 10^{-12}$ F and a total hot electron number of 10^{14}, the accumulated charge is ~ 10 μC. In the small capacitor limit, with $C = 10^{-16}$ F and maximum electron energy $E_{max} = 50$ MeV, we have $N_{esc} \approx 1 \times 10^{10}$ and an accumulated charge of 1 nC.

In Ref. [112], Link *et al.* compare the capacitor model with simulations of target charging using a 2D hybrid implicit PIC code called LSP. The LSP code contains many physical processes that are absent from the capacitor model, including: (i) resistive E-fields (ii) magnetic fields (iii) spatially-varying E-fields on the surface of the target (iv) collisions. The interplay between these four factors can significantly change the measured electron energy spectrum compared with the laser-generated spectrum. A time-varying hot electron source was used for both the capacitor model and the LSP simulations. The 50 μm-thick, 250 μm-diameter disk used in the LSP simulations was approximated in the capacitor model by a conducting sphere of the same surface area.

LSP simulations revealed that hot electrons escape to vacuum in two distinct phases, corresponding to the two exponential parts of the electron distribution (red curves in Fig. 2.10). The electrons that escape in Phase 1 are the most energetic; they pass straight out of the target without refluxing and their energy distribution qualitatively matches the source profile albeit at reduced energy. The electrons that escape in Phase 2 co-propagate with ions that are accelerated by the surface electric field. These are the hot electrons that were trapped by the electric field that developed in Phase 1. They have much lower energy than the Phase 1 electrons but are more numerous. Their energy distribution depends on many factors (e.g. sheath temperature and electric field), so they are not captured by the capacitor model. When a surface layer of protons was added to the LSP simulations, the low energy feature apparent in Fig. 2.10 appeared in the escaped distribution. Without the protons, LSP significantly underestimated the number of lower energy electrons (reduced energy < 1 MeV) that could escape. These lower energy electrons account for approximately one quarter of the escaping electrons or 1% of the input electrons and have no impact on the high energy electrons emitted during Phase 1. The important point is that sheath acceleration of ions is needed to capture the low energy exponential portion of the escaping electron distribution.

The portion of the electron distribution composed of hot electrons that escape during Phase 1 is captured extremely well by the capacitor model. Fig. 2.11 shows the effect of the capacitance on electrons produced at the peak of the laser pulse. The electron source distribution is picked out in black and those electrons with

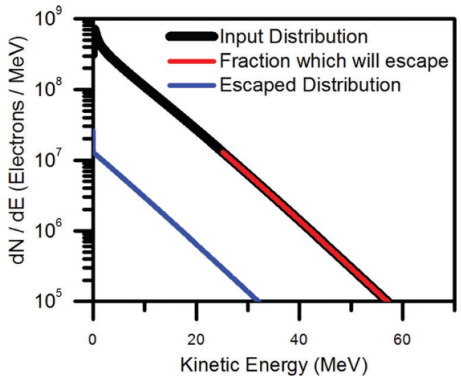

Figure 2.11: Graph demonstrating the effect of target charging on the hot electron distribution at the peak of an intense laser pulse. The black curve represents the source electron distribution - note that the y-axis scale is much smaller than in Fig. 2.10 because this is the distribution at the pulse peak. Hot electrons with sufficient energy to escape the target potential are highlighted in red. The blue curve represents the escaped electron distribution measured at infinity. Figure taken from Link *et al.* [112] with permission.

sufficient kinetic energy to escape the target are highlighted in red. The blue curve represents the energy distribution of the escaping electrons at infinity. Though the escaped electron distribution has a much lower average temperature than the source, escaping electrons experience a near-constant energy loss from the target potential and so the slope temperature is the same as the source curve.

Link's study shows the importance of understanding hot electron transport as electrons travel from the laser focus, through the target and into vacuum. Major differences between LSP and the capacitor model are found at the high (> 30 MeV) and low (< 5 MeV) energy ends of the distribution where sheath physics, electron crossing and geometrical effects cause a divergence from the capacitor model. The capacitor model was also not verified in the regime of large capacitance, when it may overestimate the target charge. The simulation results motivate further modelling of a thermal potential that accounts for slower electron population that escape with protons and light ions.

2.5.2 ChoCoLaT target charging model

In Ref. [140], Poyé *et al.* present a dynamic model of target charging that attempts to account for hot electron collisional dynamics and target thermal and electrostatic potentials in high intensity short pulse interactions ($I > 10^{17}$ Wcm^{-2}). This is useful firstly as a way to identify important physical mechanisms involved in the charging process. It is also useful as a computational tool that is much less resource intensive than LSP (or equivalent) particle-in-cell simulations. It is therefore possible

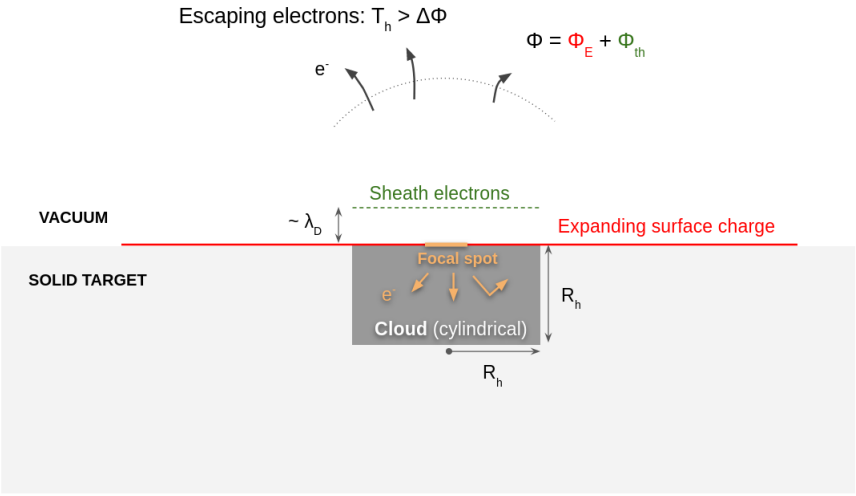

Figure 2.12: Diagram of physics in ChoCoLaT.f90 model of target charging.

to complete a systematic investigation of how target charge varies with laser and target parameters.

The model first published in [58] and then developed in [142] and [140] applies to thick targets - that is, targets where the electron mean free path is much smaller than the target thickness. The major aspects of this thick target model will be described here. In Ref. [143], Poyé *et al.* extend the model to thin targets, where electrons are able to escape via the front and rear surfaces.

A schematic representation of the charging model can be seen in Fig. 2.12. An ultra-intense laser produces a population of hot electrons that expands diffusively into the target over time as a cylindrical cloud[8]. The cloud depth and radius grow according to the average hot electron velocity in the target. As electrons start to undergo collisions in the cold material, they lose energy and change direction, causing the cloud to cool and its expansion to slow. Electrons are able to escape the cloud if they undergo sufficient collisions for them to travel backwards out of the surface and have an energy higher than the target electric potential barrier $\Delta\Phi$. The target potential can be decomposed into a thermal potential Φ_{th} - which stems from charge separation on the surface - and an electrostatic potential Φ_E - which is related to the number of electrons that have escaped the cloud and left it positively charged. The electrostatic potential is calculated based on a disk of positive charge that expands outwards from the cloud at the speed of light. The charge is equal to the number of electrons that have left the cloud and is uniformly distributed so overall it will grow and then decay as the increase in cloud charge is compensated by expansion of the surface charge distribution. The thermal potential is calculated

[8]Cylindrical symmetry is chosen to make certain integrals more tractable. In reality, the electrons would expand quasi-spherically [96].

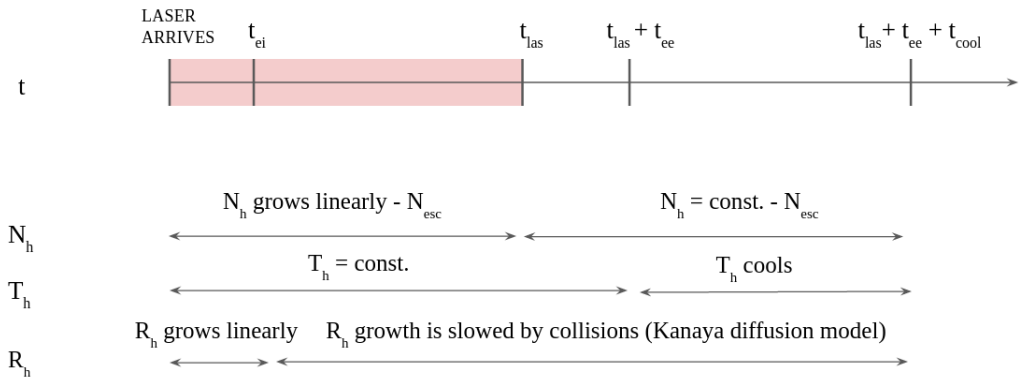

Figure 2.13: Evolution of hot electron cloud parameters in the ChoCoLaT model of target charging. N_h is the number of hot electrons in the cloud, T_h is the cloud temperature, N_{esc} is the number of electrons that have escaped the cloud and R_h is the cloud radius. The cloud evolves on several different timescales defined by the electron-ion collision time t_{ei}, the hot-cold electron collision time t_{ee}, the laser pulse duration t_{las} and the hot electron cooling time t_{cool}.

from the charge density offset at the surface as captured by the Poisson equation in 1D assuming cold ions. Collisional cooling of the hot electron cloud tends to reduce T_h and therefore reduce Φ_{th} over time. A Fortran code called ChoCoLaT.f90 is used to calculate how the cloud expansion, electron losses and target potential interact to produce an ejection current.

The hot electron cloud is defined by three variables: the number of hot electrons in the cloud N_h, the cloud temperature T_h and the cloud radius R_h. Fig. 2.13 shows how these variables evolve over time. While the laser is on, the rate of hot electron production is constant and the hot electron temperature is fixed. Then when the laser is turned off, the cloud will begin to cool and no new hot electrons are produced. The cloud expands freely at the average hot electron velocity until one electron-ion collision time t_{ei} has elapsed and diffusion begins. Once the laser pulse has ended and one hot-cold electron collision time t_{ee} has elapsed, the cloud will start to collisionally cool. The characteristic timescales t_{ee} and t_{ei} are calculated using the spherical diffusion model of Kanaya and Okayama [96]. The cooling time t_{cool} depends on t_{ee} and is defined as the time for an electron with temperature T_0 to reduce to $0.01T_0$. Throughout the laser drive and collisional cooling stages, a fraction of the hot electron distribution will scatter backwards out of the target. A small proportion of these backscattered electrons will have enough energy to overcome the target potential barrier $\Delta\Phi$ and escape the target completely. The accumulated target charge depends on the escaping electron current I_h via $Q(t) = \int_0^t I_h dt$. The ejection current will also cool the cloud. As the hot electrons cool, fewer electrons will be able to overcome the target potential and escape until target charging ceases at time $t_{las} + t_{ee} + t_{cool}$.

Evolution of the hot electron cloud

Here I will outline how the target charge is calculated in the ChoCoLaT model to help motivate how the major charge ejection regimes arise. The dynamic evolution of the target charge is captured using differential equations with growth and decay terms that represent sources and sinks of hot electrons [9].

The total number of hot electrons created during the laser drive is:

$$N_{tot} = \frac{\eta_h E_{las}}{\langle \epsilon_{h,0} \rangle} \tag{2.55}$$

where η_h is the conversion efficiency from laser energy to hot electrons, E_{las} is the laser energy and $\langle \epsilon_{h,0} \rangle$ is the initial average energy of the hot electrons. By definition:

$$\langle \epsilon_{h,0} \rangle = \int_0^\infty \epsilon f_h(T_{h,0}) d\epsilon \tag{2.56}$$

where $f_h(T_{h,0})$ is the hot electron Maxwell-Jüttner distribution function evaluated for the initial hot electron temperature $T_{h,0}$. The initial hot electron temperature depends on the reduced vector potential a_0. For $0.03 < a_0 < 1$ the temperature is calculated from Beg's empirical scaling (Eq. (2.16)) and for $a_0 > 1$ the ponderomotive scaling is used (see Eq. (2.18)). The hot electron production rate during the laser drive is assumed to be linear:

$$\partial_t N_h = \frac{N_{tot}}{t_{las}} \quad 0 < t \leq t_{las}$$

An individual hot electron is considered 'hot' until it has collided with sufficient cold electrons to lose most of its energy. On average, a hot electron will propagate freely through the bulk material until it reaches its mean free path for hot-cold electron collisions at time t_{ee}. It will then cool in further collisions over a period t_{cool}. If this cooling process takes place on a timescale $t_{ee} + t_{cool}$, the hot electron population will be reduced at a rate

$$\partial_t N_h = -\frac{N_h}{t_{ee} + t_{cool}} \quad 0 < t < t_{las} + t_{ee} + t_{cool}$$

Hot electrons also escape the cloud via the ejection current I_h. The rate at which electrons escape the target surface is given by:

$$\partial_t N_h = -\frac{I_h}{e} \quad t > 0$$

Combining these sources and sinks of hot electrons, we can write differential equations that describe the number of hot electrons in the cloud:

$$\partial_t N_h = \frac{N_h}{t_{las}} - \frac{N_h}{t_{ee} + t_{cool}} - \frac{I_h}{e} \qquad t \leq t_{las} \tag{2.57}$$

$$\partial_t N_h = -\frac{N_h}{t_{ee} + t_{cool}} - \frac{I_h}{e} \qquad t_{las} < t \leq t_{las} + t_{ee} + t_{cool} \tag{2.58}$$

These equations describe the evolution of the hot electron population, though they are dependent on the temperature T_h and the ejection current, I_h.

After the laser pulse has ended, the global hot electron temperature is no longer maintained and it will decrease through collisions:

$$\partial_t T_h = -\frac{T_h}{t_{ee}} \quad t > t_{las} + t_{ee}$$

The temperature is also reduced as electrons escape into vacuum and remove energy from the distribution. Let the temperature loss term corresponding to the ejection current I_h be denoted by κ_h (see Ref. [140] for details). Then the temperature is governed by

$$\partial_t T_h = -\frac{T_h}{t_{ee}} - \kappa_h \quad t > t_{las}$$

Combining terms for the cooling of the hot electron cloud via collisions and vacuum losses gives the temperature evolution with time:

$$\begin{aligned}
\partial_t T_h &= 0 \quad t \leq t_{las} \\
\partial_t T_h &= -\kappa_h \quad t_{las} < t \leq t_{las} + t_{ee} \\
\partial_t T_h &= -\kappa_h - \frac{T_h}{t_{ee}} \quad t > t_{las} + t_{ee}
\end{aligned}$$

Note that there is no expansional cooling term because there are no collisions between hot electrons in the cloud. Unlike a fluid, the electron cloud expands ballistically with electrons losing energy to the electric potential. The cloud radius R_h grows as the electron thermal speed $\langle v_h \rangle$ until diffusion begins at time t_{ei}:

$$\begin{aligned}
\partial_t R_h &= \langle v_h \rangle \quad t < t_{ei} \\
\partial_t R_h &= -\frac{\langle v_h \rangle^2 t_{ei}}{2R_h} \quad t \geq t_{ei}
\end{aligned}$$

However, the assumption of a fixed temperature while the laser can lead to unphysical expansion velocities. For $t_{ee} \ll t_{las}$, electrons at the edge of the cloud will be much less energetic than those in the hot spot. Radial expansion should therefore be

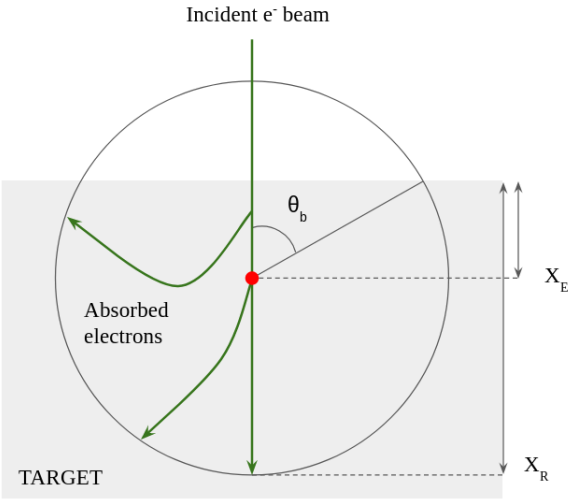

Figure 2.14: Spherical diffusion model of electron beam penetration into a material. The maximum electron range is X_R and the point of maximum energy dissipation is X_E. The image is a simplified version of Fig. 1 from Ref. [96].

slow - not fixed at the thermal velocity calculated from $f_h(\epsilon, T_h)$. As a result, $\langle v_h \rangle$ and t_{ee} are calculated using a distribution function $f(\epsilon, \Theta_h)$, where Θ_h is an ad hoc 'local temperature' that reflects the mean energy of the first electrons generated by the laser. The local temperature decays only through hot-cold electron collisions:

$$\partial_t \Theta_h = 0 \quad t < t_{ee}$$
$$\partial_t \Theta_h = -\frac{\Theta_h}{t_{ee}} \quad t \geq t_{ee}$$

The Ejection Current

The fraction of hot electrons that backscatter out of a thick target can be estimated using the Kanaya and Okayama spherical diffusion model [96]. The model estimates the maximum range and energy deposition of a monoenergetic beam of electrons by calculating the collisional cross section for one, two or three collisions. Fig. 2.14 shows a monoenergetic beam of hot electrons incident on a solid target. No electron can travel further into the target than the electron range X_R. A sphere centred on the maximum energy dissipation depth X_E with radius $X_R - X_E$ will intersect the target surface at an angle θ_b to the target normal. The angle θ_b defines a cone that subtends a solid angle $\Omega = 2\pi(1 - \cos\theta_b)$. Dividing by the solid angle of a sphere gives $\Omega_b = (1 - \cos\theta_b)/2$, which defines the fraction of hot electrons that can backscatter out of the target. Poyé *et al.* [140] extend this result to a polychromatic electron beam by averaging over the hot electron distribution function.

Hot electrons must escape the cloud through the ejection surface πR_h^2. The ejection current is defined as the flux of charge that passes through the ejection surface with energy greater than $\Delta\Phi$. If n_Φ is the number density of hot electrons with energy greater than the potential barrier $\Delta\Phi$ and Ω_b is the solid angle fraction of electrons that can backscatter out of the target, then $\Omega_b n_\Phi$ is the number density of hot electrons that can escape the target (i.e. they have backscattered and have sufficient energy to escape). The ejection current can therefore be expressed as:

$$I_h = e\Omega_b n_\Phi \pi R_h^2 \langle v_h \rangle$$

where $\langle v_h \rangle$ is the average velocity of the electrons that escape the potential barrier. Expanding $\langle v_h \rangle$ in terms of the hot electron distribution function and n_Φ in terms of N_h gives:

$$I_h = e\Omega_b \left(\frac{\eta_\Phi N_h}{V_h} \right) \pi R_h^2 \int_{\Delta\Phi}^{\infty} f_h(\epsilon) v_h d\epsilon$$

where $V_h = \pi R_h^2 (R_h - r_{las})$ is the cloud volume and $\eta_\Phi = \int_{\Delta\Phi}^{\infty} f_h(\epsilon) d\epsilon$ is the fraction of hot electrons with energy greater than $\Delta\Phi$. The ejection current impacts the electron distribution function by reducing the number of hot electrons N_h in the cloud and reducing T_h.

Ejection Regimes

Recalling Fig. 1.11 from the Introduction, ChoCoLaT parameter scans of laser energy and pulse duration reveal two target charging regimes relevant to short pulse laser interactions that depend on the relative duration of the laser pulse and hot electron cooling process [140]. The analysis of these asymptotic regimes is simpler than running the full ChoCoLaT model, where all of the variables that govern the hot electron cloud are dynamically evolving.

If the laser pulse duration is much longer than the electron cooling time ($t_{las} \gg t_{ee} + t_{cool}$), a steady state regime is reached during the laser drive. Generally this regime applies to energetic lasers with longer pulse durations because the cloud temperature, density and ejection current is sustained almost entirely by the laser. The hot electron temperature is fixed at its initial value and the ejection current remains low because the electron temperature is relatively low. Neglecting the ejection current in Eq. (2.57) and setting $\partial_t N_h = 0$ gives an estimate of $N_h \approx N_{tot}(t_{ee}+t_{cool})/t_{las}$ for the number of hot electrons. The thermal potential is roughly constant because the temperature is constant and n_h is maintained as more electrons are generated by the laser. The electrostatic potential also reaches an equilibrium as charge accumulation is compensated by charge expansion over the target surface (only valid

for large targets, as discussed in the next section). Since the potential barrier is constant, the ejection current will also be constant.

A complete ejection regime occurs when the average hot electron temperature is higher than the maximum potential barrier. This occurs for very intense laser interactions at relatively low energy, where $t_{las} \ll t_{ee} + t_{cool}$. Since the laser duration is short (e.g. < 0.1 ps) and the energy is low, the hot electron temperature is high but Eq. (2.55) implies that few hot electrons are produced. The thermal potential will remain low despite a high hot electron temperature because the electron cloud is not very dense. Similarly, the growth of the electrostatic potential is hampered by a small value of N_{tot}. Since the potential barrier is smaller than the hot electron temperature throughout the interaction, the target charge can be approximated as $Q \approx eN_{tot}$. The complete ejection regime therefore corresponds to an efficient but relatively low level of target charging.

Small Targets

The ChoCoLaT model provides an explanation for why small, mm-sized targets have been observed to accumulate less charge than cm-scale targets. Small targets tend to concentrate their charge and electrostatic potential over a small area, prematurely arresting the charging process. In ChoCoLaT, the electrostatic potential Φ_E is calculated based on a uniformly-charged disk that spreads out from the hot electron cloud at the speed of light. All of the hot electrons that are energetic enough to escape the target will be lost during the charging time $t_c = t_{las} + t_{ee} + t_{cool}$, so if a disk-like target has radius smaller than $R_{small} \sim ct_c$ then the surface charge will be restricted to the target radius during the charging process and Φ_E will grow unchecked. Since the charging time depends on laser and target parameters, the small target limit will vary from experiment to experiment. For a typical charging time of ~ 10 ps, the small target limit corresponds to a disk of radius 3 mm.

Laser scalings

Target charge scales linearly with laser energy for $E_{las} = 0.02 - 0.08$ J at $t_{las} = 30$ fs and $t_{las} = 2000$ fs [142]. At low energy ($E_{las} < 100$ mJ), target charge is almost independent of laser pulse duration - only increasing by a few nC over three orders of magnitude from $t_{las} = 10^{-2}$ ps up to $t_{las} = 10$ ps. Poyé *et al.* suggest that this weak intensity scaling is caused by Eq. (2.55): intense short-pulse interactions produce relatively few hot electrons of which a large fraction will escape, whereas long-pulse interactions produce a large number of generally cooler electrons of which a small proportion will escape [142].

Summary of ChoCoLaT

ChoCoLaT is a powerful and relatively simple model of target charging that depends on characteristics of the hot electron population produced by the laser and the target potential. The electron ejection criterion is similar to those of Benjamin *et al.* [19], Link *et al.* [112] and Sinenian *et al.* [160], though ChoCoLaT features a dynamic treatment of electron cooling and contains separate models for the electrostatic and thermal potentials. Target size and thickness are important at certain laser intensities. Charging estimates are accurate to within a factor of $2-3$ when compared with data from the Eclipse laser and predicts the correct scaling laws. Extensions of the ChoCoLaT model can be used to account for capacitor coil interactions in the long pulse regime [140] and EMP measurements [124].

2.6 Capacitor Coil Modelling

Now that laser-plasma expansion and target charging have been discussed, these ideas can be adapted to magnetic field generation in capacitor coil targets. These experiments generally involve ns-duration lasers irradiating targets in a two-plate hohlraum-like geometry. On ns timescales, the response of the entire target system must be considered: from the electron ejection current, to plasma dynamics and return currents in the coil. Though numerous different models have been developed to date [44, 46, 82], this section describes two examples that have been shown to match a range of experimental measurements relatively well.

2.6.1 Fiksel capacitor coil model

In Ref. [71], Fiksel *et al.* introduce a numerical model that can be used to estimate the current in a capacitor coil target. The model consists of two coupled first-order ordinary differential equations that describe the voltage between the capacitor plates. Ion and electron currents are considered separately. The hot electron current is maximal at early times and then decays as more charge on the anode reduces the potential and the ion current increases.

As a crude first estimate, Fiksel *et al.* use a 1D model of plasma expansion. Recalling Eq. (2.52) from Sec. 2.3.2, the space charge electric field (i.e. the electric field that develops due to the different ion and electron inertias) is given by the ratio of the electron energy to the ion characteristic scale length:

$$E = \frac{T_h}{c_s t}$$

where $c_s = (ZT_h/m_i)^{1/2} = (ZT_h/Am_p)^{1/2}$ is the ion acoustic velocity with one

degree of freedom, Z is the ion charge and A is the atomic mass. From here, the 1D potential between two conducting plates separated by a distance d is given by:

$$V = \int_0^d E dz = \frac{T_h d}{c_s t}$$

Equating to the external circuit equation, a basic estimate of the RL-circuit dynamics can be found:

$$\frac{T_h d}{c_s t} = L\frac{dI_c}{dt} + RI_c \tag{2.59}$$

where I_c is the coil current and L and R are respectively the coil inductance and resistance. Eq. (2.59) suggests that the hot electron temperature is going to play a crucial role in the field generation of a capacitor coil because the inter-plate potential is proportional to T_h. On the other hand, Eq. (2.59) does not account for the plasma ablation rate. This means that a small number of energetic electrons can charge the capacitor and drive a large current through the coil, violating charge continuity in the capacitor and external circuit. Eq. (2.59) also gives an unlimited current at early times and doesn't consider resistive heating of the external circuit, so it is unlikely to accurately capture the current peak or decay. In the following sections, I will briefly summarize how Fiksel *et al.* [71] extend their model to account for: (i) the rate of charged particle generation (ii) charging of the anode, which will evolve to repel incoming electrons (iii) non-Maxwellian electron distribution functions at laser intensities $I_L\lambda_\mu^2 > 10^{14}$ Wcm$^{-2}\mu$m^2.

Ablation Rate

Fiksel *et al.* [71] use a maximum theoretical ablation rate to define initial conditions for the laser ablation current. Considering a laser spot with area A_{spot} and electron density n_e, the Atzeni ablation model [8] says the maximum electron current is $I_0 = \dot{n}_e e A_{\text{spot}} \approx n_{cr} c_a e A_{\text{spot}}$ where n_{cr} is the critical density, $c_a \approx c_s$ is the average ablation velocity and e is the proton charge. For OMEGA-type laser parameters $\lambda = 0.35$ μm, $A_{\text{spot}} = 0.01$ mm^2 and typical plasma parameters $T_h = 10$ keV and $Z/A = 0.5$, the maximum current is $I_0 = 11$ MA. Note that this value represents the maximum current that can be produced by the laser, independent of plasma dynamics or the Alfvén current limit.

Disconnected plates

Ignoring the wire loop, a capacitor coil target consists of two metal plates held in parallel like a capacitor. In this simplified situation, the charging process is governed entirely by the ion and electron currents between the plates. Taking the derivative

of the capacitor charge equation:

$$\frac{dQ}{dt} = C\frac{dV}{dt} = I_i - I_e \tag{2.60}$$

for I_i and I_e the ion and electron currents. The electron current is assumed to start maximally and then decrease as negative charge accumulates on the anode:

$$I_e = I_0 e^{eV/T_h} \tag{2.61}$$

The exponential term accounts for the repulsion of a Maxwellian electron population with a temperature T_h by the anode voltage V. The ion current follows from the 1D plasma expansion model covered in Sec. 2.3.2:

$$n_i(x,t) = n_0 e^{-x/c_s t}$$
$$I_i = e n_i A_{spot} c_s = I_0 e^{-x/c_s t}$$

Evaluating at a distance $x = d$ (i.e. the full plate separation), one finds that

$$I_i = I_0 e^{-d/c_s t}$$

And Eq. (2.60) becomes:

$$C\frac{dV}{dt} = I_0 \left[e^{-d/c_s t} - e^{eV/T_h}\right] \tag{2.62}$$

Fig. 2.15 shows the behaviour of Eq. (2.62) for two plates separated by 1 mm with capacitance $C = 0.1$ pF and plasma parameters $T_h = 10$ keV, $c_s \sim 7 \times 10^5$ ms^{-1} and $I_0 \sim 10$ MA. A small target capacitance means the gap potential rises quickly to a maximum defined by the anode charge and then falls on the ion transit timescale $\tau_i = d/c_s$. The maximum potential that can develop in the capacitor is of order $\Phi = eV = 10T_h$.

Connected plates

With the addition of a wire loop, Eq. (2.62) becomes:

$$C\frac{dV}{dt} = I_0 \left[e^{-d/c_s t} - e^{eV/T_h}\right] + I_c \tag{2.63}$$

where I_c is the current in the external circuit. This is described by the external circuit equation as normal:

$$-V = L\frac{dI_c}{dt} + RI_c \tag{2.64}$$

By solving equations (2.64) and (2.63), the full capacitor coil system can be

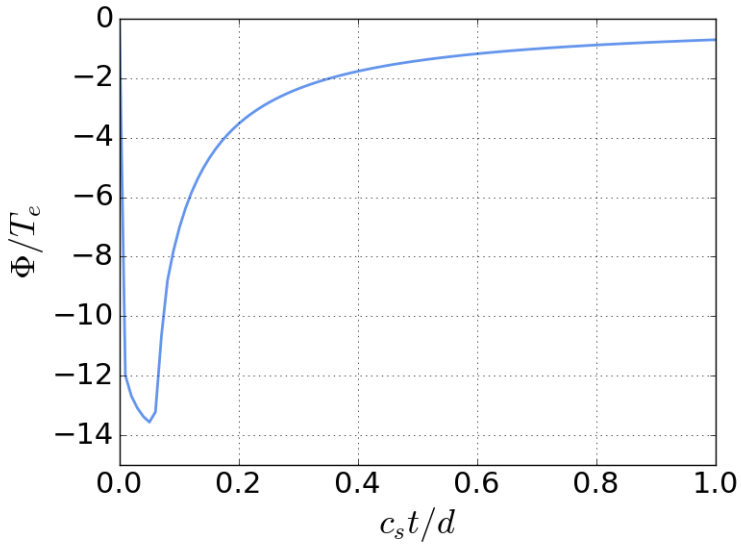

Figure 2.15: Evolution of the electric potential $\Phi = eV$ for two disconnected plates, calculated using Eq. (2.62). The time axis is normalised to the ion transit timescale $\tau_i = d/c_s$ and the capacitor potential is normalised to the hot electron temperature T_h.

modelled.

Non-Maxwellian electron distributions

Electrons produced by collisional and resonant absorption processes can be approximated by a bi-Maxwellian distribution with a high energy population of electrons ($T_e = T_h$) superimposed on top of a cooler background ($T_e = T_c$). Details of how Eq. (2.63) can be adapted to non-Maxwellian electron distributions can be found in Ref. [71].

In Fig. 2.16, I compare current profiles for a capacitor coil with a Maxwellian and bi-Maxwellian hot electron distribution with experimental parameters taken from Gao *et al.* [79]. The dashed line represents the current profile for 10% hot electrons with temperature $T_h = 11$ keV and a cold electron population with $T_c = 1$ keV. We see that the peak current only drops by a factor $\sim 2/3$ despite a 90% reduction in hot electrons at $T_h = 10.8$ keV. This suggests that the coil current is dominated by the much less numerous hot electron population, so the current can be well-approximated using a single hot Maxwellian.

Long pulse interactions

The Fiksel model consists of two coupled first order ODEs with separate electron and ion current terms and an external circuit equation:

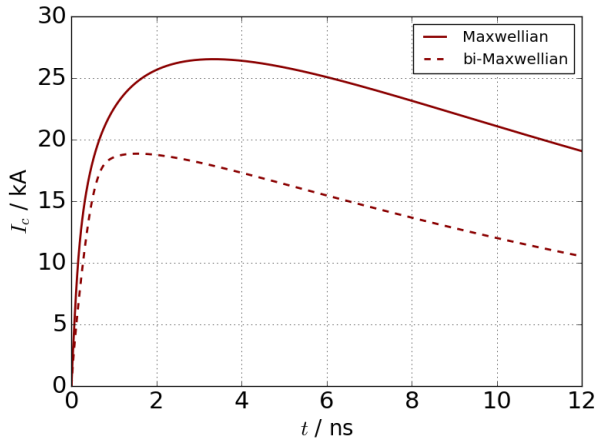

Figure 2.16: Solid line: Maxwellian hot electron population with temperature $T_h = 10.8$ keV. Dashed line: bi-Maxwellian hot electron population. 10% hot electrons with temperature $T_h = 10.8$ keV and a cold electron population with $T_c = 1$ keV. The experimental parameters match those from Gao *et al.* [79].

$$C\frac{dV}{dt} = I_0 e^{-d/c_s t} - I_0 e^{eV/k_B T_e} + I_c$$

$$-V = L\frac{dI_c}{dt} + RI_c$$

Other authors have used the same approach by coupling an ODE with a current source term to an external circuit equation[9]. In a simplified manner, the Fiksel model takes into account the laser ablation current, charging of the capacitor plates and non-Maxwellian features of the electron distribution function. It does not account for current dynamics in the external circuit brought about by resistive heating, nor does it account for space charge effects or the cooling of the plasma after the laser is turned off. Given these limitations, it is important to ascertain how accurate the Fiksel model is and to what extent we can rely on it to tell us about the physics of capacitor coils.

To test the accuracy of the Fiksel model, the predicted capacitor coil current can be compared with currents measured in different experiments. First, consider an experiment conducted on the OMEGA EP laser facility by Gao *et al.* [79]. A Helmholtz (i.e. two loop) capacitor coil target was driven with a combined laser energy of $E_L = 2.5$ kJ focused to a ~ 100 μm-diameter spot and an intensity $I_L = 3 \times 10^{16}$ Wcm^{-2}. The laser wavelength is 0.35 μm. The capacitor coil plates are separated by $d = 0.6$ mm, with approximate capacitance $C \sim 0.03$ pF; the plates were connected by a wire loop of radius $r = 0.3$ mm, inductance $L = 1.2$ nH and

[9]In Ref. [82], Goyon *et al.* use a different current source term, whose solution gave a faster initial current rise than measured using proton radiography (attributed to the very small capacitance of the target) and oscillating currents.

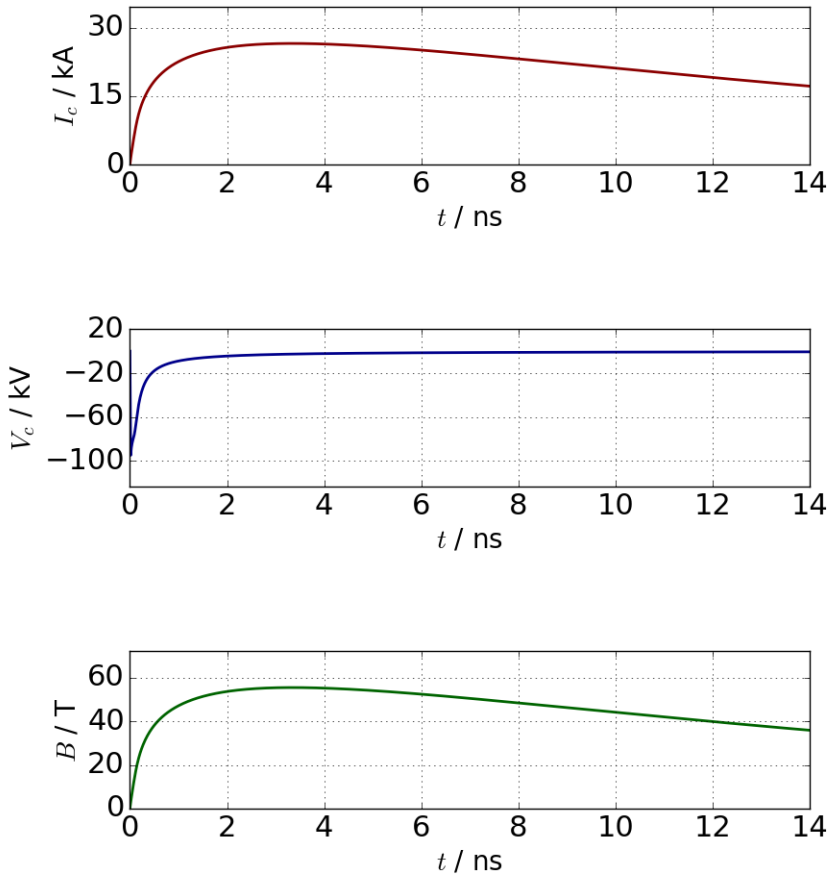

Figure 2.17: Predicted current, voltage and magnetic field profiles using the Fiksel model for a capacitor coil with experimental parameters taken from Gao *et al.* [79] and Chien *et al.* [39].

The hot electron population is modelled as Maxwellian with a temperature $T_e = 10.8$ keV.

resistance $R = 0.1\ \Omega$. Fig. 2.17 shows the predicted current, voltage and magnetic field profiles calculated using the Fiksel model for these parameters. An ionisation level of $Z/A = 0.5$ is assumed. A current of $I = 22$ kA at $t = 3.1$ ns after laser drive was measured using proton radiography, which agrees well with the Fiksel prediction of $I \sim$ 20-25 kA at the same time [71]. In Ref. [39], these measurements were repeated with an identical experimental set-up but without a plastic spacer between the capacitor coil plates. Without the spacer, there is no electrical shorting of the target and larger voltages can be supported. We therefore expect the current measurements reported in Ref. [39] to provide a more accurate comparison with the Fiksel model. The measured current increases significantly without the plastic spacer to $I = 57 \pm 4$ kA ($B \sim 110$ T at coil centre), so agreement is still within a factor ~ 2.

Goyon *et al.* report additional capacitor coil measurements at the OMEGA EP

facility using metallic ribbon-shaped coils [82]. Their target was formed from a 4 mm by 1.1 mm rectangular gold foil, 12.5 μm thick, that was bent into a U-shape. The two parallel plates were separated by 0.5 mm and two 0.4-mm- diameter laser entrance holes were cut out of the front side to allow the drive lasers access to the rear plate. Based on this information, the target has an inductance $L = 0.4$ nH, capacitance $C = 0.06$ pF and skin-depth resistance $R = 0.02$ mΩ. Two blue beams with wavelength $\lambda_L = 0.35$ μm were focused into a 170 μm-diameter spot at a combined intensity of $I_L = 4.5 \times 10^{15}$ Wcm^{-2}. A 10 μm-thick layer of CH plastic was deposited on the anode to enhance the acceleration of hot electrons via parametric instabilities. I will take $T_h = 45$ keV based on their measurements. Assuming $Z/A = 0.5$, the Fiksel model reaches 150 kA by $t = 0.75$ ns, though this continues to rise to almost 250 kA at $t = 10$ ns. This is due to the large focal spot diameter which is important for a large ablation current. Using proton radiography, Goyon *et al.* measured a linear current rise up to a maximum of 180 kA with corresponding on-axis magnetic fields of $B = 210$ T at the end of the 0.75 ns laser pulse. Agreement with the Fiksel model is good (17% discrepancy) at the end of the laser drive.

The Fiksel model can also help assess claims of kilo-tesla magnetic fields reported at several facilities [153, 105, 77]. In Ref. [153], Santos *et al.* report magnetic fields up to $B = 800$ T generated in the centre of a capacitor coil loop at the LULI 2000 facility. The laser energy incident on the capacitor coil anode had energy $E = 500$ J, a wavelength of $\lambda = 1.053$ μm, $t = 1$ ns square pulse duration and a focal intensity of 10^{17} Wcm^{-2}. The target was composed of two Cu plates separated by 0.9 mm and connected by a small loop of wire. The wire loop had a radius of 0.25 mm, a room temperature resistance of 0.03 Ω and an inductance of ~ 2 nH. Proton radiographs of the coil loop were compared with simulations of protons passing through magnetic fields, suggesting that fields on the order of $B = 100$ T were achieved. B-dot probe measurements, on the other hand, suggested peak fields of ~ 800 T for Cu targets. The proposed explanation was that hot electrons emanating from the laser focal spot could become trapped in the coil fields and modify the radiography results. With electron densities of $10 - 100$ nC distributed in a sphere around the wire loop, kilo-tesla fields could be inferred from the radiography results. According to the Fiksel model, a hot electron temperature of ~ 40 keV is required to produce a 100 T field for these experimental parameters. This is very close to the experimentally measured value of 40 ± 5 keV. However an unrealistic hot electron temperature of > 500 keV would be required to reach 800 T.

Short pulse interactions

The Fiksel model, as represented by equations (2.63) and (2.64), accounts for capacitor coil behaviour on four timescales: the laser pulse duration, the electron current,

the ion current and the time evolution of the external circuit. It is therefore quite versatile and can even be applied to short pulse laser interactions. This is important because short pulse lasers with low-to-medium laser energy are becoming more common [49] and the plasma hot electron temperature depends mainly on the laser intensity via an $I_L\lambda_\mu^2$ scaling law. In Ref. [94], Ivanov *et al.* irradiate a capacitor coil at two distinct intensities by changing the laser pulse duration from 2.8 ns to 70 ps. The focal spot diameter and laser energy were fixed at 6 μm and 25 J respectively. They found that the peak magnetic field increased by a factor of two for an intensity increase of ~ 30 (0.8×10^{16} Wcm^{-2} to 2.5×10^{17} Wcm^{-2}). They found that this peak with laser intensity scaling was accounted for very well by the Fiksel model with ion and electron current terms, but that the decay time of the current was not. The ion current term caused the current to decay on $\sim$ ns timescales when the Faraday measurements showed the field decaying slowly on $\sim \mu$s timescale. When the ion current term is removed, the peak field is only $\sim 20\%$ higher and it does not exhibit the fast relaxation time (see Fig. 2.18). As Santos *et al.* [153] have observed, the ns-duration relaxation of the coil current for kJ-class lasers is caused by resistive heating of the wire. The coil reaches high ($\sim 1\Omega$) resistance near the temperature of evaporation for the metal. Ivanov *et al.* used the skin depth resistance of the coil (based on a magnetic energy of 0.3 J heating the coil by about 20 K) to calculate the relaxation time of the magnetic field through the coil and plate plasma. The calculated value of $L/R = 0.33$ μs agrees with experiment. Thus although the Fiksel model accounts well for the maximum potential and current in the capacitor coil in different intensity regimes, the relaxation of the field is caused by the external circuit - not the arrival of the ion current. This supports the idea that a hot electron current is mainly responsible for the coil current. The rising edge of the Faraday rotation signal was measured to be 0.3-0.4 ns for the 70 ps pulse and a 1-2 ns rising edge for the 2.8 ns pulse. This is not captured by Fiksel's model, which predicts a similar rise time of $\sim$ 0.4-0.5 ns at both intensities. In an experiment with a 30 fs laser pulse at comparable energy, Wang *et al.* [173] measure a similar rise time of the magnetic field of 60 ps using proton radiography.

Summary of the Fiksel model

The Fiksel model agrees reasonably well with magnetic field measurements in capacitor coil targets, but more work is needed to correctly capture the current dynamics and provide an accurate physical picture of the system. Salient predictions from the Fiksel model are that the coil current can be maximised by increasing the hot electron temperature (equivalently the laser $I_L\lambda_\mu^2$) or the laser spot size, because the laser ablation current increases. For a fixed laser spot size, longer laser wavelengths produce stronger currents despite a lower critical density. Experimental measure-

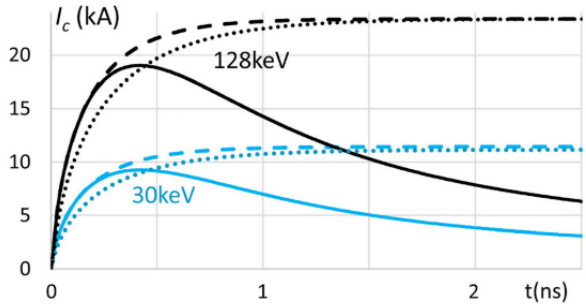

Figure 2.18: Current profiles for two different intensity regimes calculated using the Fiksel model. At higher laser intensity, the hot electron temperature is taken to be 128 keV and at lower intensity the temperature is 30 keV. The dashed lines represent solutions without the ion current term in Eq. 2.63. Dotted lines show solutions with the inductance increased by a factor 1.5. Figure reproduced from Ivanov *et al.* [94] with permission.

ments of the current profile over $\sim \mu$s suggest the ion current term can be ignored (this is expected because the ions propagate slowly and quasi-neutrally) and that the model should be replaced by an RL-circuit decay after the laser pulse has ended [94].

Given qualitative agreement between the Fiksel model and experiment, it is reasonable to ask: to what extent is the model or the measurement at fault? The Fiksel model is sensitive to plasma parameters (e.g. density, temperature) that are known only very approximately and often are not directly measured in experiments with capacitor coil targets. A discrepancy of $\sim$ 20-30% in the estimated current is therefore expected, although this could rise to a factor of 2 or so when the multi-kA measurement uncertainties from proton deflectometry are accounted for (see Chap. 5). Taking these errors into consideration, the Fiksel model suggests that maximum currents of order several tens of kA can be produced on kJ laser systems with a nominal pulse duration of $\sim$ 1ns and that the magnetic field measurements inferred from B-dot probe data in Santos *et al.* [153] have been overestimated. On the other hand, the 1D approximation of the plasma between the plates is fairly crude and may miss important physics processes. In the next section, a more complex model of plasma propagation between the capacitor coil plates is discussed.

2.6.2 Plasma diode model of a capacitor coil

In Ref. [169], Tikhonchuk *et al.* present a model of capacitor coil operation where the plate region is modelled as a plasma diode. Assuming a stationary solution for the diode voltage after the laser-plasma has bridged the plate gap, Tikhonchuk *et al.* show that large currents can be generated in a low density plasma ($n_e < 0.01 n_{cr}$) that fills just a narrow region where the current is transported. This can be contrasted

with a model presented by Goyon *et al.* [82] where the plasma is relatively dense ($n_e \geq 0.01 n_{cr}$) and fills the entire plate region.

A key assumption of the diode model is that the current flowing between the capacitor plates is equal to the current flowing through the external circuit. In other words, the capacitance of the target can be neglected. This assumption can be inferred from estimates of the diode voltage and geometrical capacitance. Given a typical Cu target connected by a wire loop, it is possible to estimate the voltage that can develop across the capacitor plates. A wire loop made from Cu with radius 1 mm and cross-sectional area 50 μm has an inductance of $L \sim 2$ nH and a room temperature resistance of $R \sim 0.02\ \Omega$. Solving for the current in an RL-circuit with constant applied voltage, the decay time $\tau = L/R = 100$ ns is large relative to the laser pulse duration of $t_{las} = 1$ ns, so the current grows almost linearly for $t < t_{las}$ (see Appendix or Daido *et al.* [48] for more details). Maximum currents of order 100 kA have been measured at the end of a ns-duration laser drive, which implies that the diode voltage is approximately $V \approx LI_c/t_{las} = 200$ kV. This value must be corrected to account for Ohmic heating of the wire, however approximately linear growth is reasonable even for a resistance of $R = 1\ \Omega$ and is consistent with B-dot measurements [48]. For millimetre-sized metal plates the inter-plate capacitance is very small - on the order of ~ 0.01 pF. Such a small capacitor could be charged by a tiny current (1 A delivered over 1 ns could charge the plates to 100 kV) - much smaller than the currents reported to traverse the loop (> 1 kA) over the same period. Tikonchuk *et al.* identify two solutions to this problem of unbalanced charges: either the diode capacitance is much higher than its geometry suggests or the plate current and coil current are equal.

A fast, linear current growth suggests that charge is transported by a quasi-stationary voltage through a quasi-neutral plasma [169]. Mora's 1D plasma expansion model [129] is valid on a scale much smaller than the plate gap, of order the focal spot radius r_h[10]. Tikhonchuk *et al.* therefore assume ions are accelerated until they reach the edge of the planar expansion zone at a distance $z \sim r_h$ from the laser spot. Ions at this distance have reached a high velocity $v_i \sim (eV/T_h)c_s \approx 10 - 15c_s = 10 - 15$ mm/ns, so a quasi-neutral plasma will reach the opposite plate after ~ 100 ps. At this point the diode operates in a quasi-stationary regime, with the laser supplying a voltage via a hot electron current until the laser drive stops. By the time the laser pulse has ended, a relatively dense plasma will have developed and shorted the metal plates, so the target is assumed to discharge as an RL-circuit with characteristic time $\tau = L/R$. An alternative

[10] As observed in Section 2.0.4, the 1D plasma expansion model breaks down on scales larger than the focal spot. This is because a rarefaction wave propagating inwards from the plasma edge will reach the centre at time $t \sim R_{spot}/c_s$, whereupon the self-similar planar expansion transitions to a self-similar spherical expansion.

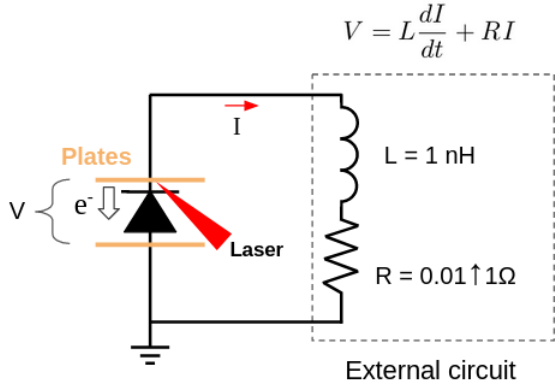

Figure 2.19: Plasma diode model of a capacitor coil. The laser drives a voltage across the plates (diode) which is connected to the coil via a standard RL-circuit equation. Typical values of the coil inductance L and resistance R are provided. Though the coil resistance will evolve as it heats up, R is assumed constant in the model.

approach pursued by Goyon *et al.* [82] and Williams *et al.* [180] supposes that the plate separation used to calculate the target capacitance is replaced with the plasma Debye length assuming the capacitor is filled with plasma. The decay can then be modelled as an RLC circuit provided the plasma is sufficiently dense and the Debye length sufficiently short.

A diagram of the plasma diode model is shown in Fig. 2.19 [169]. The capacitor coil functions as a diode connected to a series RL circuit and it is attached to ground via a target support. In the intensity regime of interest, $I_L\lambda_\mu^2 > 10^{14}$ Wcm$^{-2}\mu$m^2, the diode charging current is supplied by resonantly excited hot electrons. Electron transport between the plates defines the diode current and voltage which can then be used to solve for the current in the loop. Ion transport proceeds quasi-neutrally and is therefore ignored.

Brief summary of model equations

The diode current can be limited by the voltage on the cathode (i.e. space charge) or by magnetic pinching of the plasma column as the current approaches the Alfvén Limit [169]. Tikhonchuk *et al.* calculate the diode IV characteristic by taking the minimum of the space-charge and magnetized plasma limited currents. Knowing the current-voltage characteristic, one can then solve for the current in the external circuit using Eq. (2.64). In this section, we will briefly summarize the governing equations of a laser-diode. A detailed derivation of these equations can be found in Ref. [169].

As the laser heats the anode, hot electrons will move from the anode to the

cathode and a negative voltage will develop. The current that can pass through the diode potential barrier is given by:

$$I_{sc}(t) = I_0 e^{-eV_c(t)/T_h} = I_0 e^{-\phi(t)} \tag{2.65}$$

where I_0 is the maximum laser ablation current and $\phi(t)$ is the normalised diode electric potential. Recalling Atzeni's heuristic ablation model, but replacing the ion velocity with a hot electron velocity, the maximum ablation current is approximately given by [8]:

$$I_0 = eA_{spot} n_{h0} v_h$$

where A_{spot} is the area of the laser focal spot, n_{h0} is the hot electron density in the focal spot and v_h is the average velocity of the escaping hot electrons. Since the hot electron temperature scales strongly with laser intensity, this current can easily exceed 10 MA for lasers with $I_L \lambda_\mu^2 > 10^{14}$ Wcm^{-2}. For typical experimental parameters $T_h = 10$ keV, $\lambda_L = 1$ μm and $d = 100$ μm, we have $n_{cr} = 1.1 \times 10^{27}$ m^{-3}, $v_h = \sqrt{T_h/m_e} \sim 0.14c$ is the 1D root-mean-square electron velocity and the electron current is ~ 58 MA. This compares to ~ 1.4 MA for Fiksel's version of the ablation current with $Z/A = 1$.

Since the laser spot diameter ($\sim$ 0.01-0.1 mm) is usually much smaller than the plate separation ($\sim$ 1 mm) in capacitor coil experiments, transverse motion of the laser-plasma column must be considered. Consider a laser-generated cylinder of plasma, aligned along the z-axis, that bridges the capacitor plates with radius r_p and diode current I_d. As the plasma column moves along a fixed axis between the plates, a radial electron pressure gradient will establish a radial electric field of magnitude $\approx T_h/er_p$. This electric field causes ions to be pulled off-axis and the plasma column expands. However there is a competing effect caused by the Lorentz force that tries to pinch the plasma column. A strong axial current will generate an azimuthal magnetic field $B_\theta \approx \mu_0 I_d / 2\pi r_p$ that pulls electrons towards the axis via the Lorentz force. Plasma ions will be diverted towards the beam axis by the corresponding electric field $v_h B_\theta$, maintaining quasi-neutrality. Diagrams of the two current limits can be found in Fig. 2.20.

Competition between the electron pressure force and Lorentz force determines the maximum current that can propagate in the diode before magnetic pinching breaks up the plasma column. When the two forces are equal, the plasma column maintains a fixed radius. The two forces are equal when $ev_h B_\theta = T_h/r_p$ and the diode current satisfies:

$$I_d(t) = \frac{2\pi}{e\mu_0} \frac{T_h}{v_h}$$

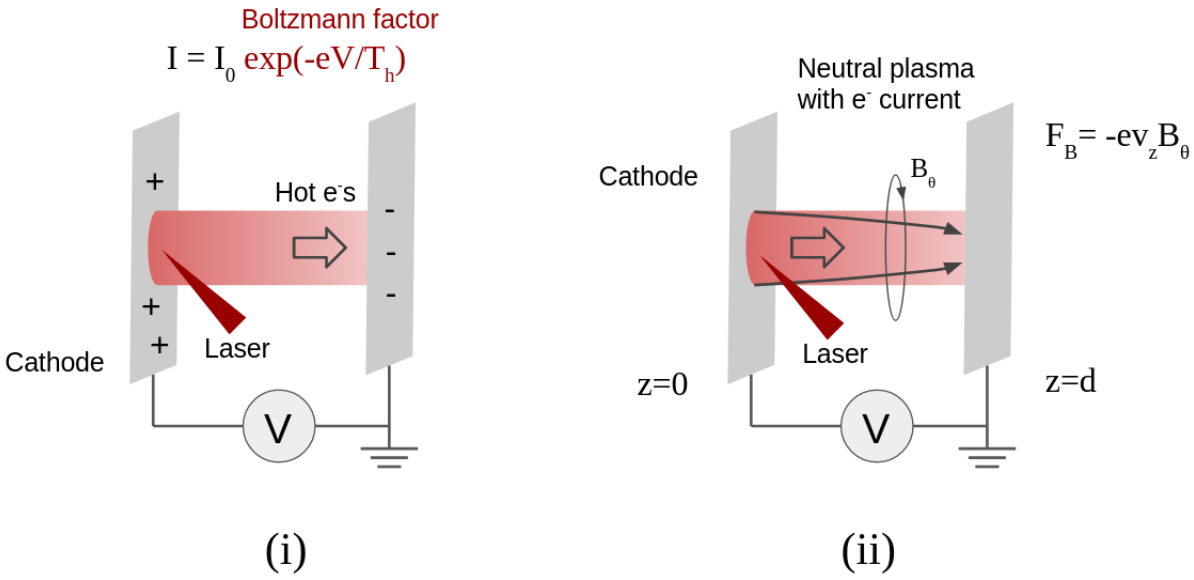

Figure 2.20: (i) Space charge limit of the diode current (ii) Magnetized plasma limit of the diode current. Plasma is oriented along the z-axis. Graphs based on images from a talk by J. Moody at the APS DPP 2018 conference [127].

Observing that $v_h = \sqrt{T_h/m_e}$ in one dimension:

$$I_d(t) = I_A \frac{v_h}{2c} \tag{2.66}$$

Here, Tikhonchuk *et al.* [169] have defined a constant $I_A = 4\pi m_e c/e\mu_0 \sim 17$ kA, equivalent to taking $\gamma v \to c$ in Eq. (2.24). If the diode current is super-Alfvénic (higher than given in Eq. (2.66)) and the plate separation is too large, the plasma column will pinch and break up before it reaches the opposite plate. The maximum diode current therefore corresponds to magnetic pinching that occurs at the plate separation distance d. Assuming a constant ion velocity along the z-axis given by $v_i = c_s eV/T_h$ (see Fig. 2.20) and a small radial velocity calculated from the plasma electric field, one can calculate the diode current I_{pm} that corresponds to a pinch at distance $z = d$:

$$I_{pm}(t) = \frac{1}{2} I_A \frac{v_h}{c} \left[1 + g\frac{eV_c(t)}{T_h}\right]^2 = \frac{1}{2} I_A \frac{v_h}{c} \left[1 + g\phi(t)\right]^2 \tag{2.67}$$

where $\phi(t) = eV(t)/T_h$ is the normalised diode potential. This is the plasma magnetization limited current, where g is a geometric factor that depends on the focal spot size and divergence angle.

By taking $I_c = \min\{I_{sc}, I_{pm}\}$ and solving with the external circuit equation (Eq. (2.64)), one can estimate the current and voltage profiles in a capacitor coil target. The voltage follows immediately from the current profile $I_c(t)$ by referring to the IV characteristic $\phi_c = \min\{\phi_{sc}(I_c), \phi_{pm}(I_c)\}$. These equations remain valid while the

laser is on.

The diode model defined by equations (2.65), (2.67) and (2.64) broadly resembles Fiksel's lumped-element circuit model from Sec. 2.6.1. Key differences are the extra component of the diode IV characteristic which accounts for Alfvénic pinching of the interstitial plasma and the loss of an ion current term. Tikhonchuk *et al.* [169] also stop the current drive entirely after the laser pulse has ended, replacing it with an RL-circuit decay.

RL-circuit decay of the diode current

After the laser pulse has ended, hot electrons stop being heated by the laser and begin to cool down. Since the electron cooling time is short relative to the nanosecond-long laser-plasma interaction ($t_{cool} < 100$ ps), Tikhonchuk *et al.* neglect gradual cooling of the electrons and assume the current immediately starts to decay as an RL circuit.

An RL-circuit decay exhibits an exponential decrease in the current $I \propto e^{-t/\tau}$ with characteristic time $\tau = L/R$ (see Appendix). The coil inductance can be estimated from the loop radius and wire diameter, however the coil impedance changes over time as the conductor is resistively heated. Fast-rising, intense currents will dissipate energy quickly into the conducting medium, causing the material resistivity and skin depth to dynamically evolve [151]. For kJ-level laser facilities like LULI and OMEGA, resistive heating of the coil can produce wire impedances on the order of 1 Ω with time constant $L/R \sim 1$ ns [169, 154]. For the metallic ribbon targets used in Ivanov *et al.* [94], the laser energy and the wire resistance are relatively low, explaining a slower decay time of ~ 0.3 μs. Though dynamic coil heating and current diffusion are outside the scope of the diode model, a representative constant impedance (e.g. 1 Ω for kJ lasers) matches the decay of the current profile reasonably well for several experiments [169].

Diode IV characteristic

At any given time, the diode current is subject to limits imposed by the space charge and plasma magnetic field. The diode IV characteristic is therefore taken to be the minimum of the space charge- and magnetization-limited IV curves. We combine the IV characteristic for the laser-diode in the space charge limit ($I_{sc}(V_c)$, Eq. 2.65) with the IV characteristic in the plasma magnetization limit ($I_{pm}(V_c)$, Eq. 2.67) to produce the full diode IV characteristic, $I_c = \min\{I_{sc}, I_{pm}\}$. This procedure is illustrated graphically in Figure 2.21, where the dashed (orange) line represents $I_{sc}(V_c)$, the dot-dashed (green) line represents $I_{pm}(V_c)$ and the solid (black) line defines the diode IV characteristic. Notice that the space charge and magnetized

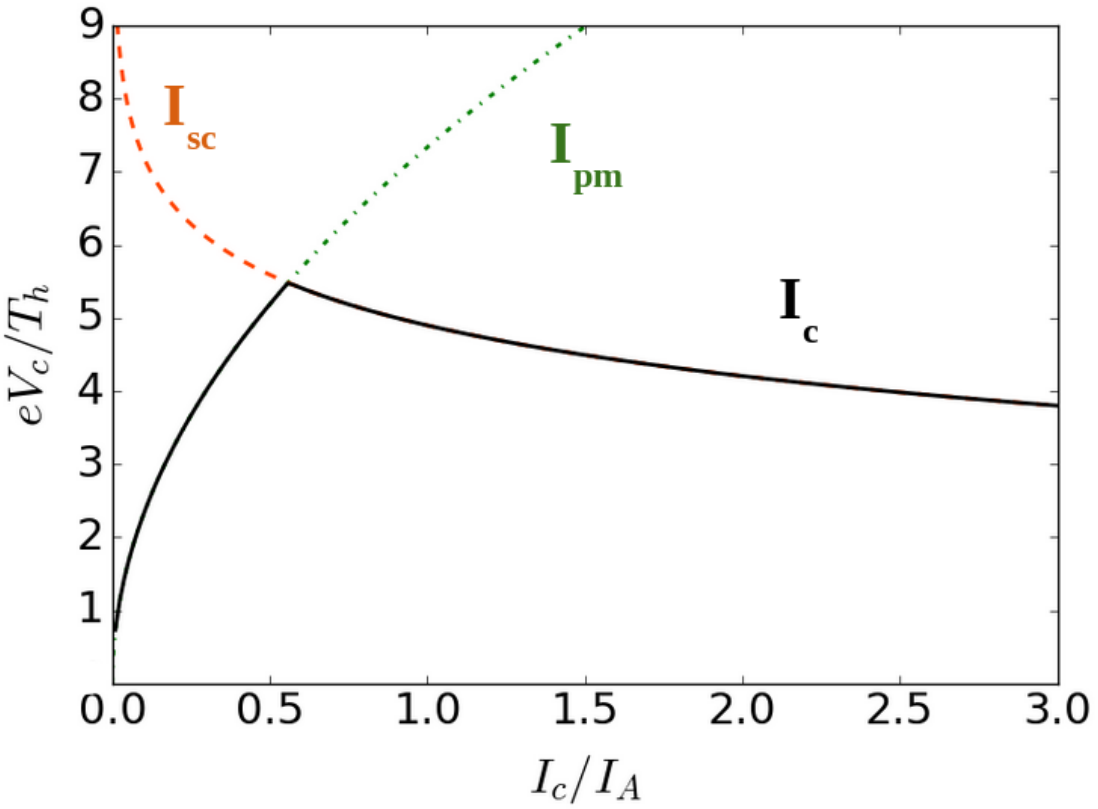

Figure 2.21: Graph of the laser diode IV characteristic for experimental parameters in Courtois *et al.* [44]. The dashed (orange) line represents the space charge limited current, $I_{sc}(V_c)$, the dot-dashed (green) line represents the plasma magnetization limited current, $I_{pm}(V_c)$, and the solid (black) line defines the diode IV characteristic $I_c = \min\{I_{sc}, I_{pm}\}$.

plasma curves cross where the voltage in the diode is at a maximum. The maximum voltage typically occurs for currents $I \sim I_A$ [169]. For currents below the Alfvén Limit, the IV curve is limited by magnetization of the plasma column; super-Alfvénic currents are, by contrast, limited by the cathode voltage.

In Fig. 2.22, I have selected three laser-diode IV characteristics corresponding to a range of different experimental parameters. The experimental parameters used to produce Fig. 2.22 are typical values, representative of the conditions reported in three separate studies of capacitor coil targets. In Ref. [169], the authors demonstrated that there is good qualitative agreement between the diode model and experimental results for Nd-glass and CO_2 lasers, with on-target intensities between 10^{14} and 10^{16} Wcm^{-2}. Here, I verify some of those findings and include additional data taken from Ivanov *et al.* [94] at lower energy. IV curves are calculated with the initial plasma beam divergence and wire impedance fixed at $\alpha_0 = 1$ and $Z_c = 1\ \Omega$ for all three panels. The laser-diode IV characteristics are plotted against the coil Ohm's Law, $V_c = Z_c I_c$, which is represented by a straight green line. The point where the two curves intersect defines the maximum current that can be supported

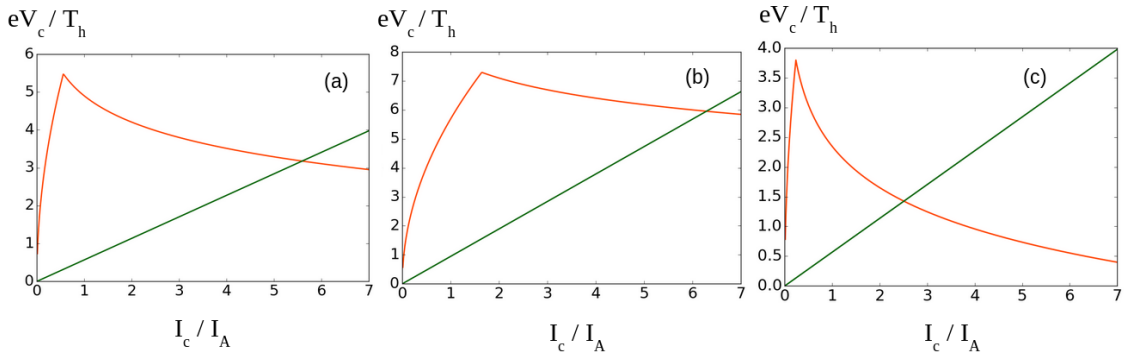

Figure 2.22: Sample IV characteristics calculated using the Tikhonchuk laser diode model of a capacitor coil. Model input parameters were taken from (a) Courtois *et al.* [44] conducted on the Vulcan laser facility (b) Gao *et al.* [79] and Chien *et al.* [39] conducted on the OMEGA EP laser facility (c) Ivanov *et al.* [94] conducted on the Multi-Terawatt Laser (MTW).

in the external circuit. Roughly speaking, the diode current grows at early times and supplies current and voltage to the external circuit. As the coil current increases, the diode voltage decreases. When the diode impedance V/I reaches the value for the external circuit impedance the current attains a maximum, steady state value.

In Fig. 2.22a, we see the IV characteristic corresponding to Courtois *et al.* [44]. The laser is Nd-glass with wavelength $\lambda_L = 1.053$ μm, energy $E_L = 300$ J and pulse duration $t_L = 1$ ns. The beam was focused to a 30 μm spot using $f/2.5$ optics. According to Ref. [169], the laser intensity of 4×10^{15} Wcm^{-2} corresponds to a hot electron temperature of ~ 30 keV (around factor two higher than measured) and a hot electron density of $n_{h0}/n_{cr} \sim 0.07$ [169]. Fig. 2.22a shows that the maximum attainable voltage is around $V = 5T_h = 150$ kV and the maximum current is $I = 6I_A \sim 100$ kA for a plate separation of $d = 2.5$ mm. Solving the model in time, however, we find that the short laser pulse duration and relatively large coil inductance of $L \sim 4$ nH limits the current to $1.3I_A = 20$ kA (see Section 2.6.2). This current estimate is in good agreement with the experimental values of $B \sim 7$ T and $I \sim 14$ kA.

Referring to Fig 2.22b, with experimental parameters taken from Gao *et al.* [79] and Chien *et al.* [39], two Nd-glass laser beams were overlapped at the third harmonic ($\lambda = 0.35$ μm), delivering $E = 2.5$ kJ in $t = 1$ ns to a 60 μm-diameter spot. The intensity of $\sim 2 \times 10^{16}$ Wcm^{-2} corresponds to a hot electron temperature of 18 keV and hot electron density $n_{h0}/n_{cr} \sim 0.045$ [169]. For a plate separation $d = 0.6$ mm, the diode tension is expected to reach $7T_h = 120$ kV with a maximum current $6I_A = 100$ kA. Solving the coupled ODEs in time, a loop inductance of $L = 2$ nH coupled with a short laser pulse duration means that a peak current of just $2I_A = 35$ kA is attained (see Section 2.6.2). This agrees reasonably well with extrapolated experimental data at the time the laser is turned off: $I(t = 1$ ns)

$= 57 \pm 4$ kA [39]. Moreover, it improves slightly on the Fiksel model prediction (see Fig. 2.17).

The IV characteristic in Fig. 2.22c was calculated using experimental parameters taken from Ivanov *et al.* [94]. During the experiment, a single Nd-glass laser beam was used to drive capacitor coil targets at a wavelength of 1.053 μm. The laser pulse delivered 25 J of energy over 2.8 ns to a 7 μm-diameter spot. Based on Eq. (2.15), a laser intensity of $0.8 \times 10^{16}\text{Wcm}^{-2}$ corresponds to $T_h \approx 30$ keV and a hot electron density $n_{h0}/n_{cr} \approx 0.1$, where we have assumed a laser energy to hot electron conversion efficiency of $\eta = 0.5$ [67]. The IV curve suggests that a peak current of $2.5I_A \approx 40$ kA can be achieved for these parameters. Solving the diode model in time, the long pulse duration ($t = 2.8$ ns) and low coil inductance ($L = 0.66$ nH) means that the current quickly rises to a maximum of 25 kA at $t = 1.5$ ns and then saturates. Faraday measurements of the magnetic field suggest the maximum coil current was $I_c = 10$ kA. Agreement with experiment is reasonable for a coil resistance of 1 Ω. If the coil skin depth is neglected, the bulk resistance is calculated as 2 mΩ [94] and the Tikhonchuk model significantly overestimates the peak current.

Consideration of the diode IV characteristic shows that the Tikhonchuk model is qualitatively consistent with experimental results across a broad range of experimental parameters. Better quantitative agreement would require additional modelling of wire resistive heating, the laser temporal profile and other factors. We see that the maximum potential that can develop in the laser-diode is of order 1-10 T_h and the maximum current is of order a few times $I_A = 17$ kA.

Time evolution of diode current

Knowing the diode IV characteristic, it is possible to solve the external circuit equation for the diode current. The IV characteristic is a function $V(I)$, so this can be substituted into the left hand side of Eq. (2.64) and then the equation can be numerically integrated to produce $I(t)$. After the laser has turned off, the current decays following an RL exponential law and the diode potential is calculated directly from the diode IV characteristic (see Sec. 2.6.2). The diode impedance is found by taking the ratio of the current and the voltage profiles.

Fig. 2.23 shows estimates of the diode current, voltage and impedance corresponding to Santos *et al.* [153]. The graphs show that a peak current of over 100 kA can be attained at the end of the laser drive, corresponding to magnetic fields of $B \sim 280$ T. This is a factor 2-3$\times$ smaller than measured and is in broad agreement with the Fiksel estimate.

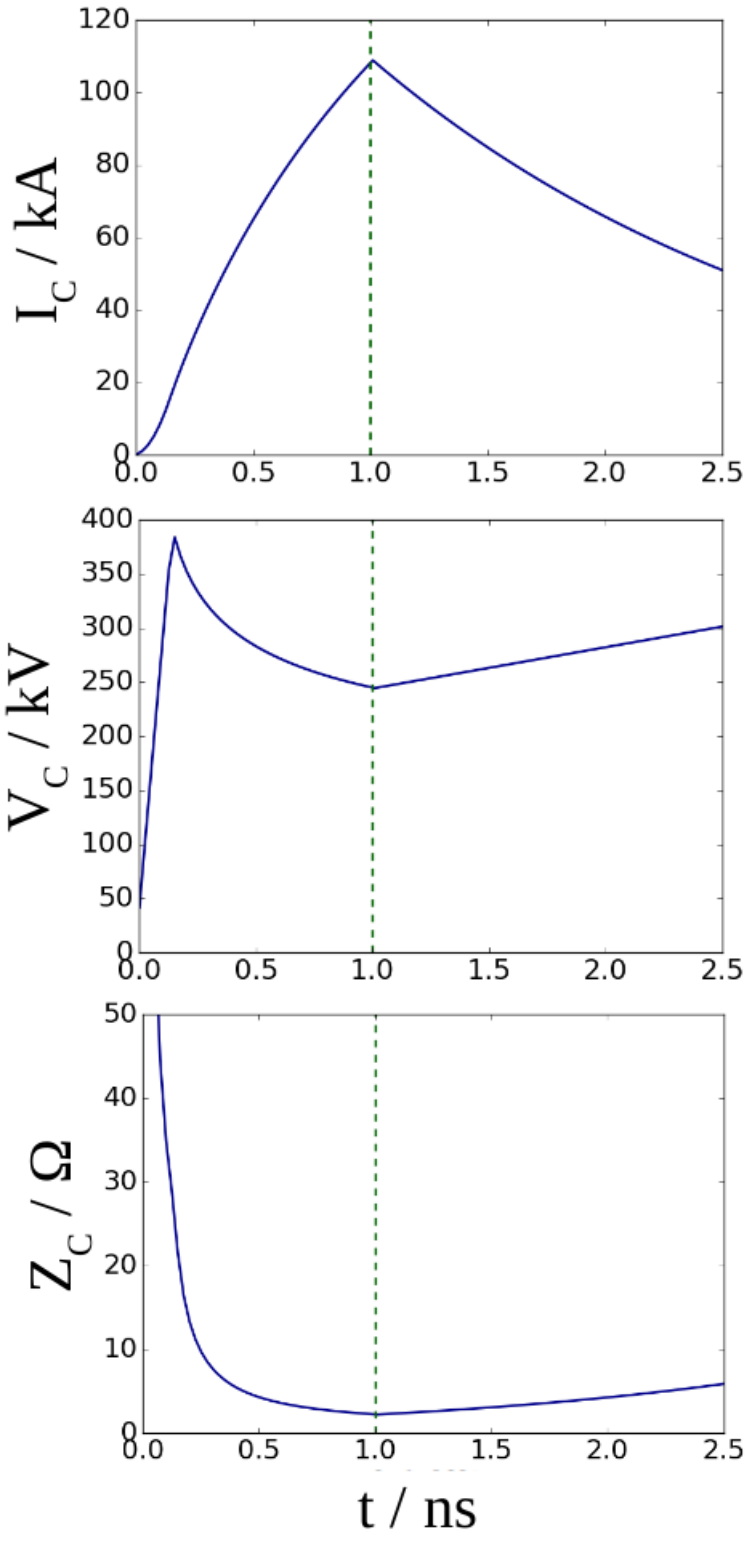

Figure 2.23: Time evolution of (a) current (b) voltage (c) impedance for a laser-driven diode with experimental parameters taken from Santos *et al.* [153]. The vertical dashed line (green) defines the end of the laser pulse.

Summary of plasma diode model

Given that Tikhonchuk's diode model [169] is only designed to capture the essential physics of a laser-driven current source, it shows good agreement with many measurements of capacitor coil magnetic fields. Comparison with results from Ref. [94] suggests that the absence of Ohmic heating and current diffusion in the model means that it may overestimate the coil magnetic field for experiments at long pulse duration. Recent work by Morita *et al.* [130] has shown, however, that good agreement can be found when the diode model is combined with a self-consistent solution of Ohmic heating in the coil.

The diode model predicts a stronger coil magnetic field with higher laser $I_L\lambda_\mu^2$, bigger r_{spot}, longer laser pulse duration t_{las}, lower impedance R, lower inductance L and smaller plate spacing d. A more intense laser with a larger focal spot will produce more energetic electrons over a wider area, thereby enhancing the diode current and helping the electrons to overcome the electrostatic potential on the anode. The longer the laser pulse, the longer the current will be able to build before the circuit begins to decay. A more divergent laser-plasma with a large focal spot will form a column that is more resistant to magnetic pinching. Reducing the plate separation will further help to reduce the impact of the pinching limit. A lower coil inductance (shorter wire) will allow the current to build more quickly over the laser pulse duration and a lower impedance will reduce current damping. Since the major parameter controlling the loop current is the laser $I_L\lambda_\mu^2$, tight focusing and longer wavelengths may improve the capacitor coil performance.

Chapter 3

Measuring electromagnetic fields

This chapter introduces various diagnostics and data processing techniques required to extract the measurements presented in Part III. Conducting probes (e.g. B-dot and D-dot probes) were used during both Vulcan experiments to measure electromagnetic fields around the target. Sections 3.1 and 3.2 explain how to extract electromagnetic field measurements from conducting probes. Then in Sec. 3.3 I will describe how proton deflectometry can be used to 'image' electromagnetic fields in experiments with high power lasers. The equations of motion for charged particles in uniform electric and magnetic fields are derived, providing scalings that are used in Chap. 5 to distinguish between electric and magnetic field measurements. At the end of this chapter, I present analytic calculations of charged particle deflection in non-uniform electromagnetic fields that can be used to estimate capacitor coil magnetic fields from proton deflectograms.

3.1 Conducting probes

Technically speaking, any conductor placed in an electromagnetic field will become a source of current (via Faraday's Law) and can be used as a measurement device. If such a device is connected to an electrical transmission line the signal can be transported to an oscilloscope where it is digitised and stored. Conducting probes such as small magnetic coils are frequently used to measure electromagnetic fields emanating from high power laser targets. These probes are highly versatile and can measure electromagnetic fields in experiments with long-pulse lasers [68, 44] or EMP from short-pulse interactions [27, 58]. An EMP signal decays to zero over several hundred nanoseconds and has a bandwidth approaching 200%[1]. A capacitor coil magnetic field will grow to a peak over $\sim$ 1 ns and decays on a timescale ranging

[1] Antenna bandwidth can be expressed in terms of the maximum f_2 and minimum f_1 frequencies in the frequency band: $BW = 2(f_2 - f_1)/(f_2 + f_1)$ [43]. EMP signals typically range from DC up to GHz or THz frequencies.

from 1 ns to 100 ns. To minimise signal distortion, it is therefore necessary that electromagnetic probes have a wide bandwidth and high maximum frequency. An ideal probe should also be non-perturbative, with high sensitivity, high dynamic range (i.e. be able to measure strong and weak signals with equal fidelity) and be able to survive contact with ionizing radiation [43]. Moreover, since the direction of the EMP field is highly variable inside a target area and is not known *a priori*, an ideal probe should be able to measure electromagnetic fields along multiple axes simultaneously. In general, an EMP signal is not a plane wave, where the electric field is proportional to the magnetic field:

$$\underline{E} = -c\,\underline{\hat{n}} \times \underline{B}$$

Here $\underline{\hat{n}}$ is the unit vector in the direction of wave propagation. A comprehensive measurement therefore requires both $\underline{E}$ and $\underline{B}$ to be recorded. The plane wave approximation is valid under certain conditions, when measurements are taken far from the radiation emitter[2] and in vacuum, with no conducting obstacles between the probe and the field source. This is true of measurements far from a dielectric window on an experimental chamber[3], but is rarely the case for probes inside the chamber itself. Over the next two sections, I will briefly discuss the B-dot magnetic field probe for measuring time-dependent magnetic fields and D-dot electric field probes for measuring time-dependent electric fields.

3.1.1 B-dot magnetic probe

An induction or B-dot probe measures the rate of change of magnetic field in a region of space defined by the circumference of a wire coil. Consider a coil of wire embedded in a changing magnetic field. By Faraday's Law, the voltage induced in the coil is [93]:

$$V(t) = NA\frac{dB}{dt}$$

where N is the number of coil turns and A is the area enclosed by each loop of the coil. For high quality B-dot sensors, the probe transfer function is flat over a wide bandwidth [50]. This is convenient for data analysis because the magnetic field can be simply related to the probe output voltage V via:

$$V(t) = A_{eq}\frac{dB}{dt} \tag{3.1}$$

[2] i.e. in the *far field* [95].

[3] A dielectric window can generally be considered a point source of radiation at a distance of several metres from the target chamber.

where A_{eq} is the probe equivalent area, which is constant over the probe's operating bandwidth. The magnetic field is extracted by integrating the voltage profile in Eq. (3.1) over time.

3.1.2 D-dot electric probe

D-dot probes are high-frequency sensors that measure the time rate of change of the electric flux density at a given point in space. They rely on the ability of an electric field to induce a current in a conductor that can be measured and recorded. A simplified picture of D-dot sensor operation is presented in Ref. [62], where a conducting disk is embedded in an electrical ground plane. The disk is placed inside a hole in the ground plane and is separated from it by a small gap at the perimeter. In the presence of an electric flux Φ_E, a charge Q will accumulate in the disk following Gauss' Law:

$$\Phi_E = \oint_{\mathrm{S}} \underline{E} \cdot \underline{dS} = \frac{Q}{\epsilon_0}$$

where S is a closed Gaussian surface that bounds the disk and ϵ_0 is the permittivity of free space. Defining the sensor equivalent area $A_{eq} = \int_{\mathrm{S}} \underline{E} \cdot \underline{dS}/E$, the electric flux reduces to:

$$EA_{eq} = \frac{Q}{\epsilon_0}$$

The quantity of accumulated charge can then be measured by allowing a current to flow out of the disk through an impedance Z_{probe}. Given that $V = IZ_{probe}$, the electric field through the disk is related to the probe output voltage V via:

$$V(t) = Z_{probe} A_{eq} \frac{dD}{dt} = Z_{probe} A_{eq} \epsilon_0 \frac{dE}{dt} \tag{3.2}$$

The electric field is extracted by integrating the voltage profile in Eq. (3.2) over time. Technical details of the free-field Prodyn FD-5C D-dot sensors used in this thesis can be found in Ref. [125] and [63].

3.2 Frequency-dependent attenuation correction in coaxial cables

When a voltage signal passes down a coaxial cable it will experience an attenuation in amplitude and a dispersive phase shift. The problem when presented with a signal on an oscilloscope screen from an electrical probe is to estimate the magnitude of the probe signal as it entered the cable based on the signal output. This is achieved by measuring the attenuation and phase shift of a known signal using a network analyzer. In this section I will outline how to recover the undistorted probe output

given knowledge of how a signal is distorted in coaxial cables.

Consider a signal with power P_{in} when it enters a length of coaxial cable and power P_{out} at the opposite end. Suppose also that the signal is monochromatic. The attenuation Q, measured in decibels (dB), of the signal is defined by:

$$P_{\text{out}}[\text{W}] = \text{P}_{\text{in}}[\text{W}]10^{\text{Q[dB]}/10} \tag{3.3}$$

A negative value of Q implies that $P_{\text{out}} < P_{\text{in}}$. For an electrical signal, the power can be written $P = V^2/R$, where V is the voltage and R the resistance of the wire medium. Eq. (3.3) can therefore be rewritten as

$$\frac{V_{\text{out}}^2}{R} = \frac{V_{\text{in}}^2}{R}10^{\frac{Q}{10}}$$

or alternatively

$$V_{\text{out}} = V_{\text{in}}10^{\frac{Q}{20}} \tag{3.4}$$

Turning to the more general case of a polychromatic signal propagating down a coaxial cable, the complex voltage amplitude measured from the central conductor to the outer conductor a distance x along a coaxial cable can be expressed as [152]:

$$V_x(\omega) = V(0)e^{-\gamma(\omega)x} \tag{3.5}$$

where $V(0)$ is the voltage applied at the source end and $\gamma(\omega)x = a(\omega) + ib(\omega)$ is the response function of the transmission line - a complex number that accounts for the attenuation loss $a(\omega)$ and phase shift $b(\omega)$ of the signal as it passes down the cable.

Attenuation and phase shift can be measured by attaching a cable to two ports of a network analyzer and sending well-characterized signals between the ports. The results of an S_{21} insertion loss test can be plotted in Bode (pronounced "BOH-dee" or "BOH-duh") diagrams, as illustrated in Fig. 3.1. For simplicity, the following derivation assumes that the coaxial cable is dispersion-free, so the phase shift of the signal can be ignored and $\gamma(\omega)x = a(\omega)$. The amplitude Bode diagram (see Fig. 3.1) plots $\frac{Re(V_x(\omega))}{Re(V_0(\omega))}$ as a function of frequency in units of decibels:

$$Q(\omega) = 20\log\frac{Re(V_x(\omega))}{Re(V_0(\omega))} \tag{3.6}$$

Voltage in frequency space is related to the voltage in time via the Fourier transform:

$$V_x(\omega) = \mathcal{F}(V_x(t)) = \int V_x(t)e^{-i\omega t}dt \tag{3.7}$$

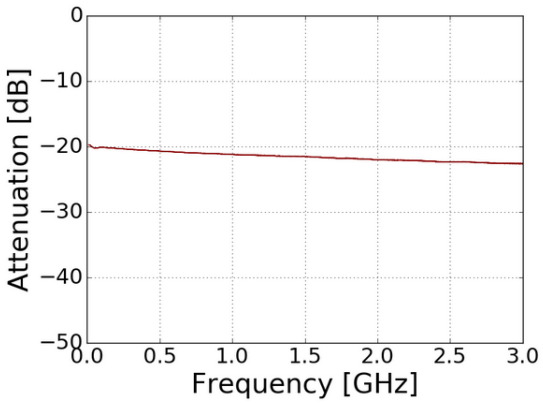

Figure 3.1: Bode attenuation diagram taken from an S_{21} insertion loss test for SMM24 coaxial cable. The test was conducted between 10 MHz and 3 GHz with -10 dB attenuators fixed to each end of the cable. The red curve shows that the cable attenuation increases linearly to a maximum of < -2 dB at 3 GHz.

The signal voltage can therefore be expressed as:

$$V_x(\omega) = V_0(\omega)e^{-\gamma x} \tag{3.8}$$

Dividing through by $V_0(\omega)$ and solving for $a(\omega)$ gives:

$$\begin{aligned} a(\omega) &= Re(\gamma) \\ &= \ln \frac{V_x(\omega)}{V_0(\omega)} \\ &= \ln \left(10^{Q(\omega)/20}\right) \end{aligned}$$

which yields a simple expression for the real component of the transfer function $a(\omega)$ in terms of $Q(\omega)$, the attenuation as a function of frequency in units of decibels:

$$a(\omega) = \frac{Q(\omega)}{20} \ln 10$$

To get the original voltage waveform that entered the cable, $V_0(t)$, one can apply the inverse Fourier transform to $V_0(\omega) = V_x(\omega)e^{\gamma x}$ and insert Eq. (3.8):

$$\begin{aligned} V_0(t) &= \mathcal{F}^{-1}(V_0(\omega)) \\ &= \mathcal{F}^{-1}(V_x(\omega)e^{\gamma x}) \\ &= \int_{-\infty}^{\infty} V_x(\omega)e^{\gamma x}e^{i\omega t}d\omega \end{aligned}$$

Working backwards from this point, the probe signal can be recovered from the oscilloscope voltage trace in three steps:

1. Take the Fourier transform of the oscilloscope trace $V_x(t)$ to yield $V_x(\omega)$
2. Multiply by $e^{\gamma(\omega)x} = e^{\frac{Q(\omega)}{20}\ln 10}$
3. Apply the inverse Fourier transform

This three-step procedure converts a distorted signal $V_x(t)$ back to its original form $V_0(t)$ using the network analysis function $Q(\omega)$. It can be used on its own or in conjunction with frequency filters to extract the probe output from oscilloscope data (see Chap. 4 Part III). Finally, for a cable that applies a fixed attenuation across all frequencies, $Q(\omega) = Q =$ constant and Eq. (3.4) is recovered:

$$V_x(t) = V_0(t)e^{\frac{Q}{20}\ln 10}$$
$$V_x(t) = V_0(t)10^{\frac{Q}{20}}$$

3.3 Proton Deflectometry

Proton deflectometry (also known as proton imaging and proton radiography) is a widely used diagnostic of high energy density plasmas and transient field phenomena. By firing a proton beam pulse through a target and measuring how the particles are deflected, one can build a 3D picture of the target density and electromagnetic field distribution with 1-10 μm spatial and 1-10 ps temporal resolution [104, 150]. For radiographic imaging to be successful the proton source must satisfy several conditions, including high particle kinetic energy, short pulse duration, small source size and high spatial uniformity. In Sec. 2.4, I described how a TNSA proton beam can be produced from short pulse laser interactions with a solid foil. These proton beams are weakly divergent with a useful energy spectrum ranging from a few MeV up to a maximum of $\sim$ 60 MeV [104]. An alternative proton source uses fusion reactions inside a D^3He capsule to produce isotropic bursts of 14.7 MeV and 3.4 MeV protons [108]. Although there are advantages and disadvantages to both approaches, this section focuses on TNSA proton sources imaged onto stacks of radiochromic film (RCF) since these were used to measure capacitor coil fields during the experiment reported in Chap. 5 Part III.

Fig. 3.2 shows the typical layout of a proton deflectometry experiment. Sometimes a thin shield (e.g. few μm-thick metal foil) is placed between the proton foil and the target in order to protect the TNSA foil from target pre-plasma which would

degrade sheath formation. The detector is placed sufficiently far away from the target to magnify the image. The desire for high magnification must be balanced by consideration of proton flux and detector sensitivity, so the detector distance (D) is usually less than ~ 20 cm when working with RCF.

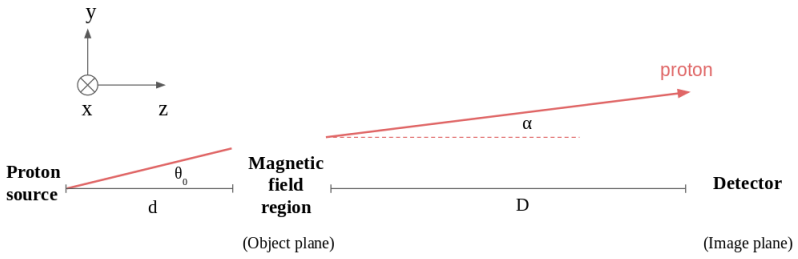

Figure 3.2: Schematic of a typical proton deflectometry experiment. The proton beam is oriented along the z-axis and directed onto a detector. Protons are produced on the left of the diagram, with an angle θ_0, propagate through free space until they reach the region containing a magnetic field. Their trajectory is perturbed by the field, which we represent by a small deflection angle, α. The source-field distance and field-detector distance are designated by d and D respectively.

An RCF detector typically consists of multiple separate layers of film placed one behind the other in a stack. As the name suggests, radiochromic film contains an active monomer that polymerizes when exposed to ionizing radiation to form a darker dye [89]. The darkening process is near-instantaneous, so RCF reveals qualitative information straight away just by looking at it. Experiments have shown that the optical density of the dye is quasi-linear over several orders of magnitude in dose, is independent of dose rate and is insensitive to proton energy [89]. The proton beam can be separated from other sources of ionizing radiation because electrons and x-rays have a much lower energy deposition rate (dE/dx) and therefore produce a more gradual signal drop-off between layers (c.f. the sharp layer-by-layer signal drop-off in Fig. 3.3). Hot electron signals can usually be resolved as a fainter, broader beam that must be background subtracted before quantitative information about proton spectrum, distribution and energy content can be extracted. A narrow spectrum of protons (energy spread $\Delta E_p < 0.4$ MeV) will be absorbed in each layer of RCF because protons deposit most of their energy suddenly in a Bragg peak. Higher energy protons will form a smeared background signal that is usually much weaker than the primary Bragg peak signal (see Fig. 5.4, Chap. 5). Each layer of film can therefore be assigned a well-defined proton energy and combining several layers in a stack will form a time history of the target interaction.

TNSA 'proton' beams are in fact a co-propagating quasi-neutral mixture of protons and hot electrons, distributed in space according to their energy. Since TNSA beams are approximately charge-neutral, space charge effects are usually ignored

when modelling proton deflectometry. This has been shown to be a safe assumption in many situations [104], but we will see in Sec. 5.3.5 that this may not always be the case. Fig. 3.3 shows typical proton images on several layers of RCF when a cold vanadium foil target is irradiated by a short-pulse drive beam at an intensity of 2×10^{19} Wcm^{-2} [72]. Darker regions correspond to areas of higher proton signal. The TNSA beam is broadly elliptical, with a smooth beam profile and minor eccentricity. Experiments with RCF stacks of different thicknesses and sensitivities have shown that higher energy protons are less divergent, which is an important consideration when probing the large (multi-mm) targets used in this work. If a high-Z grid is put in the path of the beam the shadow of the grid is clear and undistorted, demonstrating that the proton beam is laminar (i.e. there are no proton-proton collisions or path crossing) so intensity modulations can be unambiguously ascribed to interactions with the target. Of course, if the symmetry of the accelerating sheath is degraded then the quality of the proton beam will be worse than pictured in Fig. 3.3. This is commonly caused by structure in the hot electron beam that generates the TNSA field. Using thicker foils can help to smooth the beam profile, although degradation may also be caused by laser pre-pulse interactions or irregularities in the target surface [13].

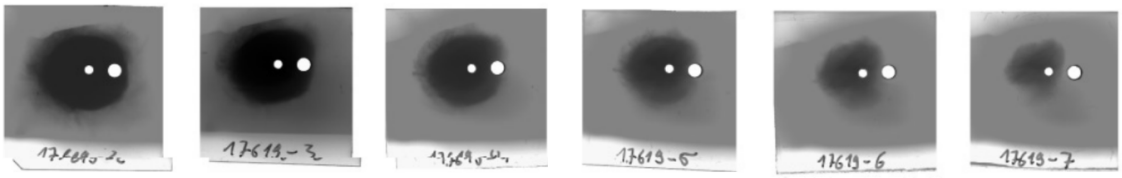

Figure 3.3: TNSA proton spatial and energy distribution for a cold vanadium foil target irradiated by a short-pulse drive beam at an intensity of 2×10^{19} Wcm^{-2}. Each image corresponds to a single layer of GAF-MD55 RCF with the range of proton energies labelled underneath. Darker regions represent areas of higher proton signal and white circles have been cut out of the film layers to act as visual references. Image taken from Flippo *et al.* [72] with permission of the publisher.

The imaging resolution of proton deflectometry is sensitive to a range of factors, including: finite source size, target dynamics (e.g. fast-evolving fields), scattering in the target and finite detector resolution [108]. The most important factor is generally scattering in the target. Radiochromic film has spatial resolution better than 1200 lines per mm, so detector resolution is unlikely to be the limiting factor in an experiment [104, 108]. TNSA beams also have a very small virtual source size (5-10 μm) so blurring from an extended source is usually insignificant [23]. If target dynamics are faster than the time it takes for different proton energies to traverse the target the beam will probe different conditions and blurring will occur. When imaging onto RCF stacks, the combination of a broadband TNSA beam and

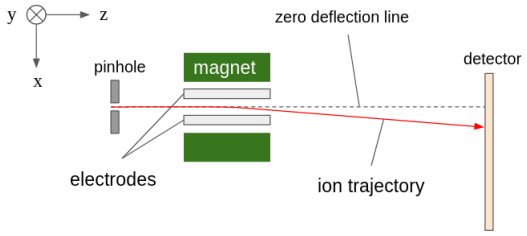

Figure 3.4: Diagram of a Thomson Parabola spectrometer, with ions incident along the z-axis and the electric and magnetic fields oriented along x.

a finite width of energy absorption in each layer means the images will be blurred. In Chapter 5, I will show that this particularly affects protons with $E_p < 4$ MeV.

3.4 Charged particle motion in uniform EM fields

Understanding how charged particles move in electrostatic and magnetostatic fields is fundamental to many diagnostics used in high energy density (HED) physics experiments including proton deflectometry (Part III Chap. 5) and electron spectrometers (Part III Chap. 4). The simplest equations of motion are found for charged particle motion in uniform electromagnetic fields, which can be used to roughly estimate the fields present in laser-plasma interactions [134, 181]. Since electric and magnetic field deflections scale differently with proton energy, the uniform field equations can also help to discriminate between radiographic measurements of electric and magnetic fields [107]. The situation is analogous to ion motion inside a Thomson parabola spectrometer or electron motion inside an electron spectrometer.

A Thomson parabola (TP) spectrometer is used to measure the energy spectrum of ions produced in laser-matter interactions over a small solid angle. Fig. 3.4 shows a standard TP set-up, with magnetic and electric fields oriented parallel to each other and perpendicular to the direction of propagation of the ion beam. As ions pass through the TP, they are deflected parallel to the electric field and perpendicular to the magnetic field according to the Lorentz force. Deflected particles strike a detector at the back of the TP that records their position relative to the zero-position of the pinhole. Consider the situation illustrated in Fig. 3.4, where the ion velocity $v_\perp$ is parallel to z and the electric and magnetic fields are oriented along the x-axis. Ignoring fringing fields, deflection in the x and y directions is given approximately by [34]:

$$x = \frac{qEL_E}{mv_\perp^2}\left(\frac{1}{2}L_E + d_E\right) \tag{3.9}$$

$$y = \frac{qBL_B}{mv_\perp}\left(\frac{1}{2}L_B + d_B\right) \tag{3.10}$$

where L_E/L_B is the length of the E/B-field in z and d_E/d_B is the distance between the E/B-fields and the detector. For the case where $L_E = L_B = \ell$ and $d_E = d_B = D$, these equations combine to yield a quadratic relationship:

$$y^2 = \frac{q}{m}\frac{B^2\ell\xi}{E}x \tag{3.11}$$

for $\xi = \ell/2 + D$. Eq. (3.11) shows that different ion species can be distinguished according their charge-to-mass ratio q/m. Ions with the same charge-to-mass ratio but different energy will lie along the same quadratic curve on the detector, as illustrated in Fig. 3.5. Ions enter the TP through a Pb pinhole (typically < 500 μm in diameter) which serves to collimate the beam and protect the detector from x-rays. The diameter of the pinhole defines the maximum energy resolution of the detector - two ions of different energy but the same q/m can only be distinguished if they are separated on the detector by a distance greater than the pinhole width.

Over the next two sections, I will derive analytic equations for charged particle deflection in uniform electrostatic and magnetostatic fields. The equations will be derived in full generality, suitable for analysing data from charged particle spectrometers, proton deflectometry or for benchmarking numerical codes.

3.4.1 Ion deflection in a uniform electrostatic field

First, consider the case of a charged particle moving through a static, uniform electric field oriented perpendicular to the direction of particle motion with scale length L_E. The particle has initial velocity $v = (0, 0, v_{z0})$. A diagram of the coordinate system and particle motion can be found in Fig. 3.6. For an electric field $\underline{E} = E\underline{\hat{y}}$, the Lorentz force on a particle with charge q is simply:

$$\underline{F} = qE\underline{\hat{y}}$$

with acceleration in the $\underline{\hat{y}}$ direction:

$$a = qE/m$$

From Newton's Laws, the deflection under constant acceleration can be expressed as $S_1 = \frac{1}{2}at_1^2$, where t_1 is the amount of time the particle spends inside the field.

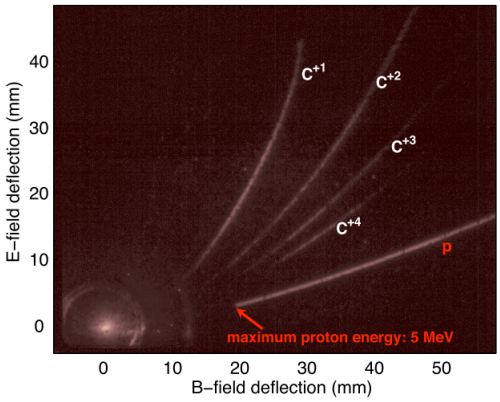

Figure 3.5: Ion spectra recorded by a microchannel plate inside a Thomson parabola. The ions were produced during the interaction of a 16.5 J laser with a 50 μm-thick Au foil at an intensity of 2×10^{19} Wcm^{-2}. Protons and carbon ions are visible as quadratic curves and the x-ray and neutral particle signal forms a bright spot in the bottom lefthand corner. More energetic particles are deflected less by the fields so can be found further to the left along each curve. Image reproduced from Ref. [150] with permission of the author. Copyright SISSA Medialab Srl. Reproduced by permission of IOP Publishing. All rights reserved.

Following Fig. 3.6,

$$t_1 = \frac{L_E}{v_{z0}}$$

So

$$S_1 = \frac{1}{2}\left(\frac{qE}{m}\right)\left(\frac{L_E}{v_{z0}}\right)^2 \tag{3.12}$$

Eq. (3.12) gives the particle deflection at the point of leaving the electric field region. After this point, the particle will travel freely through space until it reaches the detector. Further deflection in $\underline{\hat{y}}$ direction is

$$S_2 = v_y t_2$$

where $t_2 = d_E/v_{z0}$. From Newton, $v_y = 0 + at_1$ at the edge of the electric field region, so

$$v_y = \frac{qE}{m}\left(\frac{L_E}{v_{z0}}\right)$$

and

$$S_2 = \frac{qEL_E}{mv_{z0}}\frac{d_E}{v_{z0}}$$

The total particle deflection in the detector plane follows from $S_E = S_1 + S_2$:

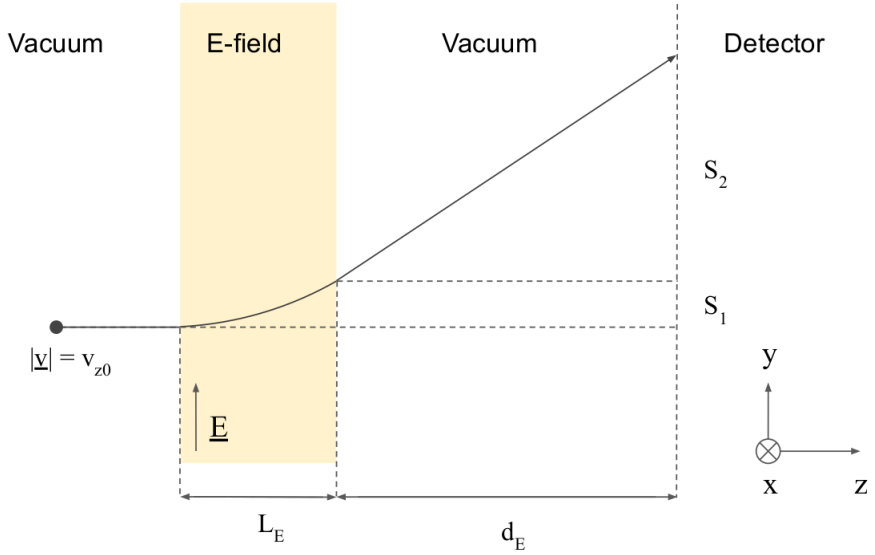

Figure 3.6: Diagram of charged particle deflection in an electric field. The particle is moving in the z-direction. A static, uniform electric field is directed along the y-axis in the yellow shaded region with scale length L_E in the z-direction. Once the particle has left the electric field, it propagates ballistically onto a detector located a distance d_E from the E-field.

$$S_E = \frac{qEL_E}{mv_{z0}^2}\left(\frac{1}{2}L_E + d_E\right) \tag{3.13}$$

This equation is exact. For a charged particle with kinetic energy E_p, Eq. (3.13) shows that the E-field deflection scales as $1/E_p$. Deflection is also linear in the electric field strength, E.

3.4.2 Ion deflection in a uniform magnetostatic field

Now consider the case of a charged particle moving through a uniform magnetic field oriented perpendicular to the direction of particle motion ($\underline{B} = B\underline{\hat{y}}$), with spatial extent (scale length) L_B. The particle has initial velocity $v = (0, 0, v_{z0})$. In Fig. 3.7 there is a diagram of the coordinate system that we will use. The Lorentz force on a particle with charge q is then:

$$\underline{F} = q\underline{v} \times \underline{B} = q\, v_{z0}\, B(-\underline{\hat{x}})$$

As with the electric field, the particle deflection S_1 will be calculated at the edge of the field region due to deflection in $\underline{\hat{x}}$ at $z = L_B$. Using the standard definition of the Larmor radius ($r_L = \frac{mv_\perp}{qB}$) and referring to Fig. 3.8:

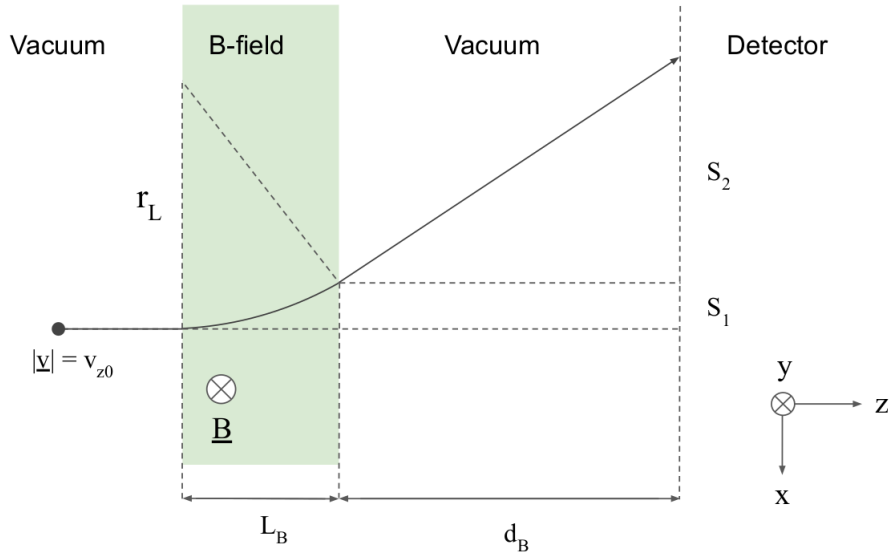

Figure 3.7: Diagram of charged particle deflection in a magnetic field. The magnetic field static, uniform and directed along the y-axis (into the page) with scale length L_B in the z-direction. Particle motion inside the B-field traces out the circumference of a circle with radius r_L. Once the particle has left the magnetic field, it propagates ballistically onto a detector located a distance d_E from the B-field. The particle speed remains constant throughout the motion: $v = v_{z0}$.

$$L_B = r_L \sin(\theta)$$
$$S_1 = r_L - r_L \cos(\theta)$$

So

$$S_1 = r_L\Big(1 - \sqrt{1 - \Big(\frac{L_B}{r_L}\Big)^2}\Big) \tag{3.14}$$

Now, with d_L the distance from the end of the B-field region to the detector plane, an expression for the deflection after the charged particle has left the B-field region can be derived. The magnitude of this deflection is:

$$S_2 = d_L \frac{v_x}{v_z}$$

Appealing again to Fig. 3.8, one observes that

$$v_x = v_{z0} \sin(\theta)$$
$$v_z = v_{z0} \cos(\theta)$$

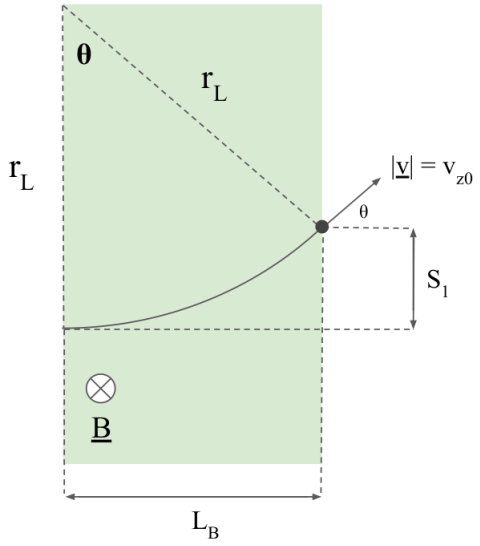

Figure 3.8: Diagram of charged particle deflection in a static, uniform magnetic field. The magnetic field is oriented into the page with scale length L_B in the z-direction. Particle motion inside the B-field traces out the circumference of a circle with radius r_L. The particle speed remains constant throughout the motion: $v = v_{z0}$.

And therefore

$$S_2 = d_L \tan(\theta) = d_L\Big(\frac{L_B}{r_L - S_1}\Big)$$

Substituting for S_1 gives a full expression for the post-field deflection:

$$S_2 = \frac{d_L L_B}{r_L}\frac{1}{\sqrt{1-\left(\frac{L_B}{r_L}\right)^2}} \tag{3.15}$$

Combining equations (3.14) and (3.15), the full solution for the deflection of the charged particle is:

$$S_B = r_L\left(1-\sqrt{1-\left(\frac{L_B}{r_L}\right)^2}\right) + \frac{d_B L_B}{r_L}\left(\frac{1}{\sqrt{1-(\frac{L_B}{r_L})^2}}\right) \tag{3.16}$$

This equation is precise provided $r_L \leq L_B$. That is, for deflections smaller than 90° where the particle does not gyrate. In the limit of small deflections, where $r_L \ll L_B$, this equation must reduce to Eq. (3.10). Expanding the first term in the limit of small $(L_B/r_L)^2$ gives:

$$r_L\left(1-\sqrt{1-\left(\frac{L_B}{r_L}\right)^2}\right) \approx r_L\left(1-\left(1+\frac{1}{2}\left(\frac{L_B}{r_L}\right)^2\right)\right) = \frac{L_B^2}{2r_L}$$

Defining $\alpha = L_B/r_L$, the second term becomes:

$$\frac{d_B L_B}{r_L}\frac{1}{\sqrt{1-(\frac{L_B}{r_L})^2}} = d_B\alpha\Big(\frac{1}{\sqrt{1-\alpha^2}}\Big) \tag{3.17}$$

Then Taylor expanding the fraction in brackets for small α, the second term reduces to:

$$d_B\,\alpha(1+0+...) = \frac{d_B L_B}{r_L} \tag{3.18}$$

Adding together the first and second terms, Eq. (3.10) is recovered for B-field deflection in the limit of small B-fields:

$$S_B = \frac{qBL_B}{mv_\perp}(\frac{1}{2}L_B + d_B)$$

Since the deflection from E- and B-fields are perpendicular to one another and are only affected by the z-component of the particle velocity, we can add the equations for S_E and S_B without loss of generality. The key result is that B-field deflections scale as $1/\sqrt{E_p}$ for particles with kinetic energy E_p. In Sec. 5.3.8, the variation of proton deflection with proton energy is used to try to break the degeneracy of electric and magnetic field measurements inferred from proton deflectometry.

3.4.3 Analytic proton deflection in capacitor coil magnetic fields

Analysis of proton deflectometry data requires an understanding of how proton deflections are affected by electromagnetic field strength and geometry. Rough estimates can be made from RCF data using Lorentz force scalings combined with estimates of the proton path length through the field [134, 181] (see Sec. 3.4.2). Much more accurate estimates can be made using ray tracing simulations, where virtual protons are propagated through a simulated electric or magnetic field [147, 154, 173], or computational inversion techniques [98, 25]. In this section, I will pursue the intermediate aim of deriving an analytic formula for the width of the teardrop-shaped proton void that is observed in RCF images of capacitor coil tar-

gets. These voids develop when protons pass at 90° to the coil axis and close to the wire loop, as shown in Fig. 3.9. For a loop current oriented out of the page at the top of the loop and into the page at the bottom, protons at the top of the loop are deflected radially outwards by the poloidal magnetic field and protons at the bottom of the loop will be pinched radially inwards. If the direction of the current is inverted then the void will too. Experiments show that these 'teardrop' voids are circumscribed by a caustic. Caustics form when strong magnetic fields near the wire surface cause proton flux layers to overlap on the detector and form regions of very high intensity[4]. Besides providing us with a good estimate of the coil magnetic field, deriving an analytic expression for the proton void radius is useful for benchmarking numerical codes (see Sec. 5.3.2) and helps to quantify the role of E-fields in proton deflectometry.

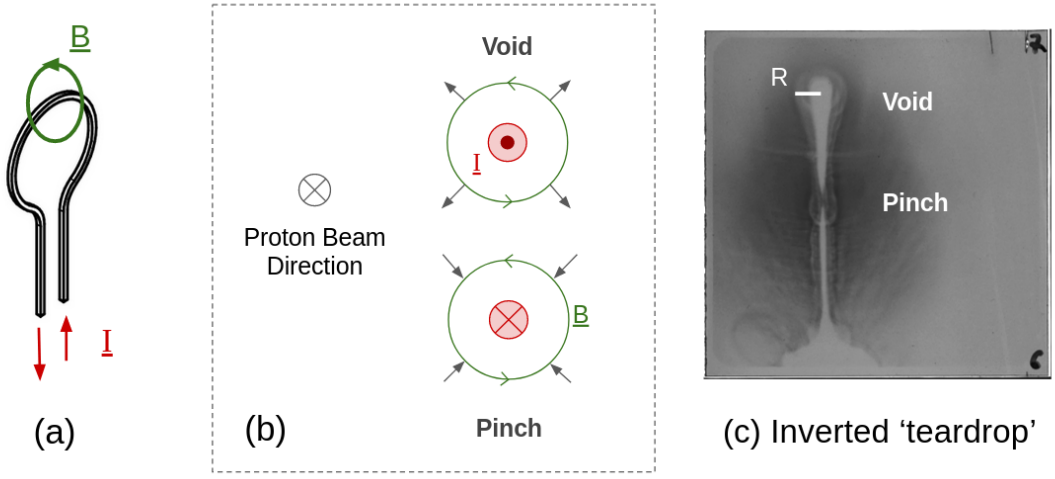

Figure 3.9: Capacitor coil diagrams with current $\underline{I}$ illustrated in red and magnetic field $\underline{B}$ in green: (a) Example of a typical capacitor coil loop (b) Schematic of proton beam deflection (grey arrows) at the top and bottom of a current loop, where the proton beam is directed into the page, perpendicular to the loop axis (c) Proton deflectogram of a 2 mm-diameter capacitor coil viewed edge-on, with void and pinch features clearly visible at the extreme edges of the loop. The RCF layer corresponds to protons with energy $E_p = 7.3$ MeV and is taken from Bradford *et al.* [28]. The void diameter, R, is picked out in white.

Following Gao *et al.* in Ref [79], I will derive an approximate expression for the proton void radius when a proton beam passes through a static capacitor coil magnetic field. The experimental layout can be seen in Fig. 3.2.

A proton ray passing through a point will be defined by a pair of Cartesian coordinates (x, y) in the object plane and a point (x_i, y_i) in the image plane. For small angles of incidence θ_0 and deflection α from the object plane, we can assume

[4] A comprehensive treatment of caustic formation in proton deflectometry can be found in Ref. [104].

that $\tan(\theta_0) \approx \theta_0$ and $\tan(\alpha) \approx \alpha$. This leads to a simple mapping equation between x and x_i:

$$\begin{aligned} x_i &= x + D(\theta_0 + \alpha_x) \\ &= x + D(\frac{x}{d} + \alpha_x) \\ &= Mx + D\alpha_x \end{aligned}$$

where M is the magnification of the system ($M = 1 + \frac{D}{d} = \frac{d+D}{d}$). Similarly, for y:

$$y_i = My + D\alpha_y$$

The next steps will produce an expression for the deflection angles in terms of the magnetic field strength. Relating α_x, α_y to components of the particle velocity $\underline{v} = (v_x, v_y, v_z)$ gives:

$$\begin{aligned} \alpha_x &= \frac{v_x}{v_z} \\ \alpha_y &= \frac{v_y}{v_z} \end{aligned}$$

The velocity components follow from the Lorentz force:

$$\underline{\ddot{x}} = \frac{e}{m_p}(\underline{v} \times \underline{B})$$

Taking the x and y components of the cross product yields:

$$\begin{aligned} \ddot{x} &= -\frac{e}{m_p} v_z B_y \\ \ddot{y} &= \frac{e}{m_p} v_z B_x \end{aligned}$$

Then integrating these equations gives the corresponding velocities:

$$\begin{aligned} v_x &= -\frac{e}{m_p} \int v_z B_y dt \\ v_y &= \frac{e}{m_p} \int v_z B_x dt \end{aligned}$$

In the v_x equation, changing the limits of integration from time to distance

($dt = dz\frac{dt}{dz} = \frac{1}{v_z}dz$) yields:

$$v_x = -\frac{e}{m_p}\int B_y dz$$

From which the deflection angles are obtained:

$$\alpha_x = -\frac{e}{m_p v_z}\int B_y dz \tag{3.19}$$

$$\alpha_y = \frac{e}{m_p v_z}\int B_x dz \tag{3.20}$$

To summarise, equations (3.19) and (3.20) are expressions for the deflection angles α_x and α_y in terms of the magnetic field strength when the angles of incidence and deflection are small. Rewriting in terms of the non-relativistic proton kinetic energy ($E_p = \frac{1}{2}m_p v^2$) gives two equations that are valid for protons with energies $E_p \lesssim 20\,\mathrm{MeV}$:

$$\alpha_x = -\frac{e}{\sqrt{2m_p E_p}}\int B_y dz$$

$$\alpha_y = \frac{e}{\sqrt{2m_p E_p}}\int B_x dz$$

The integrals can be evaluated by picking a suitable form for the magnetic field. Ideally, one would choose a dipolar geometry to approximate the fields around a capacitor coil loop. However a magnetic dipole geometry is complex and the proton void is caused by the poloidal field at the top of the capacitor coil loop, where the field can be well-approximated by the magnetic field from a straight wire oriented along the z-axis. Consider proton deflection in the magnetic field around an infinite straight wire oriented along the z-axis with a radially-symmetric B-field given by:

$$B(r) = \frac{\mu_0 I}{2\pi r} \qquad (r \geq R_0) \tag{3.21}$$

where R_0 is the wire radius, I the wire current and the radial coordinate r is given by $r = \sqrt{x^2 + y^2}$. From Fig. 3.10, the two Cartesian components of the magnetic field can be expressed in polar coordinates via:

$$B_x = B\sin(\theta) = B\frac{y}{r}$$

$$B_y = -B\cos(\theta) = -B\frac{x}{r}$$

where θ is the standard polar angular coordinate measured from the positive x-axis in the xy-plane. Substituting these identities into Eq. (3.21) gives:

$$B_x = \frac{\mu_0 I y}{2\pi r^2} \qquad (r \geq R_0)$$
$$B_y = -\frac{\mu_0 I x}{2\pi r^2} \qquad (r \geq R_0)$$

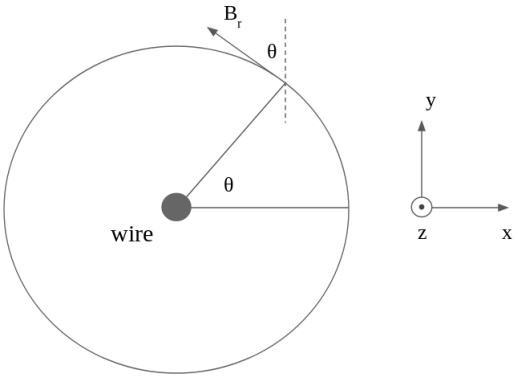

Figure 3.10: Diagram of our coordinate system. An infinite wire of static and uniform current, I, is oriented along the z-axis. The corresponding magnetic field is constant at a fixed radius from the wire centre with a value B_r.

To get an expression for the image plane coordinates (x_i, y_i) the deflection angle equations must be integrated:

$$\alpha_x \approx -\frac{e}{\sqrt{2m_p E_p}} \int_{\Delta z} B_y dz$$

$$= -\frac{e}{\sqrt{2m_p E_p}} \int_{\Delta z} \frac{-\mu_0 I x}{2\pi r^2} dz$$
$$= \left[\frac{e\mu_0 I x z}{\sqrt{2m_p E_p} 2\pi r^2} \right]_{\Delta z}$$
$$= \frac{e\mu_0 I x \Delta z}{\sqrt{2m_p E_p} 2\pi r^2}$$

And similarly for y:

$$\alpha_y \approx \frac{e\mu_0 I y \Delta z}{\sqrt{2m_p E_p} 2\pi r^2} \tag{3.22}$$

Here, Δz is the proton path length integrated over the field region. Expressions

for x_i and y_i in terms of the magnetic field follow from the deflection angles. Since the protons will be deflected radially away from the wire axis, it is useful to convert Cartesian deflections to radial deflections, r_i, in polar geometry. Recalling the definition of x_i:

$$\begin{aligned} x_i &= Mx + D\alpha_x \\ &= Mx + D\left[\frac{e\mu_0 I x \Delta z}{\sqrt{2m_p E_p}2\pi r^2}\right] \end{aligned}$$

And defining $\mu_B = \frac{e\mu_0 I}{2\pi\sqrt{2m_p E_p}}$, these equations simplify to:

$$x_i = Mx + \frac{D\mu_B x \Delta z}{r^2} \tag{3.23}$$

$$y_i = My + \frac{D\mu_B y \Delta z}{r^2} \tag{3.24}$$

Observing that $x_i = r_i\cos(\theta)$, Eq. (3.23) can be expanded:

$$r_i\cos(\theta) = Mr\cos(\theta) + \frac{D\mu_B r\cos(\theta)\Delta z}{r^2}$$

So the radial mapping for an infinite straight wire reads:

$$r_i = Mr + \frac{D\mu_B \Delta z}{r} \tag{3.25}$$

The proton void radius is defined by a caustic in the proton image running around the wire at a fixed radius. This caustic lies at the edge of the proton void, when $\frac{dr_i}{dr} = 0$ [79]:

$$\frac{dr_i}{dr} = M - \frac{D\mu_B \Delta z}{r^2} = 0 \tag{3.26}$$

which is satisfied by

$$r^* = \sqrt{\frac{D\mu_B \Delta z}{M}} \tag{3.27}$$

The proton void radius is then the value of r_i that corresponds to $r = r^*$:

$$\begin{aligned} r_i &= Mr + \frac{D\mu_B \Delta z}{r} \\ r_i(r^*) &= \sqrt{MD\mu_B \Delta z} + \sqrt{MD\mu_B \Delta z} \\ &= 2\sqrt{MD\mu_B \Delta z} \end{aligned}$$

The key result of this section is that the proton void radius in the image plane r_v can be related to the magnetic field strength and geometry, the system magnification and the proton energy via:

$$r_v = 2\sqrt{MD\mu_B\Delta z} \tag{3.28}$$

Correcting for the magnification of the imaging system also gives an expression for the proton void radius, r_M, in the object plane:

$$r_M = r_i/M = 2\sqrt{\frac{D\mu_B\Delta z}{M}} \tag{3.29}$$

In Chap. 5 Part III, Eq. (3.28) is used to estimate the capacitor coil current and magnetic field from proton images taken during an experiment at the Vulcan laser facility. Eq. (3.28) is also used to benchmark PIC simulations of proton deflection in magnetic fields. Making the crude assumption that Δz is equal to the coil radius, these analytic calculations are found to be within a factor 2 of estimates from PIC simulations of protons passing through capacitor coil fields in the experimental field geometry (see Sec. 5.3.1). It is also important to note that $r_v \propto I^{\frac{1}{2}}$ and $r_v \propto 1/E_p^{\frac{1}{4}}$. In the next section I will show how these scalings help discriminate between deflections caused by the electric and magnetic components of the Lorentz force, which can be a large source of error when proton deflectometry is used to diagnose magnetic fields in capacitor coil experiments [154].

3.4.4 Analytic proton deflection in capacitor coil electric and magnetic fields

In the previous section, an expression was derived for the proton void radius when a proton beam passes through a simple static magnetic field. Now I will extend the work of Ref. [79] to the case of a charged, current-carrying wire. The experimental layout is the same as in Fig. 3.2, except now electric and magnetic fields must be considered.

The mapping equation between proton position in the object plane, (x, y), and its corresponding position in the image plane, (x_i, y_i) continues to hold. That is, for small angles of incidence (θ_0) and deflection (α) from the object plane:

$$x_i = Mx + D\alpha_x$$
$$y_i = My + D\alpha_y$$

where M is the magnification of the imaging system ($M = 1 + \frac{D}{d} = \frac{d+D}{d}$).

As before, the deflection angles α_x and α_y are related to the proton velocity $\underline{v} = (v_x, v_y, v_z)$ by:

$$\alpha_x = \frac{v_x}{v_z}$$
$$\alpha_y = \frac{v_y}{v_z}$$

The Lorentz force on a proton with velocity $\underline{v}$ is:

$$\ddot{\underline{x}} = \frac{e}{m_p}(\underline{E} + \underline{v} \times \underline{B})$$

Taking the x and y components of the cross product gives:

$$\ddot{x} = \frac{eE_x}{m_p} - \frac{e}{m_p} v_z B_y$$
$$\ddot{y} = \frac{eE_y}{m_p} + \frac{e}{m_p} v_z B_x$$

Then integrating these equations yields the velocity components v_x and v_y:

$$v_x = \frac{e}{m_p} \int (E_x - v_z B_y) dt$$
$$v_y = \frac{e}{m_p} \int (E_y + v_z B_x) dt$$

Splitting terms in E and B and changing the limits of integration from time to distance ($dt = dz\frac{dt}{dz} = \frac{1}{v_z}dz$) yields for v_x:

$$v_x = \frac{e}{m_p v_z} \int E_x dz - \frac{e}{m_p} \int B_y dz$$

From which the deflection angles are obtained:

$$\alpha_x = \frac{e}{m_p v_z^2} \int E_x dz - \frac{e}{m_p v_z} \int B_y dz$$
$$\alpha_y = \frac{e}{m_p v_z^2} \int E_y dz + \frac{e}{m_p v_z} \int B_x dz$$

These equations connect the proton deflection angles to the electric and magnetic field provided the angles of incidence and deflection are sufficiently small. Rewriting in terms of the non-relativistic proton kinetic energy ($E_p = \frac{1}{2} m_p v^2$) yields two equations that are valid for protons with energies $E_p \lesssim 20\,\mathrm{MeV}$:

$$\alpha_x = \frac{e}{2E_p}\int E_x dz - \frac{e}{\sqrt{2m_p E_p}}\int B_y dz$$
$$\alpha_y = \frac{e}{2E_p}\int E_y dz + \frac{e}{\sqrt{2m_p E_p}}\int B_x dz$$

Since I have already dealt with the case of protons deflected by the magnetic field around an infinite straight wire carrying a uniform current, I will now consider an electric field emanating from an infinitely long, uniformly charged wire. This infinite wire is oriented along the z-axis, with a radially-symmetric E-field given by:

$$E(r) = \frac{\lambda}{2\pi\epsilon_0 r} \qquad (r \geq R_0)$$

Here, λ is the wire charge per unit length, R_0 is the wire radius and the radial coordinate is $r = \sqrt{x^2 + y^2}$. Referring again to Fig. 3.11, the electric field is oriented radially away from the wire surface everywhere in space and therefore:

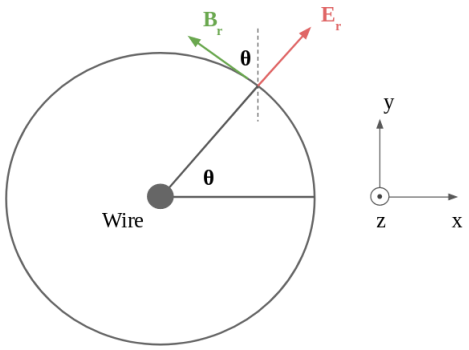

Figure 3.11: Diagram of our coordinate system. An infinite wire of static and uniform current, I, is oriented along the z-axis. The corresponding magnetic field is constant at a fixed radius from the wire centre with a value B_r. The wire is also uniformly charged with radial electric field E_r at a fixed radius from the wire.

$$E_x = E(r)\cos(\theta) = E\frac{x}{r}$$
$$E_y = E(r)\sin(\theta) = E\frac{y}{r}$$

where θ is the standard polar angular coordinate (measured from the positive x-axis in the xy-plane – see Fig. 3.11.) Substituting for $E(r)$ gives:

$$E_x = \frac{\lambda x}{2\pi\epsilon_0 r^2} \qquad (r \geq R_0)$$
$$E_y = \frac{\lambda y}{2\pi\epsilon_0 r^2} \qquad (r \geq R_0)$$

Deriving an expression for the image plane coordinates (x_i, y_i) requires knowledge of how the deflection angles (α_x, α_y) change with proton position and electromagnetic field strength. Without loss of generality, I will proceed with just the electric field terms and then add the magnetic field terms later. As before, Δz denotes the proton path length integrated over the field region:

$$\alpha_x \approx \frac{e}{2E_p}\int_{\Delta z} E_x dz$$

$$= \frac{e}{2E_p}\int_{\Delta z} \frac{\lambda x}{2\pi\epsilon_0 r^2} dz$$
$$= \frac{e}{2E_p}\left[\frac{\lambda x z}{2\pi\epsilon_0 r^2}\right]_{\Delta z}$$
$$= \frac{e\lambda x \Delta z}{4\pi\epsilon_0 E_p r^2}$$

And similarly for y:

$$\alpha_y \approx \frac{e\lambda y \Delta z}{4\pi\epsilon_0 E_p r^2} \tag{3.30}$$

The deflection equations can be simplified by defining $\mu_E = \frac{e\lambda}{4\pi\epsilon_0 E_p}$:

$$\alpha_x = \frac{\mu_E x \Delta z}{r^2}$$
$$\alpha_y = \frac{\mu_E y \Delta z}{r^2}$$

Now r_i can be extracted from x_i. Substituting the electric field equation for α_x into the definition of x_i:

$$x_i = Mx + D\alpha_x$$
$$= Mx + D\left[\frac{\mu_E x \Delta z}{r^2}\right]$$

The same technique can applied to the y_i coordinate, then the equations can be expanded to account for the electric and magnetic fields:

$$x_i = Mx + \frac{D\mu_E x\Delta z}{r^2} + \frac{D\mu_B x\Delta z}{r^2}$$
$$y_i = My + \frac{D\mu_E y\Delta z}{r^2} + \frac{D\mu_B y\Delta z}{r^2}$$

And

$$x_i = Mx + \frac{Dx\Delta z}{r^2}(\mu_E + \mu_B) \tag{3.31}$$
$$y_i = My + \frac{Dy\Delta z}{r^2}(\mu_E + \mu_B) \tag{3.32}$$

Observing that $x_i = r_i\cos(\theta)$, Eq. (3.31) becomes:

$$r_i\cos(\theta) = Mr\cos(\theta) + \frac{D[r\cos(\theta)]\Delta z}{r^2}(\mu_E + \mu_B)$$

So the radial mapping for an infinite straight wire carrying a current I and charge per unit length λ reads:

$$r_i = Mr + \frac{D\Delta z}{r}(\mu_E + \mu_B) \tag{3.33}$$

Caustics arise when $\frac{dr_i}{dr} = 0$:

$$\frac{dr_i}{dr} = M - \frac{D\Delta z}{r^2}(\mu_E + \mu_B) \tag{3.34}$$

which equals zero when

$$r^* = \sqrt{\frac{D\Delta z(\mu_E + \mu_B)}{M}} \tag{3.35}$$

The proton void radius is then the value of r_i when $r = r^*$:

$$\begin{aligned} r_i(r^*) &= M\sqrt{\frac{D\Delta z(\mu_E + \mu_B)}{M}} + \frac{D\Delta z}{\sqrt{\frac{D\Delta z(\mu_E+\mu_B)}{M}}}(\mu_E + \mu_B) \\ &= \sqrt{MD\Delta z(\mu_E + \mu_B)} + \sqrt{MD\Delta z(\mu_E + \mu_B)} \end{aligned}$$

So the void radius in the image plane can be expressed in terms of the electromagnetic field geometry and magnitude, the system magnification and the proton energy:

$$r_v = 2\sqrt{MD\Delta z(\mu_E + \mu_B)} \tag{3.36}$$

Correcting for magnification, this means that in the object plane:

$$r_M = r_i(r^*)/M = 2\sqrt{\frac{D\Delta z(\mu_E + \mu_B)}{M}} \tag{3.37}$$

Eq. (3.36) represents the major result of this section. It implies that $r_v \propto I^{\frac{1}{2}}$ and $r_v \propto E_p^{-\frac{1}{4}}$ for a proton beam passing through the magnetic field at the top a wire loop, whilst $r_v \propto \lambda^{\frac{1}{2}}$ and $r_v \propto E_p^{-\frac{1}{2}}$ in the electric field around a charged wire. This is expected because proton deflection should scale with the velocity v based on the Lorentz force and the amount of time the proton spends in the field. The electric field term scales as $1/v^2$ while the magnetic field term scales as $1/v$. For both an electric and magnetic field, the void radius is no longer a power law in E_p, so electric field effects will cause a deviation from the $r_v \propto E_p^{-\frac{1}{4}}$ law. In Sec. 5.3.8, the different scalings of r_v with E_p will be used to try to map the evolution of electric and magnetic fields in capacitor coil targets.

Part III

Experiments and Analysis

Chapter 4

Laser-Driven Radiofrequency Electromagnetic Pulses

4.1 Outline of Vulcan 2017 experiment

In this chapter I will present results from an EMP experiment conducted at the Central Laser Facility using the Vulcan laser. EMP measurements were taken from outside the target chamber for laser intensities between 10^{17} Wcm^{-2} and 10^{19} Wcm^{-2}. Previous work suggests that target charging and antenna emission through the target holder is primarily responsible for GHz EMP [58, 140]. Proton probing of laser-induced discharge currents show electric fields and charge pulses consistent with target charging models [97, 147], while experiments with optically-levitated targets highlight the importance of the target holder to the GHz emission process [144]. Expensive large-scale and multi-scale simulations show reasonable agreement with the accumulated charge [58] and peak electric field [61] measured experimentally, however a simple model that quantitatively links target charging physics to the emission of a dipole radiation field is desirable. On Vulcan, the aim was to extend our understanding of EMP emission to higher energies and longer pulse durations than those presented in Poyé *et al.* [142] and [140]. Laser and target parameters were adjusted to probe how laser charging and discharging processes affect EMP. Measurements of GHz EMP emission were taken alongside THz EMP measurements that are summarized in Liao *et al.* [110] and [109]. The second part of this chapter contains an updated antenna model described in Minenna *et al.* [124] and links EMP measurements directly to target charging physics. Major advantages of this model are that it provides a phenomenological explanation for the Vulcan experimental results and enables the relatively easy estimation of EMP fields produced at laser facilities around the world.

4.1.1 Experiment Set-Up

The EMP study used a single short-pulse beam from Vulcan Target Area West [64] to irradiate foil targets. Assuming a 60% throughput, on-target laser energies were varied from 0.7 to 70 J with a variable pulse duration of 1-23 ps. Vulcan is a Nd:glass laser with a wavelength of 1053 nm. The beam was p-polarized with an incidence angle of 30° to target normal and the focal spot size was fixed at 3.5 μm, giving a maximum laser focal intensity of $I_L \sim 2 \times 10^{19}$ Wcm^{-2}.

Three electromagnetic probes were used to monitor EMP during the experiment, as shown in Fig. 4.1. The probes were placed in air, behind glass windows, $r \approx 1.5$ m radially from target chamber centre (TCC). A B-dot and D-dot probe were placed on the East side of the chamber, 0° vertically from TCC; a second B-dot probe was placed opposite, on the West side of the chamber, 35° above the horizontal plane. The B-dot probes were Prodyn B-24 detectors [50] connected to BIB-100G matching boxes, with the East probe oriented to measure the vertical component of the magnetic field and the West probe oriented at 35° to the vertical. The D-dot was a Prodyn FD-5C model [125] designed for ground plane measurements and was sensitive to the radial electric field. To reduce the amount of EMP noise pick-up, each probe was connected to an oscilloscope positioned 10 m away from the target chamber. The oscilloscope was a Tektronix DPO 71254C model with 12.5 GHz analog bandwidth sampling at 100 GS/s.

Fig. 4.1 also shows an electron spectrometer positioned directly in line with the laser, facing the target rear surface. The spectrometer was sensitive to electrons with energy between 0.5 MeV and 10 MeV, allowing us to compare the quantity and energy of escaping electrons with the EMP amplitude. It is important to note that the real target chamber contained numerous other diagnostics and metallic objects besides those pictured in Fig. 4.1, complicating the spectral EMP signal.

Standard laser targets consisted of a 3×8 mm^2, 100 μm-thick Cu foil mounted on a 2.9 mm-diameter cylindrical stalk. Several stalks were placed along the circumference of a rotating Al wheel to allow multiple laser shots per vacuum chamber pump-down. As shown in Fig. 4.2, the stalks had a total height of 25 mm, with $\sim$ 23 mm vertical distance between the laser focus and target wheel. Stalks were composed either of Al 6031 alloy or an acrylic resin called VeroBlackPlus RGD875, which I will refer to simply as CH.

4.2 Experimental Results

Strong EMP signals were detected throughout the experiment using photodiodes and conducting probes. Desktop computers provided qualitative measurements of

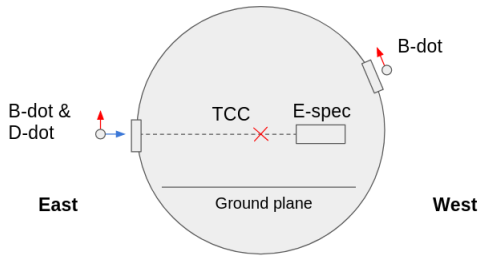

Figure 4.1: Simplified diagram of the experiment, viewed from the north side of the Vulcan target chamber. A short-pulse beam was focused onto Cu foils at target chamber centre (TCC). The locations of the probe heads are marked with circles, approximately $r = 1.5$ m from TCC. The two red arrows represent measurement axes for the B-dot probes, with the West probe oriented at 35° to the vertical. The blue arrow that is pointing towards TCC represents the measurement axis of the D-dot probe.

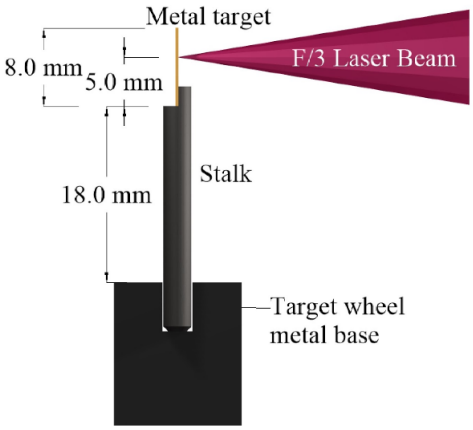

Figure 4.2: Standard target design [27]. The cylindrical stalk is made from either metal or plastic with a total height of 25 mm. The height of laser focus above the target wheel is 23 mm.

the EMP amplitude because they were knocked out during shots with Al stalks at a distance of several metres from the target chamber. A typical voltage waveform from the B-dot East probe can be seen in Fig. 4.3. EMP waveforms are characterised by a sharp initial rise and slow exponential decay over hundreds of nanoseconds. The sharp peak is caused by a spherical electromagnetic wave that is produced by charge separation in the target, then subsequent oscillations occur at decreasing amplitude as the first wave reflects off conducting surfaces inside the chamber and a current oscillates across the target stalk and along the chamber walls. A video of the antenna emission process can be found in the Supplementary Material of Poyé *et al.* [142].

Taking the time-dependent Fourier transform of probe signals allows us to isolate potential sources of noise as well as different sources of EMP. A sample spectrogram of voltage data from the D-dot East probe can be seen in Fig. 4.4. The raw data was recorded during a laser shot on a Cu foil mounted on an Al stalk and shows a broadband EMP signal stretching up to $\nu \sim 7$ GHz. Strong resonances at GHz-frequency likely come from dipole antenna emission emitted from cm-scale objects like the target stalk [58], while resonances below 0.1 GHz correspond to chamber proper modes [122].

Systematic errors in the EMP measurements are dominated by cable losses because the oscilloscopes were placed far away from the interaction, in a separate room, to help shield them from EMP noise. The total cable length from probe to oscilloscope was 20 ± 2 m. This large error is attributed to an unfortunate lapse in record-keeping during the experiment. The variation in the cable attenuation for 18 and 22 metres of cable can be seen in Fig. 4.5. A $\pm 10\%$ error in the EMP measurements can be expected based on cable length uncertainties.

Before voltage signals from conducting probes are integrated to produce the electric or magnetic field, they must be processed to account for cable attenuation, the probe transmission function and sources of noise. First, a rectangular bandpass filter was applied with a minimum frequency of 3.3 MHz to remove oscilloscope noise that prevented the integrated signal from returning to zero after the EMP pulse had ended. A maximum frequency of 3 GHz was chosen because the coaxial cables were too long to transmit reliable measurements above this frequency[1]. After the data had been frequency filtered, we accounted for the probe transmission function using the probe effective area as described in Sec. 3.1. Finally, the frequency-dependent cable attenuation was corrected for using a Bode magnitude plot for RG223 coaxial cable taken from the manufacturer [7].

[1]For 20 m of RG223 coaxial cable, signal attenuation is ~ -20 dB at 2 GHz and increases almost linearly for higher frequencies (see Fig. 4.5). When an attenuation correction was applied for $\nu > 3$ GHz, the EMP waveform was significantly distorted by amplified high-frequency noise.

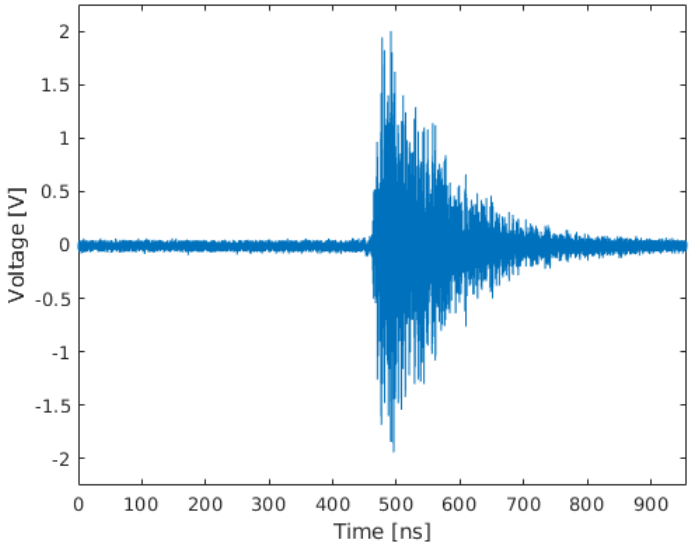

Figure 4.3: Voltage waveform from the B-dot East probe with 70 J on-target energy focused to an intensity of $\sim 2 \times 10^{19}$ Wcm^{-2}. The laser target was a standard Cu foil on CH stalk.

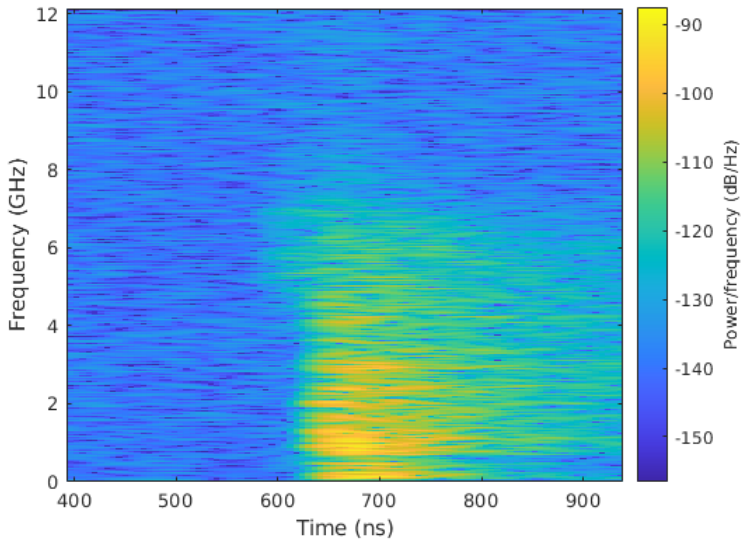

Figure 4.4: Spectrogram of voltage data from the D-dot (East) probe taken during a shot on a Cu foil mounted on an Al stalk. A Blackman-Harris window function is used to minimise spectral leakage.

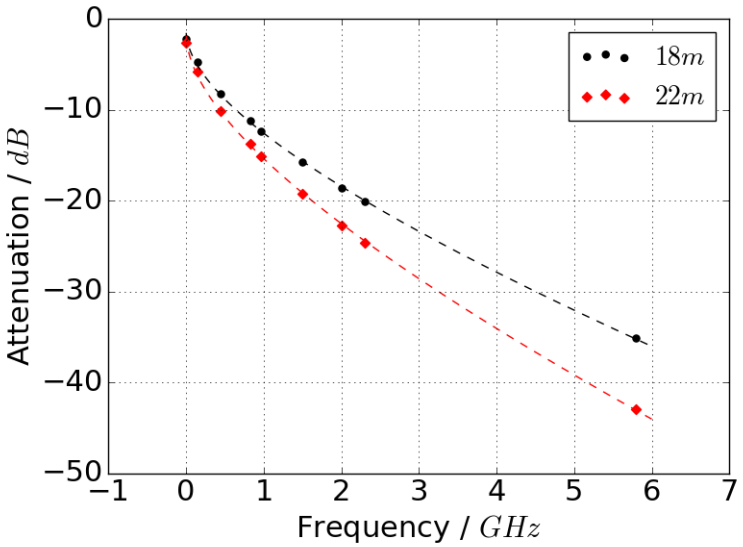

Figure 4.5: Frequency-dependent signal attenuation for RG223 cables of length 18 m (black circles) and 22 m (red diamonds). The dashed lines are attenuation curves that have been fitted to attenuation data from the manufacturer [7]. The fitted curves are composed of dielectric and conductor loss terms in the form: $A(f) = \alpha f + \beta\sqrt{f}$, for α and β arbitrary constants.

Integration of the probe voltage signal yields the electric or magnetic field strength at the probe head. Laser shots focused to an intensity of $\sim 1 \times 10^{19}$ Wcm^{-2} on Cu foils with Al mounts produced a strong EMP signal, with maximum amplitudes of $E = 300$ kVm^{-1} and $B = 0.5$ mT measured ~ 1.5 m from the target.

4.2.1 EMP variation with laser parameters

This section describes how the measured EMP amplitude varied with different laser parameters. Each parameter was varied independently, so all other laser parameters were kept fixed as far as possible. Variation in the on-target laser energy is accounted for in figures 4.7 and 4.8 by normalizing the EMP amplitude with respect to laser energy using the relation observed in Fig. 4.6b.

Laser Energy

The relationship between laser energy and EMP emission was examined by increasing the on-target laser energy from 0.7 to 70 J. Fig. 4.6 shows that the maximum electric and magnetic field recorded by the conducting probes grew roughly as the laser energy to the half power.

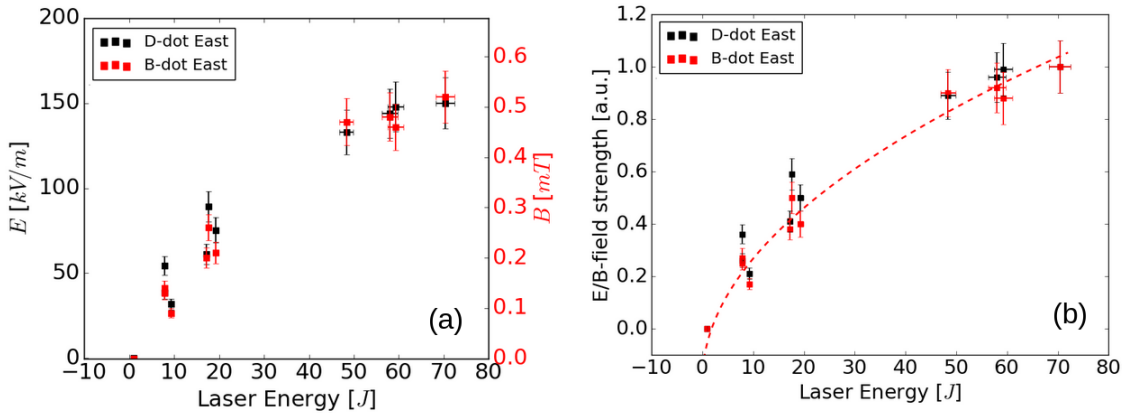

Figure 4.6: (a) Peak electric and magnetic field strength plotted as a function of laser energy. (b) Normalized peak electric and magnetic field strength plotted as a function of laser energy. The dashed (red) line represents a non-linear least squares fit to the B-dot and D-dot data using a square root function of laser energy. Measurements were taken using the D-dot and B-dot East probes.

Pulse Duration

The laser pulse duration was increased gradually from 1.4 ps up to a maximum of 23 ps and EMP measurements were compared with supplementary data from the electron spectrometer. Results shown in Fig. 4.7 indicate that the EMP field and number of emitted electrons generally decreases with increasing laser pulse duration from 2 ps up to 23 ps. Results have been scaled to reflect the EMP dependence on laser energy from Fig. 4.6b.

Pre-pulse Delay

The variation of EMP energy with pre-pulse delay is presented in Figure 4.8a. A modified Mach-Zender interferometer was used to delay the main pulse with respect to the pre-pulse by lengthening one of the interferometer arms, then a series of polarisers and wave plates was used to control the energy ratio between the pre-pulse and main pulse. The received pre-pulse energy was consistent at $\sim$ 0.6 J, while the main beam energy fluctuated between 55 and 67 J. Laser focal intensity was maintained at $I \sim 5 \times 10^{18}$ Wcm^{-2}. The maximum EMP field is higher for shots with a longer delay between the laser pre-pulse and main drive.

Laser Defocus

Fig. 4.8b shows data from a laser defocus scan, where the laser focal spot diameter was varied by driving the focusing parabola normal to the target surface. Negative defocus corresponds to the laser focusing in front of the target. While the EMP energy is higher when the laser is more tightly focused, significant scatter makes it

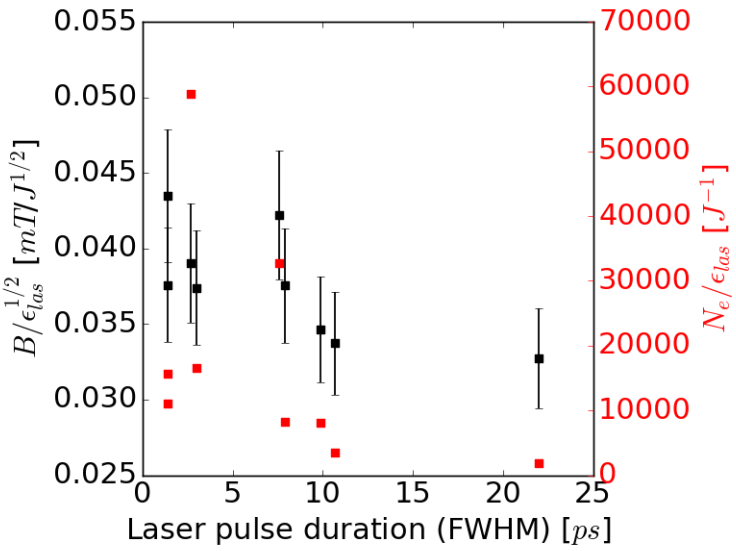

Figure 4.7: Peak magnetic field strength divided by the square root of on-target energy is plotted in black for a variety of laser pulse durations (B-dot East probe). Red squares are the number of emitted electrons measured by the electron spectrometer divided by the on-target laser energy. B-dot data is divided by the square root of the laser energy to account for the energy-dependence of EMP presented in Fig. 4.6b. The laser intensity ranged from 8.7×10^{17} Wcm^{-2} to 2.4×10^{18} Wcm^{-2} on these shots. The y-axis scale for the magnetic field should be read as millitesla per $J^{1/2}$.

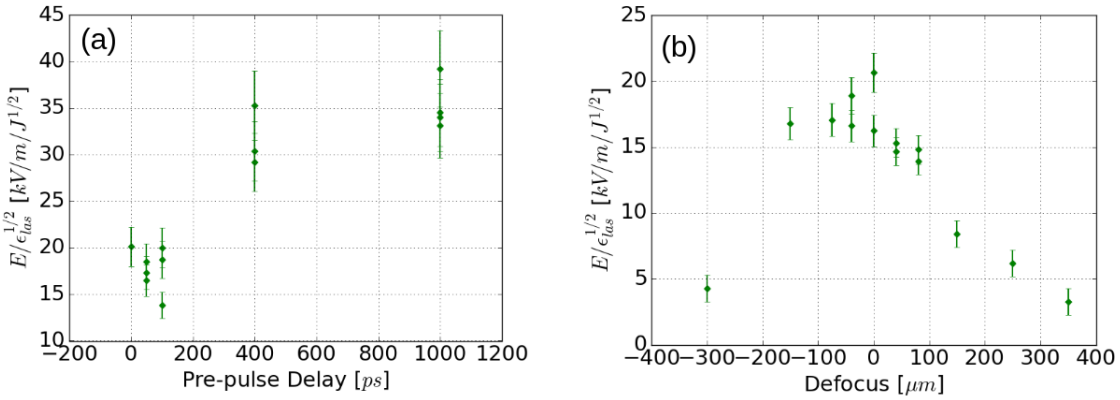

Figure 4.8: Normalized peak electric field strength plotted against (a) Laser pre-pulse delay (b) Laser defocus. Horizontal errors in pre-pulse delay and defocus are too small for this scale. The y-axis scales should be read as kilovolts per metre per $J^{1/2}$.

hard to identify whether the distribution has a single maximum or multiple maxima.

Discussion of EMP scaling with laser parameters

The measured EMP scaling with laser energy, pulse duration, pre-pulse delay and defocus is in qualitative agreement with the expectation based on laser absorption physics. A square root relationship between the maximum EMP field and laser energy suggests that EMP energy is proportional to on-target laser energy for $I_L \approx 10^{17}$ Wcm^{-2} to 10^{19} Wcm^{-2} [27]. A more energetic laser pulse will produce more hot electrons and the higher intensity implies the hot electron temperature will be higher as well. This will increase the amount of charge that can accumulate on the target and produce a stronger EMP.

Increasing the laser pulse duration has the compound effect of increasing the duration of the discharge current pulse and reducing the laser intensity. Longer current pulses will radiate less efficiently, though the effect is only significant for ns-duration pulses. The downward trend observed in Fig. 4.7 is probably due to a reduced hot electron temperature from less intense laser interactions [179].

Fig. 4.8a suggests that the greater the delay between the pre-pulse and main drive, the greater the EMP energy. Since the pre-pulse and main drive were both delivered via the same beamline, we attribute the change in EMP to the formation of a pre-plasma on the front of the target [121]. Scott *et al.* have shown that laser absorption is a strong function of plasma density and scale length [157] which are both dependent on the pre-pulse delay. The longer the delay between the pre-pulse and main drive, the greater the pre-plasma expansion and the greater the transfer of laser energy to hot electrons that can escape the target.

Fig. 4.8b suggests that the EMP field is generally stronger for more tightly focused laser pulses, however the data is too noisy to define an optimal defocus for EMP emission. A smaller focal spot will increase the on-target laser intensity, but it will also reduce the area over which electrons are accelerated in the laser field. A smaller focal spot therefore produces fewer hot electrons overall. As the focal spot increases and the laser intensity decreases, more electrons will be produced but at lower energy. Since the hot electron temperature T_h is smaller at lower laser intensities, the thermal barrier ϕ_{th} is also reduced. The electrostatic potential ϕ_E is not directly related to the laser intensity, so it will begin to dominate the target potential barrier. As the intensity continues to drop, the hot electron distribution cools and ϕ_E causes the target charge to fall. It is therefore possible that there exists an optimum focal spot diameter for target charging that is larger than the best focus of the laser optical system. This is consistent with ChoCoLaT simulations of target charging (see Fig. 5 in Ref. [43]). If the optimal defocus is non-zero, it should produce local maxima at positive and negative values of the defocus. The influence

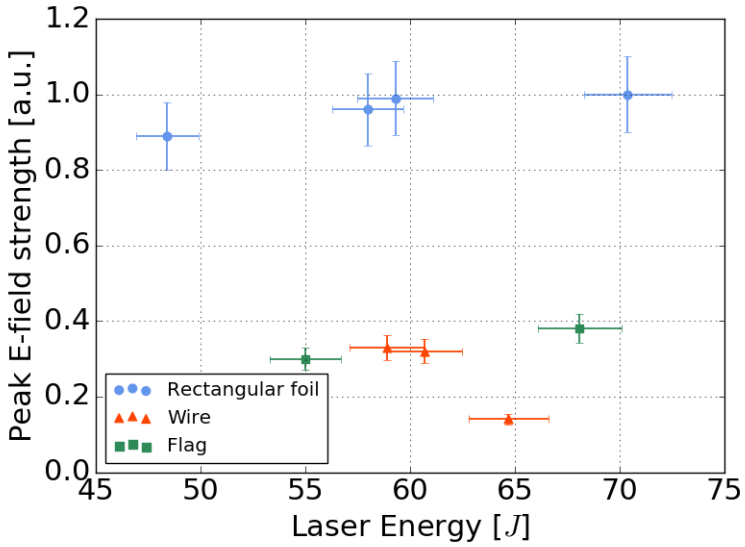

Figure 4.9: Normalized peak electric field strength plotted as a function of laser energy for wire, flag and rectangular foil targets (D-dot probe East). Targets with a smaller surface area emit much weaker EMP. Laser focal intensity ranges from 8×10^{17} Wcm^{-2} to 2×10^{19} Wcm^{-2} on these shots. Notice how changing the wire diameter may have led to a deviation from the relationship between EMP and on-target laser energy established in Fig. 4.6.

of laser defocus on hot electron emission and the x-ray spectrum are explored further by Armstrong *et al.* in Ref. [6].

4.2.2 EMP variation with target parameters

Target Size

Multiple authors have observed that target surface area can have a significant impact on electron and EMP emission from the target [38, 61, 58]. Our surface area study featured three different target designs, each made from Cu and mounted on CH stalks. Rectangular foils (3×8 mm^2), square flag foils (0.5×0.5 mm^2 and 1×1 mm^2) and wire targets (25 μm, 50 μm, 100 μm diameter) were used. Fig. 4.9 shows that EMP emission was substantially reduced on shots involving smaller targets, with the lowest fields observed for 25 μm-diameter wires.

As laser-accelerated hot electrons are ejected from the target surface, they leave behind a positive potential that spreads over the target and prevents less energetic electrons from escaping. Targets with a smaller surface area confine this positive potential and so enhance the electric fields that keep electrons in the target. In their 2009 report, Eder *et al.* [61] observed that larger targets continued to produce more escaping electrons and a stronger EMP until they reached 50 mm in size. This suggests that multi-MeV electrons persist in the target for at least 20 ps – ten

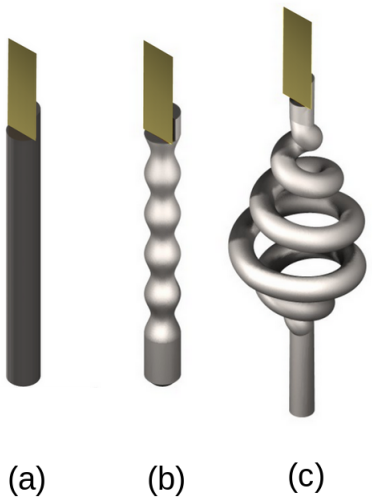

Figure 4.10: The three different stalk designs: (a) Standard cylindrical geometry (b) Sinusoidally modulated stalk with the same maximum cross-section as the standard cylinder (c) Spiral stalk design with an identical diameter to (a).

times longer than the laser pulse duration of 2 ps. Our study extends these findings to the Vulcan laser system, demonstrating that collisional cooling and emission of suprathermal electrons takes place on timescales at least 5× longer than the laser pulse duration. We also find that the peak electric field strength of the EMP does not scale linearly with target surface area or lateral size.

Although smaller targets produce reduced EMP fields, they also change the conditions of the laser-matter interaction. For example, electrons heated by the laser can be guided along the target surface and produce fringing electric fields that will alter the accelerating properties of the electrostatic sheath [170]. It is therefore desirable to search for a means of reducing EMP emission independent of the target size.

Target Holder

The major source of laser-driven EMP at GHz frequencies is thought to be dipole antenna emission as a discharge current oscillates between the laser target and the nearest ground [43]. If true, this suggests that changing the inductance, impedance or capacitance of the target mount could significantly modify the emitted EMP. The target mounting system for the Vulcan laser consists of a target on top of a thin stalk that is positioned along the circumference of a rotating metallic target wheel. By changing the material and geometry of the stalk that supports the laser target, one can study the influence of the target mount on EMP. In switching from Al to CH stalks, a factor 2 reduction in the peak electric and magnetic fields was observed. This meant that computers placed outside of the target chamber, ~ 3 m

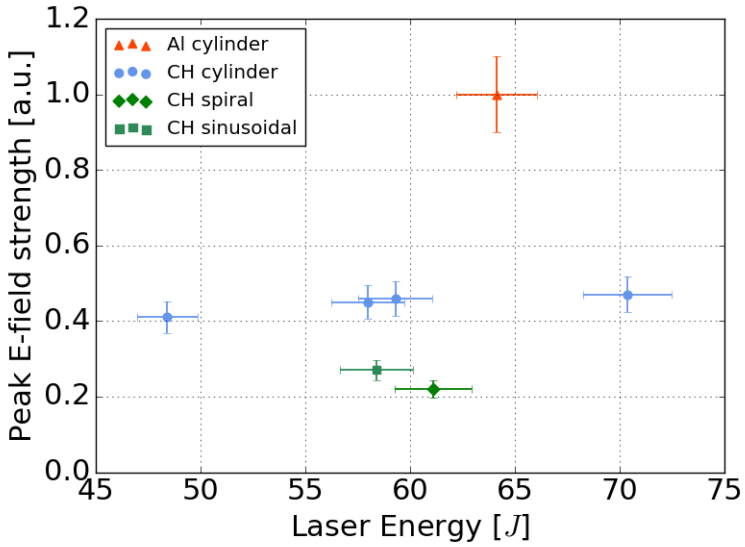

Figure 4.11: Normalized peak electric field strength plotted as a function of laser energy for Al and CH stalks with cylindrical, spiral and sinusoidal geometries. The EMP field is very sensitive to stalk material and geometry. Data is taken from the D-dot East probe and presented as a fraction of the peak electric field for the Al stalk. Laser focal intensity varies between 8×10^{17} Wcm^{-2} and 2×10^{19}Wcm^{-2} for these shots.

from TCC, were no longer knocked out by the EMP. Three different stalk geometries were investigated, as illustrated in Fig. 4.10. Fig. 4.11 summarizes experimental results for the modified stalks. The spiral stalk design was most effective, with a factor 4.5 reduction in the peak electric field measured by the D-dot East probe.

Analysis of raw Fourier spectra from the B-dot and D-dot probes reveals high frequency resonances (> 0.7 GHz) for both CH and Al cylindrical stalks, although they are broader and more energetic in the case of the metal stalks. The CH spiral stalk, by contrast, showed much reduced activity at GHz frequency. Data from the electron spectrometer shows that the number and temperature of ejected electrons did not change significantly for shots involving the modified stalks [27]. This suggests the reduction in EMP is independent of the target charging process.

4.2.3 PIC and EM wave simulations

To test if stalk geometry measurements were consistent with changes in the antenna properties of the target holder, F. Consoli from ENEA ran combined PIC and electromagnetic wave simulations of EMP emission. In these simulations, a target holder was placed at the centre of a cuboidal chamber, with 5 nC of hot electrons emitted in a cone from the holder tip. A PIC code was used to model electron beam transport and COMSOL multiphysics [41] was used to calculate chamber electromagnetic fields as the beam propagated in vacuum and struck the chamber wall.

Electron beam properties were fixed and EMP fields were detected at three separate locations inside the simulation box. The target holder material was taken to be either a perfect electrical conductor or Teflon plastic and the holder geometry was matched to the three designs in Fig. 4.10. As observed in the Vulcan experiment, dielectric and dielectric spiral stalks reduced the EMP energy significantly versus conducting stalks. The degree of EMP reduction calculated with COMSOL was quantitatively different to experimental measurements, however. A greater than $10\times$ reduction in the EMP energy was calculated when switching from conducting to dielectric stalks and only a small additional reduction was found for the spiral stalk [28]. One possible explanation for this discrepancy could be photoionisation of the holder surface by UV or x-rays and the formation of a charged surface layer. Simulations with a half conducting and half dielectric stalk showed that EMP radiation was more intense for stalks with a shorter low-conductance path to ground.

4.3 Summary of Vulcan EMP experiment

Control and characterisation of laser-driven EMP has been achieved on the Vulcan laser by altering laser, target and holder properties. A correlation between EMP field strength and the number and energy of escaping electrons was observed. The measured scaling of EMP with different laser parameters is qualitatively consistent with models of laser absorption and electron escape. For laser intensities between 10^{17} Wcm^{-2} and 10^{19} Wcm^{-2}, the peak EMP field was found to increase as the square root of the laser energy. Significant reductions in EMP field strength were achieved by reducing the size of the laser target, switching to dielectric stalks and lengthening the non-conducting path to ground. Foil targets with transverse dimensions greater than 3 mm produced much stronger EMP fields than targets with transverse dimensions smaller than 1 mm. Experiments with different holder materials and geometries suggest that EMP is strongly related to antenna emission from the target holder. Crucially, switching from a cylindrical Al to a CH spiral stalk was shown to reduce the peak EMP electric field strength by a factor of ~ 4.5 without altering the conditions of the laser-matter interaction. PIC and EM wave simulations support experimental data that shows modified dielectric stalks reduce EMP.

4.4 Frequency-domain dipole model of EMP

Understanding the results from Sec. 4.1 requires a theoretical model that connects the physics of laser-target charging to the electromagnetic fields measured by conducting probes. Results show that EMP fields are sensitive to target size and shape,

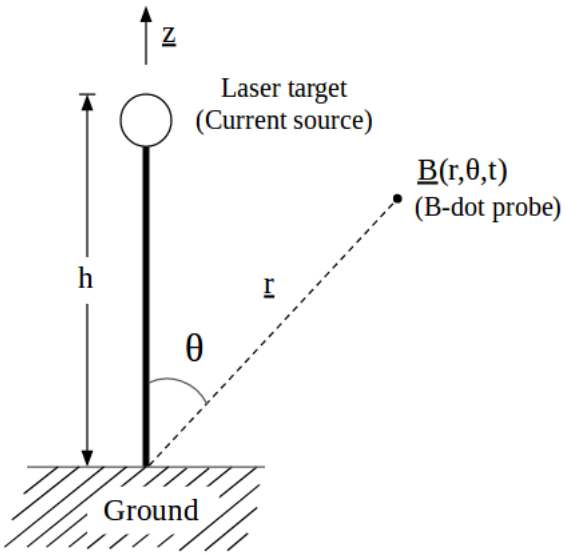

Figure 4.12: Schematic of an idealised laser target, positioned at height $z = h$ above the experimental chamber (ground). The bold vertical line represents the target holder. During a laser shot, electrons will be ejected from the target and a return current will propagate down the target holder to ground. Magnetic field measurements are made using a B-dot probe positioned in the antenna far field ($r \gg \lambda$).

so our model must also take into account basic radiative properties of the target holder. The combined target-target holder system acts as an antenna composed of a target capacitance and holder inductance. EMP emission from this system is governed by two characteristic times: the charging time of the target (electron ejection period, t_e) and the antenna time (oscillation period of the return current, τ).

In Poyé *et al.* [141] and Minenna *et al.* [124], the authors present a frequency-domain dipole antenna model that can be used either to provide order-of-magnitude estimates of the EMP magnetic flux or, reciprocally, to estimate the positive charge accumulated in a target based on magnetic field measurements. The magnetic flux is computed as a function of the total charge ejected by the laser using a classical dipole antenna model in the frequency-domain [95]. The target holder is approximated by a thin metallic wire of height h (see Fig. 4.12) and the charging time is assumed to be much less than the antenna time ($t_e \ll \tau = 4h/c$). This ensures that, after the laser pulse has ended, the target-holder system is qualitatively equivalent to a point charge $+Q$ connected to a perfect ground by a vertical wire of height h. Applying the Method of Images [95], the target-holder system is electrically equivalent to a straight wire with charge $+Q$ on one end and charge $-Q$ on the other; the ground acts as a plane of symmetry and the system operates as an oscillating electric dipole of length $2h$ (see Fig. 4.13). At time $t = 0$, both charges propagate down the wire at speed $\sim c$, reaching the ground plane at time $t = h/c$. The charges continue

until they reflect at the opposite end of the "wire", oscillating up and down at a frequency $\omega = \pi c/2h$. Radiation is emitted in a sequence of bursts, when the polarity of the current reverses and the mirror charges accelerate ($t \approx 2hn/c$, for $n \in \mathbb{Z}^+$). The assumption that the charging time is small relative to the antenna time means that the emission frequency is precisely equal to the antenna frequency and EMP radiation will be maximal. If, conversely, the charging time is large relative to the antenna time, the current pulse will form an extended profile that broadly follows the laser intensity profile (e.g. Gaussian) of temporal width $\Delta t = t_e$ and spatial width $c\Delta t \ll h$. The dipole approximation no longer applies in this case, so antenna emission will be weak and the bandwidth will be large. Long ($\sim$ ns) neutralisation pulses can be considered a constant supply of current for cm-scale target holders, producing weak EMPs in the GHz domain. This idea represents a condition for efficient EMP generation: $t_e \ll \tau$, where $\tau = 1/f_\tau$ is the time period of the emission. A simple wire holder has antenna time $\tau = 4h/c$ - holders with different shapes may have different antenna times.

A qualitative understanding of the EMP emission process can be gained by looking at the radiation from accelerating charges. The Larmor formula for the total power radiated by an accelerating, non-relativistic point charge is [146]:

$$P = \frac{|Q\ddot{z}|^2}{6\pi\epsilon_0 c^3}$$

where Q is the particle charge and $\ddot{z}$ is the particle acceleration. A dipole antenna consists of many oscillating non-relativistic charges.[2] Defining the dipole moment $d(t) = Qz(t)$ for a dipole like that in Fig. 4.13, the Larmor formula for a dipole antenna becomes:

$$P = \frac{|\ddot{d}|^2}{6\pi\epsilon_0 c^3}$$

For a point charge Q that propagates along the antenna at fixed velocity $v = c$ with no current damping or dispersion, the system will have a dipole moment $d = 2Qz(t) = 2Q(h - ct)$ as shown in Fig. 4.14. Since the second order derivative of d is identically zero, no EMP radiation is emitted. Considering instead a standing wave of frequency ω with $d = 2Q\sin(\omega t)$, the second derivative of the dipole moment is non-zero and the radiated power is equal to:

$$P(\omega) = \frac{\omega^4 Q^2 \sin^2(\omega t)}{3\pi\epsilon_0 c^3}$$

The real current distribution will not be a simple sinusoid, but this approximation

[2] Although the charge pulse propagates at speed $\sim c$ along the antenna, individual electrons in the conductor are moving non-relativistically.

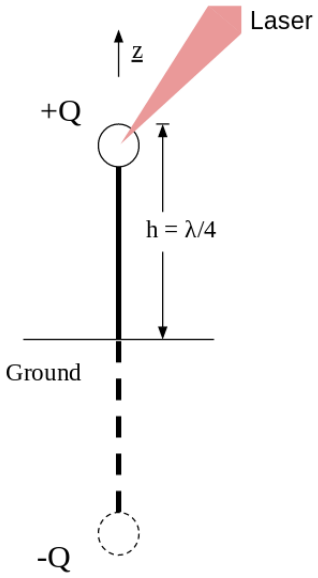

Figure 4.13: The Method of Images applied to a laser-generated charge distribution, $+Q$, connected to ground by a straight wire. We assume the laser charges the target sufficiently quickly that the mirror charges $\pm Q$ can be considered point-like. At time $t > 0$, the mirror charges travel towards each other at speed $v \sim c$, with dipole moment $d(t) = 2Q(h - ct)$.

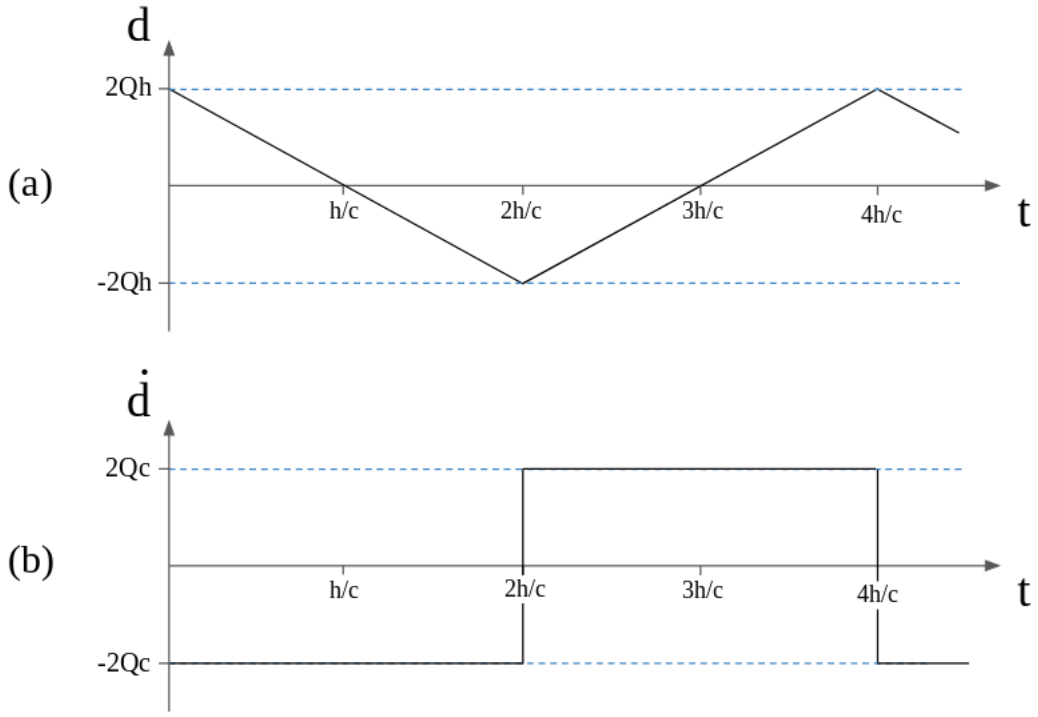

Figure 4.14: Graph of (a) the dipole moment and (b) the first derivative of the dipole moment for a pair of mirror charges $\pm Q$ moving at velocity $v = c$. There is no electromagnetic radiation because the charges are not accelerating (the second derivative of the dipole moment is identically zero).

is sufficient for a basic understanding of antenna emission.

Fig. 4.14 shows that the EMP radiation field is created at distinct intervals, when the current pulse reverses direction [43]. The duration of each EMP pulse is equal to the current pulse duration, Δt. In Fourier space, the current is concentrated at the antenna frequency with weaker emission at higher harmonics. The number of higher harmonics will depend on the precise shape of the current pulse. In practice, resistive losses quickly attenuate the current, causing the emission to last only a few oscillation periods and increasing the bandwidth of the radiation [58]. A target holder of height $h \sim 7$ cm corresponds to an oscillation frequency of 1 GHz. The majority of target holders at major laser facilities measure between 0.1-1 m in length, so antenna emission is likely to be concentrated at $\sim$ GHz frequency.

4.4.1 Antenna equation for EMP

In this section I will compute the magnetic field at an arbitrary position in the experimental chamber as a function of the total charge ejected by the laser. Target holders shaped like straight wires radiate like a ground plane monopole antenna or, equivalently, the top half of a half-wavelength dipole antenna. Therefore consider a half-wavelength antenna of total length $2h$. It is "long" (i.e. it does not satisfy $2h \ll \lambda$), so the current is not the same all the way along the length of the antenna. For simplicity, the current distribution is sinusoidal and forms a standing wave along the length of the antenna. This approximation is crude, but sufficient for an order of magnitude estimation of the maximum magnetic field. The current is defined as:

$$I(z,t) = I_0 e^{i\omega t}\cos(kz)$$

with wave number k. Then, in the far field of a dipole antenna of length $2h$, the equation for the electric field is:

$$E_\theta = \frac{-iZ_0 I(z,t)}{2\pi r}\frac{\cos(kh\cos(\theta)) - \cos(kh)}{\sin\theta}$$

For a linear half-wavelength dipole antenna, $k = k_\tau = \pi/2h$. Thus:

$$E_\theta = \frac{-iZ_0 \tilde{I_{k_\tau}}(z,t)}{2\pi r}\frac{\cos(\frac{\pi}{2}\cos(\theta))}{\sin\theta}$$

where $\tilde{I_{k_\tau}}(z,t)$ is the current evaluated for $k_\tau = \pi/2h$ and $\omega = c/4h$. Observing that $E_\theta = Z_0 H_\phi = Z_0\mu_0 B_\phi$ in the far field:

$$B_\phi = \frac{-i\mu_0 \tilde{I_{k_\tau}}(z,t)}{2\pi r}\frac{\cos(\frac{\pi}{2}\cos(\theta))}{\sin\theta}$$

At the antenna wave number k_τ (equivalently, the antenna frequency), the mag-

nitude of the magnetic field for a linear half-wavelength antenna in the far-field region is therefore

$$|\mathbf{B}_{\phi,k_\tau}(r,\theta)| = \frac{\mu_0 \left|\tilde{I}_{k_\tau}\right|}{2\pi r} \left| \frac{\cos\left((\pi/2)\cos\left(\theta\right)\right)}{\sin\theta} \right| , \tag{4.1}$$

where $\tilde{I}_k$ is the antenna current at the antenna characteristic frequency, r is the radial distance measured from the base of the antenna, θ is the angle with respect to the antenna axis and the oscillation wavelength satisfies $\lambda \ll r$.

Eq. (4.1) shows that the EMP magnetic field is directly proportional to the antenna current. Dipole emission will be maximal when the return current oscillates at the antenna characteristic frequency. The return current at the antenna frequency can be expressed as:

$$\tilde{I}_{k_\tau} = Q f_\tau \, , \tag{4.2}$$

with Q the total target charge and f_τ the antenna frequency. The target charge can be quickly estimated with the ChoCoLaTII.f90 code or some alternative model, while the antenna frequency can be inferred from the length of the target holder. For a straight wire stalk like the one in Fig. 4.12, the antenna frequency is $f_\tau = c/(4h)$. If the shape of the antenna is more complicated, it can be directly measured in a preliminary experiment at low energy.

Combining Eq. (4.1) and (4.2) for the radiation and return current yields an estimate the EMP magnetic field. This procedure can also be used in reverse to calculate the target charge based on magnetic field measurements. In Ref. [124], it is shown that the dipole model breaks down for target holders with complex geometries, although it applies well if the target holder is a thin metallic stalk with a large metallic ground.

4.4.2 The target charging time

To decide when the frequency-domain dipole model can be applied to a given experimental arrangement, one first needs to ascertain whether the target holder geometry is sufficiently close to a grounded monopole to radiate like a half-wavelength dipole and second whether the target charging time t_e is significantly shorter than the antenna characteristic time, τ.

In Ref. [124], Minenna *et al.* show that target holders shaped like straight wires, cones and spirals radiate like dipole antennas. That is, the EMP spectra for these holders contain a resonant frequency close to the dipole antenna frequency and an estimate of the peak magnetic field from Eq. (4.1) matches the measured value.

Precise measurement of the target charging time can be difficult because the

return current is measured far away from the laser focal spot, where the target holder connects to ground. A discharge current pulse will therefore be stretched as it propagates towards the ground because the target holder acts as a distributed inductance [43]. Using ChoCoLaT, it is possible to extract t_e from the output charge profile $Q(t)$. The charging time can also be calculated analytically [96] based on the average time it takes hot electrons to travel to their maximum range in the target [140, 124].

4.4.3 Discussion of the dipole antenna model

Modelling the target holder as a monopole antenna means that its radiation pattern is the same as the top half of a classical half-wavelength dipole antenna [95]. Fig. 4.15 shows the 2D radiation pattern for a half-wavelength dipole antenna, with the antenna axis directed along $\theta = 0°$. The maximum EMP power is radiated perpendicular to the base of the antenna, falling gradually to zero at the antenna axis. Naturally, these observations neglect experimental chamber effects that homogenize the field distribution over time. Once the EMP has been emitted, its wavefront will expand in vacuum until it is reflected by conducting objects or the chamber walls. After several antenna oscillations, the EMP distribution is highly structured and permeates the entire chamber [142].

Eq. (4.1) provides an explanation for why EMP was reduced on shots with spiral-shaped stalks in Sec. 4.2.2. For target holders in the form of a straight wire, the magnetic field is directly proportional to the antenna frequency and therefore inversely proportional to the stalk length h. To decrease the EMP amplitude, one can simply increase the stalk length. In Ref. [124], Minenna *et al.* demonstrate that spiral-shaped stalks emit radiation like a dipole antenna, which means that the frequency-domain model can be applied to results from the Vulcan experiment.

Combining Eq. (4.1) and Eq. (4.2) shows that the maximum EMP field strength is proportional to the accumulated target charge. EMP variation with laser and target parameters should therefore follow the predictions of target charging models like ChoCoLaT [58].

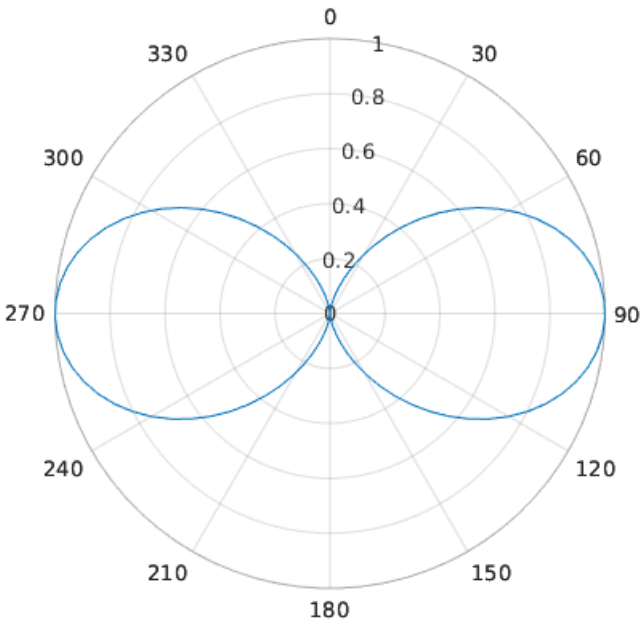

Figure 4.15: 2D radiation pattern for a half-wavelength dipole antenna, normalised to the maximum emitted power. The antenna axis is defined by $\theta = 0°$ and the radiated power is proportional to $\sin^2\theta$. Since emission is symmetric in ϕ, the 3D radiation pattern broadly resembles a torus. In the context of EMP emission, the target holder behaves like a monopole antenna attached to a perfect ground; radiation is emitted from the top half of the polar plot ($\theta < 90°$, $\theta > 270°$) and the total radiated power will be half that from the equivalent half-wavelength antenna.

Summary of dipole antenna model.
The dipole antenna model is useful for explaining some important properties of GHz EMP:

- The majority of target holders at major laser facilities measure between 0.01-0.5 m in length, so antenna emission will be concentrated at $\sim$ MHz to GHz frequency.
- EMP radiation is spherical in the antenna far-field. The field strength falls off as $1/r$ and the power as $1/r^2$.
- The EMP field strength is proportional to the accumulated target charge, so the EMP field should scale with the target charge as predicted by models like ChoCoLaT.
- Long-pulse facilities have much reduced EMP compared with short pulse facilities. Though long pulse lasers have relatively high energy and can eject similar quantities of hot electrons from the target, the charging time is $> 100\times$ longer than for short pulse lasers. Since the wavelength of the discharge current pulse is of order the antenna wavelength, long pulse lasers act as constant current sources that radiate weakly.
- EMP field strength is inversely proportional to target holder length, so spiral-shaped stalks should produce weaker EMPs than a straight wire of the same vertical height.

4.4.4 Comparison of dipole model with Vulcan data

In Ref. [124], Minenna *et al.* test the frequency-domain dipole antenna model against experimental data for laser energies between 10 mJ and 70 J. I reproduce here a comparison between the Vulcan data described in Sec. 4.1 and the dipole antenna model. Recalling the experimental set-up, laser energy was varied from $E_{\rm las} = 0.7$ J to 70 J and laser pulse duration from $t_{\rm las} = 1$ to 22 ps. The laser intensity contrast was about 10^{-8} [64]. Magnetic field measurements were taken at $r = 1.5$ m and $\theta = 90°$. The antenna frequency is $f_\tau = 2.9$ GHz based on the height of the target holder. The total charge on the target is evaluated using the ChoCoLaTII.f90 model for thin targets [143] according to the experimental laser parameters. The electron ejection time, $t_{\rm e}$, is much smaller than the antenna characteristic time, so we can apply Eq. (4.1) to get the maximum magnetic field. The maximum magnetic field (both measured and simulated) is plotted in Fig. 4.16

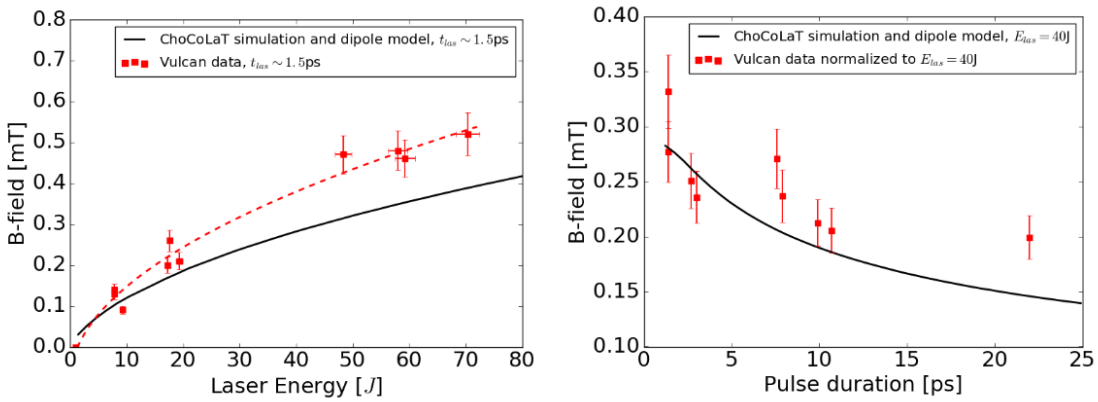

Figure 4.16: Maximum EMP magnetic field plotted as a function of the laser energy (left plot) and the laser pulse duration (right plot). Red points with error bars represent experimental data from the Vulcan laser facility and the red dashed line is a square root fit [27]. Black lines are calculated using ChoCoLaTII.f90 and Eq. (4.1) at $r = 1.5$ m and $\theta = 90°$ [124].

as a function of the laser energy E_{las} and separately as a function of the laser pulse duration, t_{las}. Since the laser energy varied significantly during the pulse duration scan, the Vulcan data has been normalized to a reference energy of 40 J using a square root fit to the energy scan data (red dashed line in the left plot of Fig 4.16). There is reasonable agreement between the measurements (red points with error bars) and our simulations (black lines).

4.5 EMP Chapter Summary

In this chapter, I have presented an experimental study of EMP produced by the Vulcan laser and shown that the results can be explained by a frequency-domain dipole antenna model. The peak EMP field was shown to be sensitive to target lateral size, laser energy and laser intensity and broadly follows scalings predicted by the ChoCoLaT target charging model. Using dielectric and spiral-shaped target holders, I show here how to significantly reduce EMP emission on high power laser systems around the world. Major results from this chapter have been summarised in Bradford *et al.* [27] and a review paper by Consoli *et al.* [43].

Chapter 5

Laser-driven solenoids: Capacitor Coil targets

5.1 Outline of Vulcan Experiment

Previous capacitor coil experiments have focused on proton deflectometry perpendicular to the loop axis [79, 153], where protons on one side of the loop are deflected radially outwards and protons on the opposite side are pinched radially inwards by the poloidal magnetic field. In Part II Sec. 3.4.3, it was shown that these experiments produce distinctive teardrop-shaped proton voids, with a width proportional to the square root of the loop current [79]. It is difficult to extract a definitive measurement of the magnetic field, however, because the void width is also affected by electric fields in the target (see Part II Sec. 3.4.4). Breaking the degeneracy of the electric and magnetic fields is essential when assessing the suitability of capacitor coil targets for magnetized high energy density experiments. To reliably quantify the magnetic field strength in a capacitor coil target, we require monoenergetic proton images of the loop at different energies, or proton probing from multiple directions.

Here, proton probing of a capacitor coil target along two axes is presented. Fig. 5.1 shows RCF data parallel and perpendicular to the axis of a capacitor coil loop. In the perpendicular orientation, an inverted teardrop is formed as protons are deflected radially away from the top of the loop where the wire current is directed out of the page and the magnetic field is oriented anticlockwise. Towards the bottom of the loop, protons are pinched radially inwards because the wire current is directed into the page and the magnetic field is clockwise. The proton beam was centred lower on the target in the parallel orientation, so both the wire loop and capacitor coil plates are clearly visible. Also notice that a Au grid has been interposed between the proton source and capacitor coil, leaving a mesh imprint in the beam that is warped by non-uniform electromagnetic fields. An expanding plate plasma can be

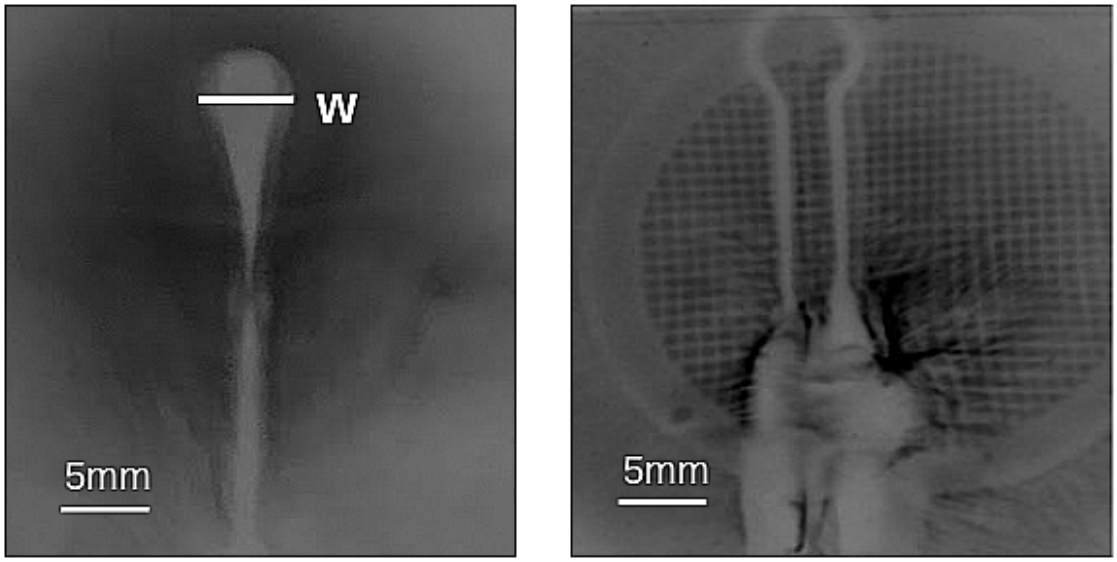

Figure 5.1: LEFT: Sample proton radiograph taken perpendicular to the axis of a 2 mm-diameter wire loop with $E_p = 7.3 \pm 0.05$ MeV protons. The void width, w, is proportional to the square root of the current flowing in the coil loop [79], though w is also affected by electric fields. RIGHT: Sample proton radiograph taken parallel to the axis of a 1 mm-diameter wire loop with $E_p = 6.5 \pm 0.07$ MeV protons. Notice how the outline of a Au grid has been imprinted in the proton beam as a fiducial. Each RCF image has a magnification of $M \approx 7$, so a distance of 5 mm in the detector plane (indicated above) equates to 0.7 mm in the coil plane.

seen in the lower half of the parallel image and there are caustics caused by electric potentials.

The combination of proton deflectometry parallel and perpendicular to the loop axis allows one to differentiate between electric and magnetic fields because the field geometry is different in each orientation. One can check that the electric and magnetic fields required to reproduce an RCF image along one axis is consistent with a different image taken at 90° to the first. Ultimately, this allows the magnetic field evolution and dependence on target parameters such as loop diameter to be characterised.

5.2 Experimental Set-up

Our experiment was conducted on the Vulcan Target Area West (TAW) laser system at the Central Laser Facility. Three long pulse beams were used to drive the capacitor coil with a combined energy of $E_{las} \sim 550$ J and a peak laser intensity of $I_L \sim 5 \times 10^{15}$ Wcm^{-2}. The long pulse beams had a supergaussian intensity profile with 0.9 ns FWHM, a rise time of 0.2 ns and 1.1 ns footprint. The beginning of laser drive is defined at the leading edge of this intensity profile, accurate to approximately ±50 ps. Two picosecond-duration beams at $E_{las} \sim 80$ J were used for

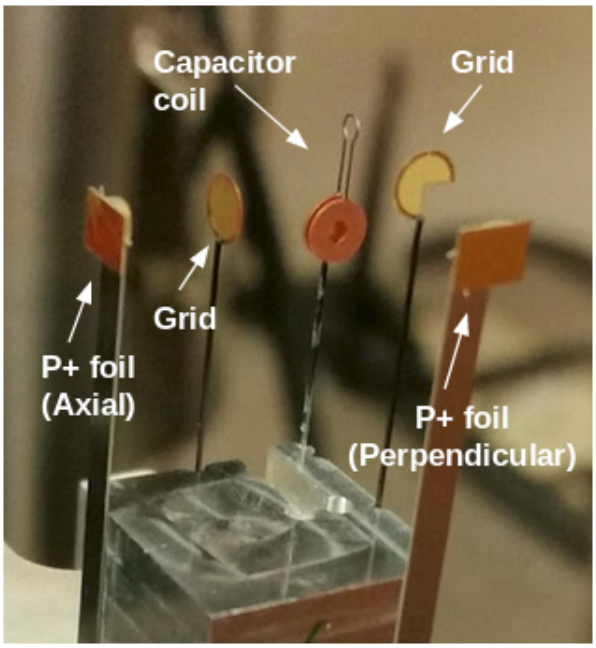

Figure 5.2: Photograph of full capacitor coil target assembly with two proton foils and Au grids. Two rectangular Au foils of 40 μm thickness with 5 μm Au shields were used for TNSA proton radiography. Between the proton foils and the capacitor coil, two Au grids were installed to act as visual references in the proton images. RCF stacks were positioned 70 mm behind the target to detect the protons along two axes.

orthogonal target normal sheath acceleration (TNSA) proton radiography [121]. All laser beams had wavelengths in the infrared with $\lambda = 1053$ nm. Fig. 5.2 shows the full target assembly, with a capacitor coil target, two grids and two proton foils attached to an Al block. A schematic representation of the same assembly can be found in Fig. 5.3. The capacitor coil targets consisted of two 3 mm-diameter, 250 μm-thick Cu plates separated by 500 μm and connected by a 100 μm-thick loop of Cu wire. The wire forming the circular loop had a square cross-section and was joined to the topmost surface of the plates using a conducting adhesive. The front plate contained a 1 mm diameter hole at the centre to allow the drive lasers access to the rear plate, while a 10 μm-thick plastic coating was applied to the rear plate to enhance the non-linear acceleration of hot electrons [82]. Targets were laser-machined to ensure high reproducibility and each was supported by a single carbon fibre stalk attached to the rear plate. TNSA proton beams accelerated off the rear surface of the proton foils passed through Au grids that imprinted a mesh structure into the beam as a visual reference. We fielded two grid designs with 300 lines per inch and 600 lines per inch. RCF stacks were then positioned behind the target to detect protons with energies between 1.2 ± 0.02 MeV and 14 ± 0.02 MeV. The proton foil to capacitor coil distance was 11.82 mm, while the capacitor coil to RCF distance was 70 ± 5 mm with a magnification of $M \approx 7$.

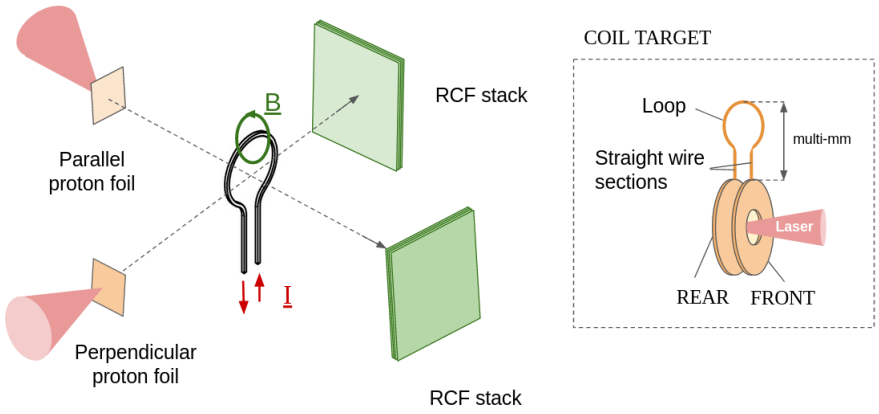

Figure 5.3: Schematic representation of the dual-axis experiment. Two Cu foils were placed orthogonally and irradiated with ps-duration lasers, firing TNSA proton beams across the capacitor-coil target (plates not shown) and onto the RCF detectors. Cu grids were interposed between the proton foil and the capacitor-coil on several shots in order to imprint a mesh fiducial into the proton images. The loop current I and corresponding magnetic field B are indicated with arrows in red and green, while the dashed lines represent the two orthogonal axes of the proton beams. Spatial dimensions are grossly exaggerated in this image. Inset on the right-hand side is a diagram of the coil target. Underneath the wire loop are two straight wire sections that connect the front and rear plates together. The rear plate was supported by an insulating rod that separated the target from the ground.

A radiation-hardened RB-230 B-dot probe [148] was also positioned as an independent measure of the coil magnetic field. The probe was placed 52 mm vertically above the wire coil, with the probe axis parallel to the coil axis for maximum sensitivity. It was connected to a BIB-100G balun to ensure an unbalanced symmetrized signal [148]. The balun and oscilloscope were kept in a Faraday cage to isolate them from EMP noise. The oscilloscope was a Tektronix DPO 71254C model with 12.5 GHz analog bandwidth, sampling at 20 GS/s (i.e. 10 ps/pt resolution).

Fig. 5.4 shows the proton energy absorption for Stack Design 1 calculated using D. Carroll's RCF response curve builder in Matlab [123]. The code calculates the RCF response curves from SRIM look-up tables [187]. Stack Design 1 consisted of a 15 μm Al shield, followed by 6 layers of HDV2 film and 6 layers of EBT3 film. Final layers of 15 μm Al and 1.5 mm Fe were used to help shield the film from ionizing sources around the chamber. The width of the peaks in Fig. 5.4a and Fig. 5.4b show that blurring is worst in RCF layers 1-3, which absorb protons over a wide range of energies and probe the target at significantly different times. The approximate proton time of flight corresponding to each layer of RCF is given in panel (c).

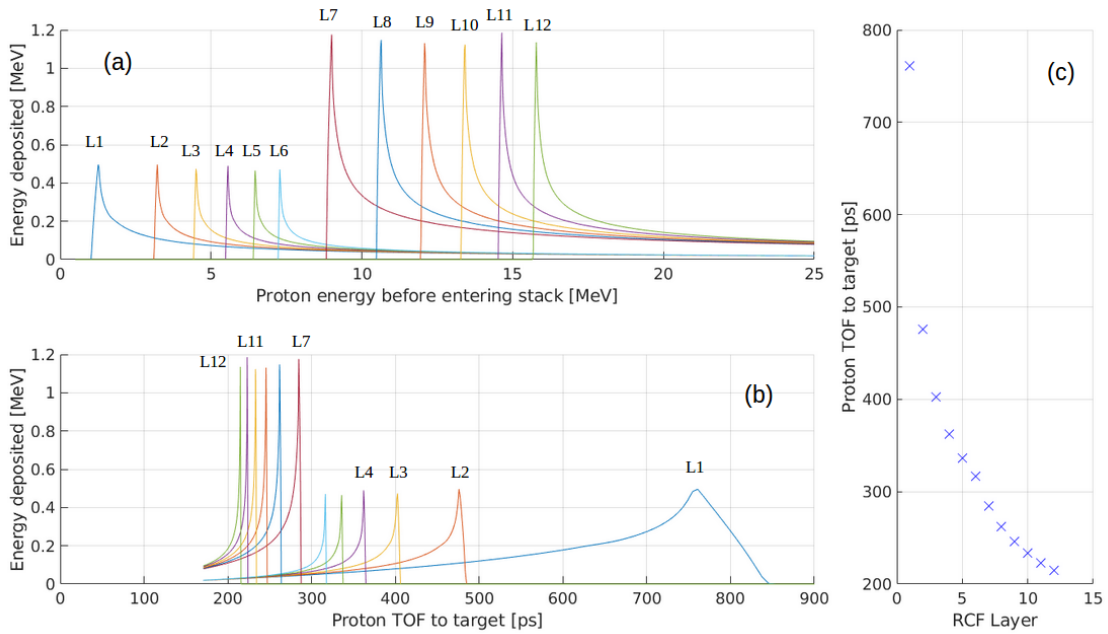

Figure 5.4: Calculated RCF response for Stack Design 1 (6×HDV2, 6×EBT3): (a) RCF response curves - the amount of energy deposited in the RCF active layer for a range of different proton energies (b) Energy deposited in each RCF layer as a function of proton probing time (c) The target probing time for protons that are absorbed in each layer.

5.3 Proton Radiography

The whole problem of proton radiography consists in identifying what strength and distribution of electromagnetic field could produce the type of radiographs seen in Fig. 5.1. In Ref. [104], Kugland *et al.* demonstrated that *line-integrated* magnetic field measurements can be inferred from experimental proton radiographs by inverting a 2D Poisson equation. This inversion method is valid for point-like proton sources in the limit of small proton deflections, though Kasim *et al.* [98] have extended Kugland's results to the regime of large proton deflections using techniques from computational geometry. The image inversion techniques detailed in Ref. [83, 98, 104] cannot be applied to the case of capacitor coil radiographs because (i) collisional stopping in the coil and caustic formation means that the proton source-image mapping is not injective and (ii) strong electric fields in the target (see Sec. 5.3.4) mean that electric and magnetic field measurements are degenerate and require careful separation. In this thesis, I have elected to use an analytic model combined with ray-tracing simulations to extract measurements of the magnetic field strength and geometry in capacitor coils. First, an analytic model is used to estimate the coil magnetic field based on the width of the teardrop-shaped caustic observed in perpendicular radiographs. The stronger the wire current, the stronger the magnetic field and the wider the caustic feature. Later, particle-in-cell simulations are used

to make these estimates more precise and break the degeneracy of the electric and magnetic fields. Future work may benefit from machine learning algorithms, which can reproduce 3D magnetic field structures from simulated radiographic data with errors of $\sim 5\%$ [37].

5.3.1 Analytic method for extracting the magnetic field

In Sec. 3.4.3, I derived an expression for the radius of the caustic void that is formed when a proton beam passes through the magnetic field of a current-carrying wire. It was based on a paraxial mapping between a proton in the source plane and its image in the detector plane. Approximating a capacitor coil B-field using the magnetic field from an infinite straight wire over a path length Δz, the void diameter recorded on a layer of RCF is given by:

$$d_v = 4\left(\frac{e\mu_0 I \Delta z M D}{2\pi}\right)^{\frac{1}{2}}\left(\frac{1}{2m_p E_p}\right)^{\frac{1}{4}} \tag{5.1}$$

For the Vulcan experimental geometry, Eq. (5.1) predicts a void diameter of 6.3 mm for a 2 mm-diameter loop with 7.3 MeV protons and a wire current of 10 kA. This is raised to $d_v = 8.9$ mm for a wire current of 20 kA. The calculation is sensitive to the coil radius through Δz, which is an unknown parameter. I have taken $\Delta z = R = 1$ mm as a first order approximation of the proton path length through the B-field at the top of the wire loop.

Fig. 5.5 shows the variation of void diameter with wire current for a 2 mm-diameter loop. Coloured lines represent protons of different energy and shaded regions show how the deflection changes for a range of integrated path lengths, $\Delta z = 1 \pm 0.25$ mm. The shaded regions demonstrate how a small error in Δz can produce large differences in the inferred wire current/magnetic field. Shot 15 was typical of data for 2 mm-diameter coils, with $d_v \sim$ 6-8 mm for protons with energy $7.3 < E_p < 14.6$ MeV. The capacitor coil received $\sim$ 600 J total on-target energy and was probed at times $t > 1.1$ ns. Fig. 5.5 suggests that shot 15 had a wire current of $\sim$ 15 kA, corresponding to a central coil B-field of $\sim$ 16 T.

Fig. 5.6 shows how the void diameter varies with proton energy and coil magnetic field. The magnetic field at the coil centre is estimated via $B_0 = \mu_0 I/2R$. Comparison with the Vulcan RCF data suggests that the maximum coil current is likely to be between 10 kA and 25 kA for 1 and 2 mm loops, with corresponding magnetic fields between 6 and 30 T.

The analytic method provides us with bounding estimates of the coil current and magnetic field. Ray-tracing simulations can be used to improve on the paraxial approximation and simplified B-field geometry.

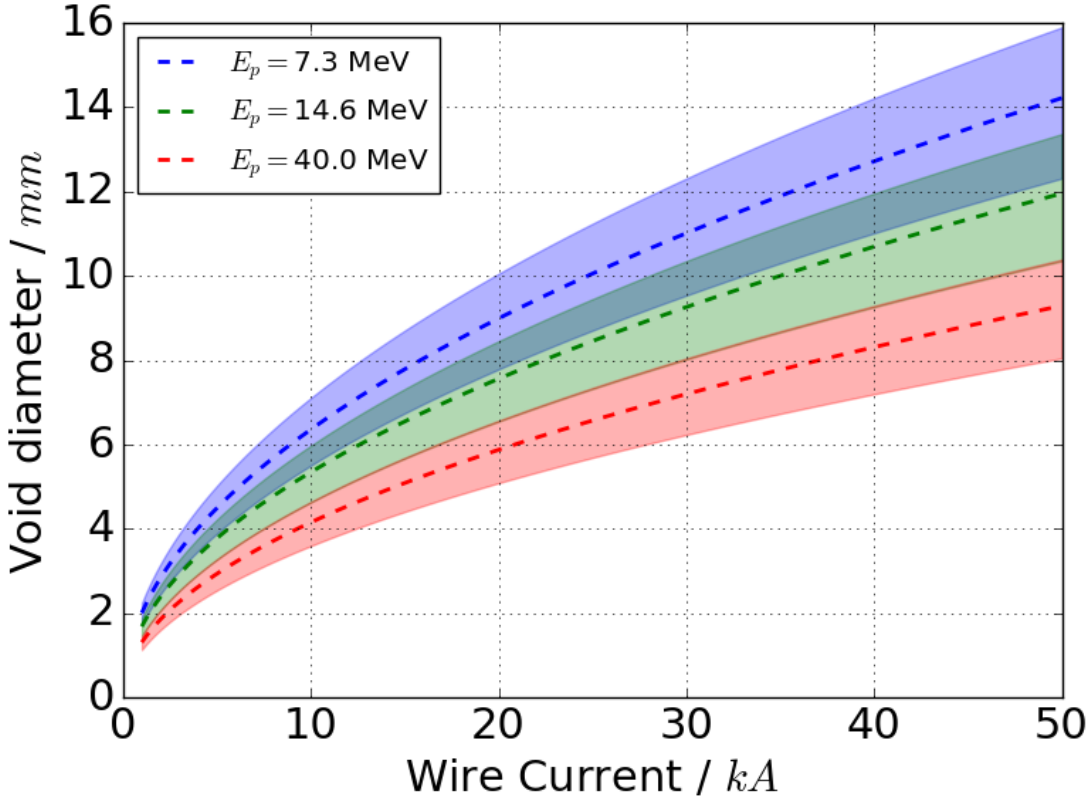

Figure 5.5: Proton void diameter plotted against wire current for a paraxial model of proton deflection around a 2 mm-diameter capacitor coil. Each coloured line represents the deflection for protons of a different energy. Distance parameters are taken from the Vulcan 2018 experimental set-up. Shaded regions representing $\Delta z = 1 \pm 0.25$ mm demonstrate the sensitivity of these calculations to the Δz parameter.

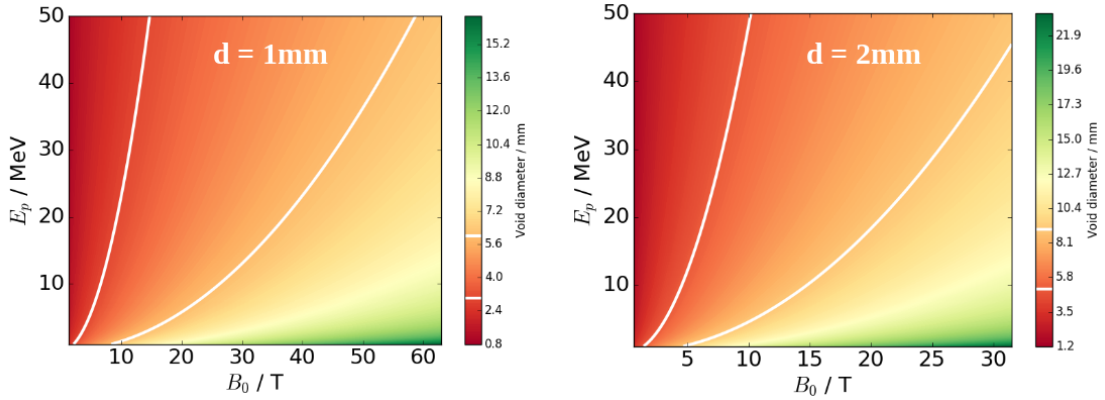

Figure 5.6: Filled contour plots of proton void diameter for proton deflection around 1- and 2 mm-diameter capacitor coils. The void diameter is plotted for different proton energies and magnetic fields. The void diameter is calculated using the analytic method from Ref. [79] and geometrical parameters are taken from the Vulcan experimental set-up. The white contour lines demarcate the range of void sizes observed on our Vulcan 2018 experiment. For example, most shots with 1 mm loops produced voids between 3 and 6 mm across.

Electric fields around the target might also contribute towards the deflected proton signal. The caustic void diameter from protons passing parallel to a charged wire with charge per unit length λ is:

$$d_v = 2\left(\frac{MD\Delta zze\lambda}{\pi\epsilon_0 E_p}\right)^{\frac{1}{2}} \tag{5.2}$$

Deflections from nC charges can be significant. For example, 10 MeV protons passing across $\Delta z = 2$ mm of electric fields from a 2 mm-long wire charged to 10 nC would produce a caustic void 8.3 mm in diameter - enough to swamp the magnetic field signal from kA currents.

5.3.2 Proton radiography simulations with EPOCH

There are two main simulation methods that can be used to extract a magnetic field from experimental radiographs. The first specifies proton and magnetic field distributions *a priori*, producing synthetic radiographs that can then be compared to experimental data. When there is agreement between the synthetic and experimental radiographs, we say that the physical conditions are equivalent. The second technique allows a magnetic field distribution to be inferred based on the assumption of a point source of protons and computational inversion of the measured proton intensity profile [104, 25, 98]. In the literature, capacitor coil experiments are overwhelmingly analyzed using the first approach. Some authors use handmade Biot-Savart solvers to calculate the magnetic field around the coil [173, 79], while others use commercial software [155, 105, 153, 82]. Ray-tracing programs can then be used to calculate the motion of protons through the fields and onto a detector.

Fig. 5.7 shows the computational scheme used to produce the synthetic proton radiographs in this thesis and Bradford *et al.* [28]. Proton trajectories are calculated ballistically outside of the mm-scale 'EM field region' where the capacitor coil is located and electromagnetic fields have a significant impact on proton trajectories. Inside the EM field region, proton trajectories are iteratively calculated using the EPOCH particle-in-cell code. Static EM fields are imported into EPOCH and the EPOCH field solver is disabled so the protons only respond only to these imported fields. This allows the beam to behave quasi-neutrally.

Studying how protons move in the EM fields created by currents and charges inside a capacitor coil is difficult because the magnetic field geometry around the bent wire loop used in the Vulcan experiment is more complicated than the analytic solution for a straight wire or magnetic dipole. Using a finite element method in Python, magnetic fields are calculated using the Biot-Savart Law with small current vector elements and electric fields are calculated using Coulomb's Law on small

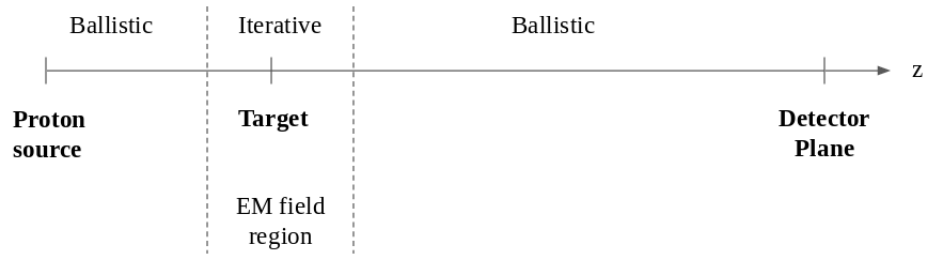

Figure 5.7: Computational scheme of proton radiography simulations. Proton trajectories can be calculated ballistically outside of the EM field region. Inside the mm-scale EM field region, proton trajectories must be calculated iteratively using a particle pushing scheme like Leapfrog or RK4 or Boris.

scalar charge elements. Current and charge elements are equally spaced along a line that defines the experimental geometry, then the field is calculated on a separate grid of points used by EPOCH.

A point-like virtual TNSA proton source is modelled as a point source of protons located on the foil rear surface. Fig. 5.8 shows how the beam expands at fixed divergence angle ϕ, tracing out the profile of a cone. At the beginning of each EPOCH simulation, a mono-energetic proton beam is defined in a z-plane at one edge of the simulation box. The protons have a 2D Gaussian density distribution centred on the beam axis. The beam is divergent with angular width ϕ and initial beam radius r_b, calculated from the source-target distance and the dimensions of the box. Each proton is assigned a divergence angle θ that increases linearly with distance from zero on the z-axis up to a maximum $\theta = \phi/2$ at $r = r_b$.

The choice of beam angular width is arbitrary and need not be inferred from the experiment. The dimensions of the simulation box will limit the maximum beam divergence that can be simulated to a value $\phi = \phi_{\text{box}}$. Protons with a higher angular divergence than ϕ_{box} will leave the simulation prematurely and not be counted. If the measured beam divergence is smaller than ϕ_{box}, then simulating a broader beam does not matter. On the other hand, if the beam is broader than ϕ_{box}, then these protons will leave the simulation early and be lost. Simulation boxes that are too small will produce a narrow beam that does not completely fill the RCF. The choice of beam divergence angle does not affect the physical accuracy of the simulation, provided the beam radius at the edge of the simulation is calculated correctly from the source-target position and the dimensions of the box.

Electromagnetic fields were calculated on a $6\times6\times6$ mm^3 grid for 1 mm and 2 mm-diameter capacitor coil loops with 50 grid points per side. This grid is sufficiently fine-scale and large to accurately model caustic formation around the wire (see next section). There will be an error associated with using a cubic grid to sample the

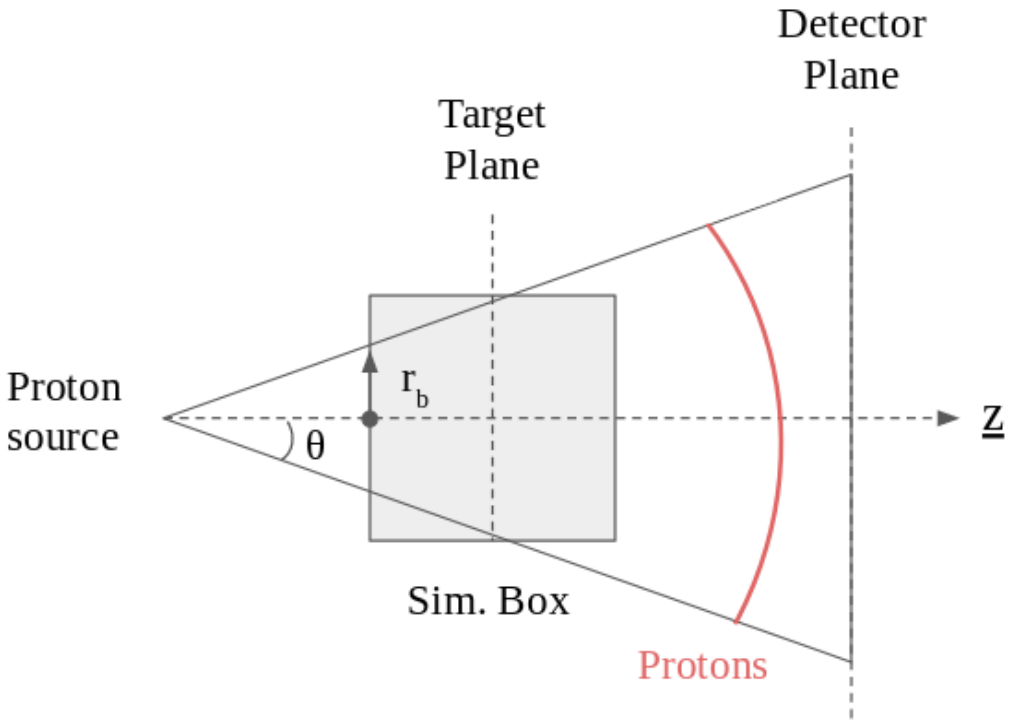

Figure 5.8: Model of a TNSA proton beam used in EPOCH simulations of proton radiography. The angular divergence of the beam is $\phi = 2\theta$.

magnetic field because close to the wire, where the field gradient is very high, it is desirable to sample the field more often. Far from the wire, where the field does not change much, it doesn't need to be sampled so often. Ideally, we would use an adaptive mesh to make the calculation more efficient, but EPOCH is only compatible with a cuboidal mesh [5]. The RCF response function (energy-dependent absorption sensitivity) was not accounted for.

Benchmarking the Finite element EM field calculator

Before we embark on analysis of the experimental data, it is important to check that the numerical Biot-Savart calculation is accurate. In Fig. 5.9, we compare proton deflections in magnetic fields calculated analytically [159] and using Biot-Savart in Python. Panels (a) and (b) show results for a circular loop of wire carrying a 40 kA current. The loop axis is perpendicular to the axis of proton propagation and centred at the origin. The horizontal caustic diameter is 15.7 mm in both radiographs and the proton distribution is indistinguishable in all other respects. In panels (c) and (d) we compare proton deflections around two parallel wires carrying 40 kA currents in opposite directions. Again, there is excellent agreement between the two radiographs and the maximum width of the caustic voids are 4.22 mm in both panels. We can therefore be confident that the Biot-Savart finite element calculation is accurate.

As a global test of the hybrid Python and EPOCH radiography simulations, the void generated when a divergent proton beam is fired parallel to the axis of a straight, current-carrying wire can be compared with the theoretical expectation. Python was used to calculate the EPOCH void diameter by placing vertical lines at the extreme edges of the void and taking the difference of their horizontal positions. The width of the caustic boundary is approximately 0.01 mm in these simulations. Fig. 5.10a shows a synthetic radiograph calculated for 7.3 MeV protons passing close to a straight wire segment of length 2 mm with wire current 20 kA. The source-target and target-detector distances are identical to those used in the experiment. The EPOCH simulation was run on a cubic box of side length 6 mm with 50 grid points per side. There is good agreement between the EPOCH void diameter of 12.4 ± 0.01 mm and the theoretical estimate of 12.6 mm taken from Eq. (5.5), although the void is not precisely spherical as we would expect. This is comparable to the deflection error caused by uncertainty in the detector distance and provides accuracy to within ~ 1 kA for currents ≤ 20 kA (see Fig. 5.11a). The straight wire radiograph is similar to that presented in Fig. 5.10b, which represents a 2 mm-diameter wire loop in the experimental geometry carrying a 20 kA current. As expected, there is minimal proton deflection in the fields around the vertical wire sections because the magnetic field is approximately parallel to the proton trajectories there; protons are primarily deflected when they pass across the top of the wire loop.

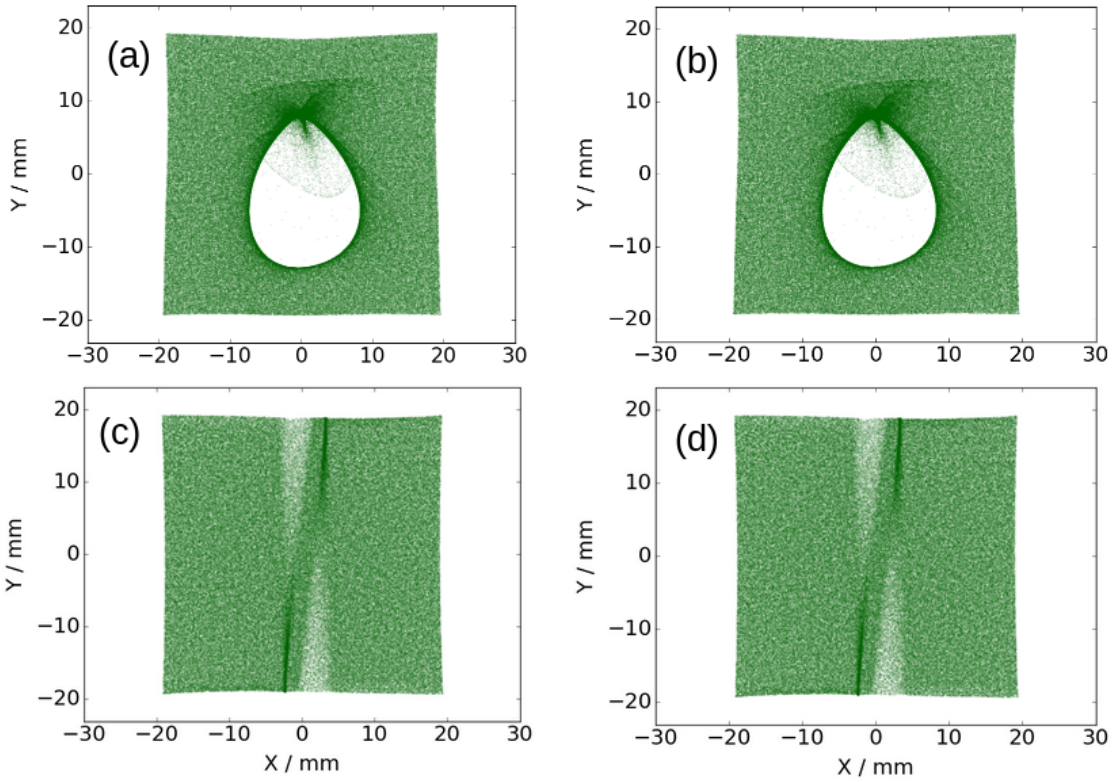

Figure 5.9: Comparison of synthetic radiographs generated using EPOCH for different imported magnetic fields. Radiographs were calculated for 7.3 MeV protons. The magnetic fields were calculated using: (a) Finite element Biot-Savart solver for a 2 mm-diameter magnetic dipole carrying a current of 40 kA (b) Analytic solution for the magnetic field around a 2 mm-diameter current loop carrying a 40 kA current, taken from Ref. [159]. (c) Finite element Biot-Savart solver for two parallel wires (total length 10 mm) carrying opposite 40 kA currents (d) Analytic solution for two infinite parallel wires carrying opposite 40 kA currents. Simulations were run inside a cubic box with 50 grid points and 6 mm per side.

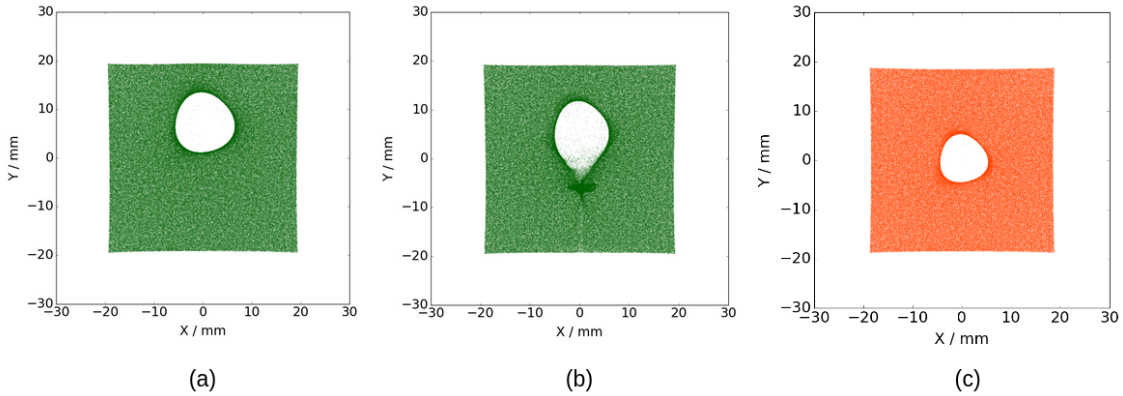

Figure 5.10: EPOCH proton radiographs generated using 7.3 MeV protons and different wire geometries: (a) Straight wire geometry of length 2 mm, centred at (x, y) =(0,1 mm) and 20 kA current (b) Wire loop geometry used in the Vulcan experiment with a loop diameter of 2 mm and wire current of 20 kA (c) Straight wire geometry of length 6 mm, centred at (x, y) =(0,0) with charge per unit length of 2 nC/mm.

The same global testing procedure can be applied to a Python code that calculates the electric field around arbitrary, discretized charge distributions using Coulomb's Law. Fig. 5.10c contains a synthetic radiograph calculated for 7.3 MeV protons passing close to a straight wire with fixed charge density $\lambda = 2$ nC/mm and length 6 mm. The simulated void diameter of 10 ± 0.01 mm agrees tolerably with the value of 10.4 mm predicted by Eq. (5.2). We can therefore say that the cumulative error arising from a discrete charge distribution, cubic grid mesh and finite simulation box are probably $\lesssim 0.5$ mm, equivalent to $\lesssim 0.5$ nC/mm wire charge density. This is an important result of my analysis: deflectometry measurements must be made carefully because a small error in the measured void diameter can produce a relatively large error in the inferred current or charge distribution.

5.3.3 Perpendicular deflectometry: B-field only simulations

In this section, EPOCH simulations of proton beams passing through magnetic fields are used to provide estimates of the capacitor coil current and magnetic field generated on the Vulcan experiment. Simulations of protons passing perpendicular to the axis of a capacitor coil loop produce a clear, inverse teardrop void. The horizontal diameter of the void can be used to extract information about the magnetic field strength and spatial distribution. Fig. 5.11a shows the variation of the simulated void diameter with loop current, while Fig. 5.11b shows the void diameter as a function of B_0 for capacitor coils probed with different proton energies. The smooth lines represent an analytic fit ($\propto \sqrt{I}$) with Δz a free parameter. The capacitor-coil to RCF distance is 70 mm and corrections have been made for the thickness of

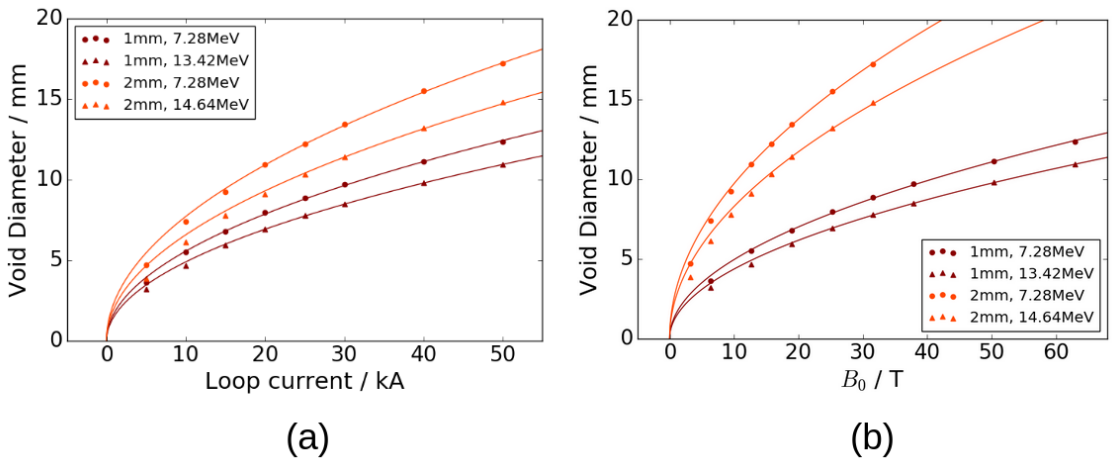

Figure 5.11: (a) Proton void diameter as a function of coil current (b) Proton void diameter as a function of axial magnetic field

different RCF layers in the stack. The analytic fit is very good above $I \sim 10$ kA but deviates slightly at lower currents because the analytic solution is anchored to the origin. The free parameter Δz is found to be a fixed fraction of the coil radius ($\Delta z/R \sim 1.5$), which is specific to the Vulcan experimental geometry. Once this fraction has been calculated, it allows us to make current predictions based on void diameter measurements for different loop diameters and proton energies *without running EPOCH*.

In contrast to the EPOCH simulations, some of the experimental radiographs feature proton voids with a two layer structure: an inner lobe where almost all of the protons have been evacuated and an outer halo that is partially filled (see Fig. 5.17a). To estimate the current in the loop, it is necessary to choose which void - inner or outer - to compare the simulations to.

In Table 5.3.3, I present the inferred coil current and magnetic field for two data shots from the experiment. The current is interpolated from EPOCH simulations via a quadratic fit to the *inner* void diameter ($I(d_{\text{void}}) = Ad_{\text{void}}^2 + C$ with $A, C \in \mathbb{R}$) to get better agreement with the simulations across the full range of currents. To estimate the magnetic field at the coil centre, B_0, the coil is assumed to be perfectly circular. The table shows data for a 1 mm-diameter loop target with on-target energy ~ 580 J and a 2 mm-diameter loop target with on-target energy ~ 600 J. There is broad agreement between the magnetic field estimates for different layers of RCF. Variation in the magnetic field may be the result of a dynamic current profile.

Fig. 5.12 shows how the capacitor coil current varies with applied laser energy for targets with 1 mm-diameter loops, 1-1.4 ns after the beginning of the laser drive. Current measurements inferred from the inner void diameter (Fig. 5.12a) and outer halo diameter (Fig. 5.12b) do not change significantly for laser energies between

Coil diameter / mm	Laser Drive Energy / J	Proton Energy / MeV	Probe Time / ps	Void diameter / mm	Current / kA	B_0 / T
1	580 ± 30	$7.3^{+0.1}_{-0.1}$	820 ± 50	3.9 ± 0.3	5.0 ± 1.3	6.3 ± 1.6
1	580 ± 30	$13.4^{+0.2}_{-0.1}$	740 ± 50	2.8 ± 0.2	3.9 ± 1.2	4.9 ± 1.5
2	600 ± 30	$7.3^{+0.1}_{-0.1}$	1200 ± 50	4.3 ± 0.3	4.0 ± 1.2	2.5 ± 1.5
2	600 ± 30	$14.6^{+0.2}_{-0.1}$	1100 ± 50	3.8 ± 0.3	4.9 ± 1.2	3.1 ± 1.5

Table 5.1: Coil current and central magnetic field for two capacitor coil data shots - one with a 1 mm-diameter loop and the other with a 2 mm-diameter loop. Errors in proton energy and probe time are estimated the FWHM of the RCF response function (see Fig. 5.4a), although probe time errors are limited to ±50 ps by experimental factors. Errors in the current and magnetic field are calculated from uncertainty in the capacitor coil to RCF distance, $D = 70 \pm 5$ mm, added in quadrature with a representative 1 kA error from the EPOCH simulations.

540 J and 660 J.

The temporal evolution of the capacitor coil current is plotted in Fig. 5.13 for 1 mm and 2 mm-diameter loops. Since the loop current appears to be stable with laser energy, the data in Fig. 5.13 has not been normalised. Error bars are slightly larger for the data points at $t_{\text{probe}} < 0.5$ ns because the proton beam was oriented at an oblique angle to the loop that has been estimated from RCF images. Both 1 mm and 2 mm loop targets exhibit similar behaviour. Fig. 5.13 suggests the magnetic field rises to a maximum a few hundred picoseconds after the beginning of the laser drive, decays to under half its maximum value in the same time and then remains approximately constant for at least a further nanosecond. This behaviour is interesting because the sub-ns rise time and decay on two different timescales contradicts the B-dot measurements (see Sec. 5.5). The B-dot waveforms rise steadily to a maximum on a multi-ns timecale and decay much more slowly. It is likewise significant that the maximum currents ($I_{\text{max}} > 20$ kA) that develop on a 100 ps timescale are higher than the Alfvén Limit, $I_A = 17$ kA. The Tikonchuk diode model [169] suggests the target will operate in a steady-state regime once the laser-plasma has bridged the plates at $t_{\text{probe}} \sim 100$ ps, after which the loop current will increase until the end of the laser drive at $t_{\text{probe}} = 1$ ns.

Fig. 5.14 shows experimental radiographs at two different probe times. While EPOCH simulations with magnetic fields agree reasonably well with experimental RCF images for $t_{\text{probe}} > 0.5$ ns, the correspondence is not so good earlier in the

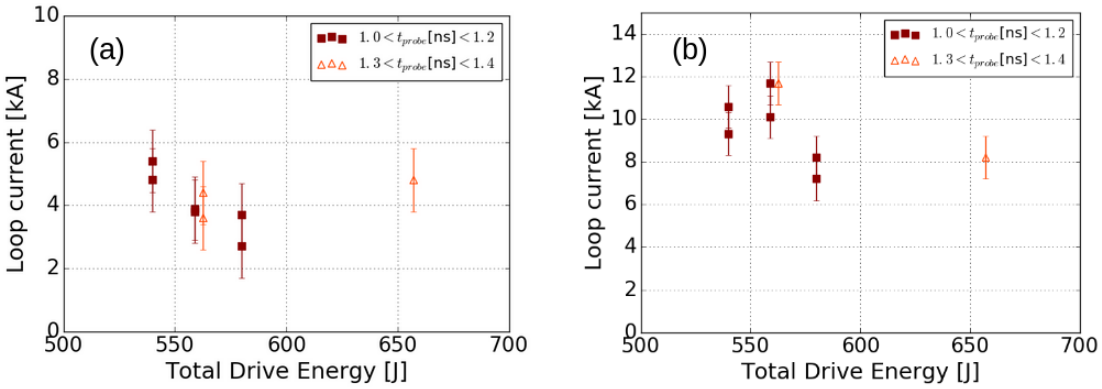

Figure 5.12: Variation in loop current with total applied laser energy for 1 mm-diameter capacitor coil targets. The loop current is inferred from B-field only simulations using measurements of (a) Inner void diameter (b) Outer halo diameter. Corresponding target probe times are shown in the legends.

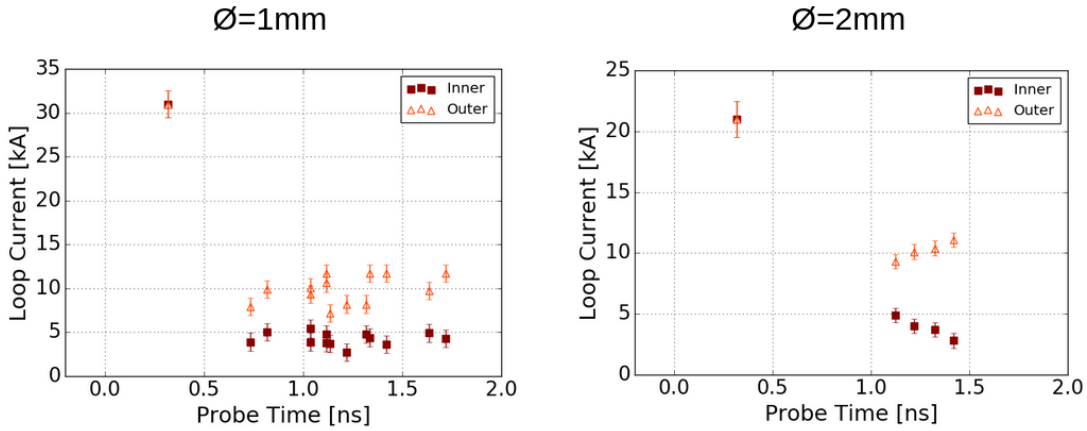

Figure 5.13: Temporal evolution of B-field for 1 mm- and 2 mm-diameter capacitor coil targets. The laser arrives at time $t_{probe} = 0$ ns. Red squares indicate inner void measurements, while orange triangles represent measurements of the outer halo.

interaction. For $t_{\text{probe}} \sim 0.3$ ns, significant proton deflections are present along the full length of the wire in the RCF images. This is less pronounced in the EPOCH simulations. Furthermore, the shape of the voids is more circular in the 2 mm RCF image, without a pinch at the base of the loop. It is possible that simulations with electric fields may help explain some of these discrepancies. In the next few sections, I will investigate how electric fields affect magnetic field measurements made using proton radiography; I will also look at different methods to estimate the spatial and temporal distribution of these fields independent of the teardrop void diameter.

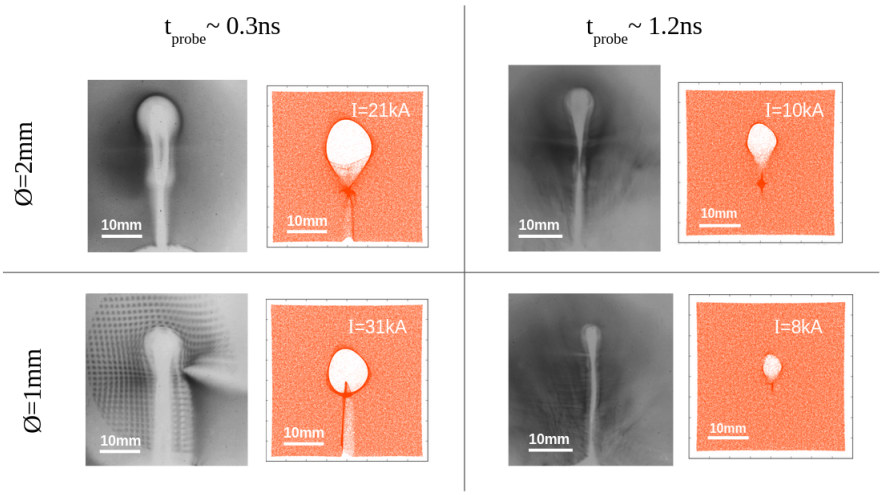

Figure 5.14: Comparison of EPOCH simulations with RCF data for 1 mm- and 2 mm-diameter capacitor coil loops. EPOCH simulations used a monoenergetic $E_p = 7.3$ MeV proton beam to match the RCF data. The synthetic radiographs corresponding to $t_{probe} \sim 0.3$ ns were made with B-fields rotated by $\theta = 8°$ (2 mm) and $\theta = 15°$ (1 mm) from the perpendicular. The magnification of each RCF image is M = 7, so a distance of 10 mm in the detector plane (indicated above) equates to 1.4 mm in the coil plane.

Summary of results using "B-field only" simulations

- Several proton radiographs feature proton voids with a two layer structure: an inner void and outer halo. This separation is not present in synthetic radiographs.
- The loop current appears to be insensitive to laser drive energy for $540 < E_{las}[\mathrm{J}] < 660$.
- Similar currents are observed for 1 mm and 2 mm-diameter loops throughout the experiment.
- Measurements at $t_{\mathrm{probe}} < 0.5$ ns suggest very large currents are present at early times that decay quickly during the laser drive. Comparison with experimental RCF images suggests we may need to account for electric fields at these times.
- Measurements at $t_{\mathrm{probe}} > 0.5$ ns suggest the current and magnetic field are quasi-static over 1 ns and persist after the end of the drive. Peak currents based on the inner and outer void diameters are ~ 5 kA and ~ 10 kA respectively.

5.3.4 Perpendicular deflectometry: Combined E and B-field simulations

Proton trajectories can be changed by positive and negative electric fields as well as magnetic fields. For example, a multi-nC accumulation of negative charge in the vicinity of the wire loop can produce strong electric fields that reduce the size of the proton void generated by magnetic fields. Simulations that include negative electric fields will therefore predict higher loop currents than simulations with just a magnetic field alone. In the Introduction, we saw how Santos *et al.* [153] used this mechanism to explain an apparent discrepancy in B-field measurements made with B-dot probes and proton radiography [153]. The authors described how a cloud of hot electrons ejected from the laser focal spot may become trapped in the capacitor coil fields, pulling protons inwards and counteracting the expulsion caused by magnetic fields.

A build-up of negative charge may also be sustained by the target capacitance. Given an inter-plate capacitance of $C = \epsilon_0 A/d = 0.1$ pF (with A the plate area and d the plate separation) and voltage $V = 30 - 50$ kV, the coil may accumulate a charge of magnitude $Q = CV \sim$ 3-5 nC distributed over the wire surface. Simulations run with spherical charge distributions placed near the wire loop and Cu plates do not agree well with experimental data, so I have chosen to study two alternative charge geometries: a circular ring and a capacitor coil loop. Fig. 5.15 shows a synthetic proton radiograph made with a uniform, negatively-charged circular ring and a current in the experimental wire geometry. The inferred current for a 1 mm-diameter loop with a $Q = -10$ nC ring of charge is $I \sim 18$ kA – almost twice as large as the current taken from B-field only simulations.

It has been observed in numerous publications that charge separation in the laser focal spot will generate a time-varying positive potential that spreads out over the target surface [38, 147, 97]. This is important when trying to interpret proton radiographs of capacitor coils because a positively-charged wire will act to deflect protons radially away from the wire surface. These protons are deflected outwards by a similar amount all along the wire, so positive electric fields cannot reproduce a teardrop-shaped void without magnetic fields. Electric fields can, however, increase the width of the proton void generated by a magnetic field as well as the apparent thickness of the vertical wire sections (see Figure 5.16). This phenomenon may help to explain the compound void structure observed in some radiographs as well as unusually large proton voids observed early in the interaction.

Fig. 5.17a shows a proton radiograph taken using 7.3 MeV protons, $t = 1.4$ ns after the beginning of the laser drive. Notice that the teardrop-shaped void is composed of two layers: an inner lobe where almost all of the protons have been

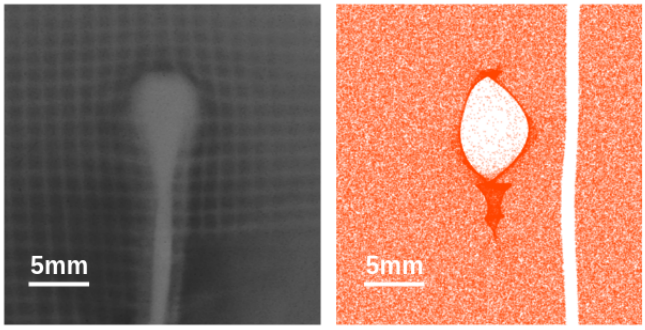

Figure 5.15: LEFT: Experimental RCF data for a 1 mm-diameter loop taken at $t \sim 0.8$ ns with $E_p = 7.3$ MeV protons. RIGHT: Synthetic proton radiograph corresponding to 7.3 MeV protons passing across a 1 mm-diameter loop carrying 18 kA and a circular ring with uniform charge $Q = -10$ nC. A vertical line has been cut out of the proton distribution to act as a fiducial. The magnification of each RCF image is $M \sim 7$, so a distance of 5 mm in the detector plane (indicated above) equates to 0.7 mm in the coil plane.

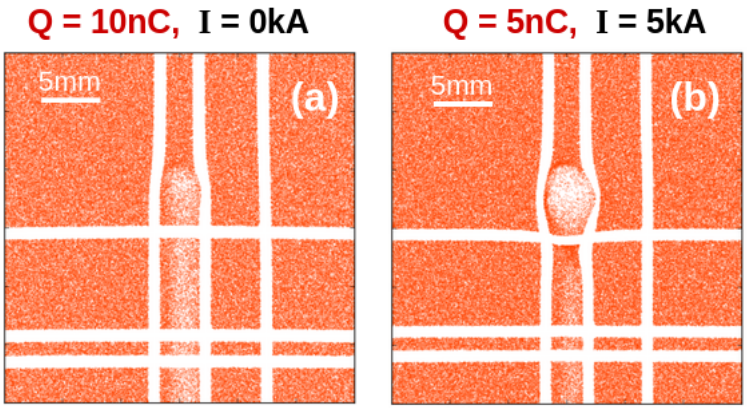

Figure 5.16: Demonstration of the effect of positive electric fields on proton void structure. In these deflectometry simulations, 7.3 MeV protons were propagated perpendicularly across a 1 mm-diameter wire loop. Horizontal and vertical lines have been cut out of the proton distribution to act as fiducials. (a) Simulation run with electric fields only. Electric fields were calculated for a uniformly charged wire loop with total charge $Q = 10$ nC. Proton displacement is approximately constant across the entire length of the wire. Distortion of the fiducial grid is only observed near the top of the loop - not near the vertical wire sections. (b) Simulation run with electric and magnetic fields. Electric fields were calculated for a uniformly charged wire loop with total charge $Q = 5$ nC, while magnetic fields were generated from a uniform wire current of $I = 5$ kA. The proton void width is approximately 1 mm larger than observed for the same simulation without an electric field.

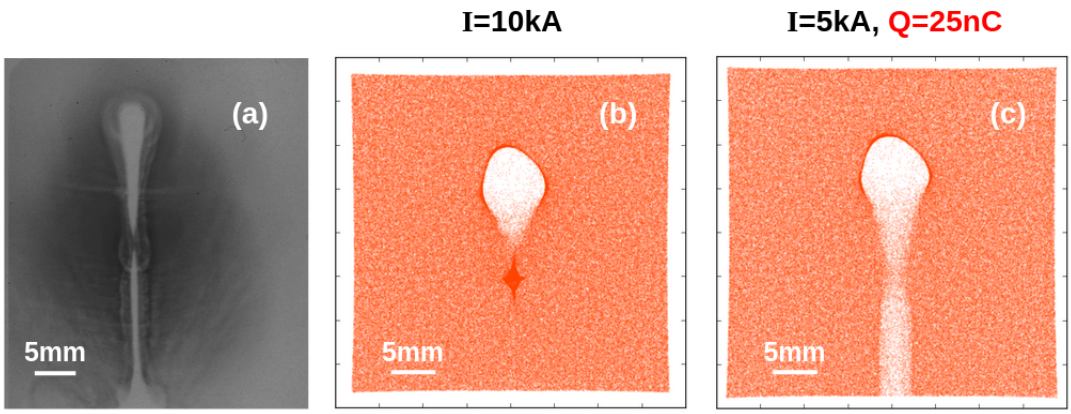

Figure 5.17: (a) RCF image taken $t = 1.4$ ns after the beginning of the laser drive using 7.3 MeV protons. The coil is 2 mm in diameter (b) B-field only simulation with a wire current of 10 kA (c) B-field and E-field simulation with 5 kA current and +25 nC charge distributed uniformly along the wire. Both simulations were run with 7.3 MeV protons.

evacuated and an outer halo that is partially filled. This distinction is maintained along the full length of the wire, even to the top of the capacitor coil plates. EPOCH simulations with just magnetic fields suggest a current of ~ 10 kA matches the diameter of the outer halo, but this current is too low to produce multi-mm deflections around the straight wire sections (Fig. 5.17b). Alternatively, we can match deflections along the vertical wires using a positive charge distribution and then we can add a magnetic field to fit the diameter of the outer halo. The simulation results in Fig. 5.17c agree with the measured radiograph, although a two-layer structure and caustic is not reproduced. The estimated current is approximately half that calculated using only magnetic fields.

To see how the electric and magnetic fields evolve with time, this simulation procedure can be repeated at different probing times. E-field simulations can be compared with pronounced wire broadening at early times (see Fig. 5.14 and 5.22) and the fainter, more intricate caustic that runs along the shadow of the wire at later times (see Fig. 5.17a). B-fields are then added to recover the teardrop feature at the top of the loop. Fig. 5.18 shows the evolution of the coil current and electric field with time. The orange triangles show that the electric field at the wire surface does not change very much over the course of the laser interaction. Though the positive electric fields have considerably reduced the current estimates compared with Fig. 5.13, the current remains strong for $t_{probe} < 0.5$ ns. In the case of the 1 mm loop, the current still exceeds the Alfvén Limit.

There are several possible explanations for a two-layer void structure. In Fig. 5.17a, the diameter of the inner lobe corresponds to a current of $I \sim 3$ kA and forms a pinch at the base of the loop, which suggests the inner void may be closely

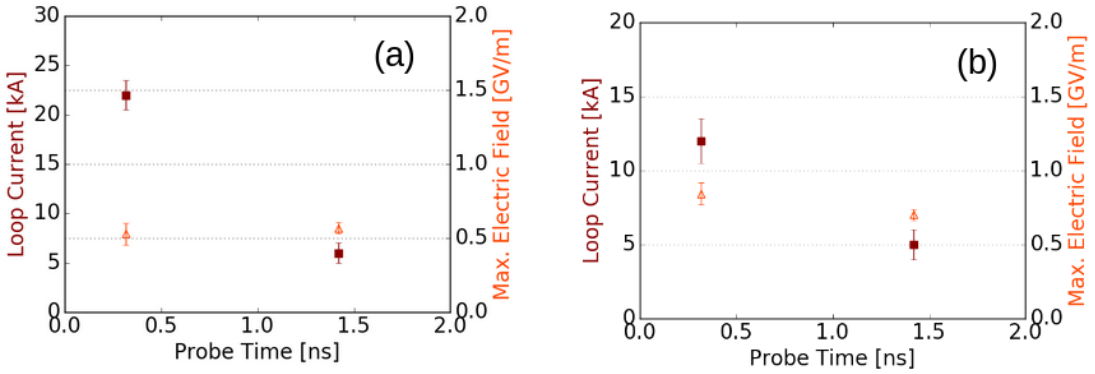

Figure 5.18: Temporal evolution of coil current and electric field for (a) 1 mm- and (b) 2 mm- diameter capacitor coil targets. Red squares represent the wire current and orange triangles represent the electric field at the wire surface. Measurements are based on the diameter of the outer halo.

related to the magnetic field. I will return to this idea in Sec. 5.3.8, when proton energy scalings are used to try to break the degeneracy of the electric and magnetic fields. The outer halo is also much stronger at early times, so Fig. 5.17a may show the effects of a residual electric field. For $t > 0.5$ ns, we find upper limits on the electric field of $E \sim 0.5$ GVm^{-1} based on deflections around the vertical wire sections. Intricate bubble-like structures in several radiographs for $t > 0.5$ ns may be evidence of a plasma sheath.

5.3.5 Axial deflectometry: Combined E and B-field simulations

The larger the electrostatic charge, the stronger the grid deflection around the loop. In the following sections, grid deflection in axial RCF images is used to estimate the likely charge geometry and amplitude.

Fig. 5.19a shows a typical axial proton radiograph for a 2 mm-diameter capacitor coil loop. At the centre of the loop there is an area of reduced proton signal that I will refer to as an *axial void*. EPOCH simulations of a uniformly-charged capacitor coil wire with an overlapped circular ring of negative charge produce similar axial features for a wire current of $I = 40$ kA and charge $Q = -100$ nC (see Fig. 5.19b), however they are not true axial voids because the on-axis proton density has not decreased. Simulations also show enhanced proton signal and cm-scale grid distortion inside the negatively-charged loop, which is not supported by experiment. Though the grid shadow is significantly distorted in Fig 5.19a, this distortion is concentrated around the vertical wires and parallel plates rather than the wire loop. It therefore seems likely that the axial void is caused by something other than negative charges around the loop. In Ref. [173], Wang *et al.* observe a similar void-feature in their

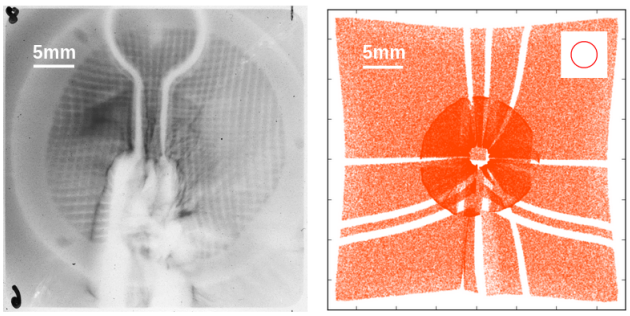

Figure 5.19: (a) Axial proton radiograph for a 2 mm diameter loop, $t_{probe} \sim 0.8$ ns after the beginning of the laser drive. Image taken using $E_p = 7.3$ MeV protons (b) Synthetic proton radiograph of a capacitor coil wire ($I = 40$ kA) with an overlapped circular ring of charge ($Q = -100$ nC). Three vertical and three horizontal lines have been cut out of the proton distribution to act as fiducials. Inset in the top right hand corner is a diagram of the circular charge geometry, which contrasts with the keyhole-shaped current geometry.

axial radiographs. They use PIC simulations to show that it may be a sheath field effect caused by the interaction of electrons and protons in the quasi-neutral proton beam.

Comparing grid deflection in RCF data with EPOCH simulations suggests that $Q \sim -10$ nC can be seen as a likely upper limit on the quantity of negative charge present in the loop. This charge corresponds to a maximum probable current of $I \sim 20$ kA for $t_{probe} > 0.5$ ns. It does not satisfactorily explain the axial proton void, nor is it consistent with the deflections observed along the straight wire sections.

5.3.6 Axial deflectometry: Upper limits on capacitor coil magnetic field

EPOCH simulations of protons passing through a current loop suggest that the beam will rotate as it passes through the magnetic field (clockwise or anticlockwise depending on the polarisation of the current). Thus if a fiducial (e.g. high-Z metallic grid) is inserted between the proton foil and the capacitor coil target, the imprint of the fiducial in the proton image will twist as a function of the applied magnetic field (see Figure 5.20a). This effect is analogous to a proton gyrating around magnetic field lines. In Figure 5.20b, the straight line represents protons rotating at their gyrofrequency in a 1 mm-scale uniform magnetic field. The magnitude of the magnetic field is taken to be $B = \mu_0 I/2R$, where I is the loop current and R the loop radius. It is important to note that the beam rotation angle is not significantly affected by electric fields or proton beam divergence and it is also present in simulations of the experimental current geometry [28]. Analysis of the RCF data does not show any

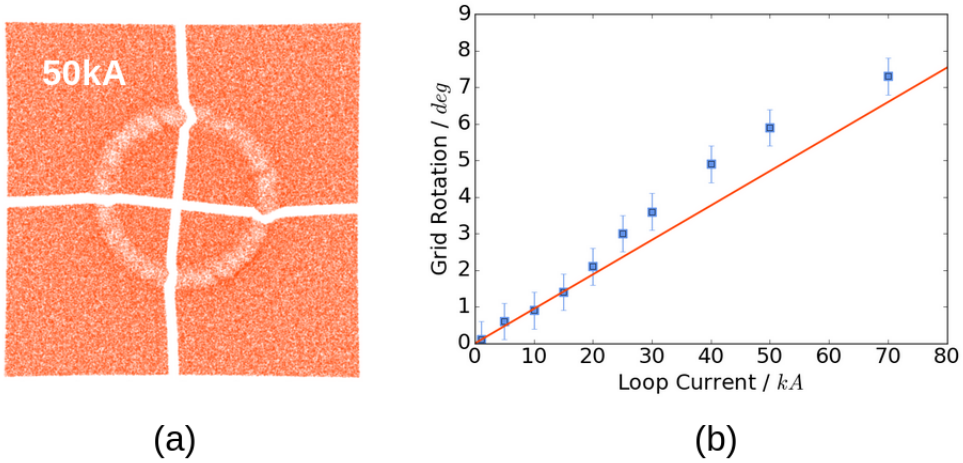

Figure 5.20: (a) Synthetic radiograph for a 7 MeV divergent proton beam passing through the magnetic field of a 2 mm-diameter current loop carrying a current $I = 50$ kA. Horizontal and vertical slots have been cut out of the Gaussian proton distribution, which rotate through an approximately fixed angle inside the loop (b) Blue points: Graph of loop current plotted against rotation angle of the fiducial grid for a 2 mm-diameter current loop. The straight line represents proton gyration angle for protons passing perpendicularly through a uniform magnetic field of 1 mm spatial scale. The magnitude of this magnetic field is equivalent to the B-field at the centre of a 2 mm-diameter current loop.

evidence of a fixed rotation angle inside the loop which suggests the wire current is below $I \sim 10$ kA for both 1 mm and 2 mm targets.

Grid deflection close to the wire surface can also be used as a measure of the magnetic field. The vertical wires under the capacitor coil loop provide a simplified geometry for conducting simulations of the magnetic field. Figure 5.21 shows a simulation of two infinitesimally thin current-carrying wires placed in parallel with opposite polarisations. The wires carry a uniform current of 20 kA and produce wedge-shaped proton voids terminating in an extended pinch. Horizontal and vertical fiducials show minimal (sub-mm) deflections close to the wire surface, consistent with the experimental result shown in Fig. 5.21b. The absence of measurable grid deflections suggest the wire current is below $I \sim 20$ kA.

5.3.7 Simultaneous dual-axis proton probing

Simultaneous proton probing along two perpendicular axes enables us to check whether our field modelling is consistent. Fig. 5.22 shows perpendicular and axial radiographs for a single plate target probed early in the interaction, $t_{probe} = 0.3$ ns after the beginning of the laser drive. The perpendicular radiograph (Fig. 5.22a) features a substantial void at the top of the 2 mm-diameter loop and strong proton deflections all along the length of the straight wire sections. Using EPOCH B-field

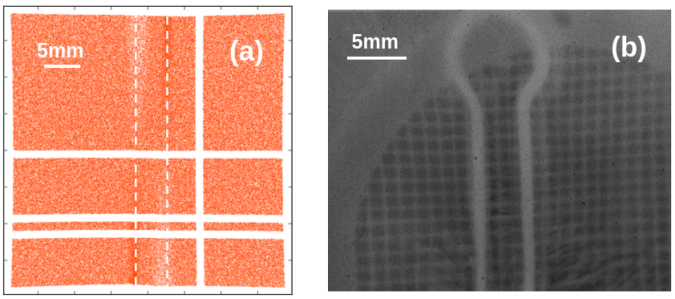

Figure 5.21: (a) Synthetic radiograph for two vertical wires carrying $I = \pm 20$ kA. The right-hand wire carries a current vertically upwards and the left-hand wire carries a current vertically downwards. Horizontal fiducials show minimal grid deflection close to the wire surface. The approximate location of each wire is picked out with vertical dashed lines (b) Detail from RCF image of 1 mm-diameter loop taken $t = 0.8$ ns after the beginning of the laser drive. Current is flowing clockwise around the loop.

simulations, a loop current of 33 kA (on-axis B-field of $\sim$ 20 T) can be matched to the void diameter of $\sim$ 14 mm at the top of the loop. However, there is no magnetic pinch at the bottom of the loop and a loop current exceeding 100 kA is required to match the $\sim$ 6.5 mm caustic around the vertical wires - inconsistent with proton deflections at the top of the loop. These observations suggest the wire may be positively charged, generating an electric field that significantly perturbs proton trajectories close to the wire surface. Since magnetic field deflections are small around the straight wire sections for currents below $\sim$ 50 kA, electric field simulations were run to match deflections around the vertical wires before magnetic fields were added to enlarge the void at the top of the loop. The optimised results can be seen in Fig. 5.22b, for a wire current of 15 kA and wire charge of 60 nC, with the charge spread uniformly across the full length of the wire loop for a linear charge density of $\lambda = 6.7$ nC/mm and an electric field at the wire surface of $\sim 10^9$ Vm^{-1}. Turning now to the axial radiograph in Fig. 5.22c, a faint caustic can be distinguished around the outside of the wire which I have demarcated by dashed lines set $\sim$ 1.5 mm from the centre of the wire. A wire current of 40 kA is required to produce an apparent wire thickness of 1 mm in the axial orientation, which suggests the current can be ignored in axial simulations. A wire linear charge density of 3.3 nC/mm gives a caustic width of 3 mm, which matches the caustic on the outside of the wire (see Fig. 5.22d). This is approximately half the charge density and electric field inferred from Fig. 5.22a.

Simultaneous proton probing was also conducted later in time, at $t_{probe} = 1.7$ ns, as shown in Fig. 5.23. A clear void in the perpendicular radiograph shows that the magnetic field is still significant even 0.7 ns after the laser drive has ended. This teardrop-shaped void has a two-layer structure: an inner lobe where almost all of the

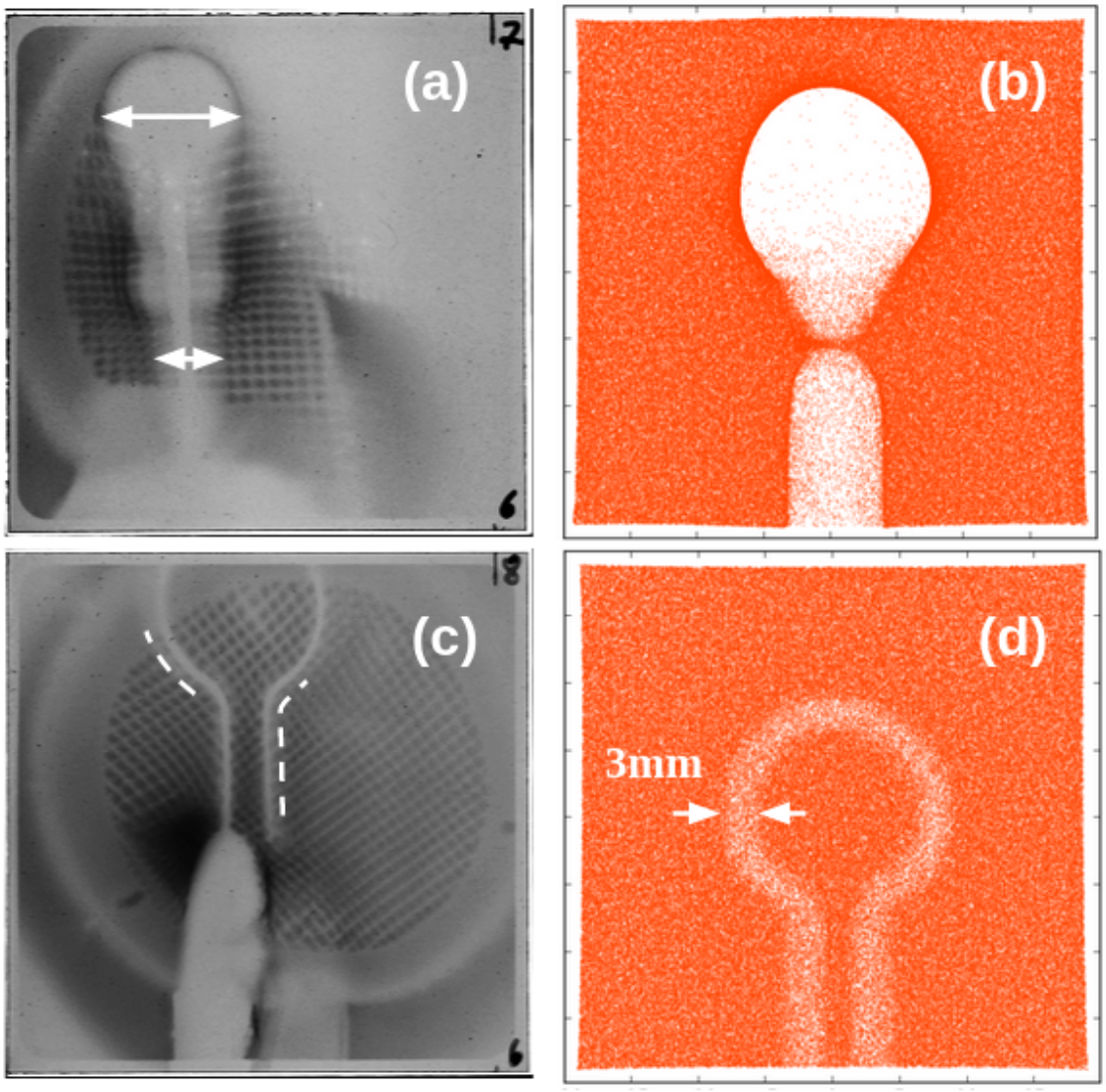

Figure 5.22: Simultaneous proton probing of a 2 mm-diameter single plate capacitor coil target (a) Perpendicular radiograph with t_{probe} = 0.3 ns and E_p = 7.3 MeV protons (b) Combined E- and B-field EPOCH simulation with wire current I = 15 kA and wire charge Q = +60 nC (c) Axial radiograph with t_{probe} = 0.3 ns and E_p = 7.3 MeV protons (d) EPOCH E-field only simulation with Q = +30 nC wire charge.

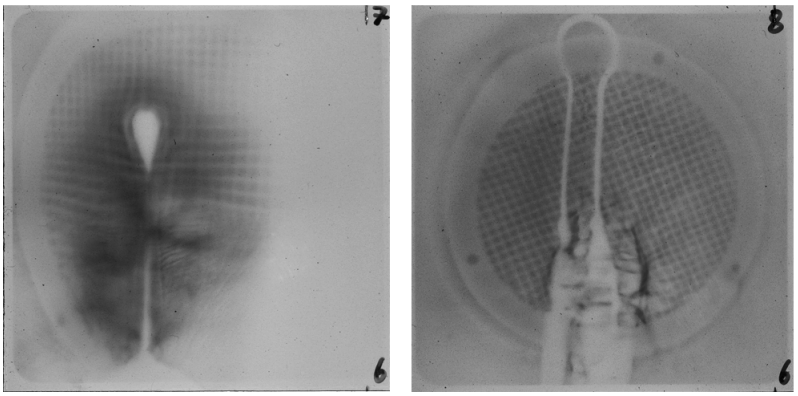

Figure 5.23: Simultaneous proton probing of a 1 mm-diameter capacitor coil target with $t_{probe} = 1.3$ ns and $E_p = 7.3$ MeV protons. The left image corresponds to the perpendicular orientation and the right image to the axial orientation.

protons have been evacuated and an outer halo that is partially filled. Comparing the measured void diameter with EPOCH simulations gives inferred loop currents of 4.3 kA and 11.7 kA for the inner and outer voids respectively. Though there is a lot of activity close to the parallel plates, the axial radiograph shows no clear proton deflection around the wire loop. This is consistent with a loop current of 11.7 kA or below.

5.3.8 Scaling of proton deflection with proton energy

When a proton passes through an electric or magnetic field, the amount of deflection it experiences will depend on its kinetic energy. In Sec. 3.4.4, the proton void diameter was shown to vary as $E_p^{-\frac{1}{4}}$ in a magnetic field and $E_p^{-\frac{1}{2}}$ in an electric field. In an electromagnetic field, the void diameter will vary as a combination of these two factors depending on the relative strength of the electric and magnetic fields.

The energy dependence of the inner void and outer halo were tested separately to see if there was a difference between the two. The void diameter was measured on RCF layer 4 ($E_p = 5.6$ MeV) and RCF layer 11 ($E_p = 14.6$ MeV), then the ratio of these values were compared to the expected energy scalings. The boundary of each void was identified by taking the average of five horizontal lineouts of the proton signal and recording local minima. The inner void was found to match the magnetic field scaling well on those shots where an inner void could be reliably distinguished ($t_{probe} > 0.5$ ns). The outer halo varies more strongly than the magnetic field scaling on some shots, though it is always closer to $E_p^{-\frac{1}{4}}$ than $E_p^{-\frac{1}{2}}$. The void diameter of the single plate target, which appears to show good qualitative evidence for electric fields, is almost constant with proton energy.

In addition to proton void diameter, grid deflections are sensitive to proton energy and change on successive layers of RCF. Close to the target, the regular grid

pattern is warped by electromagnetic fields and the displacement of each grid line can be measured relative to the undisturbed grid further from the target. Ref. [108] suggests grid deflections should vary as $E_p^{-\frac{1}{2}}$ in the presence of a magnetic field, consistent with the uniform field equations from Sec. 3.4.2. Examination of linear grid deflections in our data at $t_{\text{probe}} > 0.5$ ns shows that they vary roughly as $E_p^{-\frac{1}{4}}$.

Rapid changes in capacitor coil fields could be responsible for a deviation from the expected proton energy scaling. This is particularly important early in the interaction, when Fig. 5.13 suggests the current may rise as swiftly as 100 kA/ns. At later times ($t_{\text{probe}} > 0.7$ ns) the coil current stays roughly constant, so correcting for dynamic B-fields is less important.

5.4 Discussion

Comparing synthetic proton radiographs with a range of current and charge distributions is necessary to place upper and lower limits on the capacitor coil magnetic field. RCF data at $t_{\text{probe}} < 0.5$ ns features striking cm-scale proton voids and deflections along the full length of the wire loop. Magnetostatic simulations suggest the void diameter corresponds to super-Alfvénic currents exceeding 20 kA, though the shape of the proton void and extent of the deflections underneath the loop are not very well reproduced. Moreover the rise of the magnetic field to a maximum value on the order of 100 ps contradicts the Fiksel and Tikhonchuk models, which suggest the loop current should continue to build until the end of the laser drive. Positive wire charging can help explain strong proton deflection away from the wires at $t_{\text{probe}} < 0.5$ ns, as well as reduce the magnetic field inferred from measurements of the proton void diameter. EPOCH simulations that include electric fields reduce the magnetic field estimates considerably, but still require large currents ($I > 10$ kA) to match the void at the top of the loop.

At $t_{\text{probe}} > 0.5$ ns, B-field only simulations match the experimental radiographs well. Prominent voids shaped like inverted teardrops are a clear signature of a magnetic field and the scaling of these voids with proton energy also suggests that magnetic fields are dominant at these times. Measurements at different proton probing times suggest that the current stays approximately constant at $I \sim 10$ kA between 0.7 ns and 1.7 ns for both 1 mm and 2 mm-diameter loops. The 1 mm loops produce the strongest fields, measuring approximately $B_0 = 12$ T at the loop centre. A caustic feature that runs along the edge of the straight wire sections is of unclear origin. It could be indicative of a positive electric field of order 0.5 GV/m at the wire surface, plasma sheath fields or smearing of the thermal proton distribution. Simulations with both E and B-fields predict magnetic fields approximately half that from B-field only simulations, although they do not reproduce the caustic feature

very well.

Simultaneous dual-axis probing provides good evidence for positive electric fields at $t_{\text{probe}} < 0.5$ ns, even though the magnitude of the electric field calculated from perpendicular and axial orientations do not agree. For $t_{\text{probe}} > 1$ ns, electric fields appear to be less significant and B-field only simulations are probably justified. A single plate target may produce stronger fields than an equivalent two-plate target.

EPOCH simulations show that negative charges around the wire allow us to infer larger loop currents, but there is no clear experimental evidence for this effect in the axial RCF data. Enhanced current estimates of $I > 15$ kA are contradicted by axial grid rotation measurements at $t_{\text{probe}} > 0.5$ ns and spherical charge distributions are likewise ruled out by simulations. Naturally, this does not exclude electron clouds having a significant impact on B-field estimates for different capacitor coil targets, where the loop is positioned closer to the laser focal spot[154, 105].

The approximate magnetic field energy for the 1 mm diameter targets is given by $E_B = \frac{1}{2}LI^2 \sim 0.5$ J, with L the loop inductance and I the wire current, which corresponds to a laser energy conversion efficiency of $\sim 0.1\%$. This is $\sim 10\times$ lower than that quoted for experiments at LULI [153, 154], though the discrepancy can be explained by a lower hot electron temperature. At Vulcan, the operating intensity was $20\times$ lower than LULI and $T_e = T_e(I\lambda^2)$ is an important parameter governing loop current in theoretical models of capacitor coils [169, 71, 82].

The hot electron temperature achieved in the laser focal spot can be estimated using the $I\lambda^2$ scaling from Eq. (2.14). For our experimental parameters, this gives a value of $T_e \sim 14$ keV. Although we used a layer of CH plastic to try to enhance the hot electron temperature, the measured current/magnetic field was actually slightly lower when using plastic coated targets. Since the loop current is thought to vary sensitively with T_e [71, 82, 169] this suggests the plastic layer did not increase the hot electron temperature. We note that T_e was not measured directly during the experiment.

Fig. 5.24 shows the expected current and voltage profiles in the capacitor coil based on a plasma diode model of the target [169]. A hot electron temperature of $T_e \sim 14$ keV, wire inductance $L = 10$ nH and wire resistance $R = 1\ \Omega$, corresponds to a maximum potential of $V \approx 2\text{-}3T_e = 30\text{-}50$ kV between the plates. The current rise time is $V/L = dI/dt \sim 3\text{-}5$ kA/ns which is in agreement with the experimental value of $I \sim 5$ kA at $t > 0.5$ ns. Looking towards future experiments with capacitor coils, magnetic field measurements appear to support the plasma diode model [169], suggesting that $B \sim 100$ T magnetic fields may be attained at high laser intensity ($I = 10^{16} - 10^{17}$ Wcm^{-2}) with sub-millimetre diameter wire loops.

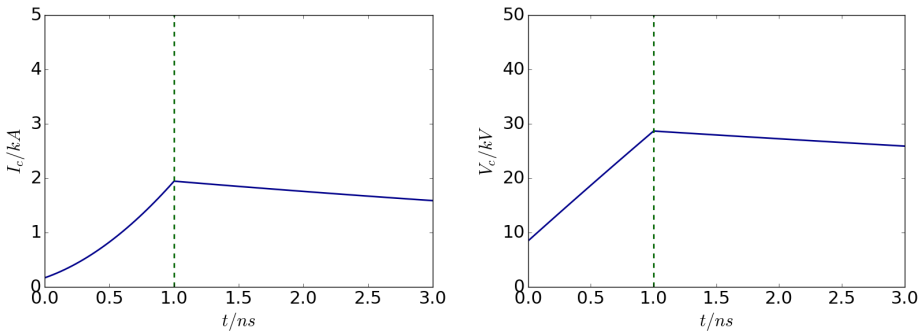

Figure 5.24: Current and voltage profiles for the Vulcan experiment calculated using a plasma diode model of the capacitor coil. The vertical dashed green lines represent the end of the laser pulse. Peak currents of $I_c = 2$ kA and peak voltages of 30 kV are expected for a hot electron temperature of $T_h = 14$ keV.

Summary of proton radiography measurements:

- Perpendicular and axial radiographs show evidence of positive wire electric fields at $t_{\text{probe}} < 0.5$ ns. Combined electric and magnetic field simulations suggest strong currents exceeding 10 kA develop on a ~ 100 ps timescale with electric fields of ~ 0.5 GV/m at the wire surface.
- Measurements at $t_{\text{probe}} > 0.5$ ns suggest the current and magnetic field are quasi-static over 1 ns and persist after the end of the laser drive. Peak currents based on the inner and outer void diameters are ~ 5 kA and ~ 10 kA respectively, corresponding to a maximum magnetic field of $B_0 \sim 12$ T at the centre of the 1 mm-diameter targets.

5.5 B-dot probe results

Two B-dot spectrograms are shown in Fig. 5.25, corresponding to shots on 5 mm-diameter coils. Even though the laser drive energy was roughly the same on both shots ($E_{las} \approx 600$ J), there are significant differences in the recorded spectra. The spectrum for the long-pulse only shot (Fig. 5.25a) is dominated by two modes below $f = 1.5$ GHz, whereas the shot involving two short-pulse radiography beams (Fig. 5.25b) exhibits a broadband frequency response that is characteristic of EMP. For shots where the ps radiography beams and ns drive beams arrive at different times, the expectation is for multi-GHz EMP noise to arrive separately from the sub-GHz B-dot signal. In Fig. 5.26, we present a spectrogram of B-dot data taken during a shot on a 1 mm-diameter capacitor coil, where the ps-duration radiography beams arrive 1.4 ns after the beginning of the laser drive. Narrowing the Blackman-Harris

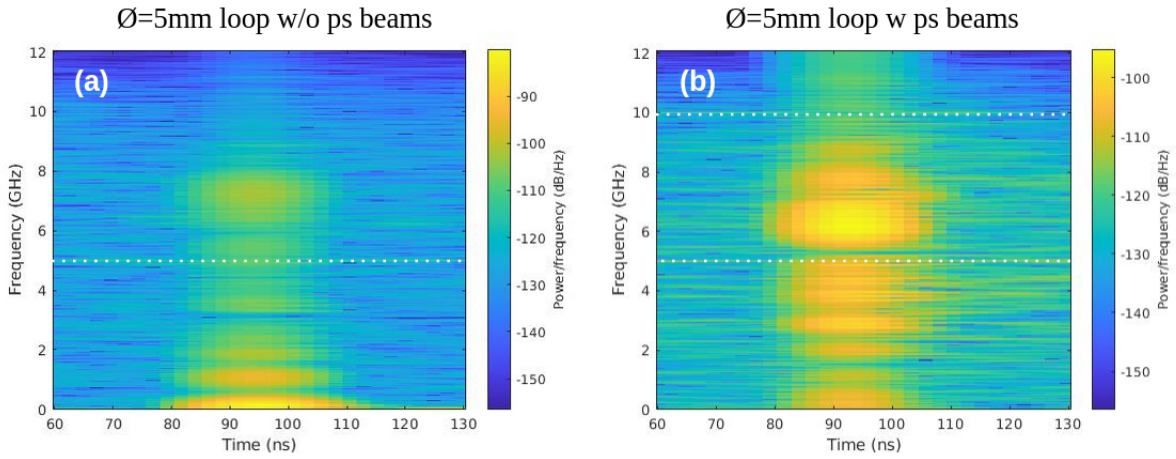

Figure 5.25: Spectrograms of voltage data from an RB-230 B-dot probe (a) 5 mm-diameter coil without ps-duration radiography beams (b) 5 mm-diameter coil with ps-duration radiography beams. Dotted white lines are overlaid on top of oscilloscope noise signatures at 5 GHz and 10 GHz.

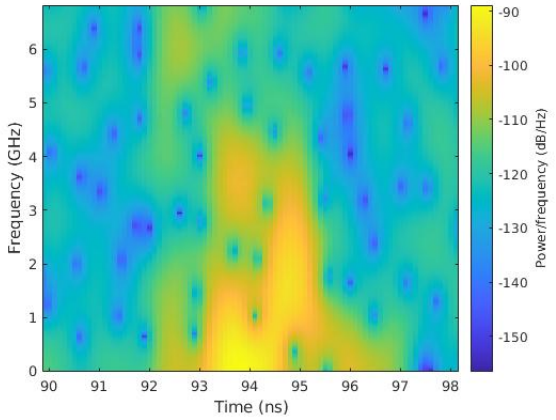

Figure 5.26: Spectrogram of B-dot measurement taken during a shot on a 1 mm-diameter capacitor coil where the ps-duration radiography beams arrive 1.4 ns after the beginning of the laser drive.

window function for better temporal resolution, high-frequency modes appear to lag behind the sub-GHz modes by ~ 1.4 ns.

In general, B-dot measurements taken with short-pulse beams feature strong EMP resonances from 0.001 GHz up to almost 10 GHz which must be carefully filtered out before the signal can be integrated to yield $B(t)$. In some cases, however, it may not be possible to isolate the sub-GHz EMP signal from the capacitor coil B-field. Fig. 5.27 shows the integrated B-dot signal for a 1 mm-diameter capacitor coil with a variety of different bandpass filters. An optimal waveform was recovered with a minimum frequency of $f_{min} = 1$ MHz and a maximum frequency of $f_{max} = 0.5$ GHz. Data from the B-dot probes was processed in the following steps: (i) a bandpass filter was applied to the signal fast Fourier transform (FFT)

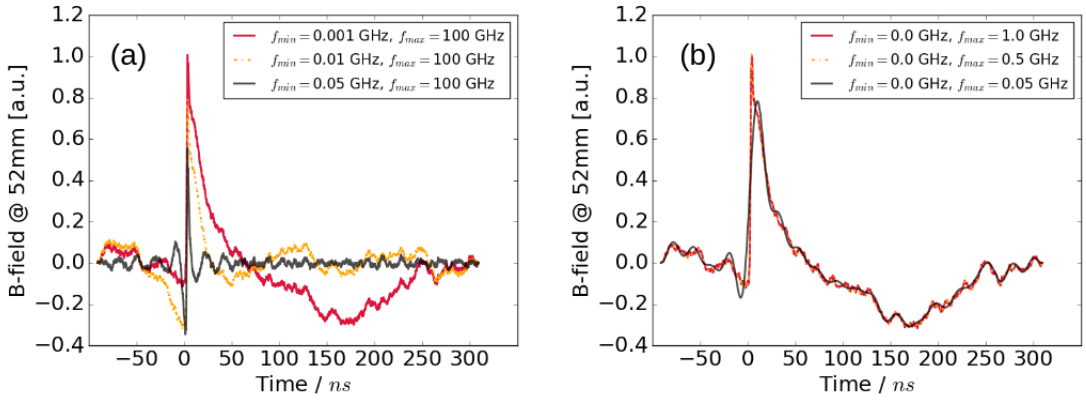

Figure 5.27: Bandpass filter study for B-dot measurement with noise from ps beams: (a) High-pass filter study (b) Low-pass filter study. The voltage data is taken from shot 19, with a 1 mm-diameter capacitor coil, and the cut-off frequencies are denoted by f_{min} and f_{max}.

to eliminate sources of noise, (ii) the raw signal was corrected for external attenuation on the oscilloscope and 8 dB balun attenuation, which was assumed to be constant across the probe bandwidth, (iii) the frequency-dependent attenuation of the coaxial cable was corrected using a fit to network analyzer data, (iv) an inverse FFT was performed to obtain a clean dB/dt signal, (v) $B(t)$ was found by numerical integration of dB/dt and division by the probe equivalent area, $A_{eq} = 2 \times 10^{-5}$ m^{-2}.

Magnetic field waveforms measured at the probe head show a B-field that rises to a peak over 2 ns and decays to zero over $\sim$ 100 ns. Fig. 5.28 shows that a maximum magnetic field of 8 mT was measured at the probe head for a 1 mm-diameter loop, compared with 6 mT for a 5 mm-diameter loop. The 1 mm shot is much noisier than the 5 mm shot because the ps radiography beams were fired and 40 dB attenuation was put at the oscilloscope. It is interesting that the peak B-field is larger on the shot with the 1 mm loop, since both shots received the same energy and the field of a 1 mm loop decays more quickly over space than the field of a 5 mm loop. The stronger 1 mm signal may be caused by EMP pick-up at the probe head.

To calculate the magnetic field strength at the centre of the capacitor coil loop, I used static simulations of the magnetic field geometry to extrapolate from measurements at the probe head. Simulations were run with the same finite difference routine used to generate capacitor coil fields for insertion into EPOCH (see Sec. 5.3.2). First, the number of current elements per unit wire length was increased until simulations matched the analytical results from Ref. [159] for a magnetic dipole field, then simulations were run for two further wire geometries: (i) an open keyhole geometry that approximates the current path from between the two capacitor plates but omits the plasma current (ii) a closed keyhole geometry that connects the vertical wire sections to account for the plasma current. Fig. 5.29a shows the calculated

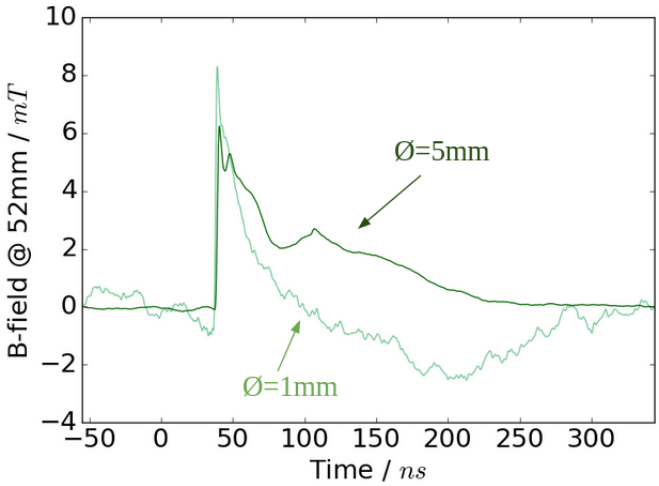

Figure 5.28: Bandpass-filtered and attenuation-corrected B-field waveforms for 1 mm- and 5 mm-diameter capacitor coil loops. The waveform for the 1 mm shot, with 40 dB scope attenuation and radiography beams, is much noisier than the 5 mm shot with 20 dB scope attenuation and no radiography beams.

Current geometry	B_0/B_{probe}	
	Ø=1mm	Ø=5mm
Mag. Dipole	2.2×10^6	1.8×10^4
Open keyhole	5.2×10^4	7.3×10^3
Closed keyhole	9.4×10^5	1.7×10^4

Table 5.2: Ratio between the magnetic field at the loop centre to the magnetic field at the probe position, B_0/B_{probe}, simulated using a Python finite difference code. Values are given to two significant figures.

magnetic field for a 5 mm-diameter capacitor coil in the closed keyhole geometry, carrying a wire current of 100 kA. Though the magnetic field is very intense close to the wire surface, it drops off sharply with distance. For a 5 mm loop in our experimental conditions, Fig. 5.29b shows that the magnetic field must be extrapolated over almost four orders of magnitude from the probe position at $(0, 52\text{ mm}, 0)$ to the centre of the wire loop at $(0, 0, 0)$. Results for the ratio of the magnetic field at the loop centre to the magnetic field at the probe position, B_0/B_{probe}, can be found in Table 5.2.

The importance of accurately simulating the coil geometry is evident from the factor 40 difference in B_0/B_{probe} for a 1 mm-diameter magnetic dipole compared with the equivalent open keyhole geometry. Indeed, assuming a dipolar B-field geometry implies a measured field of $B_0 = 10$ kT for the 1 mm-diameter loop - a

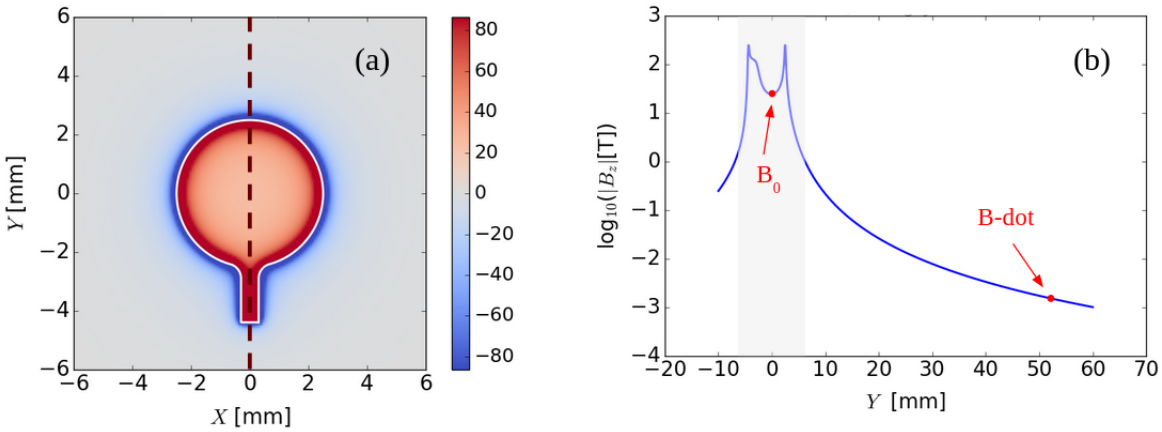

Figure 5.29: Finite-difference magnetic field calculations for a 5 mm-diameter capacitor coil loop (closed keyhole geometry) carrying a static current of 100 kA. (a) B_z calculated in $z = 0$ plane in units of Tesla. The vertical dashed line indicates the position of the lineout taken in panel (b) and the wire current profile is picked out in white. (b) $\log_{10}(|B_z|)$ plotted as a function of y (vertical displacement), with the magnetic field at coil centre (B_0) and the B-dot probe position indicated in red. The transparent grey region shows the extent of the magnetic fields pictured in panel (a).

truly egregious overestimate. Of the three wire geometries listed in Table 5.2, an open keyhole gives peak magnetic fields most similar to the proton radiography, with a peak magnetic field of $B_0 \approx 40$ T for the 5 mm-diameter loop measurement and $B_0 \approx 420$ T for the 1 mm-diameter loop.

Since the B-dot probe is placed at a distance of several centimetres from the coil, any magnetic fields present in the target chamber can contribute towards the probe voltage signal. This means that the inferred coil magnetic field may be modified by the laser-target interaction or EMP from a range of sources. In the Vulcan experiment, strong magnetic fields generated spontaneously in the laser-plasma may have contributed towards the signal measured by the B-dot probe. These magnetic fields grow via the Biermann battery effect [84, 164, 88] or magnetized plasma instabilities [156, 21]. Biermann magnetic fields in particular have a poloidal geometry centred on the laser focal spot and run clockwise around the plasma density gradient vector, so they would been aligned anti-parallel to the capacitor coil field. Proton radiography measurements suggest Biermann fields can reach $B \sim 100$ T during long-pulse laser interactions and decay on the timescale of the laser pulse duration [78, 108, 165]. Since no control shots without a wire loop were made during this experiment, the possibility that the B-dot measurements have been affected by magnetic fields originating in the laser-plasma cannot be ruled out.

The discrepancy in the peak magnetic field measured using B-dot probes and proton deflectometry has been observed on other experiments with capacitor coils,

where perpendicular proton deflectometry was thought to have been affected by a cloud of negative charges caught in the coil magnetic field [153]. Perpendicular and axial deflectometry on Vulcan does not show clear evidence of an electron cloud that could reduce the magnetic field inferred from proton deflections by a factor 10 or more. Instead, results in this section suggest that EMP pick-up and stray magnetic fields from the laser spot can alter the B-dot probe output, while large errors in B-dot measurements can be incurred from imperfect knowledge of the spatial and temporal profile of the coil current. It is interesting to note that there are significant variations in B-dot measurements between experiments with quite similar laser and target parameters, such as Ref. [44] compared with references [153, 105] (see Table 1.1). Though previous experiments have tended to focus on generating the strongest magnetic field possible, understanding whether these B-dot measurements are reliable will require broad parameter scans that can be compared with estimates from theoretical models.

5.6 Summary of Vulcan capacitor coil experiment

Results are reported from a capacitor coil experiment driven by the Vulcan Nd:glass laser at an energy of $E_{las} \sim 0.5$ kJ and pulse duration 1 ns with peak intensity $I_L \sim 5\times10^{15}$ Wcm^{-2} [28]. Proton deflectometry measurements of the coil electromagnetic field were taken throughout the interaction up to $t \sim 1.7$ ns after the beginning of the laser drive. EPOCH simulations suggest that proton deflections at $t < 0.5$ ns are caused by ~ 0.5 GV/m electric fields on the wire surface. Inferred current measurements at $t > 0.5$ ns are between 5 kA and 10 kA for both 1 mm- and 2 mm-diameter loop targets. Current measurements at these late times agree well with predictions from a plasma diode model. An analytic model of proton deflection taken from Gao *et al.* [79] has been shown to give good agreement with the proton deflectometry diagnostic and has been extended to include wire electric fields. A laser shot on a single plate target unexpectedly produced stronger deflections than targets with two parallel plates. Magnetic fields measured using a B-dot probe were 10-100$\times$ larger than those calculated from proton deflectometry. This may be caused by broadband EMP noise, errors stemming from long-distance probing or perhaps some contribution from the laser-plasma.

Looking towards future experiments, it would be interesting to simplify the set-up by irradiating a single plate target. Instead of a separate wire loop, the plate support wire could be modified to accommodate a small loop [9] that can be probed using proton deflectometry and a direct voltage diagnostic (see Williams *et al.* [180], Dubois *et al.* [58] or Pearlman and Dahlbacka [136]). An open geometry would make it easier to diagnose the plasma density and temperature and to model plasma

evolution. It would also be interesting to probe a two-plate capacitor coil in opposite directions shortly after the beginning of the laser drive ($t_{las} < 0.5$ ns) to see if the proton void inverts. Following Courtois *et al.* [44], control shots should be taken without a connecting wire loop to check the sensitivity of the B-dot probe to self-generated plasma fields and EMP. The RCF analysis may be improved by background-subtracting the electron signal and applying a proton dose calibration [70] to produce a 2D intensity pattern. Corrections can also be made for blurring using the Richardson-Lucy deconvolution algorithm [115]. Fitting an RL-circuit decay to the B-dot voltage profile would provide an estimate of coil resistance that could be compared with numerical or analytic models of coil resistive heating.

Future EPOCH simulations would benefit from more realistic current and charge geometries, either with extended wires or dynamic fields. Simulations with fine-scale fiducial grids would aid comparison with experimental radiographs, as would combining multiple simulations with different proton energies to investigate blurring. Contour plots and log-compression of simulation outputs might be used to represent RCF dose profiles [104]. Modelling coil magnetic fields with COMSOL [41] or a similar program that uses adaptive field meshing would significantly benefit both the radiography and B-dot probe diagnostics [155].

Chapter 6

Conclusion

Over the course of this thesis I have looked at how laser-driven discharge currents can lead to the production of strong electromagnetic fields far from the laser focal spot. An experiment on the Vulcan laser demonstrated that radiofrequency EMPs are intimately connected to target charging and antenna emission. EMP amplitude was found to vary much more strongly with laser energy than intensity in the range $1\text{ ps} < t_{las} < 10\text{ ps}$. Conducting probes measured EMP fields of $10 - 100$ kV/m at a distance of 1.5 m from the target and good agreement was seen with a frequency-domain dipole model of EMP emission. A square root scaling with laser energy suggests that EMP fields may increase to $\gtrsim 1$ MV/m on multi-PW facilities like the Extreme Light Infrastructure [183]. The Vulcan EMP measurements highlighted the importance of using well-characterised cables that are relatively short, since a small (~ 1 m) increase in the length of poor quality cables could lead to significant further attenuation of the EMP signal. It was also discovered that EMP noise can enter oscilloscopes directly, even when positioned behind a wall at a distance of 10 m from the laser target. Placing oscilloscopes inside a grounded Cu box was found to reduce the amplitude of the EMP pick-up by a factor 5. When the oscilloscope was placed inside a Faraday cage with a filtered power supply and cable ports this direct pick-up was eliminated entirely, consistent with established theories of electromagnetic compatibility [11, 92, 95]. Fig. 6.1 shows a B-dot probe waveform recorded by an unshielded oscilloscope outside the Vulcan target chamber. Direct EMP pick-up (blue) obfuscates the B-dot measurement that is coloured in green. A new EMP mitigation scheme was introduced to help protect facility equipment. By modifying the target holder to disrupt its radiative properties, a factor ~ 4.5 reduction in EMP amplitude was achieved without significant impact on the laser interaction. Subsequent work by other authors has shown that EMP can be reduced further using a 'bird cage' enclosure [57] or resistive holder [12]. Beyond the practical considerations of reducing EMP, it would be interesting to see to what extent EMP emission can be used as a plasma diagnostic. Comparing the Vulcan laser defocus and pre-pulse

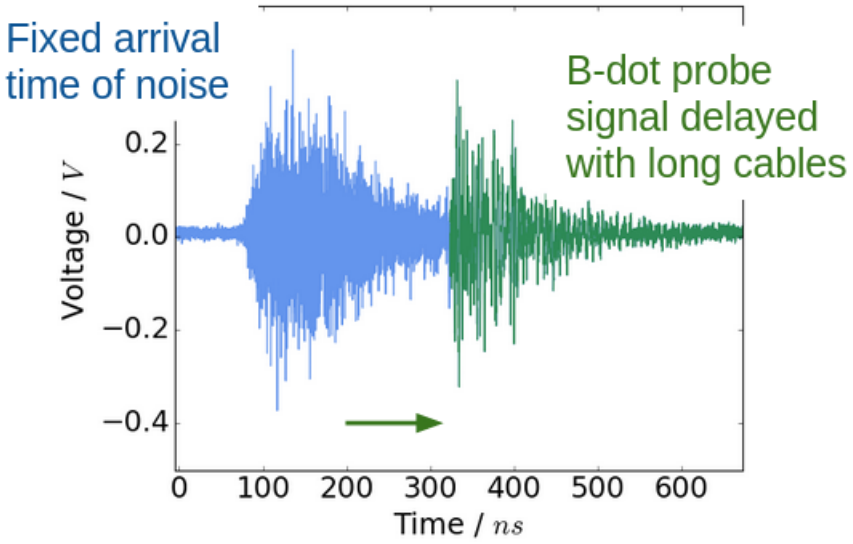

Figure 6.1: Voltage waveform from an unshielded oscilloscope placed ∼ 10 m from the Vulcan target chamber. A B-dot probe EMP signal is visible in green, lagging behind direct EMP pick-up in the oscilloscope that is picked out in blue. Using longer probe cables produced a commensurate temporal delay in the arrival of the B-dot signal.

delay scans with a dipole antenna model may be useful for this, especially if they are supplemented by multi-axis EMP measurements from electro-optic probes. Dielectric electro-optic probes developed by Consoli *et al.* [42] have measured significantly higher fields than previously recorded by conducting B-dot and D-dot probes. A new experiment led by D. Carroll on the Vulcan Petawatt laser will compare EMP field measurements from different diagnostics and examine how they correlate with discharge currents and charged particles. Ultimately, improved models of target charging brought about by more accurate measurements may contribute towards the development of x-ray [6] and THz [110, 109] radiation sources.

The second major preoccupation of this thesis was to see if an all-optical platform for magnetized high energy density (HED) physics can be achieved with capacitor coil targets. There are promising results from an experiment on the Vulcan laser at an intensity of $I_L = 5 \times 10^{15}$ Wcm^{-2}. Strong electric fields observed at early times were succeeded by an unambiguous magnetic field signal towards the end of the laser drive. Maximum currents of 10 kA were measured in both 1 mm and 2 mm diameter targets via proton deflectometry, corresponding to a peak central magnetic field of $B_0 \approx 12$ T in the 1 mm loop. Good agreement was found with a plasma diode model of the capacitor coil, though further study of resistive heating may be required to match the slow decay of the magnetic field.

The results seen on Vulcan suggest that multi-tesla magnetic fields can be sustained for hundreds of ps and used to magnetize secondary targets. Two shots were

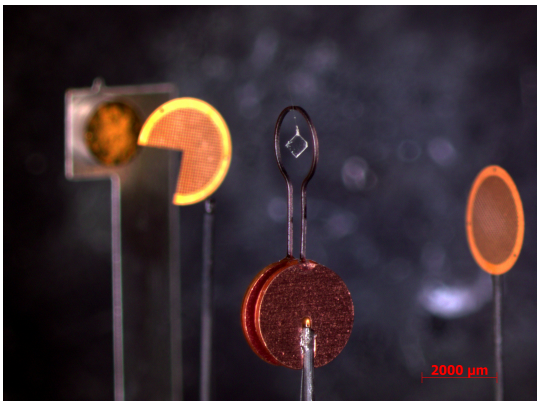

Figure 6.2: Capacitor coil target with CH foil suspended inside a 2 mm-diameter wire loop. Two fiducial grids and a proton foil for orthogonal TNSA deflectometry are visible in the background.

taken with a CH foil target placed inside a 2 mm-diameter capacitor coil loop, as shown in Fig. 6.2. The 20 μm-thick, 500 μm-wide foil was suspended from the top of a capacitor coil loop, oriented with its long edge in line with the loop axis. A single ns beam was used to irradiate the foil at an energy of $\sim$ 180 J, leaving two ns beams to drive the capacitor coil with $\sim$ 350 J combined energy. Fig. 6.3 shows proton radiographs of an exploding CH foil with and without an applied capacitor coil field. Inspection of the axial radiographs reveals that the capacitor coil field has a marked impact on hydrodynamic expansion. Increasing the laser $I_L\lambda_\mu^2$ and using ribbon-shaped targets [46, 82, 94] should produce stronger magnetic fields suitable for many applications including magnetized fusion schemes. Prospects for magnetized ICF are complicated, however, by extended-MHD phenomena like the Nernst effect that dynamically distort the magnetic field profile inside the hot spot and degrade confinement [172, 52]. Recent measurements of magnetic cavitation caused by the Nernst effect in a laser-produced plasma[1] may help to improve modelling of magnetic fields in fusion and HED contexts.

An interesting synergy between the two projects described in this thesis is apparent from capacitor coil experiments with a short-pulse laser drive [185, 173, 9, 94]. These experiments have demonstrated central coil magnetic fields up to tens of tesla that last for a fraction of the duration of the ns experiments. Following Poyé *et al.* [142, 9], it would be instructive to extend the ChoCoLaT model of target charging to capacitor coil targets and longer pulse durations. To further our understanding of the laser-produced plasma and discharge current, one could also conduct experiments on single plate targets with support stalks that can be simultaneously proton probed and connected to an oscilloscope for direct voltage measurements [136, 19]. The stalk could be a straight wire [58] or bent into a loop [9] for applications in

[1] C. Arran *et al.* Measurement of magnetic cavitation in a plasma driven by the Nernst effect, *in prep.*

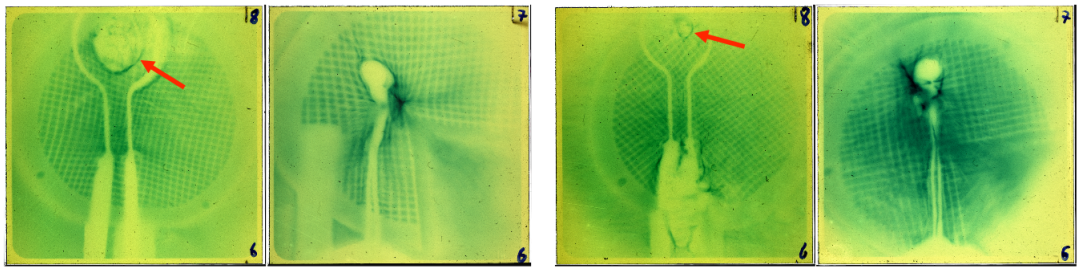

Figure 6.3: Proton radiographs of an ablating CH foil inside a 2 mm-diameter capacitor coil loop. The CH foil is shown *without* a magnetic field (left two images) and *with* a magnetic field (right two images). The leftmost image of each pair corresponds to axial proton probing and the rightmost image to perpendicular probing at $\sim$ 1 ns after the beginning of the laser drive. Note the significant changes in hydrodynamic expansion indicated by the red arrows when the laser is on/off.

magnetized HED physics. This would allow for current and electromagnetic field scalings with laser and target parameters to be established, similar to the work presented in Chap. 4 and Bradford *et al.* [27]. During the experiment reported in Chap. 5, direct voltage measurements of capacitor coil targets were made in order to extract information about target circuit parameters at low energy. Fig. 6.4a shows a capacitor coil attached to the top of a printed circuit board by two metal struts. The base of the circuit board was connected to a coaxial cable and an oscilloscope. A clear voltage scaling with laser energy E_L was observed for $E_L \lesssim 0.8$ J, although evidence of electrical shorting was seen at higher energies. Absolute measurements of the target voltage were not extracted because transmission properties of the Cu struts and printed circuit board were difficult to calculate (see Fig. 6.4a). Future measurements may benefit from a simpler target mounting design. In particular, Williams *et al.* [180] have presented voltage measurements of capacitor coils that were achieved by soldering one side of the target to the centre conductor of a coaxial cable. In the absence of a voltage stripline diagnostic, Rogowski coil measurements of the stalk current can be taken if the coil is placed relatively far away from the laser interaction. Rogowski coil measurements of capacitor coil currents were also taken during the Vulcan experiment described in Chap. 5. Fig. 6.4b shows a miniature Rogowski coil wrapped around the 5 mm-diameter loop of a capacitor coil target. Voltage traces from the coil show evidence of electrical shorting that may have been caused by photoionisation of the coil plastic coating or contact with plasma erupting from the target surface. These problems may be averted if the coil is placed further from the interaction, for example around a metallic support stalk, or by physically shielding the coil from the target plasma. If used on a platform like Vulcan or LULI, long-pulse and short-pulse drives could be employed to characterise behaviour across a broad range of intensities. A single plate geometry would be much easier to model than a hohlraum-like two-plate capacitor coil. It would also be easier to take mea-

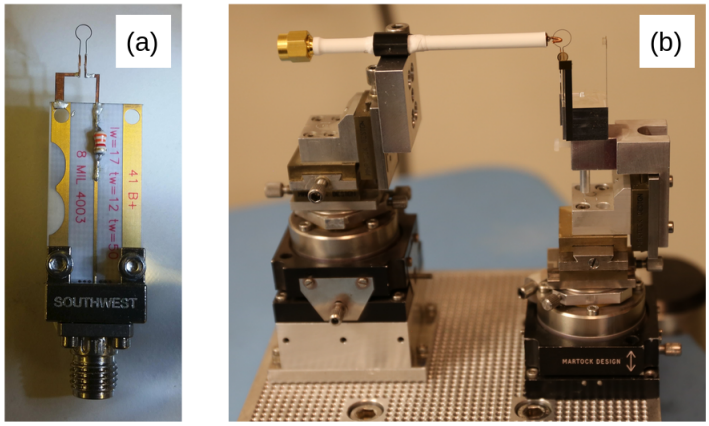

Figure 6.4: (a) Voltage stripline attached to a capacitor coil target via two Cu struts. Targets with and without a 3.3 kΩ resistor were used. (b) Miniature Rogowski coil wrapped around the 5 mm-diameter loop of a capacitor coil target. The Rogowski diagnostic is made from Cu wire soldered to the end of a length of shielded coaxial cable.

surements of the plasma density and hot electron temperature - crucial parameters that determine the amplitude of the discharge current. Thomson scattering measurements of plasma temperature taken on the Vulcan experiment from Chap. 5 were hampered by a closed target geometry [28]. On a fast repetition rate laser system, parameter scans of single plate targets could be made more robust and the lensing of charged particle beams [66] could be explored for applications in advanced fusion schemes [168] or radio-isotope production for medicine [76].

Appendix A

Appendix

A.1 Equivalent circuits

Collections of electrostatic charge inside high power laser targets will discharge on a variety of timescales depending on the resistance, capacitance and impedance of the target and target mount. The behaviour of the target-chamber system can therefore be understood in terms of equivalent circuits [160, 48, 124]. In this Appendix I will examine solutions for the current and voltage of three fundamental series circuits: the RC circuit, the RL circuit and the RLC circuit.

A.1.1 RC series circuits

Consider a standard RC series circuit, as shown in Fig. A.1a. A voltage source is connected in series with a resistor R, capacitor C and path to ground. The voltage source can be separated from the rest of the circuit by opening a switch.

Charging

The voltage source has constant value $V(t) = V_0$ with the switch open at time $t = 0$ so the capacitor is initially uncharged. When the switch is closed, the voltage across the capacitor will be zero ($Q(0) = CV(0)$), so the current through the resistor will be at its maximum ($I(0) = V_0/R$). This current will decrease as charge builds up on the capacitor plates and the capacitor voltage increases. When the switch is closed, the voltage drop across each circuit element can be related by:

$$V_0 = V_R + V_C = IR + Q/C$$

Differentiating:

$$\dot{I} = -I/RC$$

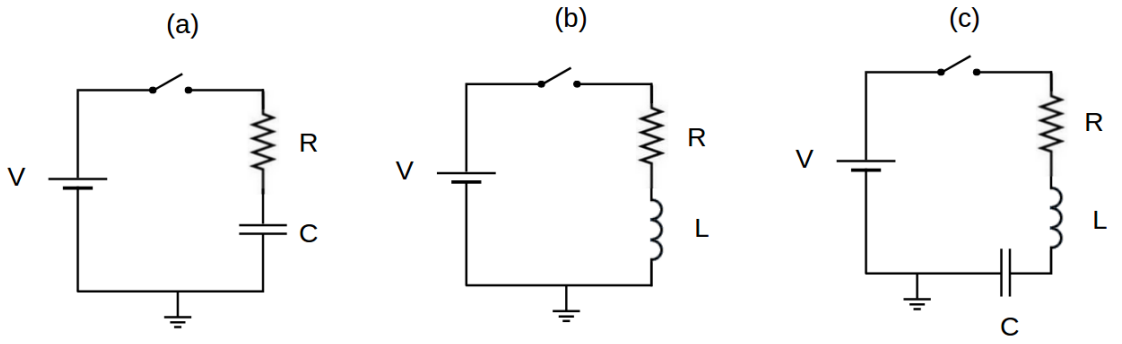

Figure A.1: Schematic diagram of three series circuits with constant applied voltage, V: (a) RC circuit. When the switch is closed, the capacitor will charge and the current will decrease exponentially to zero. If the switch is opened when the capacitor is charged, the current will exponentially decay from a maximum value to zero. (b) RL circuit. When the switch is closed, the circuit will charge and the current increases to a maximum value, $I = V/R$. If the switch is opened while current is flowing, the current will decay exponentially. (c) RLC circuit. Evolution of the circuit current depends on the size of the damping factor, $D = (R/2)\sqrt{C/L}$.

where an overdot is used to represent a derivative with respect to time. Defining $\tau = RC$ and recalling that $I(0) = I_0 = V_0/R$, both sides integrate to yield an exponentially-decaying current profile:

$$I(t) = I_0 e^{-t/\tau} \tag{A.1}$$

where $\tau = RC$ is the time constant of the decay. To solve for the voltage across the capacitor, it suffices to observe that the voltage drop across the resistor is $V_R = I(t)R$. The capacitor voltage follows:

$$V_C(t) = V_0 - V_R = V_0\left(1 - e^{-t/\tau}\right) \tag{A.2}$$

Thus the capacitor voltage grows from zero to the source voltage, V_0. Fig. A.2 shows some example current and voltage profiles relevant to capacitor coil targets. A mm-sized capacitor might have a capacitance of $C = 0.1$ pF and a wire resistance of $R \sim 1\ \Omega$ accounting for Ohmic heating of the wire [169]. For these circuit parameters, the capacitor is charged on a timescale $\sim 5RC = 0.5$ ps.

Discharging

Now I will examine the discharge response of an RC circuit. Consider the capacitor in Fig. A.1a, fully charged to $Q = CV_0$ by an external voltage source. When the voltage source is disconnected (or the switch is suddenly opened), the charge that was held in place by the voltage will discharge to ground. Kirchhoff's Law dictates that:

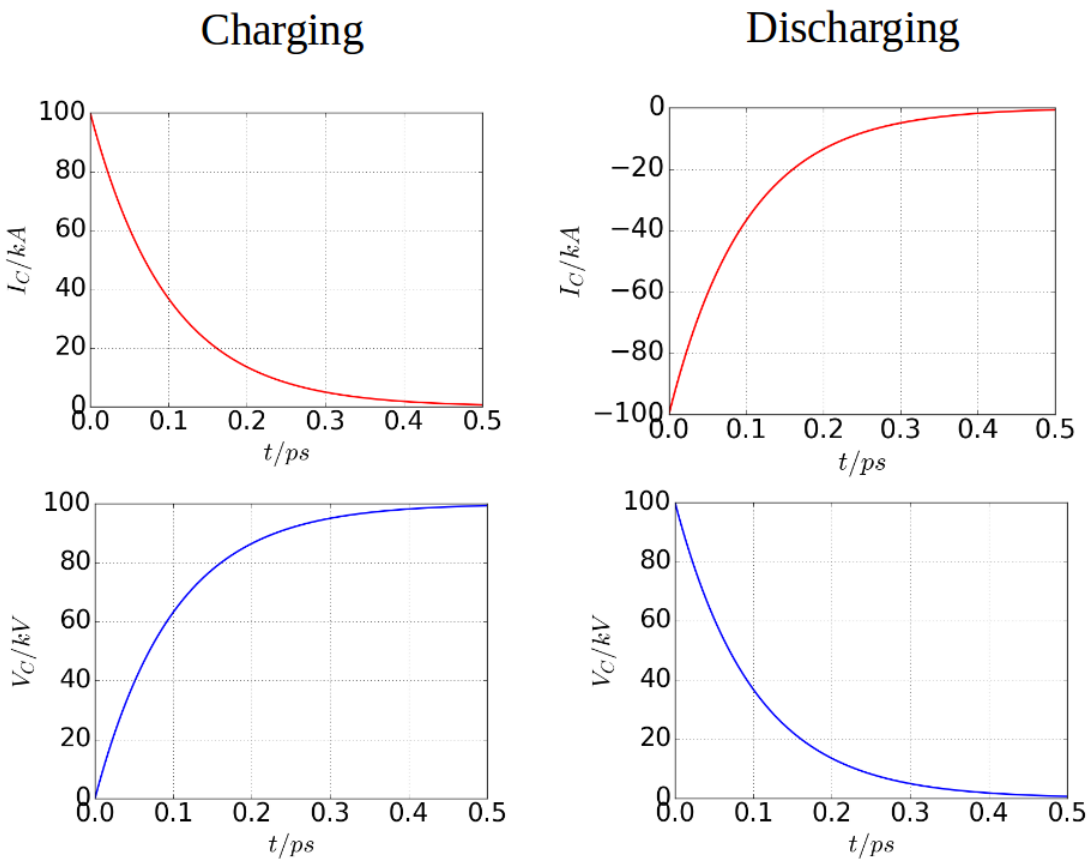

Figure A.2: Current and voltage profiles for a capacitor in a series RC circuit. The left hand column contains profiles for a capacitor that is charging, while the right hand column contains profiles for a capacitor discharge. The top row shows current profiles; the bottom row voltage profiles. Circuit parameters are relevant to capacitor coil discharges, with $R = 1\ \Omega$, $C = 0.1$ nF and $V_0 = 100$ kV. Notice how the charging and discharging takes place on a sub-ps timescale.

$$0 = IR + Q/C$$

Differentiating,

$$0 = \dot{I}R + I/C$$

And

$$\dot{I} = -\frac{I}{RC}$$

This equation can be integrated by separation of variables provided we have an initial condition on the current. Notice that, when the circuit was charging, current flowed clockwise round the circuit in Fig. A.1a. Now, as the capacitor discharges, the current flow reverses as the charge imbalance is restored. Taking $I(0) = I_0 = -V_0/R$, the solution is:

$$I(t) = I_0 e^{-t/\tau} \tag{A.3}$$

where the current now flows in the opposite direction to when the capacitor was charging up and $\tau = RC$. The voltage on the resistor is $V_R = I(t)R$, so the voltage across the capacitor must be:

$$V_C(t) = 0 - V_R(t) = V_0 e^{-t/\tau} \tag{A.4}$$

Here the current decays from a maximum to zero, but in the opposite direction to when the capacitor was charging. The capacitor voltage likewise decays exponentially to zero. Fig. A.2 shows some sample discharge profiles. These profiles might represent a capacitor coil discharge if the wire inductance is ignored. Taking a capacitance of $C = 0.1$ pF and resistance $R = 1\ \Omega$ as in Sec. A.1.1, the current decays on the order of 0.5 ps. In reality, the wire inductance would be non-negligible and the discharge would be significantly slowed by the growth of magnetic fields.

A.1.2 RL series circuits

Consider a standard RL series circuit, as shown in Fig. A.1b. A voltage source is connected in series with a resistor, inductor and path to ground. The voltage source can be separated from the rest of the circuit by opening a switch.

Charging

To charge the RL circuit in Fig. A.1b, a fixed voltage source of magnitude $V = V_0$ is applied and the switch is closed. Adding up the voltage drop across each circuit

element yields an expression for the total voltage in the circuit ($V_0 = V_R + V_L$):

$$V_0 = IR + L\frac{dI}{dt} \tag{A.5}$$

This is a first order linear ordinary differential equation which can be solved using Laplace transforms. First, take the Laplace Transform of both sides of Eq. (A.5):

$$I(s)R + L\left[sI(s) - I(0)\right] = V_0/s$$

for s an arbitrary complex parameter. Thus

$$I(s) = \frac{[V_0/s + LI(0)]}{R + Ls}$$

Applying the initial condition that $I(0) = 0$,

$$I(s) = \frac{V_0}{s(R + Ls)}$$

Then, defining $\tau = L/R$,

$$I(s) = \frac{V_0}{Ls(1/\tau + s)}$$

By linearity of the inverse transform $\mathcal{L}^{-1}$,

$$I(t) = \frac{V_0}{L}\mathcal{L}^{-1}\left(\frac{1}{s(1/\tau + s)}\right) \tag{A.6}$$

The following identity is useful here [22]:

$$\mathcal{L}\left(\frac{e^{-at} - e^{-bt}}{b - a}\right) = \frac{1}{(s + a)(s + b)} \tag{A.7}$$

for a, b real constants, $\mathrm{Re}(s + a) > 0$ and $\mathrm{Re}(s + b) > 0$. Applying this identity to Eq. (A.6), the solution for the current is

$$I(t) = \frac{V_0\tau}{L}\left(1 - e^{-t/\tau}\right)$$

Finally, taking $I_0 = V_0/R$, gives

$$I(t) = I_0\left(1 - e^{-t/\tau}\right) \tag{A.8}$$

Notice that the current grows exponentially towards the value $I_0 = V_0/R$ on a timescale $\tau = L/R$. Since $V(t) = LdI/dt$ for an inductor, the potential across the inductor follows immediately:

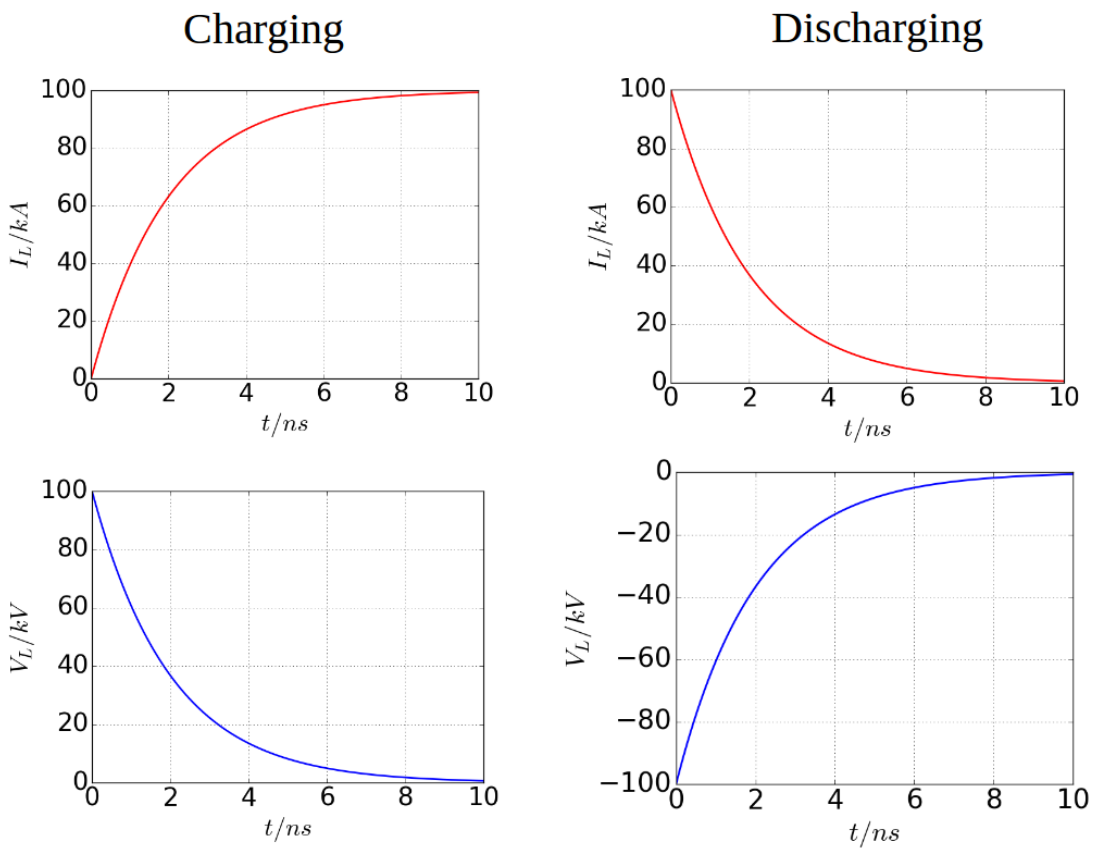

Figure A.3: Current and voltage profiles for an inductor in an RL circuit. Left hand column represents profiles for a circuit that is charging. Right hand column is for an RL circuit discharge. The top row shows current profiles and the bottom row shows voltage profiles. Circuit parameters are relevant to capacitor coil discharges, with $R = 1\ \Omega$, $L = 2$ nH, $V_0 = 100$ kV. Notice how the charging and discharging takes place over ~ 10 ns.

$$V_L = \frac{I_0}{\tau}\left(e^{-t/\tau}\right) \tag{A.9}$$

Graphs of these solutions can be found in Fig. A.3. At early times, as the current builds, the inductor has a large resistance because the electrical energy passing through it is being stored as a magnetic field. Later, when the current has reached a steady value $I = I_0$, the voltage across the inductor is zero and the inductor acts as a short circuit.

Discharging

Now consider the case of an RL circuit with initial current $I(0) = I_0$ and zero voltage, as though the switch has been suddenly opened after the current has achieved its maximum in the charging scenario.

The situation is the same as in Eq. (A.5), except that now the voltage across

the resistor and inductor equals zero because the switch has been opened:

$$IR + L\frac{dI}{dt} = 0 \tag{A.10}$$

Applying the Laplace Transform:

$$I(s)\left[R + Ls\right] - LI_0 = 0$$

and

$$I(s) = \frac{LI_0}{R + Ls}$$

Defining $\tau = L/R$, this expression simplifies to:

$$I(s) = \frac{I_0}{(1/\tau) + s}$$

Referring to Eq. (A.7) (and recalling that the inverse Laplace Transform is a linear operator), yields a solution for $I(t)$:

$$I(t) = I_0 e^{-t/\tau} \tag{A.11}$$

The time constant of the decay is $\tau = L/R$, so a larger inductance and smaller resistance will slow the circuit discharge. The potential across the inductor is given by:

$$V_L = -\frac{I_0}{\tau} e^{-t/\tau} \tag{A.12}$$

Graphs of these solutions are plotted in Fig. A.3. The magnetic energy stored in the inductor at $t = 0$ is returned to electrical energy in the circuit and the resistor dissipates a portion of the electrical energy through Ohmic heating.

A.1.3 RLC series circuits

A series RLC circuit is the simplest example of an oscillating circuit. The solution is different depending on the level of current damping: the circuit may oscillate without decaying (constant amplitude oscillations), the circuit may oscillate but decay in amplitude, or the current may decay to zero without oscillation. I will consider a circuit as shown in Fig. A.1c.

Charging

When the switch is closed, the capacitor begins to charge and build up a voltage ($Q = CV$). The current will drop in proportion to the amount of charge already transported onto the capacitor.

Discharging

Consider a constant voltage V_0, where $V_0 = V_L + V_C + V_R$. Then:

$$V_0 = L\frac{dI}{dt} + \frac{Q}{C} + IR \tag{A.13}$$

Taking the derivative of both sides yields an equation exclusively involving derivatives of the current:

$$0 = \frac{d^2I}{dt^2} + \frac{R}{L}\frac{dI}{dt} + \frac{1}{LC}I \tag{A.14}$$

Equivalently:

$$0 = \frac{d^2I}{dt^2} + 2\alpha\frac{dI}{dt} + \omega^2 I \tag{A.15}$$

where I have defined $\alpha = R/2L$, the attenuation (angular frequency) and $\omega = 1/\sqrt{(LC)}$ (angular frequency). Eq. (A.15) is a second order linear ordinary differential equation that admits three families of solutions depending on the relative sizes of α and ω. For convenience, we can define the damping factor, $D = \alpha/\omega = (R/2)\sqrt{C/L}$. Then, for $D > 1$, the circuit is over-damped and the current decays without oscillation. For $D < 1$, the circuit is under-damped and it will oscillate as it decays. For $D = 1$, the circuit is critically damped and will decay to zero as fast as possible with no oscillation.

Bibliography

[1] H. Ahmed et al. "Proton probing of laser-driven EM pulses travelling in helical coils". In: *High Power Laser Science and Engineering* 5 (2017), pp. 1–5. ISSN: 20523289. DOI: 10.1017/hpl.2016.47.

[2] Hannes Alfvén. "On the Motion of Cosmic Rays in Interstellar Space". In: *Phys. Rev.* 55 (5 Mar. 1939), pp. 425–429. DOI: 10.1103/PhysRev.55.425. URL: https://link.aps.org/doi/10.1103/PhysRev.55.425.

[3] J. E. Allen and J. G. Andrews. "A note on ion rarefaction waves". In: *Journal of Plasma Physics* 4.1 (1970), pp. 187–194. ISSN: 14697807. DOI: 10.1017/S0022377800004906.

[4] T. D. Arber et al. "Contemporary particle-in-cell approach to laser-plasma modelling". In: *Plasma Physics and Controlled Fusion* 57.11 (2015). ISSN: 13616587. DOI: 10.1088/0741-3335/57/11/113001.

[5] T. D. Arber et al. *Users Manual for the EPOCH PIC codes*. http://kfe.fjfi.cvut.cz/~valenpe7/files/12VUIF/epoch_user-4.3.pdf. Accessed: 01-11-2020.

[6] C D Armstrong et al. "Bremsstrahlung emission profile from intense laser-solid interactions as a function of laser focal spot size". In: *Plasma Physics and Controlled Fusion* 61.3 (2018), p. 034001. ISSN: 0741-3335. DOI: 10.1088/1361-6587/aaf596.

[7] *Attenuation for Coleman RG-223 coaxial cable*. https://www.rfparts.com/coax/coax-other/rg223.html. Accessed: 01-08-2017.

[8] S. Atzeni and J. Meyer-ter-Vehn. *The Physics of Inertial Fusion: Beam Plasma Interaction, Hydrodynamics, Hot Dense Matter*. International Series of Monographs on Physics. OUP Oxford, 2004. ISBN: 9780191524059. URL: https://books.google.co.uk/books?id=HiaQDwAAQBAJ.

[9] M. Bailly-Grandvaux. "Laser-driven strong magnetic field generation and high discharge currents: measurements and applications to charged particle transport". PhD thesis. Université de Bordeaux, 2017.

[10] M. Bailly-Grandvaux et al. "Guiding of relativistic electron beams in dense matter by laser-driven magnetostatic fields". In: *Nature Communications* 9 (2018), p. 102. ISSN: 2041-1723. DOI: 10.1038/s41467-017-02641-7. URL: http://dx.doi.org/10.1038/s41467-017-02641-7.

[11] G. H. Baker et al. *Electromagnetic Pulse (EMP) Protection and Resilience Guidelines for Critical Infrastructure and Equipment*. https://www.cisa.gov/sites/default/files/publications/19_0307_CISA_EMP-Protection-Resilience-Guidelines.pdf. Accessed: 29-03-2021.

[12] M. Bardon et al. "Mitigation of strong electromagnetic pulses on the LMJ-PETAL facility". In: *Phys. Rev. Research* 2 (3 Sept. 2020), p. 033502. DOI: 10.1103/PhysRevResearch.2.033502. URL: https://link.aps.org/doi/10.1103/PhysRevResearch.2.033502.

[13] D. Batani et al. "Effects of laser prepulse on proton generation". In: *Nuclear Instruments and Methods in Physics Research, Section A: Accelerators, Spectrometers, Detectors and Associated Equipment* 620.1 (2010), pp. 76–82. ISSN: 01689002. DOI: 10.1016/j.nima.2010.01.064.

[14] C. E. Baum. "From the electromagnetic pulse to high-power electromagnetics". In: *IEEE Proceedings* 80.6 (June 1992), pp. 789–817.

[15] A. Bayramian et al. "Compact, Efficient Laser Systems Required for Laser Inertial Fusion Energy". In: *Fusion Science and Technology* 60.1 (2011), pp. 28–48. DOI: 10.13182/FST10-313. eprint: https://doi.org/10.13182/FST10-313. URL: https://doi.org/10.13182/FST10-313.

[16] F. N. Beg et al. "A study of picosecond laser–solid interactions up to 1019 Wcm-2". In: *Physics of Plasmas* 4.2 (1997), pp. 447–457. DOI: 10.1063/1.872103. eprint: https://doi.org/10.1063/1.872103. URL: https://doi.org/10.1063/1.872103.

[17] A R Bell et al. "Fast-electron transport in high-intensity short-pulse laser-solid experiments". In: *Plasma Physics and Controlled Fusion* 39.5 (May 1997), pp. 653–659. DOI: 10.1088/0741-3335/39/5/001. URL: https://doi.org/10.1088/0741-3335/39/5/001.

[18] A. R. Bell and R. J. Kingham. "Resistive Collimation of Electron Beams in Laser-Produced Plasmas". In: *Phys. Rev. Lett.* 91 (3 July 2003), p. 035003. DOI: 10.1103/PhysRevLett.91.035003. URL: https://link.aps.org/doi/10.1103/PhysRevLett.91.035003.

[19] Robert F. Benjamin, Gene H. McCall, and A. Wayne Ehler. "Measurement of Return Current in a Laser-Produced Plasma". In: *Phys. Rev. Lett.* 42 (14 Apr. 1979), pp. 890–893. DOI: 10.1103/PhysRevLett.42.890. URL: https://link.aps.org/doi/10.1103/PhysRevLett.42.890.

[20] R Betti and O A Hurricane. "Inertial-confinement fusion with lasers". In: *Nature* 12.May (2016), pp. 435–448. DOI: 10.1038/NPHYS3736. URL: https://www.nature.com/nphys/journal/v12/n5/full/nphys3736.html.

[21] J. J. Bissell, C. P. Ridgers, and R. J. Kingham. "Field Compressing Magnetothermal Instability in Laser Plasmas". In: *Phys. Rev. Lett.* 105 (17 Oct. 2010), p. 175001. DOI: 10.1103/PhysRevLett.105.175001. URL: https://link.aps.org/doi/10.1103/PhysRevLett.105.175001.

[22] Mary L Boas. *Mathematical methods in the physical sciences*. John Wiley & Sons, 2006.

[23] M. Borghesi et al. "Electric field detection in laser-plasma interaction experiments via the proton imaging technique". In: *Physics of Plasmas* 9.5 (2002), pp. 2214–2220. ISSN: 1070664X. DOI: 10.1063/1.1459457.

[24] Marco Borghesi. "Laser-driven ion acceleration: State of the art and emerging mechanisms". In: *Nuclear Instruments and Methods in Physics Research Section A: Accelerators, Spectrometers, Detectors and Associated Equipment* 740 (2014). Proceedings of the first European Advanced Accelerator Concepts Workshop 2013, pp. 6–9. ISSN: 0168-9002. DOI: https://doi.org/10.1016/j.nima.2013.11.098. URL: http://www.sciencedirect.com/science/article/pii/S016890021301663X.

[25] A. F. A. Bott et al. "Proton imaging of stochastic magnetic fields". In: *Journal of Plasma Physics* 83.6 (2017), p. 905830614. DOI: 10.1017/S0022377817000939.

[26] Thomas Brabec and Ferenc Krausz. "Intense few-cycle laser fields: Frontiers of nonlinear optics". In: *Rev. Mod. Phys.* 72 (2 May 2000), pp. 545–591. DOI: 10.1103/RevModPhys.72.545. URL: https://link.aps.org/doi/10.1103/RevModPhys.72.545.

[27] P. Bradford et al. "EMP control and characterization on high-power laser systems". In: *High Power Laser Science and Engineering* 6 (2018), e21. DOI: 10.1017/hpl.2018.21.

[28] P. Bradford et al. "Proton deflectometry of a capacitor coil target along two axes". In: *High Power Laser Science and Engineering* 8 (2020), e11. DOI: 10.1017/hpl.2020.9.

[29] C J Brown Jr. et al. "Electromagnetic Pulses at Short-Pulse Laser Facilities". In: *Journal of Physics: Conference Series* 112 (2008), p. 032025. DOI: 10.1088/1742-6596/112/3/032025.

[30] Brown, C.G. et al. "Analysis of electromagnetic pulse (EMP) measurements in the National Ignition Facility's target bay and chamber". In: *EPJ Web of Conferences* 59 (2013), p. 08012. DOI: 10.1051/epjconf/20135908012. URL: https://doi.org/10.1051/epjconf/20135908012.

[31] F. Brunel. "Not-so-resonant, resonant absorption". In: *Phys. Rev. Lett.* 59 (1 July 1987), pp. 52–55. DOI: 10.1103/PhysRevLett.59.52. URL: https://link.aps.org/doi/10.1103/PhysRevLett.59.52.

[32] A.I. Bykov et al. "VNIIEF achievements on ultra-high magnetic fields generation". In: *Physica B: Condensed Matter* 294-295 (2001). Proceedings of the Sixth International Symposium on Research in High Magnetic Fields, pp. 574–578. ISSN: 0921-4526. DOI: https://doi.org/10.1016/S0921-4526(00)00723-7. URL: http://www.sciencedirect.com/science/article/pii/S0921452600007237.

[33] Hong-bo Cai et al. "Enhancing the Number of High-Energy Electrons Deposited to a Compressed Pellet via Double Cones in Fast Ignition". In: *Phys. Rev. Lett.* 102 (24 June 2009), p. 245001. DOI: 10.1103/PhysRevLett.102.245001. URL: https://link.aps.org/doi/10.1103/PhysRevLett.102.245001.

[34] D.C. Carroll et al. "A modified Thomson parabola spectrometer for high resolution multi-MeV ion measurements—Application to laser-driven ion acceleration". In: *Nuclear Instruments and Methods in Physics Research Section A: Accelerators, Spectrometers, Detectors and Associated Equipment* 620.1 (2010). COULOMB09, pp. 23–27. ISSN: 0168-9002. DOI: https://doi.org/10.1016/j.nima.2010.01.054. URL: http://www.sciencedirect.com/science/article/pii/S0168900210001221.

[35] P Y Chang et al. "Fusion Yield Enhancement in Magnetized Laser-Driven Implosions". In: *Physical Review Letters* 107.July (2011), p. 035006. DOI: 10.1103/PhysRevLett.107.035006.

[36] F.F. Chen. *Introduction to Plasma Physics and Controlled Fusion*. Introduction to Plasma Physics and Controlled Fusion v. 1. Springer, 1984. ISBN: 9780306413322. URL: https://books.google.co.uk/books?id=ToAtqnznr80C.

[37] Nicholas F. Y. Chen et al. "Machine learning applied to proton radiography of high-energy-density plasmas". In: *Phys. Rev. E* 95 (4 Apr. 2017), p. 043305. DOI: 10.1103/PhysRevE.95.043305. URL: https://link.aps.org/doi/10.1103/PhysRevE.95.043305.

[38] Zi-yu Chen et al. "Influence of lateral target size on hot electron production and electromagnetic pulse emission from laser-irradiated metallic targets". In: *Physics of Plasmas* 19.2012 (2012), p. 113116. DOI: 10.1063/1.4767910.

[39] Abraham Chien et al. "Study of a magnetically driven reconnection platform using ultrafast proton radiography". In: *Physics of Plasmas* 26.6 (2019), p. 062113. DOI: 10.1063/1.5095960. eprint: https://doi.org/10.1063/1.5095960. URL: https://doi.org/10.1063/1.5095960.

[40] E. L. Clark et al. "Measurements of Energetic Proton Transport through Magnetized Plasma from Intense Laser Interactions with Solids". In: *Phys. Rev. Lett.* 84 (4 Jan. 2000), pp. 670–673. DOI: 10.1103/PhysRevLett.84.670. URL: https://link.aps.org/doi/10.1103/PhysRevLett.84.670.

[41] *COMSOL multiphysics®*. www.comsol.com.

[42] F Consoli et al. "Time-resolved absolute measurements by electro-optic effect of giant electromagnetic pulses due to laser-plasma interaction in nanosecond regime". In: *Scientific Reports* 6.1 (2016), p. 27889. ISSN: 2045-2322. DOI: 10.1038/srep27889. URL: http://www.nature.com/articles/srep27889.

[43] Fabrizio Consoli et al. "Laser produced electromagnetic pulses: generation, detection and mitigation". In: *High Power Laser Science and Engineering* 8 (2020), e22. DOI: 10.1017/hpl.2020.13.

[44] C Courtois et al. "Creation of a uniform high magnetic-field strength environment for laser-driven experiments". In: *Journal of Applied Physics* 98 (2005), p. 054913. DOI: 10.1063/1.2035896.

[45] J. E. Crow, P. L. Auer, and J. E. Allen. "The expansion of a plasma into a vacuum". In: *Journal of Plasma Physics* 14.1 (1975), pp. 65–76. DOI: 10.1017/S0022377800025538.

[46] H. Daido et al. "Generation of a Strong Magnetic Field by an Intense CO2 Laser Pulse". In: *Physical Review Letters* 56.8 (1986). DOI: 10.1103/PhysRevLett.56.846.

[47] Hiroyuki Daido, Mamiko Nishiuchi, and Alexander S Pirozhkov. "Review of laser-driven ion sources and their applications". In: *Reports on Progress in Physics* 75.5 (Apr. 2012), p. 056401. DOI: 10.1088/0034-4885/75/5/056401. URL: https://doi.org/10.1088%2F0034-4885%2F75%2F5%2F056401.

[48] Hiroyuki Daido et al. "Ultrahigh Pulsed Magnetic Field Produced by a CO2Laser". In: *Japanese Journal of Applied Physics* 26.Part 1, No. 8 (Aug. 1987), pp. 1290–1295. DOI: 10.1143/jjap.26.1290. URL: https://doi.org/10.1143/jjap.26.1290.

[49] Colin N. Danson et al. "Petawatt and exawatt class lasers worldwide". In: *High Power Laser Science and Engineering* 7 (2019), e54. DOI: 10.1017/hpl.2019.36.

[50] *Data sheet for B-24 magnetic field sensor*. https://www.prodyntech.com/wp-content/uploads/2013/09/B-Dot-B-24.pdf. Accessed: 01-08-2017.

[51] J. R. Davies. "Alfvén limit in fast ignition". In: *Phys. Rev. E* 69 (6 June 2004), p. 065402. DOI: 10.1103/PhysRevE.69.065402. URL: https://link.aps.org/doi/10.1103/PhysRevE.69.065402.

[52] J. R. Davies et al. "The importance of electrothermal terms in Ohm's law for magnetized spherical implosions". In: *Physics of Plasmas* 22.11 (2015), p. 112703. DOI: 10.1063/1.4935286. eprint: https://doi.org/10.1063/1.4935286. URL: https://doi.org/10.1063/1.4935286.

[53] J.R. Davies. "The Alfvén limit revisited and its relevance to laser-plasma interactions". In: *Laser and Particle Beams* 24.2 (2006), pp. 299–310. DOI: 10.1017/S0263034606060460.

[54] François Debray and Paul Frings. "State of the art and developments of high field magnets at the "Laboratoire National des Champs Magnétiques Intenses"". In: *Comptes Rendus Physique* 14.1 (2013). Physics in High Magnetic Fields / Physique en champ magnétique intense, pp. 2–14. ISSN: 1631-0705. DOI: https://doi.org/10.1016/j.crhy.2012.11.002. URL: http://www.sciencedirect.com/science/article/pii/S1631070512001545.

[55] J. F. Drake et al. "Parametric instabilities of electromagnetic waves in plasmas". In: *The Physics of Fluids* 17.4 (1974), pp. 778–785. DOI: 10.1063/1.1694789. eprint: https://aip.scitation.org/doi/pdf/10.1063/1.1694789. URL: https://aip.scitation.org/doi/abs/10.1063/1.1694789.

[56] R.P. Drake. *High-Energy-Density Physics: Foundation of Inertial Fusion and Experimental Astrophysics*. Graduate Texts in Physics. Springer International Publishing, 2018. ISBN: 9783319677118.

[57] J. L. Dubois et al. "Experimental demonstration of an electromagnetic pulse mitigation concept for a laser driven proton source". In: *Review of Scientific Instruments* 89.10 (2018), p. 103301. DOI: 10.1063/1.5038652. eprint:

https://doi.org/10.1063/1.5038652. URL: https://doi.org/10.1063/1.5038652.

[58] J. L. Dubois et al. "Target charging in short-pulse-laser-plasma experiments". In: *Physical Review E - Statistical, Nonlinear, and Soft Matter Physics* 89.1 (2014), pp. 1–15. ISSN: 15393755. DOI: 10.1103/PhysRevE.89.013102.

[59] P. H. Duncan. "Analysis of the Moebius Loop Magnetic Field Sensor". In: *IEEE Transactions on Electromagnetic Compatibility* EMC-16.2 (1974), pp. 83–89.

[60] M. Dunne et al. "Timely Delivery of Laser Inertial Fusion Energy (LIFE)". In: *Fusion Science and Technology* 60.1 (2011), pp. 19–27. DOI: 10.13182/FST10-316. eprint: https://doi.org/10.13182/FST10-316. URL: https://doi.org/10.13182/FST10-316.

[61] D C Eder et al. "Mitigation of Electromagnetic Pulse (EMP) Effects from Short-Pulse Lasers and Fusion Neutrons". In: *Lawrence Livermore National Laboratory Report* LLNL-TR-411183 (Mar. 2009). DOI: 10.2172/950076.

[62] W. R. Edgel. *Prodyn Application Note 192: Electric and Magnetic Field Sensor Application*. https://www.prodyntech.com/wp-content/uploads/2013/10/PAN192.pdf. Accessed: 01-06-2018.

[63] W. R. Edgel. *Prodyn Application Note 895: Primer on Electromagnetic Field Measurements*. https://www.prodyntech.com/wp-content/uploads/2014/07/Pan-895-07012014.pdf. Accessed: 01-06-2018.

[64] C. B. Edwards et al. "200TW upgrade of the Vulcan Nd:glass laser facility". In: *AIP Conference Proceedings* 426.1 (1998), pp. 485–490. DOI: 10.1063/1.55212. eprint: https://aip.scitation.org/doi/pdf/10.1063/1.55212. URL: https://aip.scitation.org/doi/abs/10.1063/1.55212.

[65] M. J. Edwards et al. "Progress towards ignition on the National Ignition Facility". In: *Physics of Plasmas* 20.7 (2013), p. 070501. DOI: 10.1063/1.4816115. eprint: https://doi.org/10.1063/1.481611. URL: https://doi.org/10.1063/1.4816115.

[66] M. Ehret et al. *Energy selective focusing of TNSA beams by picosecond-laser driven ultra-fast EM fields*. News and Reports from HEDgeHOB GSI-2017-2. Version 2014-06-30. GSI, June 1, 2017. URL: https://indico.gsi.de/event/5681/attachments/19125/24066/HEDP_2016_web_version_new.pdf.

[67] Kent Estabrook and W. L. Kruer. "Properties of Resonantly Heated Electron Distributions". In: *Phys. Rev. Lett.* 40 (1 Jan. 1978), pp. 42–45. DOI: 10.1103/PhysRevLett.40.42. URL: https://link.aps.org/doi/10.1103/PhysRevLett.40.42.

[68] E. T. Everson et al. "Design, construction, and calibration of a three-axis, high-frequency magnetic probe (B-dot probe) as a diagnostic for exploding plasmas". In: *Review of Scientific Instruments* 80.11 (2009), pp. 1–8. ISSN: 00346748. DOI: 10.1063/1.3246785.

[69] B. Fasenfest and D. White. "Electrostatic Breakdown Analysis using EM-solve and BEMSTER". In: *Lawrence Livermore National Laboratory Report* UCRL-TR-212727 (June 2005). DOI: 10.2172/877855.

[70] Yiwei Feng et al. "Spectral calibration of EBT3 and HD-V2 radiochromic film response at high dose using 20 MeV proton beams". In: *Review of Scientific Instruments* 89.4 (2018), p. 043511. DOI: 10.1063/1.4996022. eprint: https://doi.org/10.1063/1.4996022. URL: https://doi.org/10.1063/1.4996022.

[71] Gennady Fiksel et al. "A simple model for estimating a magnetic field in laser-driven coils". In: *Applied Physics Letters* 109.13 (2016), p. 134103. DOI: 10.1063/1.4963763. eprint: https://doi.org/10.1063/1.4963763. URL: https://aip.scitation.org/doi/10.1063/1.4963763.

[72] K. FLIPPO et al. "Laser-driven ion accelerators: Spectral control, monoenergetic ions and new acceleration mechanisms". In: *Laser and Particle Beams* 25.1 (2007), pp. 3–8. DOI: 10.1017/S0263034607070012.

[73] D. W. Forslund, J. M. Kindel, and K. Lee. "Theory of Hot-Electron Spectra at High Laser Intensity". In: *Phys. Rev. Lett.* 39 (5 Aug. 1977), pp. 284–288. DOI: 10.1103/PhysRevLett.39.284. URL: https://link.aps.org/doi/10.1103/PhysRevLett.39.284.

[74] J. S. Foster et al. "Report of the Commission to Assess the Threat to the United States from Electromagnetic Pulse (EMP) Attack". In: *Congressional Report* 1 (2004).

[75] C. M. Fowler, W. B. Garn, and R. S. Caird. "Production of very high magnetic fields by implosion". In: *Journal of Applied Physics* 31.3 (1960), pp. 588–594. ISSN: 00218979. DOI: 10.1063/1.1735633.

[76] S. Fritzler et al. "Proton beams generated with high-intensity lasers: Applications to medical isotope production". In: *Applied Physics Letters* 83.15 (2003), pp. 3039–3041. DOI: 10.1063/1.1616661. eprint: https://doi.org/10.1063/1.1616661. URL: https://doi.org/10.1063/1.1616661.

[77] Shinsuke Fujioka et al. “Kilotesla magnetic field due to a capacitor-coil target driven by high power laser”. In: *Scientific Reports* 3 (2013), pp. 1–7. ISSN: 20452322. DOI: 10.1038/srep01170.

[78] L. Gao et al. “Precision Mapping of Laser-Driven Magnetic Fields and Their Evolution in High-Energy-Density Plasmas”. In: *Phys. Rev. Lett.* 114 (21 May 2015), p. 215003. DOI: 10.1103/PhysRevLett.114.215003. URL: https://link.aps.org/doi/10.1103/PhysRevLett.114.215003.

[79] Lan Gao et al. “Ultrafast proton radiography of the magnetic fields generated by a laser-driven coil current”. In: *Physics of Plasmas* 23.4 (2016), p. 043106. DOI: 10.1063/1.4945643. eprint: https://doi.org/10.1063/1.4945643. URL: https://doi.org/10.1063/1.4945643.

[80] P. Gibbon. *Short Pulse Laser Interactions with Matter: An Introduction*. Imperial College Press, 2005.

[81] S. J. Gitomer et al. “Fast ions and hot electrons in the laser–plasma interaction”. In: *The Physics of Fluids* 29.8 (1986), pp. 2679–2688. DOI: 10.1063/1.865510. eprint: https://aip.scitation.org/doi/pdf/10.1063/1.865510. URL: https://aip.scitation.org/doi/abs/10.1063/1.865510.

[82] C Goyon et al. “Ultrafast probing of magnetic field growth inside a laser-driven solenoid”. In: *Physical Review E* 95 (2017), p. 033208. ISSN: 15502376. DOI: 10.1103/PhysRevE.95.033208.

[83] C. Graziani et al. “Inferring morphology and strength of magnetic fields from proton radiographs”. In: *Review of Scientific Instruments* 88.12 (2017), p. 123507. DOI: 10.1063/1.5013029. eprint: https://doi.org/10.1063/1.5013029. URL: https://doi.org/10.1063/1.5013029.

[84] G. Gregori et al. “Generation of scaled protogalactic seed magnetic fields in laser-produced shock waves”. In: *Nature* 481.7382 (2012), pp. 480–483. ISSN: 00280836. DOI: 10.1038/nature10747.

[85] Seungyong Hahn et al. “45.5-Tesla Direct-Current Magnetic Field Generated With a High-Temperature Superconducting Magnet”. In: *Nature* 570.7762 (2019), pp. 496–499. ISSN: 14764687. DOI: 10.1038/s41586-019-1293-1. URL: http://dx.doi.org/10.1038/s41586-019-1293-1.

[86] M G Haines. “A review of the dense Z-pinch”. In: *Plasma Physics and Controlled Fusion* 53.9 (June 2011), p. 093001. DOI: 10.1088/0741-3335/53/9/093001. URL: https://doi.org/10.1088/0741-3335/53/9/093001.

[87] M. G. Haines. "Magnetic-field generation in laser fusion and hot-electron transport". In: *Canadian Journal of Physics* 64.8 (1986), pp. 912–919. DOI: 10.1139/p86-160. eprint: https://doi.org/10.1139/p86-160. URL: https://doi.org/10.1139/p86-160.

[88] M. G. Haines. "Saturation Mechanisms for the Generated Magnetic Field in Nonuniform Laser-Matter Irradiation". In: *Phys. Rev. Lett.* 78 (2 Jan. 1997), pp. 254–257. DOI: 10.1103/PhysRevLett.78.254. URL: https://link.aps.org/doi/10.1103/PhysRevLett.78.254.

[89] D. S. Hey et al. "Use of GafChromic film to diagnose laser generated proton beams". In: *Review of Scientific Instruments* 79.5 (2008), p. 053501. DOI: 10.1063/1.2901603. eprint: https://doi.org/10.1063/1.2901603. URL: https://doi.org/10.1063/1.2901603.

[90] M. Hohenberger et al. "Inertial confinement fusion implosions with imposed magnetic field compression using the OMEGA Laser". In: *Physics of Plasmas* 19.5 (2012), p. 056306. DOI: 10.1063/1.3696032. eprint: https://doi.org/10.1063/1.3696032. URL: https://doi.org/10.1063/1.3696032.

[91] J. Howard et al. "Measured close lightning leader-step electric field–derivative waveforms". In: *Journal of Geophysical Research: Atmospheres* 116.D8 (2011). DOI: https://doi.org/10.1029/2010JD015249. eprint: https://agupubs.onlinelibrary.wiley.com/doi/pdf/10.1029/2010JD015249. URL: https://agupubs.onlinelibrary.wiley.com/doi/abs/10.1029/2010JD015249.

[92] T. Hubing and N. Hubing. *Practical EM Shielding*. http://learnemc.com/practical-em-shielding. Accessed: 29-03-2021.

[93] I. H. Hutchinson. "Magnetic diagnostics". In: *Principles of Plasma Diagnostics*. 2nd ed. Cambridge University Press, 2002, pp. 11–54. DOI: 10.1017/CBO9780511613630.004.

[94] V. V. Ivanov et al. "Study of laser-driven magnetic fields with a continuous wave Faraday rotation diagnostic". In: *Physics of Plasmas* 27.3 (2020), p. 033102. DOI: 10.1063/1.5141753. eprint: https://doi.org/10.1063/1.5141753. URL: https://doi.org/10.1063/1.5141753.

[95] John David Jackson. *Classical electrodynamics; 2nd ed.* New York, NY: Wiley, 1975.

[96] K Kanaya and S Okayama. "Penetration and energy-loss theory of electrons in solid targets". In: *Journal of Physics D: Applied Physics* 5.1 (Jan. 1972), pp. 43–58. DOI: 10.1088/0022-3727/5/1/308. URL: https://doi.org/10.1088/0022-3727/5/1/308.

[97] Satyabrata Kar et al. "Guided post-acceleration of laser-driven ions by a miniature modular structure". In: *Nature Communications* 7 (2016), pp. 1–7. ISSN: 20411723. DOI: 10.1038/ncomms10792. URL: http://dx.doi.org/10.1038/ncomms10792.

[98] Muhammad Firmansyah Kasim et al. "Quantitative shadowgraphy and proton radiography for large intensity modulations". In: *Phys. Rev. E* 95 (2 Feb. 2017), p. 023306. DOI: 10.1103/PhysRevE.95.023306. URL: https://link.aps.org/doi/10.1103/PhysRevE.95.023306.

[99] H. Kishan. *Differential Calculus*. Atlantic Publishers & Distributors (P) Limited, 2007. ISBN: 9788126908202. URL: https://books.google.co.uk/books?id=90mk7qPAvb4C.

[100] J P Knauer et al. "Compressing magnetic fields with high-energy lasers ". In: *Physics of Plasmas* 17 (2010), p. 056318. DOI: 10.1063/1.3416557.

[101] A. S. Kompaneets. "Radio Emission from an Atomic Explosion". In: *Journal of Experimental and Theoretical Physics* 35 (June 1958), pp. 1538–1544. URL: http://www.jetp.ac.ru/cgi-bin/dn/e_008_06_1076.pdf.

[102] VV Korobkin and SL Motylev. "On a possibility of using laser radiation for generation of strong magnetic fields". In: *Sov. Tech. Phys. Lett* 5 (1979), p. 474.

[103] W. L. Kruer and Kent Estabrook. "J×B heating by very intense laser light". In: *The Physics of Fluids* 28.1 (1985), pp. 430–432. DOI: 10.1063/1.865171. eprint: https://aip.scitation.org/doi/pdf/10.1063/1.865171. URL: https://aip.scitation.org/doi/abs/10.1063/1.865171.

[104] N. L. Kugland et al. "Invited Article: Relation between electric and magnetic field structures and their proton-beam images". In: *Review of Scientific Instruments* 83.10 (2012), p. 101301. ISSN: 00346748. DOI: 10.1063/1.4750234.

[105] K. F. F. Law et al. "Direct measurement of kilo-tesla level magnetic field generated with laser-driven capacitor-coil target by proton deflectometry". In: *Applied Physics Letters* 108.9 (2016), p. 091104. DOI: 10.1063/1.4943078. eprint: https://doi.org/10.1063/1.4943078. URL: https://doi.org/10.1063/1.4943078.

[106] K. F. F. Law et al. "Relativistic magnetic reconnection in laser laboratory for testing an emission mechanism of hard-state black hole system". In: *Phys. Rev. E* 102 (3 Sept. 2020), p. 033202. DOI: 10.1103/PhysRevE.102.033202. URL: https://link.aps.org/doi/10.1103/PhysRevE.102.033202.

[107] C K Li et al. "Diagnosing indirect-drive inertial-confinement-fusion implosions with charged particles". In: *Plasma Physics and Controlled Fusion* 52.12 (2010), p. 124027. ISSN: 0741-3335. DOI: 10.1088/0741-3335/52/12/124027.

[108] C. K. Li et al. "Monoenergetic proton backlighter for measuring e and B fields and for radiographing implosions and high-energy density plasmas (invited)". In: *Review of Scientific Instruments* 77.10 (2006), 10E725. ISSN: 00346748. DOI: 10.1063/1.2228252.

[109] Guo-Qian Liao et al. "Towards Terawatt-Scale Spectrally Tunable Terahertz Pulses via Relativistic Laser-Foil Interactions". In: *Phys. Rev. X* 10 (3 Sept. 2020), p. 031062. DOI: 10.1103/PhysRevX.10.031062. URL: https://link.aps.org/doi/10.1103/PhysRevX.10.031062.

[110] Guoqian Liao et al. "Multimillijoule coherent terahertz bursts from picosecond laser-irradiated metal foils". In: *Proceedings of the National Academy of Sciences* 116.10 (2019), pp. 3994–3999. ISSN: 0027-8424. DOI: 10.1073/pnas.1815256116. eprint: https://www.pnas.org/content/116/10/3994.full.pdf. URL: https://www.pnas.org/content/116/10/3994.

[111] John Lindl. "Development of the indirect-drive approach to inertial confinement fusion and the target physics basis for ignition and gain". In: *Physics of Plasmas* 2 (1995), p. 3933. DOI: 10.1063/1.871025.

[112] A. Link, Douglass Schumacher, and Linn Van Woerkom. "Effects of target charging and ion emission on the energy spectrum of emitted electrons". In: *Physics of Plasmas* 18 (May 2011). DOI: 10.1063/1.3587123.

[113] C. L. Longmire. "Justification and Verification of High-Altitude EMP Theory". In: *Lawrence Livermore National Laboratory Report* LLNL-9323905 (June 1963).

[114] C. L. Longmire. "On the Electromagnetic Pulse Produced by Nuclear Explosions". In: *IEEE Transactions on Electromagnetic Compatibility* EMC-20.1 (1978), pp. 3–13. DOI: 10.1109/TEMC.1978.303688.

[115] L. B. Lucy. "An iterative technique for the rectification of observed distributions". In: *The Astronomical Journal* 79 (June 1974), p. 745. DOI: 10.1086/111605. URL: https://ui.adsabs.harvard.edu/abs/1974AJ.....79..745L.

[116] Andrea Macchi, Marco Borghesi, and Matteo Passoni. "Ion acceleration by superintense laser-plasma interaction". In: *Rev. Mod. Phys.* 85 (2 May 2013), pp. 751–793. DOI: 10.1103/RevModPhys.85.751. URL: https://link.aps.org/doi/10.1103/RevModPhys.85.751.

[117] G. Malka and J. L. Miquel. "Experimental Confirmation of Ponderomotive-Force Electrons Produced by an Ultrarelativistic Laser Pulse on a Solid Target". In: *Phys. Rev. Lett.* 77 (1 July 1996), pp. 75–78. DOI: 10.1103/PhysRevLett.77.75. URL: https://link.aps.org/doi/10.1103/PhysRevLett.77.75.

[118] M. J.-E. Manuel et al. "Mapping return currents in laser-generated Z-pinch plasmas using proton deflectometry". In: *Applied Physics Letters* 100.20 (2012), p. 203505. DOI: 10.1063/1.4718425. eprint: https://doi.org/10.1063/1.4718425. URL: https://doi.org/10.1063/1.4718425.

[119] D Mariscal et al. "First demonstration of ARC-accelerated proton beams at the National Ignition Facility". In: *Physics of Plasmas* 26.4 (2019), p. 043110.

[120] C. R. McDonald et al. "Tunnel Ionization Dynamics of Bound Systems in Laser Fields: How Long Does It Take for a Bound Electron to Tunnel?" In: *Phys. Rev. Lett.* 111 (9 Aug. 2013), p. 090405. DOI: 10.1103/PhysRevLett.111.090405. URL: https://link.aps.org/doi/10.1103/PhysRevLett.111.090405.

[121] Paul McKenna et al. "High-intensity laser-driven proton acceleration: influence of pulse contrast". In: *Philosophical Transactions of the Royal Society A: Mathematical, Physical and Engineering Sciences* 364.1840 (2006), pp. 711–723. DOI: 10.1098/rsta.2005.1733. eprint: https://royalsocietypublishing.org/doi/pdf/10.1098/rsta.2005.1733. URL: https://royalsocietypublishing.org/doi/abs/10.1098/rsta.2005.1733.

[122] M. J. Mead et al. "Electromagnetic pulse generation within a petawatt laser target chamber". In: *Review of Scientific Instruments* 75.10 (2004), pp. 4225–4227. DOI: 10.1063/1.1787606. eprint: https://doi.org/10.1063/1.1787606. URL: https://doi.org/10.1063/1.1787606.

[123] S. J. Millington, D. C. Carroll, and J. S. Green. *Validity of the Analysis of Radiochromic Film Using Matlab Code*. https://www.clf.stfc.ac.uk/Pages/ar14-15_Development_Millington.pdf. Accessed: 01-06-2020. 2016.

[124] Damien F. G. Minenna et al. "Electromagnetic pulse emission from target holders during short-pulse laser interactions". In: *Physics of Plasmas* 27.6 (2020), p. 063102. DOI: 10.1063/5.0006666. eprint: https://doi.org/10.1063/5.0006666. URL: https://doi.org/10.1063/5.0006666.

[125] *Model FD-5 series D-dot sensors*. https://www.prodyntech.com/wp-content/uploads/2013/09/D-Dot-FD-5-11-22-2013.pdf. Accessed: 01-08-2017.

[126] Ralph W. Moir. "The High-Yield Lithium-Injection Fusion-Energy (HYLIFE)-II inertial fusion energy (IFE) power plant concept and implications for IFE". In: *Physics of Plasmas* 2.6 (1995), pp. 2447–2452. DOI: 10.1063/1.871269. eprint: https://doi.org/10.1063/1.871269. URL: https://doi.org/10.1063/1.871269.

[127] J. Moody et al. *Time-dependence of laser-driven magnetic field generation for long laser drive conditions.* https://ui.adsabs.harvard.edu/abs/2018APS..DPPPO7002M/abstract. Accessed: 25-03-2020.

[128] J. D. Moody et al. "Transient magnetic field diffusion considerations relevant to magnetically assisted indirect drive inertial confinement fusion". In: *Physics of Plasmas* 27.11 (2020), p. 112711. DOI: 10.1063/5.0022722. eprint: https://doi.org/10.1063/5.0022722. URL: https://doi.org/10.1063/5.0022722.

[129] P. Mora. "Plasma Expansion into a Vacuum". In: *Phys. Rev. Lett.* 90 (18 May 2003), p. 185002. DOI: 10.1103/PhysRevLett.90.185002. URL: https://link.aps.org/doi/10.1103/PhysRevLett.90.185002.

[130] Hiroki Morita et al. "Dynamics of laser-generated magnetic fields using long laser pulses". In: *Phys. Rev. E* 103 (3 Mar. 2021), p. 033201. DOI: 10.1103/PhysRevE.103.033201. URL: https://link.aps.org/doi/10.1103/PhysRevE.103.033201.

[131] D. Nakamura et al. "Record indoor magnetic field of 1200 T generated by electromagnetic flux-compression". In: *Review of Scientific Instruments* 89.9 (2018). ISSN: 10897623. DOI: 10.1063/1.5044557. URL: http://dx.doi.org/10.1063/1.5044557.

[132] K. Nakao et al. "A laboratory instrument for generating magnetic fields over 200 T with single turn coils". In: *Journal of Physics E: Scientific Instruments* 18.12 (1985), pp. 1018–1026. ISSN: 00223735. DOI: 10.1088/0022-3735/18/12/006.

[133] M. Nakatsutsumi et al. "Self-generated surface magnetic fields inhibit laser-driven sheath acceleration of high-energy protons". In: *Nature Communications* 9.1 (2018), pp. 1–9. ISSN: 20411723. DOI: 10.1038/s41467-017-02436-w. URL: http://dx.doi.org/10.1038/s41467-017-02436-w.

[134] P. M. Nilson et al. "Magnetic Reconnection and Plasma Dynamics in Two-Beam Laser-Solid Interactions". In: *Phys. Rev. Lett.* 97 (25 Dec. 2006), p. 255001. DOI: 10.1103/PhysRevLett.97.255001. URL: https://link.aps.org/doi/10.1103/PhysRevLett.97.255001.

[135] H.-S. Park et al. "High-Adiabat High-Foot Inertial Confinement Fusion Implosion Experiments on the National Ignition Facility". In: *Phys. Rev. Lett.* 112 (5 Feb. 2014), p. 055001. DOI: 10.1103/PhysRevLett.112.055001. URL: https://link.aps.org/doi/10.1103/PhysRevLett.112.055001.

[136] J. S. Pearlman and G. H. Dahlbacka. "Charge separation and target voltages in laser-produced plasmas". In: *Applied Physics Letters* 31.7 (1977), pp. 414–417. DOI: 10.1063/1.89729. eprint: https://doi.org/10.1063/1.89729. URL: https://doi.org/10.1063/1.89729.

[137] X. X. Pei et al. "Magnetic reconnection driven by Gekko XII lasers with a Helmholtz capacitor-coil target". In: *Physics of Plasmas* 23.3 (2016), p. 032125. DOI: 10.1063/1.4944928. eprint: https://doi.org/10.1063/1.4944928. URL: https://doi.org/10.1063/1.4944928.

[138] L. J. Perkins et al. "Two-dimensional simulations of thermonuclear burn in ignition-scale inertial confinement fusion targets under compressed axial magnetic fields". In: *Physics of Plasmas* 20.7 (2013), p. 072708. DOI: 10.1063/1.4816813. eprint: https://doi.org/10.1063/1.4816813. URL: https://doi.org/10.1063/1.4816813.

[139] T Pisarczyk et al. "Magnetized plasma implosion in a snail target driven by a moderate-intensity laser pulse". In: *Scientific reports* 8.1 (Dec. 2018), p. 17895. ISSN: 2045-2322. DOI: 10.1038/s41598-018-36176-8. URL: https://europepmc.org/articles/PMC6297252.

[140] A Poyé et al. "Dynamic model of target charging by short laser pulse interactions". In: *Physical Review E - Statistical, Nonlinear, and Soft Matter Physics* 92.4 (2015), p. 043107. ISSN: 15502376. DOI: 10.1103/PhysRevE.92.043107.

[141] A. Poyé et al. "Erratum: Physics of giant electromagnetic pulse generation in short-pulse laser experiments [Phys. Rev. E 91, 043106 (2015)]". In: *Phys. Rev. E* 97 (1 Jan. 2018), p. 019903. DOI: 10.1103/PhysRevE.97.019903. URL: https://link.aps.org/doi/10.1103/PhysRevE.97.019903.

[142] A. Poyé et al. "Physics of giant electromagnetic pulse generation in short-pulse laser experiments". In: *Phys. Rev. E* 91 (4 Apr. 2015), p. 043106. DOI: 10.1103/PhysRevE.91.043106. URL: https://link.aps.org/doi/10.1103/PhysRevE.91.043106.

[143] A. Poyé et al. "Thin target charging in short laser pulse interactions". In: *Phys. Rev. E* 98 (3 Sept. 2018), p. 033201. DOI: 10.1103/PhysRevE.98.033201. URL: https://link.aps.org/doi/10.1103/PhysRevE.98.033201.

[144] C. J. Price et al. "An in-vacuo optical levitation trap for high-intensity laser interaction experiments with isolated microtargets". In: *Review of Scientific Instruments* 86.3 (2015), p. 033502. DOI: 10.1063/1.4908285. eprint: https://doi.org/10.1063/1.4908285. URL: https://doi.org/10.1063/1.4908285.

[145] W. Priedhorsky et al. "Hard-X-Ray Measurements of 10.6-μm Laser-Irradiated Targets". In: *Phys. Rev. Lett.* 47 (23 Dec. 1981), pp. 1661–1664. DOI: 10.1103/PhysRevLett.47.1661. URL: https://link.aps.org/doi/10.1103/PhysRevLett.47.1661.

[146] E.M. Purcell and D.J. Morin. *Electricity and Magnetism*. Electricity and Magnetism. Cambridge University Press, 2013. ISBN: 9781107014022. URL: https://books.google.co.uk/books?id=A2rS5vlSFq0C.

[147] K. Quinn et al. "Laser-Driven Ultrafast Field Propagation on Solid Surfaces". In: *Phys. Rev. Lett.* 102 (19 May 2009), p. 194801. DOI: 10.1103/PhysRevLett.102.194801. URL: https://link.aps.org/doi/10.1103/PhysRevLett.102.194801.

[148] P. Raczka et al. "Strong electromagnetic pulses generated in high-intensity short-pulse laser interactions with thin foil targets". In: *Laser and Particle Beams* 35.4 (2017), pp. 677–686. DOI: 10.1017/S026303461700074X.

[149] A P L Robinson et al. "Radiation pressure acceleration of thin foils with circularly polarized laser pulses". In: *New Journal of Physics* 10.1 (Jan. 2008), p. 013021. DOI: 10.1088/1367-2630/10/1/013021. URL: https://doi.org/10.1088/1367-2630/10/1/013021.

[150] Markus Roth. "The diagnostics of ultra-short pulse laser-produced plasma". In: *Journal of Instrumentation* 6.09 (Sept. 2011), R09001–R09001. DOI: 10.1088/1748-0221/6/09/r09001. URL: https://doi.org/10.1088/1748-0221/6/09/R09001.

[151] Dean Curtis Rovang, Kenneth William Struve, and John Larry Jr Porter. "Megagauss field generation for high-energy-density plasma science experiments." In: (Oct. 2008). DOI: 10.2172/944387.

[152] E. Salt. *Transmission over Coaxial Cable Notes for EE456 University of Saskatchewan*. http://www.engr.usask.ca/classes/EE/456/slides/directional_coupler_notes_V2.pdf. Accessed: 01-06-2018.

[153] J J Santos et al. "Laser-driven platform for generation and characterization of strong quasi-static magnetic fields". In: *New Journal of Physics* 17.8 (Aug. 2015), p. 083051. DOI: 10.1088/1367-2630/17/8/083051. URL: https://doi.org/10.1088%2F1367-2630%2F17%2F8%2F083051.

[154] J. J. Santos et al. "Laser-driven strong magnetostatic fields with applications to charged beam transport and magnetized high energy-density physics". In: *Physics of Plasmas* 25.5 (2018), p. 056705. DOI: 10.1063/1.5018735. eprint: https://doi.org/10.1063/1.5018735. URL: https://doi.org/10.1063/1.5018735.

[155] F. Schillaci et al. "Numerical simulations to model laser-driven coil-capacitor targets for generation of kilo-Tesla magnetic fields". In: *AIP Advances* 8.2 (2018), p. 025103. DOI: 10.1063/1.5019219. eprint: https://doi.org/10.1063/1.5019219. URL: https://doi.org/10.1063/1.5019219.

[156] K. M. Schoeffler et al. "Magnetic-Field Generation and Amplification in an Expanding Plasma". In: *Phys. Rev. Lett.* 112 (17 Apr. 2014), p. 175001. DOI: 10.1103/PhysRevLett.112.175001. URL: https://link.aps.org/doi/10.1103/PhysRevLett.112.175001.

[157] G. G. Scott et al. "Optimization of plasma mirror reflectivity and optical quality using double laser pulses". In: *New Journal of Physics* 17 (2015). ISSN: 13672630. DOI: 10.1088/1367-2630/17/3/033027.

[158] J. F. Seely. "Pulsed megagauss fields produced by laser-driven coils". In: *Applied Physics B Photophysics and Laser Chemistry* 31.1 (1983), pp. 37–43. ISSN: 07217269. DOI: 10.1007/BF00693904.

[159] James C Simpson et al. "Simple analytic expressions for the magnetic field of a circular current loop". In: *NASA Technical Report* (2001).

[160] N Sinenian et al. "An empirical target discharging model relevant to hot-electron preheat in direct-drive implosions on OMEGA". In: *Plasma Physics and Controlled Fusion* 55.4 (Feb. 2013), p. 045001. DOI: 10.1088/0741-3335/55/4/045001. URL: https://doi.org/10.1088/0741-3335/55/4/045001.

[161] N. Sinenian et al. "Total energy loss to fast ablator-ions and target capacitance of direct-drive implosions on OMEGA". In: *Applied Physics Letters* 101.11 (2012). ISSN: 00036951. DOI: 10.1063/1.4752012.

[162] Stephen A. Slutz and Roger A. Vesey. "High-Gain Magnetized Inertial Fusion". In: *Phys. Rev. Lett.* 108 (2 Jan. 2012), p. 025003. DOI: 10.1103/PhysRevLett.108.025003. URL: https://link.aps.org/doi/10.1103/PhysRevLett.108.025003.

[163] R. A. Snavely et al. "Intense High-Energy Proton Beams from Petawatt-Laser Irradiation of Solids". In: *Phys. Rev. Lett.* 85 (14 Oct. 2000), pp. 2945–2948. DOI: 10.1103/PhysRevLett.85.2945. URL: https://link.aps.org/doi/10.1103/PhysRevLett.85.2945.

[164] J. A. Stamper. "Review on spontaneous magnetic fields in laser-produced plasmas: Phenomena and measurements". In: *Laser and Particle Beams* 9.4 (1991), pp. 841–862. DOI: 10.1017/S0263034600006595.

[165] J. A. Stamper et al. "Spontaneous Magnetic Fields in Laser-Produced Plasmas". In: *Phys. Rev. Lett.* 26 (17 Apr. 1971), pp. 1012–1015. DOI: 10.1103/PhysRevLett.26.1012. URL: https://link.aps.org/doi/10.1103/PhysRevLett.26.1012.

[166] Christopher J. Stolz. "The National Ignition Facility: the path to a carbon-free energy future". In: *Philosophical Transactions of the Royal Society A: Mathematical, Physical and Engineering Sciences* 370.1973 (2012), pp. 4115–4129. DOI: 10.1098/rsta.2011.0260. eprint: https://royalsocietypublishing.org/doi/pdf/10.1098/rsta.2011.0260. URL: https://royalsocietypublishing.org/doi/abs/10.1098/rsta.2011.0260.

[167] BC Stuart et al. "The Titan Laser at LLNL-Technical Digest (CD)". In: *Conference on Lasers and Electro-Optics/Quantum Electronics and Laser Science Conference and Photonic Applications Systems Technologies. Long Beach, California: Optical Society of America*. 2006, p. 33.

[168] M. Tabak et al. "Ignition and high gain with ultrapowerful lasers". In: *Physics of Plasmas* 1 (1994), pp. 1626–1634.

[169] V. T. Tikhonchuk et al. "Quasistationary magnetic field generation with a laser-driven capacitor-coil assembly". In: *Phys. Rev. E* 96 (2 Aug. 2017), p. 023202. DOI: 10.1103/PhysRevE.96.023202. URL: https://link.aps.org/doi/10.1103/PhysRevE.96.023202.

[170] O Tresca et al. "Controlling the properties of ultraintense laser–proton sources using transverse refluxing of hot electrons in shaped mass-limited targets". In: *Plasma Physics and Controlled Fusion* 53.10 (Sept. 2011), p. 105008. DOI: 10.1088/0741-3335/53/10/105008. URL: https://doi.org/10.1088/0741-3335/53/10/105008.

[171] Richard F. Voss and John Clarke. "Flicker ($\frac{1}{f}$) noise: Equilibrium temperature and resistance fluctuations". In: *Phys. Rev. B* 13 (2 Jan. 1976), pp. 556–573. DOI: 10.1103/PhysRevB.13.556. URL: https://link.aps.org/doi/10.1103/PhysRevB.13.556.

[172] C. A. Walsh et al. "Extended-magnetohydrodynamics in under-dense plasmas". In: *Physics of Plasmas* 27.2 (2020), p. 022103. DOI: 10.1063/1.5124144. eprint: https://doi.org/10.1063/1.5124144. URL: https://doi.org/10.1063/1.5124144.

[173] Weiwu Wang et al. “Efficient production of strong magnetic fields from ultraintense ultrashort laser pulse with capacitor-coil target”. In: *Physics of Plasmas* 25.8 (2018), p. 083111. DOI: 10.1063/1.5000991. eprint: https://doi.org/10.1063/1.5000991. URL: https://doi.org/10.1063/1.5000991.

[174] Yuwei Wang et al. “Investigation of a high power electromagnetic pulse source”. In: *Review of Scientific Instruments* 83.9 (2012), p. 094702. DOI: 10.1063/1.4751855. eprint: https://doi.org/10.1063/1.4751855. URL: https://doi.org/10.1063/1.4751855.

[175] D. White. “A Code to Model Electromagnetic Phenomena”. In: *Science and Technology Review* (Nov. 2007), pp. 3–9. URL: https://core.ac.uk/download/pdf/208904416.pdf.

[176] S. C. Wilks. “Simulations of ultraintense laser–plasma interactions”. In: *Physics of Fluids B: Plasma Physics* 5.7 (1993), pp. 2603–2608. DOI: 10.1063/1.860697. eprint: https://doi.org/10.1063/1.860697. URL: https://doi.org/10.1063/1.860697.

[177] S. C. Wilks et al. “Absorption of ultra-intense laser pulses”. In: *Phys. Rev. Lett.* 69 (9 Aug. 1992), pp. 1383–1386. DOI: 10.1103/PhysRevLett.69.1383. URL: https://link.aps.org/doi/10.1103/PhysRevLett.69.1383.

[178] S. C. Wilks et al. “Energetic proton generation in ultra-intense laser–solid interactions”. In: *Physics of Plasmas* 8.2 (2001), pp. 542–549. DOI: 10.1063/1.1333697. eprint: https://doi.org/10.1063/1.1333697. URL: https://doi.org/10.1063/1.1333697.

[179] Scott C. Wilks and William L. Kruer. “Absorption of ultrashort, ultra-intense laser light by solids and overdense plasmas”. In: *IEEE Journal of Quantum Electronics* 33.11 (1997), pp. 1954–1968. ISSN: 00189197. DOI: 10.1109/3.641310.

[180] G. J. Williams et al. “Laser intensity scaling of the magnetic field from a laser-driven coil target”. In: *Journal of Applied Physics* 127.8 (2020). ISSN: 10897550. DOI: 10.1063/1.5117162.

[181] L Willingale et al. “Proton probe measurement of fast advection of magnetic fields by hot electrons”. In: *Plasma Physics and Controlled Fusion* 53.12 (Nov. 2011), p. 124026. DOI: 10.1088/0741-3335/53/12/124026. URL: https://doi.org/10.1088/0741-3335/53/12/124026.

[182] N. C. Woolsey et al. “Collisionless shock and supernova remnant simulations on VULCAN”. In: *Physics of Plasmas* 8.5 (2001), pp. 2439–2445. DOI: 10.1063/1.1351831. eprint: https://doi.org/10.1063/1.1351831.

[183] Zamfir, N.V. "Extreme Light Infrastructure - Nuclear Physics (ELI-NP) European Research Centre". In: *EPJ Web of Conferences* 66 (2014), p. 11043. DOI: 10.1051/epjconf/20146611043. URL: https://doi.org/10.1051/epjconf/20146611043.

[184] Zhe Zhang et al. "Generation of strong magnetic fields with a laser-driven coil". In: *High Power Laser Science and Engineering* 6 (Jan. 2018). DOI: 10.1017/hpl.2018.33.

[185] Baojun Zhu et al. "Ultrafast pulsed magnetic fields generated by a femtosecond laser". In: *Applied Physics Letters* 113.7 (2018), pp. 1–5. ISSN: 00036951. DOI: 10.1063/1.5038047. URL: http://dx.doi.org/10.1063/1.5038047.

[186] C. Zhu et al. "Observation of the Evolution of a Current Sheet in a Solar Flare". In: *The Astrophysical Journal* 821.2 (Apr. 2016), p. L29. DOI: 10.3847/2041-8205/821/2/l29. URL: https://doi.org/10.3847/2041-8205/821/2/l29.

[187] James F. Ziegler, M.D. Ziegler, and J.P. Biersack. "SRIM – The stopping and range of ions in matter (2010)". In: *Nuclear Instruments and Methods in Physics Research Section B: Beam Interactions with Materials and Atoms* 268.11 (2010). 19th International Conference on Ion Beam Analysis, pp. 1818–1823. ISSN: 0168-583X. DOI: https://doi.org/10.1016/j.nimb.2010.02.091. URL: http://www.sciencedirect.com/science/article/pii/S0168583X10001862.